

ADDRESS OF PUBLISHER  
& EDITOR'S OFFICE:

GDAŃSK UNIVERSITY  
OF TECHNOLOGY

Faculty of Ocean Engineering  
& Ship Technology  
G. Narutowicza 11/12  
80-233 Gdańsk, POLAND

EDITORIAL STAFF:

Wiesław Tarełko  
| Editor in Chief  
Janusz Kozak  
| Deputy Editors-in-Chief  
Wojciech Litwin  
| Deputy Editors-in-Chief

Price:  
single issue: 25 PLN

Prices for abroad  
single issue:  
- in Europe EURO 15  
- overseas USD 20

WEB:  
[pg.edu.pl/pmr](http://pg.edu.pl/pmr)

e-mail : [pmr@pg.edu.pl](mailto:pmr@pg.edu.pl)

ISSN 1233-2585

## CONTENS

6	<b>Valeriy Nekrasov</b> <i>MEAN-SQUARE NON-LOCAL STABILITY OF SHIP IN STORM CONDITIONS OF OPERATION</i>
16	<b>Kun Dai, Yunbo Li</b> <i>MANOEUVRING PREDICTION OF KVLCC2 WITH HYDRODYNAMIC DERIVATIVES GENERATED BY A VIRTUAL CAPTIVE MODEL TEST</i>
27	<b>Lei Zhang, Jia-ning Zhang, Yu-chen Shang, Guo-xiang Dong, Wei-min Chen</b> <i>A PRACTICAL APPROACH TO THE ASSESSMENT OF WATERJET PROPULSION PERFORMANCE: THE CASE OF A WATERJET-PROPELLED TRIMARAN</i>
39	<b>Ozgur Ozguc</b> <i>STRUCTURAL ASSESSMENT OF THE HULL RESPONSE OF AN FPSO UNIT TO DROPPED OBJECTS: A CASE STUDY</i>
47	<b>Leszek Samson, Maciej Kahsin</b> <i>A METHOD TO DETERMINE THE TIGHTENING SEQUENCE FOR STANDING RIGGING OF A MAST</i>
56	<b>Wojciech Leśniewski</b> <i>SELECTED ISSUES OF HYBRID OUTBOARD MOTORS</i>
61	<b>Dongqin Li, Yili Zhang, Peng Li, Jingjing Dai, Guohuan Li</b> <i>AERODYNAMIC PERFORMANCE OF A NEW DOUBLE-FLAP WING SAIL</i>
69	<b>Rafał Szłapczyński, Hossein Ghaemi</b> <i>FRAMEWORK OF AN EVOLUTIONARY MULTI-OBJECTIVE OPTIMISATION METHOD FOR PLANNING A SAFE TRAJECTORY FOR A MARINE AUTONOMOUS SURFACE SHIP</i>
80	<b>Marcin Życzkowski, Joanna Szłapczyńska, Rafał Szłapczyński</b> <i>REVIEW OF WEATHER FORECAST SERVICES FOR SHIP ROUTING PURPOSES</i>
90	<b>Jacek Łubiński, Henryk Olszewski</b> <i>HYBRID FINITE ELEMENT METHOD DEVELOPMENT FOR OFFSHORE STRUCTURES' CALCULATION WITH THE IMPLEMENTATION OF INDUSTRY STANDARDS</i>
101	<b>Eugeniusz Kozaczka, Grażyna Grelowska</b> <i>AUTONOMOUS PLATFORM TO PROTECT MARITIME INFRASTRUCTURE FACILITIES</i>
109	<b>Paweł Dymarski, Czesław Dymarski, Ewelina Ciba</b> <i>STABILITY ANALYSIS OF THE FLOATING OFFSHORE WIND TURBINE SUPPORT STRUCTURE OF CELL SPAR TYPE DURING ITS INSTALLATION</i>

**ADDRESS OF PUBLISHER  
& EDITOR'S OFFICE:**

**GDAŃSK UNIVERSITY  
OF TECHNOLOGY**

**Faculty of Ocean Engineering  
& Ship Technology  
G. Narutowicza 11/12  
80-233 Gdańsk, POLAND**

- 117 **Wojciech Zeńczak, Agata Krystosik- Gromadzińska**  
*IMPROVEMENTS TO A FIRE SAFETY MANAGEMENT SYSTEM*
- 124 **Andrzej Tomporowski, Ali Al-Zubiedy, Józef Flizikowski, Weronika Kruszelnicka, Patrycja Bałdowska-Witos, Jacek Rudnicki**  
*ANALYSIS OF THE PROJECT OF INNOVATIVE FLOATING TURBINE*
- 134 **Przemysław Król**  
*BLADE SECTION PROFILE ARRAY LIFTING SURFACE DESIGN METHOD FOR MARINE SCREW PROPELLER BLADE*
- 142 **Paweł Grudziński, Konrad Konowalski**  
*COMPARATIVE STUDIES OF THE SEATINGS OF PROPULSION PLANTS AND AUXILIARY MACHINERY ON CHOCKS MADE OF METAL AND CAST OF RESIN PART I. MOUNTING ON STEEL CHOCKS*
- 149 **Oleksandr Cherednichenko, Serhiy Serbin, Marek Dzida**  
*INVESTIGATION OF THE COMBUSTION PROCESSES IN THE GAS TURBINE MODULE OF AN FPSO OPERATING ON ASSOCIATED GAS CONVERSION PRODUCTS*
- 157 **Teresa Abramowicz-Gerigk, Zbigniew Burciu**  
*DESIGN AND OPERATIONAL INNOVATIONS IN ADAPTING THE EXISTING MERCHANT RIVER FLEET TO COST-EFFECTIVE SHIPPING*
- 165 **Xian-wei Kong, Lei Ding, Hai-cheng Liu, Jing Qu, Xiao-song Li**  
*EFFECTS OF WATER INTAKE LAYOUT ALONG THE WHARF SHORELINE ON SHIPS*

---

## Editorial

POLISH MARITIME RESEARCH is the scientific journal with a worldwide circulation. This journal is published quarterly (four times a year) by Gdansk University of Technology (GUT). On September, 1994, the first issue of POLISH MARITIME RESEARCH was published. The main objective of this journal is to present original research, innovative scientific ideas, and significant findings and application in the field of :

### Naval Architecture, Ocean Engineering and Underwater Technology,

The scope of the journal covers selected issues related to all phases of product lifecycle and corresponding technologies for offshore floating and fixed structures and their components.

All researchers are invited to submit their original papers for peer review and publications related to methods of the design; production and manufacturing; maintenance and operational processes of such technical items as:

- all types of vessels and their equipment,
- fixed and floating offshore units and their components,
- autonomous underwater vehicle (AUV) and remotely operated vehicle (ROV).

We welcome submissions from these fields in the following technical topics:

- ship hydrodynamics: buoyancy and stability; ship resistance and propulsion, etc.,
  - structural integrity of ship and offshore unit structures: materials; welding; fatigue and fracture, etc.,
  - marine equipment: ship and offshore unit power plants: overboarding equipment; etc.
- 

### Scientific Board

**Chairman : Prof. JERZY GIRTLEK - Gdańsk University of Technology, Poland**

**Vice-chairman : Prof. CARLOS GUEDES SOARES, Universidade de Lisboa, Lisbon, Portugal**

**Vice-chairman : Prof. MIROSŁAW L. WYSZYŃSKI - University of Birmingham, United Kingdom**

<b>Prof. POUL ANDERSEN</b> Technical University of Denmark Kongens Lyngby Denmark	<b>Prof. STOJCE DIMOV ILCEV</b> Durban University of Technology Durban South Africa	<b>Prof. JERZY EDWARD MATUSIAK</b> Aalto University Espoo Finland
<b>Prof. JIAHN-HORNG CHEN</b> National Taiwan Ocean University Keelung Taiwan	<b>Prof. YORDAN GARBATOV</b> Universidade de Lisboa, Lisbon Portugal	<b>Prof. JERZY MERKISZ</b> Poznan University of Technology Poznan Poland
<b>Prof. VINCENZO CRUPI</b> University of Messina Messina Italy	<b>Prof. STANISŁAW GUCMA</b> Maritime University of Szczecin Szczecin Poland	<b>Prof. VALERI NIEKRASOV</b> Admiral Makarov National University of Shipbuilding Mikolaiv Ukraine
<b>Prof. MAREK DZIDA</b> Gdansk University of Technology Gdansk Poland	<b>Prof. ANTONI ISKRA</b> Poznan University of Technology Poznan Poland	<b>Prof. JOZEF SZALA</b> UTP University of Science and Technology Bydgoszcz Poland
<b>Prof. ODD MAGNUS FALTINSEN</b> Norwegian University of Science and Technology Trondheim Norway	<b>Prof. JAN KICINSKI</b> Institute of Fluid-Flow Machinery - Polish Academy of Sciences Gdansk Poland	<b>Prof. TADEUSZ SZELANGIEWICZ</b> Maritime University of Szczecin Szczecin Poland
<b>Prof. MASSIMO FIGARI</b> University of Genova Genova Italy	<b>Prof. ZBIGNIEW KORCZEWSKI</b> Gdansk University of Technology Gdansk Poland	<b>Prof. DRACOS VASSALOS</b> University of Strathclyde Glasgow United Kingdom
<b>Prof. HASSAN GHASSEMI</b> Amirkabir University of Technology Tehran Iran	<b>Prof. JOZEF LISOWSKI</b> Gdynia Maritime University Gdynia Poland	



## GDAŃSK UNIVERSITY OF TECHNOLOGY FACULTY OF OCEAN ENGINEERING AND SHIP TECHNOLOGY

- 1200 students
- 100 academic Staff
- 35 technical staff
- 3 BSc Courses (7 semesters)
  - Ocean Engineering
  - Power Engineering (in cooperation with Mechanical Eng. and Electrical Eng. faculties), both in Polish and English
  - Marine Transport
- 4 MSc courses (3 or 4 semesters)
  - Ocean Engineering, both in Polish and English
  - Power Engineering (in cooperation with Mechanical Eng. and Electrical Eng. faculties)
  - Marine Transport
  - Coastal and Offshore Engineering (in cooperation with Faculty of Civil and Environmental Eng.), both in Polish and English
- New and modern facilities, including new towing tank, ship technology, equipment, systems and power plants laboratories, propulsion system simulator and access to up-to-date CAE and CFD software
- Close cooperation with ship design offices, shipyards, ports, terminals, manufacturers and industrial partners like as GE or REMONTOWA Holding, as well classifications societies including PRS, DNV.GL, ABS and RINA
- Vast possibilities for students activities, including Students Research Centre in Iława on a large lake, Student Scientific Clubs KORAB, PIKSEL and SYNERTECH, participation in international solar regatta and waterbike regatta
- Well-indexed open-access Polish Maritime Research!

### FACULTY OF OCEAN ENGINEERING AND SHIP TECHNOLOGY

Gdańsk University of Technology  
address: G. Narutowicza 11/12, 80-233 Gdańsk, Poland  
phone: +48 58 3471567  
fax: +48 58 3486372  
e-mail: [dziekoce@pg.edu.pl](mailto:dziekoce@pg.edu.pl)  
[www.pg.edu.pl/international/study-in-english](http://www.pg.edu.pl/international/study-in-english)

[www.oio.pg.edu.pl](http://www.oio.pg.edu.pl)





## **MSc IN OCEAN ENGINEERING**

Specialization: Ship Technology and Offshore Engineering

Specialization: Marine Engineering and Offshore Energy

➤ Degree to be obtained	▪ Master of Science
➤ Duration	▪ 2 years (4 semesters)
➤ Language	▪ English
➤ ECTS points	▪ 120 ECTS
➤ Programme description	▪ The aim is providing advanced engineering knowledge in the field of Ocean Engineering including two main specializations: Ship Technology and Offshore Engineering, Marine Engineering and Offshore Energy. Students will gain detailed knowledge within the subjects such as Marine Applied Informatics, CAE and Design Tools, Ship and Offshore Power Systems Design, Dynamics of Ship and Offshore Structures, Advanced Mechanics of Marine Structures, Ship and Offshore Structures Design, Marine and Offshore Systems and Equipments, Modelling and Simulation in Ocean Engineering, Reliability, Safety and Risk Analysis, Advanced Material Engineering and Manufacturing Technology, Marine and Intermodal Transport, Finance and Economy in Engineering Design, Maritime Environmental Protection and Optimisation in Engineering Design. Students deal with a real design process and prepare the final thesis in cooperation with the industrial partners of the Faculty.
➤ Entry requirements	▪ B.Sc. in Naval Architecture, Marine Engineering, Mechanical Engineering, Civil Engineering, Energy/ Power Engineering, Electrical Engineering, Transport (or similar fields of study)
➤ Comments	<ul style="list-style-type: none"> <li>▪ The programme is supported and organised in cooperation with Det Norske Veritas – Germanischer Lloyd (DNV GL)</li> <li>▪ Details of the programme and admission process are available online: <a href="http://oio.pg.edu.pl/en">oio.pg.edu.pl/en</a></li> </ul>



## MEAN-SQUARE NON-LOCAL STABILITY OF SHIP IN STORM CONDITIONS OF OPERATION

Valeriy Nekrasov

Admiral Makarov National University of Shipbuilding, Ukraine  
Gdańsk University of Technology, Poland

### ABSTRACT

*The purpose of the paper is to create a method for studying nonlocal stability in the mean and in the mean square of the ship, positioned on the beam of an intensive wind-waves mode, which is based on the use of the correlation theory of random functions close to continuous Markov processes. With the help of this method and the integral formula of event probability, a method for determining the reliability indicator of the ship in respect of the existing wind-waves excitations of the operating area is formed. An example of investigating the nonlinear motion of the ship, determining its local and nonlocal stability in the first approximation of the theory of considered random functions, is given. Such approximation uses correlation theory with models of acting excitations represented by the generalised derivatives of the Wiener process. Moreover, special attention is paid to reflecting the connection of the proposed methods for investigating the ship stability under constantly acting random excitations with the traditional methods of studying ship stability at small and large inclinations. The established connection defines the proposed methods as a development of the traditional methods of ship stability deterministic theory during the transition to its formation in the class of random functions, with the addition to these methods of the missing link of determining the level of reliability of ships towards the acting wind-waves excitations of the operation area.*

**Keywords:** wind-waves mode; local and nonlocal stability; nonlocal stability in mean; nonlocal stability in mean square; reliability indicator

### INTRODUCTION

This work is devoted to the presentation of methods for determining the probabilistic characteristics of ships' nonlinear motion processes and their stability based on the application of the methods of random functions close to continuous Markov random processes. First, the most complete consideration of the application of such methods to solving problems of determining the probabilistic characteristics of ship motion and the stability of motion has already been given in the monograph by the current paper's author [5]. In this monograph, the Fokker-Planck-Kolmogorov equation and the kinetic equations of a more complex structure are used to determine the probability

densities and characteristic functions of nonlinear ship motion. The characteristics of the amplitudes and phases of nonlinear motion and parametrically excited random oscillations of the ships are studied as well. It is shown that a significant extension of the method of random amplitudes and phases is the method of statistical moments. Using this method, the investigation of ship nonlinear motion stability is effective not only at small, but also at large inclinations. Subsequent development of the proposed method is only partially described in [6-8].

In this work, the results obtained in [5-8] are combined into a united complex of the investigation of ship stability and reliability under constantly acting random wind-waves excitations. The first approximation of the developed

theory, which operates with the first two statistical moments of random functions, is presented. For this, the concepts of a ship's local and nonlocal stability in the mean and in the mean square are introduced. The criteria of these types of stability and the relationship between them are given. Particular attention is paid to the connection of the proposed methods with traditional methods of studying the stability of ships and to determining their reliability indicators under the wind-waves action of the operation area.

## FEATURES OF TRADITIONAL METHODS OF SHIP STABILITY THEORY

The study of ship stability under the action of stationary applied heeling moment is presented in Fig. 1. This figure shows that the local stability of the equilibrium position of the ship at the roll angle  $\theta_s$  under the action of heeling moment  $M_h$  is determined by the method of additional small perturbations, and the nonlocal stability of the ship under the gradual increase in the heeling moment from the initial equilibrium position  $\theta = 0$  in calm water is determined by the region of the existence of real solutions of the equation of acting moments realised in the interval  $[-M_{hmax}, M_{hmax}]$ .

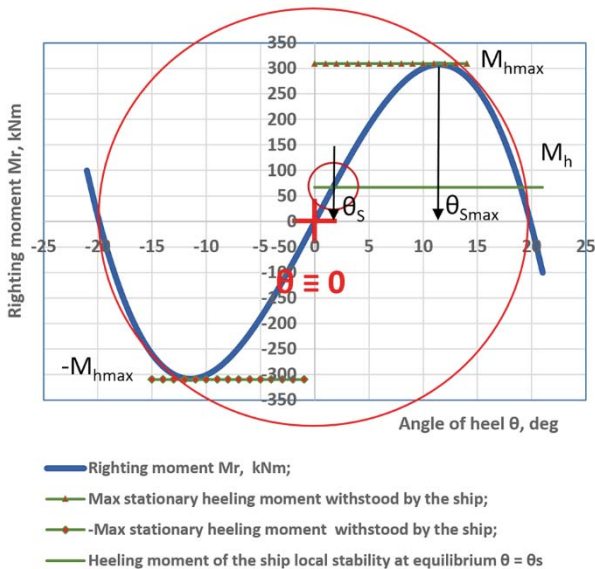


Fig. 1. Local and nonlocal (maintaining position of ship in the neighbourhood of equilibrium position in calm water  $\theta \equiv 0$ ) stability when stationary heeling moment is applied to the ship

The investigation of ship stability under the action of dynamically applied heeling moment is shown in Fig. 2. This figure determines that, under the action of dynamically applied heeling moment, the region of nonlocal stability of the ship (maintaining the position of the ship in the neighbourhood of the equilibrium position in calm water  $\theta \equiv 0$ ) is determined by the region of the existence of real solutions of the equation of works (energies) of the operating moments.

Thus, the traditional study of ship stability and determination of the boundaries  $\Gamma_s$  and  $\Gamma_d$  of regions  $\Omega_s$  and  $\Omega_d$  of its nonlocal stability under the action of stationary and nonstationary forces uses:

- nonlinear equation of roll inclinations of ship under the action of heeling moment

$$(J_x + \mu_{44})\ddot{\theta} + M_r(\theta) = M_h(t) \quad (1)$$

- equation of ultimate ship position under the stationary action of external forces

$$M_r(\theta)_{max} - M_h = 0; \quad (2)$$

- equation of the maximal possible equality of works of heeling and righting moments (energies of external forces and potential resources of ship) under the dynamic action of heeling moment

$$A_r(\theta)|_0^{\theta_{Dmax}} - A_h(\theta)|_0^{\theta_{Dmax}} = 0. \quad (3)$$

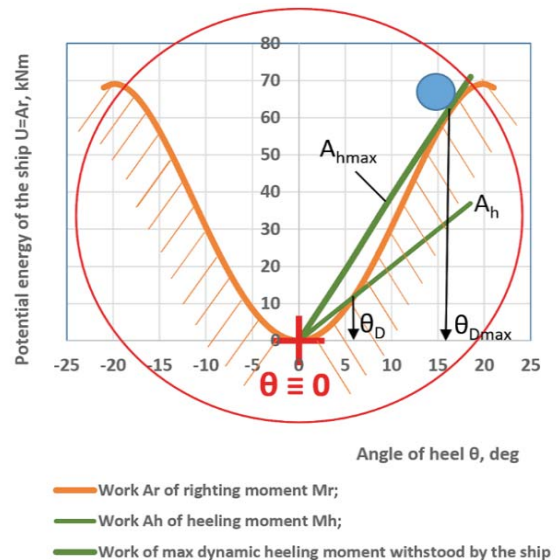


Fig. 2. Nonlocal stability of ship under the action of dynamically applied heeling moment

## METHOD FOR SOLVING THE PROBLEM OF SHIP STABILITY IN STORM AS PROBLEM OF LOCAL AND NONLOCAL STABILITY IN THE MEAN SQUARE

### GENERAL POSITIONS

The method uses:

- stochastic nonlinear differential equations simulating the processes of wind-waves actions and ship motion, which are built on the basis of representing the acting forces by

segments of multi-dimensional Taylor series in degrees of the displacements and velocities of the ship and in degrees of the kinematic characteristics of the wind-waves fields in the neighbourhood of the ship's equilibrium position in calm water [5];

- presentation of initial acting excitations in stochastic models of external wind-waves actions in the form of “white noise” in the sense of Stratonovich [9], i.e., in the form of random processes with finite power values;
- conditions of the Germaidze-Krasovsky theorem on the stability of dynamic systems under constantly acting excitations that are bounded in the mean [3].

## EQUATIONS FOR THE PROBABILISTIC CHARACTERISTICS OF THE SHIP MOTION

Under the stated preconditions, the system of nonlinear differential equations of ship motion under the action of wind and waves is written in the following general form [5]:

$$\frac{dY}{dt} = F(Y, X, \psi, t)$$

where  $\psi(t)$  is the vector of generalised derivatives of the Wiener process (“white noise”);  $X(t)$  is the vector of the processes of wind-waves actions;  $Y(t)$  is the vector of the ship's motion processes.

To determine the probabilistic characteristics of ship motion processes  $Y(t)$  based on the stochastic equations (4) of the motion of the considered dynamic system “ship-excited media”, an infinite system of equations for statistical moments is constructed. The construction of the system is carried out either using the equation for the characteristic function, or using the Fokker-Planck-Kolmogorov equation [5]. The presence of nonlinearities in equations of motion (4) leads to the appearance in the subsystems of equations for statistical moments of lower orders 1 ...  $m$  statistical moments of higher orders  $m + 1$  ...  $n$ . If we restrict ourselves to considering statistical moments no higher than the order of  $p$ , this circumstance will require the closure of the considered subsystems of equations. The closure is carried out on the basis of introducing the hypothesis about the nature of the distribution law of the processes under consideration. This can be the normal distribution when the problem is considered within the framework of the correlation theory. Under fuller use of the mentioned positions of the Germaidze-Krasovsky theorem, it is the beta distribution, the Pearson distribution of type I, etc. [8].

In a first approximation, the approximation of the correlation theory of random functions, the closure of the considered subsystems is carried out by expressing the statistical moments of higher orders through the statistical moments of lower orders using relations between the moments of the normal distribution. As a result, the following system of nonlinear differential equations is formed:

$$\frac{d\alpha_1}{dt} = Q_1(\alpha_1, \mu_2, G_1, G_2, t); \quad (5)$$

$$\frac{d\mu_2}{dt} = Q_2(\alpha_1, \mu_2, G_1, G_2, t), \quad (6)$$

where  $\alpha_1(t)$  is the vector of statistical moments of the first order, i.e., the vector of the expected values of the processes of motion of the dynamic system “ship-environment”;  $\mu_2(t)$  is the vector of second-order central moments, which includes variances (dispersions) and mutual correlation moments of the dynamic system processes;  $G_1(t)$  and  $G_2(t)$  are the vectors of the first- and second-order intensity coefficients characterising the average values and average powers of the acting excitations (in limited cases, these vectors are represented by random functions with non-differentiable realisations, by “white noise”  $\psi(t)$ ).

Compared to the characteristic temporary constants of the ship, such as the period of its free oscillations and the time of their relaxation, the storm develops very slowly, in a quasi-stationary way. Due to the quasi-stationary nature of the random wind-waves processes acting on the ship in the storm, the system of differential equations for statistical moments (5) is transformed into the following system of nonlinear algebraic equations:

$$Q_1(\alpha_1, \mu_2, G_1, G_2) = 0; \quad (7)$$

$$Q_2(\alpha_1, \mu_2, G_1, G_2) = 0, \quad (8)$$

The solution of the system of algebraic equations (7)–(8) for given intensities of external excitations  $G_1^{(0)}, G_2^{(0)}$  determines the quasi-stationary mode of the ship motion with expected values  $\alpha_1^{(0)}$  and statistical moments of second-order  $\mu_2^{(0)}$ .

The solution to the system of equations (7)–(8) is found using nonlinear programming methods [1], which are applied in the process of solving the following problem of unconstrained minimisation of the objective function:

$$OF_1(\alpha_1, \mu_2) = Q_1^2(\alpha_1, \mu_2) + Q_2^2(\alpha_1, \mu_2) \rightarrow \min \quad (9)$$

for fixed values of  $G_1^{(0)}, G_2^{(0)}$  and variations of the independent variables  $\alpha_1^{(0)}, \mu_2^{(0)}$ .

## RESEARCHING SHIP MOTION MODES STABILITY

If, in the formation of subsystems of equations for statistical moments, we restrict ourselves to considering statistical moments of order no more than  $p$ , then the corresponding stability investigation will be called the investigation of  $p$ -stability [2]. In this case, local and nonlocal  $p$ -stability should be distinguished.

In the first approximation, the study of  $p$ -stability is carried out in the framework of the correlation theory of random functions, which operates with two types of statistical moments: the first and the second orders. In this case  $p = 2$ .

In the investigation of local stability of this type, small perturbations are introduced into the quasi-stationary mode of ship motion under consideration, and statistical moments  $\alpha_1^{(0)}, \mu_2^{(0)}$  acquire additional increments  $\Delta\alpha_1(t)$  and  $\Delta\mu_2(t)$ .

The values of the additional increments of the moments  $\Delta\alpha_1(t)$  and  $\Delta\mu_2(t)$  are determined by the solution of the following system of equations:

$$\frac{d\Delta\alpha_1}{dt} = \frac{dQ_1}{d\alpha_1}\Delta\alpha_1 + \frac{dQ_1}{d\mu_2}\Delta\mu_2; \quad (10)$$

$$\frac{d\Delta\mu_2}{dt} = \frac{dQ_2}{d\alpha_1}\Delta\alpha_1 + \frac{dQ_2}{d\mu_2}\Delta\mu_2 \quad (11)$$

For this system of differential equations, the roots  $\lambda_{il}$ ,  $i = 1, 2; l = 1, 2, 3, \dots, N$  of the characteristic equation are determined:

$$Ch(\lambda) = 0. \quad (12)$$

In accordance with Lyapunov theory [4], the quasi-stationary motion of the ship, determined by the probabilistic characteristics  $\alpha_1^{(0)}, \mu_2^{(0)}$ , is stable if the real parts of the roots of the characteristic equation (12) are negative, i.e.  $\text{Re}[\lambda_{il}] < 0$ .

According to the accepted terminology [2], if the solution of the subsystem of equations for expected values (5) satisfies the noted Lyapunov stability requirements, then the solution of the original differential equations (4) is called stable in the mean. Correspondingly stable in the mean is the process of the ship's motion. If the noted stability requirements according to Lyapunov are satisfied for the solution of the equation of the second-order statistical moments (6), then the solution of the original differential equations (4) is called stable in the mean square. From stability in the mean square follows stability in the mean [2]. Obviously, in all the considered cases, the local stability of the quasi-stationary modes of ship motion is meant.

For investigation of the nonlocal stability, a ship that is locally stable in the equilibrium position in calm water at  $\theta = 0$  is considered. The nonlocal stability of this equilibrium position of the ship under storm conditions can be investigated by gradually increasing the intensities of the existing wind-waves excitations in the ship motion equations (4). Obviously, such increase of excitations without the loss of ship stability, as in the traditional theory of ship stability represented by equations (1)–(3), can be realised only in the region of the existence of the real solutions of equations (7)–(8) for statistical moments. In this region, the kinematic characteristics of the ship movement are represented by surfaces having extremes. Therefore, the limiting values of real solutions and, correspondingly, the boundary  $\Gamma$  of the

region  $\Omega$  of ship nonlocal stability will be at the extrema of these surfaces.

In this regard, the boundary  $\Gamma_1$  of the region  $\Omega_1$  of nonlocal stability in the mean of ship equilibrium position  $\theta \equiv 0$  as the boundary of the stability region of the average roll angle  $\alpha_1$  is determined using the necessary condition for the extremum of the surface  $Q_1$ , presented in the form

$$\frac{\partial Q_1(\alpha_1, \mu_2, G_1, G_2)}{\partial \alpha_1} = 0. \quad (13)$$

The second main characteristic of the ship roll motion is the variance of the roll oscillations  $\mu_2$ . Therefore, the boundary  $\Gamma_2$  of the region  $\Omega_2$  of nonlocal stability in the mean square of the ship is found using the necessary condition for the extremum of the surface  $Q_2$ :

$$\frac{\partial Q_2(\alpha_1, \mu_2, G_1, G_2)}{\partial \mu_2} = 0. \quad (14)$$

In the sequence of increasing intensities of the acting wind excitations  $G_1^{(0)}$ , the boundary  $\Gamma_2$  is determined by solving the corresponding sequence of nonlinear programming tasks with the objective function

$$OF_2(\alpha_1, \mu_2, G_1, G_2) = Q_1^2(\alpha_1, \mu_2, G_1, G_2) + Q_2^2(\alpha_1, \mu_2, G_1, G_2) + \left(\frac{\partial Q_2(\alpha_1, \mu_2, G_1, G_2)}{\partial \mu_2}\right)^2 \quad (15)$$

under variations of the independent variables  $\alpha_1^{(0)}, \mu_2^{(0)}$  and  $G_2^{(0)}$ .

It was shown in [5,6] that the regions of nonlocal stability  $\Omega_1, \Omega_2$  and their boundaries  $\Gamma_1, \Gamma_2$  should be considered not only in the space of kinematic characteristics  $\alpha, \mu$ , but also in the space of the parameters of the excitations  $G_1, G_2$ .

If the main parameters of the acting wind-waves excitations are the average wind velocity  $V$ , significant wave height  $H_{1/3}$  and average period of sea  $T$ , then the nonlocal stability regions  $\Omega_1, \Omega_2$  and their boundaries  $\Gamma_1, \Gamma_2$  should be considered as functions of the variables  $V, H_{1/3}$ , and  $T$ . Such functions are determined as a result of solving a sequence of nonlinear programming tasks for the objective function (15).

In the general case, depending on the structure of the initial nonlinear ship motion equations, in the regions  $\Omega_1, \Omega_2$  of nonlocal stability defined by the boundaries  $\Gamma_1, \Gamma_2$  of real solutions of the equations for statistical moments, locally unstable ship motion modes may appear. Therefore, a generalised approach to the investigation of the stability of ship nonlinear motion processes should include not only a search for the boundaries of real solutions of the equations for statistical moments, but also a check of the local stability of solutions within these regions. This approach is implemented through a joint investigation of the local and nonlocal stability of the ship at the stages of increasing the intensity of constantly acting wind-wave excitations.

## METHOD OF DETERMINING THE RELIABILITY OF SHIP WITH LOSSES OF NONLOCAL STABILITY IN THE MEAN SQUARE

Consideration is given to ship failures associated with capsizing under the action of wind and waves, i.e. failures which are caused by the losses of nonlocal stability of the ship equilibrium position  $\theta \equiv 0$ .

In this case, for the  $k$ th state of the weight load and the heading angle  $\varphi$  of the ship meeting with the wind and waves in the  $l$ th geographical area of its operation, the weather conditions in which are determined by the joint probability density of the long-term (regime) distribution of wind and wave characteristics  $f(V, H_{1/3}, T)$ , the probability of the ship nonlocal stability remaining in the mean square is determined by the expression [5,6]

$$P_{kl}(\varphi) = \frac{\Gamma_2(\bar{V}, H_{1/3}, T)}{\int_0^{\Gamma_2(\bar{V}, H_{1/3}, T)} \int_0^{\Gamma_2(\bar{V}, H_{1/3}, T)} f(\bar{V}, H_{1/3}, T) d\bar{V} dH_{1/3}, dT, \quad (16)$$

where  $\Gamma_2[V, H_{1/3}, T]$  is the boundary surface of the region  $\Omega_2\{V, H_{1/3}, T\}$  of the values of parameters of the wind-waves modes withstood by the ship.

### AN EXAMPLE OF SOLVING THE PROBLEM OF SHIP NONLOCAL STABILITY IN THE MEAN SQUARE

We consider a ship in beam seas ( $\varphi = 90$  deg).

It is assumed that the frequency bandwidth of this ship is relatively small, therefore its roll motion is implemented in accordance with the solution of the following equation:

$$(J_x + \mu_{44})\ddot{\theta} + \lambda_{44}^{(1)}\dot{\theta} + \lambda_{44}^{(3)}\theta^3 + Dh_1\dot{\theta} + Dh_3\theta^3 = M_h^{wind}(t) + M_h^{wave}(t), \quad (17)$$

where the heeling moment from the wind action  $M_h^{wind}(t)$  is a function of the wind velocity  $V = \bar{V} + \tilde{V}(t)$ , and its component  $\tilde{M}_h^{wind}(t)$ , caused by the pulsations of the wind velocity  $\tilde{V}(t)$ , and the heeling moment from the waves action  $\tilde{M}_h^{wave}(t)$  are represented by "white noise" in the sense of Stratonovich [9].

After introducing the notation  $\theta = Y_1$ ;  $\dot{\theta} = Y_2$ , equation (17) is written in the form:

$$\begin{aligned} \frac{dY_1}{dt} &= a_{1,1_2} Y_2; \\ \frac{dY_2}{dt} &= a_{2,1_1} Y_1 + a_{2,3_1} Y_1^3 + a_{2,1_2} Y_2 + a_{2,3_2} Y_2^3 \\ &\quad + X_2(t), \end{aligned} \quad (18)$$

where

$$\begin{aligned} a_{1,1_2} &= 1; \\ a_{2,1_1} &= \frac{Dh_1}{J_x + \mu_{44}}; \quad a_{2,3_1} = \frac{Dh_3}{J_x + \mu_{44}}; \\ a_{2,1_2} &= \frac{\lambda_{44}^{(1)}}{J_x + \mu_{44}}; \quad a_{2,3_2} = \frac{\lambda_{44}^{(3)}}{J_x + \mu_{44}}; \\ X_2(t) &= X_h^{wind}(t) + X_h^{wave}(t); \\ X_h^{wind}(t) &= \frac{M_h^{wind}(t)}{J_x + \mu_{44}}; \quad X_h^{wave}(t) = \frac{M_h^{wave}(t)}{J_x + \mu_{44}}. \end{aligned}$$

The probabilistic characteristics of the nonlinear roll motion of the ship are considered as:

– initial statistical moments of the first order or average values of roll angles and angular velocities

$$\mathbf{M}[\theta] = \alpha_{1_1}, \quad \mathbf{M}[\dot{\theta}] = \alpha_{1_2};$$

– initial statistical moments of the second order

$$\mathbf{M}[\theta^2] = \alpha_{2_1}, \quad \mathbf{M}[\dot{\theta}^2] = \alpha_{2_2}, \quad \mathbf{M}[\theta\dot{\theta}] = \alpha_{1_1 1_2};$$

– central moments of the second order or roll angles and angular velocities dispersions

$$\mathbf{M}[\tilde{\theta}^2] = \mu_{2_1}, \quad \mathbf{M}[\tilde{\dot{\theta}}^2] = \mu_{2_2}.$$

Based on the system of stochastic differential equations (18), an appropriate system of equations for the statistical moments of the first and second orders is constructed. After the closure of this system of equations for statistical moments, using the relations for the moments of the normal distribution, we have [5]

$$\begin{aligned} \frac{d\alpha_{1_1}}{dt} &= a_{1,1_2} \alpha_{1_2}; \\ \frac{d\alpha_{1_2}}{dt} &= a_{2,1_1} \alpha_{1_1} + a_{2,3_1} (3\alpha_{1_1} \alpha_{2_1} - 2\alpha_{1_1}^3) \\ &\quad + a_{2,1_2} \alpha_{1_2} + a_{2,3_2} (3\alpha_{1_2} \alpha_{2_2} - 2\alpha_{1_2}^3) + G_{1_2}(t); \\ \frac{1}{2} \frac{d\alpha_{2_1}}{dt} &= a_{1,1_2} \alpha_{1_1 1_2}; \\ \frac{d\alpha_{1_1 1_2}}{dt} &= a_{1,1_2} \alpha_{2_2} + a_{2,1_1} \alpha_{2_1} \\ &\quad + a_{2,3_1} (3\alpha_{2_1}^2 - 2\alpha_{1_1}^4) + a_{2,1_2} \alpha_{1_1 1_2} \\ &\quad + a_{2,3_2} (3\alpha_{1_1 1_2} \alpha_{2_2} - 2\alpha_{1_1} \alpha_{1_2}^3) + \alpha_{1_1} G_{1_2}(t); \\ \frac{1}{2} \frac{d\alpha_{2_2}}{dt} &= a_{2,1_1} \alpha_{1_1 1_2} + a_{2,3_1} (3\alpha_{1_1 1_2} \alpha_{2_1} - 2\alpha_{1_1}^2 \alpha_{1_2}) + a_{2,1_2} \alpha_{2_2} + a_{2,3_2} (3\alpha_{2_2}^2 - 2\alpha_{1_2}^4) + \alpha_{1_2} G_{1_2}(t) \\ &\quad + \frac{1}{2} G_{2_2}(t), \end{aligned} \quad (19)$$

where  $G_{1_2}(t)$  and  $G_{2_2}(t)$  are the coefficients of the intensity of the first and the second orders [9].

The assumption that the storm is developing slowly allows us to transform the system of differential equations (19) into the following system of nonlinear algebraic equations to determine the probabilistic characteristics of the quasi-stationary modes of ship roll motion [5]:

$$\begin{aligned} \mathbf{M}[\dot{\theta}] &= \alpha_{12} = 0; \quad \mathbf{M}[\theta\dot{\theta}] = \alpha_{112} = 0; \\ -Dh_1 \mathbf{M}[\theta] - Dh_3(\mathbf{M}[\theta])^3 \\ -3 Dh_3 \mathbf{M}[\theta] \mathbf{M}[\dot{\theta}^2] + G_{12}(\bar{V})(J_x + \mu_{44}) &= 0; \\ \frac{1}{2} (J_x + \mu_{44}) \mathbf{M}[\dot{\theta}^2] \\ -\frac{1}{2} \left\{ Dh_1 \mathbf{M}[\dot{\theta}^2] + 3 Dh_3 (\mathbf{M}[\dot{\theta}^2])^2 \right. \\ \left. + 3 Dh_3 (\mathbf{M}[\theta])^2 \mathbf{M}[\dot{\theta}^2] \right\} &= 0; \end{aligned} \quad (20)$$

$$-\lambda_{44}^{(1)} \mathbf{M}[\dot{\theta}^2] - 3\lambda_{44}^{(3)} (\mathbf{M}[\dot{\theta}^2])^2 + \frac{1}{2} [G_{22}(\bar{V}) + G_{22}(H_{1/3})](J_x + \mu_{44}) = 0,$$

where

$$G_{12}(\bar{V})(J_x + \mu_{44}) = \mathbf{M}[M_h^{wind}(\bar{V})] = (\bar{V})^2 / 2c(z_s)(z_s - z_h)A_s$$

is the average heeling moment of the wind action;

$c(z_s)$  is the coefficient of air flow resistance,  $A_s$  and  $z_s$  are the sail area and the applicate of the sail area centre,  $z_h$  is the applicate of the line of the drift force action;

$$G_{22}(\bar{V}) = [\rho_A (\bar{V})^2 / 2c(z_s)(z_s - z_h)A_s]^2 \times (\omega_\theta)(J_x + \mu_{44})^{-2}$$

is the average power of the pulsation component of the wind exciting moment;

$S_v(\omega_\theta)$  is the spectral density of the wind velocity;

$\omega_\theta$  is the frequency of small free roll oscillations of the ship;

$$G_{22}(H_{1/3}) = [Dh_1 \kappa(\omega_\theta)(\omega_\theta)^2 / g]^2 \times S_\zeta(\omega_\theta)(J_x + \mu_{44})^{-2}$$

is the average power of the wave exciting moment;

$\kappa(\omega_\theta)$  is the reduction coefficient of the main part of the wave exciting moment;

$S_\zeta(\omega_\theta)$  is the wave spectral density.

In equations (20), the second-order intensity factor  $G_{22}$  is written without taking into account the correlation between wind and wave heeling moments.

The physical interpretation of the last three equations of the system of equations for statistical moments (20) is determined by the following expressions:

$$-\bar{M}_r + \bar{M}_h = 0; \quad (21)$$

$$-\bar{E}_k + \bar{E}_p = 0; \quad (22)$$

$$-\bar{P}_d + \bar{P}_w = 0, \quad (23)$$

where  $\bar{M}_r$  is the average value of the righting moment of the ship;  $\bar{M}_h$  is the average value of the heeling moment from the wind action;  $\bar{E}_k$  is the average kinetic energy of the ship roll oscillations;  $\bar{E}_p$  is the average potential energy of the ship position during roll motion;  $\bar{P}_d$  is the average power of the energy dissipation of the oscillating ship;  $\bar{P}_w$  is the average power of the exciting moment due to the action of excitations.

Equations (21)–(23) will be called, respectively, the equations of average moments, average energies and average powers of the quasi-stationary ship motion mode. The first two of these equations are similar to the relations of the traditional theory of ship stability at large angles of inclination – the equation of moments (2) and the equation of works (energies) (3).

The boundary  $\Gamma_2$  of the region  $\Omega_2$  of nonlocal stability in the mean square in the considered case is determined by the maximum of the average potential energy  $\bar{E}_p$ , the position of which, as shown by the system of equations (20), depends on the average angle of heel. The value of this maximum is determined by the formula

$$\frac{\partial Q_2(\alpha_1, \mu_2, G_1, G_2)}{\partial \mu_2} = \frac{\partial \bar{E}_p}{\partial \mu_2} = \frac{1}{2} \{ Dh_1 + 6 Dh_3 \mathbf{M}[\dot{\theta}^2] + 3 Dh_3 (\mathbf{M}[\theta])^2 \} = 0. \quad (24)$$

In accordance with the method for investigating the nonlocal stability of the ship under constant action of random wind–waves excitations, an analysis of the capsizing of ship No 6010 with a displacement of  $\Delta = D = 4905$  kN ( $L = 38.7$  m,  $B = 7.0$  m,  $d = 2.98$  m) in beam position to the wind and waves was performed. The diagrams of the static and dynamic stability of this ship are presented in Figs. 1 and 2. The accident of the ship took place with wind of  $\sim 7$  state under the conditions of developing waves with the intensity of  $\sim 4$  state. The dependence of the average wave period  $T$  on the wave intensity  $H_{1/3}$  was estimated by the relation  $T = 3.217 \sqrt{H_{1/3}}$ .

To analyse this accident, a number of solutions of the system of quasi-stationary equations for statistical moments (18) were obtained with a gradual increase in the intensity of wind–waves excitations from the equilibrium position of the ship in calm water at  $\theta = 0$  to the loss of nonlocal stability in the mean square. The solution of equations (20) and calculation of the criterion of nonlocal stability in the mean square (24) were obtained by using the generalised reduced gradient method in nonlinear programming problems (9) and (15).

The characteristics of the considered stages of increasing wind and wave intensity and the results of solving the equations for statistical moments (20) are presented in Table 1. Table 2 summarises the main characteristics of the corresponding roll motion modes under conditions of increasing storm intensity.

Tab. 1. Results of solving the system of equations for statistical moments (20)

Stages of storm	$\bar{V}$ , m/s	$H_{1/3}$ , m	$\alpha_1$ , rad	$\mu_2$ , rad <sup>2</sup>	$\mu_{22}$ , (rad/s) <sup>2</sup>	$G_1(\bar{V})$ , s <sup>-2</sup>	$G_2(H_{1/3})$ , s <sup>-3</sup>
1	1.00	0.0043	0.00009	0.00000	0.00000	0.00000	0.00000
2	5.00	0.1076	0.00234	0.00000	0.00000	0.00204	0.00000
3	9.00	0.3485	0.00761	0.00003	0.00003	0.00662	0.00000
4	14.00	0.8433	0.01866	0.00048	0.00041	0.01603	0.00002
5	15.00	0.9680	0.02163	0.00081	0.00069	0.01840	0.00004
6	16.00	1.1014	0.02533	0.00187	0.00153	0.02093	0.00009
7	17.00	1.2434	0.03199	0.00577	0.00418	0.02363	0.00016
8	17.50	1.3176	0.04140	0.01169	0.00678	0.02504	0.00040
9	17.65	1.3403	0.05690	0.01840	0.00737	0.02547	0.00044

Tab. 2. Main characteristics of the ship roll motion modes

Stages of storm	$\bar{V}$ , m/s	$\bar{M}_h$ , kNm	$\bar{P}_w$ , kW	$\alpha_{i_1}$ , deg	$\sqrt{\mu_{2_1}}$ , deg	$2\bar{E}_k$ , kNm	$2\bar{E}_p$ , kNm
1	1.00	0.00000	0.00000	0.00537	0.00000	0.00000	0.00000
2	5.00	5.41510	0.00005	0.13437	0.01812	0.00001	0.00001
3	9.00	17.54494	0.00414	0.43586	0.31352	0.03450	0.03450
4	14.00	42.45441	0.06346	1.06932	1.25622	0.54350	0.54350
5	15.00	48.73593	0.10620	1.23922	1.63369	0.90860	0.90860
6	16.00	55.45066	0.23718	1.45137	2.47762	2.02344	2.02344
7	17.00	62.59860	0.42076	1.83292	4.35219	5.53135	5.53135
8	17.50	66.33502	1.07138	2.37244	6.19519	8.97896	8.97896
9	17.65	67.46685	1.16741	3.26011	7.77259	9.76429	9.76429

Tab. 3. Results of the investigation of local stability of ship roll motion modes in developing storm, i.e. the roots of the characteristic equation (12) corresponding to the system of differential equations for statistical moments (19)

Stages of storm	$\bar{V}$ , m/s	$\alpha_{1_1}$	$\alpha_{1_2}$	$\mu_{2_1}$	$\alpha_{1_1,2}$	$\mu_{2_2}$
1	1.00	-0.028 +0.964i	-0.028 -0.964i	-0.028 +0.906i	-0.028 -0.906i	-0.062
2	5.00	-0.028 +0.964i	-0.028 -0.964i	-0.028 +0.905i	-0.028 -0.905i	-0.062
3	9.00	-0.028 +0.964i	-0.028 -0.964i	-0.028 +0.897i	-0.028 -0.897i	-0.062
4	14.00	-0.028 +0.964i	-0.028 -0.964i	-0.028 +0.867i	-0.028 -0.867i	-0.062
5	15.00	-0.028 +0.964i	-0.028 -0.964i	-0.028 +0.854i	-0.028 -0.854i	-0.062
6	16.00	-0.028 +0.958i	-0.028 -0.958i	-0.028 +0.825i	-0.028 -0.825i	-0.063
7	17.00	-0.029 +0.919i	-0.029 -0.919i	-0.027 +0.722i	-0.027 -0.722i	-0.065
8	17.50	-0.029 +0.858i	-0.029 -0.858i	-0.026 +0.529i	-0.026 -0.529i	-0.068
9	17.65	-0.030 +0.800i	-0.030 -0.800i	-0.000 +0.000i	-0.000 -0.000i	-0.093

For each stage of the developing storm, the local stability of the quasi-stationary modes of the ship roll motion was also investigated. The roots of the characteristic equation (12) corresponding to the system of differential equations for statistical moments (19) are given in Table 3. This table shows the fulfillment of the criterion of nonlocal stability in the mean square (24) on the boundary  $\Gamma_2$  of the domain  $\Omega_2$ .

The data of Tables 1 and 2 are presented in Figs. 3–6.

Fig. 3 shows the diagram of the average righting moments  $\bar{M}_r = f_1(\alpha_{1_1}, \sqrt{\mu_{2_1}})$  as a function of the average heel angle  $m_\theta = \alpha_{1_1}$  and the mean square deviation of the ship's roll oscillations  $SD_\theta = \sqrt{\mu_{2_1}}$ . At  $SD_\theta = \sqrt{\mu_{2_1}}$ , the function  $\bar{M}_r = f_1(\alpha_{1_1}, \sqrt{\mu_{2_1}})$  represents the diagram of ship static stability shown in Fig. 1.

Fig. 4 represents the dependence of the ship average potential energy  $2\bar{E}_p = 2f_2(\alpha_{1_1}, \sqrt{\mu_{2_1}})$  on the kinematic characteristics of the ship roll motion and.

Figs. 3 and 4 respectively show: the boundary  $\Gamma_1$  (Boundary 1) of the region  $\Omega_1$  of nonlocal stability in the mean and the boundary  $\Gamma_2$  (Boundary 2) of the region  $\Omega_2$  of nonlocal stability in the mean square of the ship equilibrium position in calm water  $\theta \equiv 0$ .

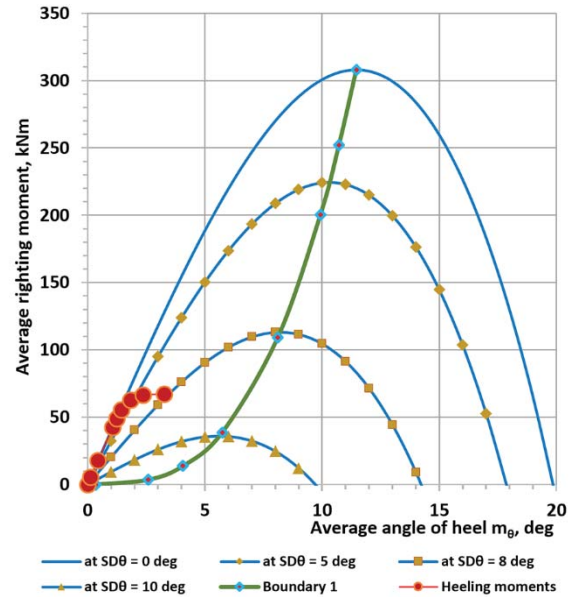


Fig. 3. Diagram of average righting moments with boundary  $\Gamma_1[\alpha_1, \mu_2]$  (Boundary 1) of the domain  $\Omega_1\{\alpha_1, \mu_2\}$  nonlocal stability in the mean of the ship equilibrium position in calm water  $\theta \equiv 0$  and values of average heeling moments  $\bar{M}_h$  of the wind action considered in Tables 1, 2 on the stages of storm growth

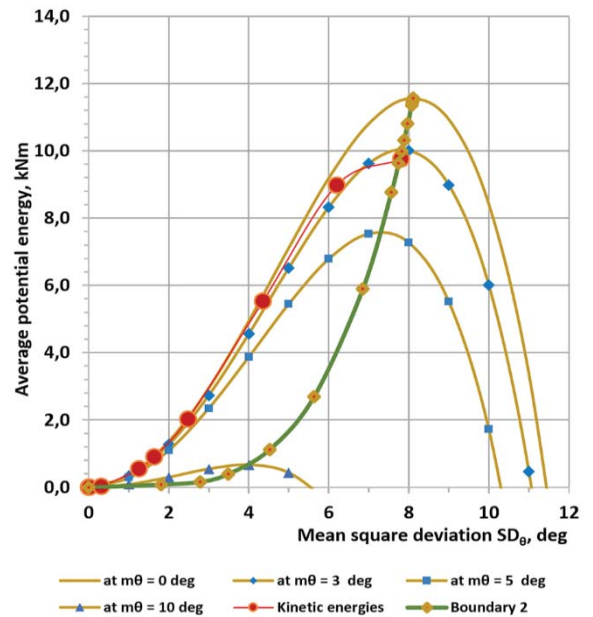


Fig. 4. Diagram of the average potential energies  $2\bar{E}_p$  with the boundary  $\Gamma_2[\alpha_1, \mu_2]$  (Boundary 2) of the region  $\Omega_2\{\alpha_1, \mu_2\}$  of nonlocal stability in the mean square of the ship equilibrium position in calm water  $\theta \equiv 0$  and the average kinetic energies  $2\bar{E}_k$  of the wind and waves action considered in Tables 1, 2 on the stages of storm growth

In Figs. 5 and 6, the surfaces  $\bar{M}_r = f_1(\alpha_{1_1}, \sqrt{\mu_{2_1}})$  and  $2\bar{E}_p = 2f_2(\alpha_{1_1}, \sqrt{\mu_{2_1}})$  are presented in the coordinates  $m_\theta = \alpha_{1_1}, SD_\theta = \sqrt{\mu_{2_1}}$  together with the solutions of the equations for statistical moments (20) as the stages of storm intensity increase.

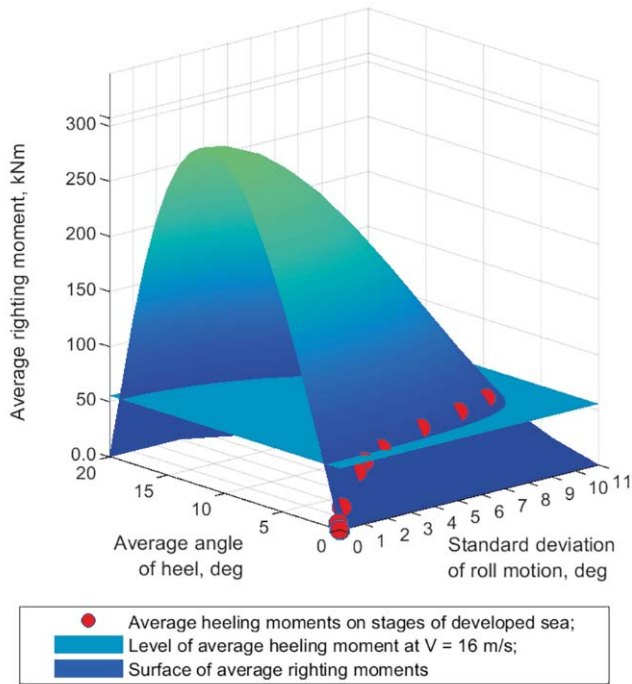


Fig. 5. Diagram of average righting moments with average values of heeling moments  $\bar{M}_h$  of the wind action on the stages of storm growth presented in Tables 1, 2

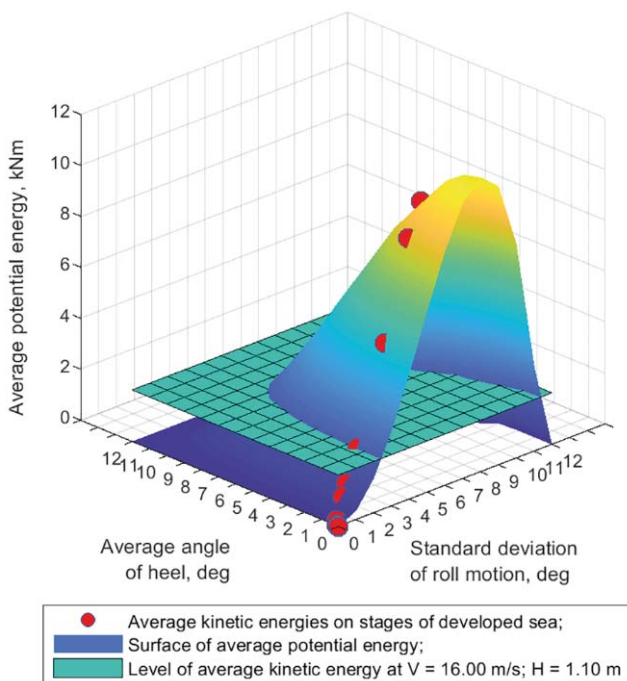


Fig. 6. Diagram of average potential energies  $2\bar{E}_p$  with values of average kinetic energies  $2\bar{E}_k$  of the wind and waves action on the stages of storm growth presented in Tables 1, 2

The algorithm for reflecting the region of nonlocal stability of a ship, from the space of kinematic characteristics of motion to the space of the parameters of the acting wind-waves excitations described in [5], was implemented in the considered example when solving the sequence of tasks for the equations of statistical moments (20) by the method of

nonlinear programming with the objective function (15). As a result of using the one-parameter spectra of wind velocity  $S_v(\omega)$  and sea  $S_s(\omega)$ , the boundary  $\Gamma_2$  of the region  $\Omega_2$  of the ship nonlocal stability in the mean square in the space parameters of wind-waves modes (regimes) such as the average wind velocity  $V$ , m/s and the characteristic wave height  $H_{1/3}$ , m was received. This boundary is shown in Fig. 7.

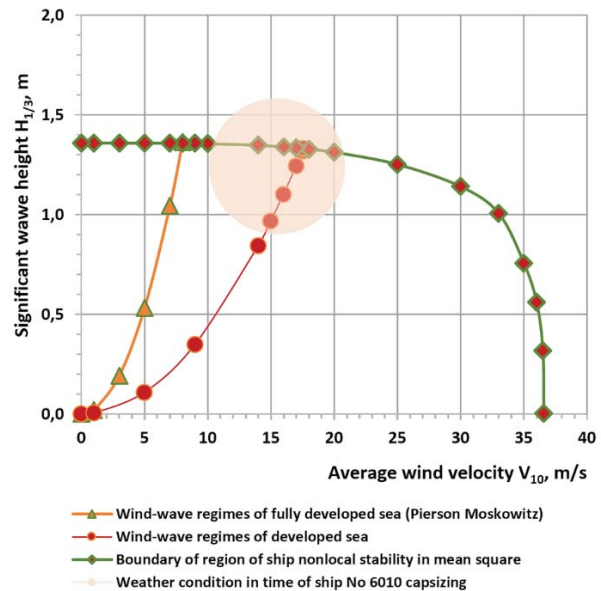


Fig. 7. Boundary  $\Gamma_2[V, H_{1/3}]$  of the region  $\Omega_2[V, H_{1/3}]$  of ship nonlocal stability in the mean square and wind-waves modes withstood by the ship at the stages of storm intensity increasing specified in Tables 1, 2

Fig. 7 also shows a number of the wind-waves modes withstood by the ship when searching for the boundary of the region of the existence of real solutions of equations (20) by using the nonlinear programming algorithm with the objective function (9). At the limit point of the sequence of solutions with the objective function (9), the same results were obtained as in determining the boundary of the region of ship nonlocal stability in the mean square, the solution of which is realised using the nonlinear programming task with the objective function (15). This means that the boundary of the region of nonlocal stability in the mean square of the ship equilibrium position  $\theta \equiv 0$  is the boundary of the real solutions of the equations for the statistical moments (20), and at this boundary the potential resources of the ship are exhausted with respect to increasing constantly acting wind-waves excitations.

## AN EXAMPLE OF SOLVING THE PROBLEM OF SHIP RELIABILITY UNDER ACTION OF WIND AND WAVES

An event of maintaining the nonlocal stability of ship under the action of the wind-waves modes of its operating area is considered. The probability of such event  $P_{kl}(\varphi)$  when using one-parameter characteristics of the wind and waves is calculated by the formula

$$P_{kl}(\varphi) = \iint_0^{\Gamma_2(\bar{V}, H_{1/3})} f(\bar{V}, H_{1/3}) d\bar{V} dH_{1/3}. \quad (25)$$

The calculation scheme for the determination of such reliability indicator  $P_{kl}(\varphi)$  is presented in Fig. 8. This indicator determines the relative number of wind-waves modes of the operation area withstood by the ship.

When calculating the reliability indicator by formula (25), we use in the equations for statistical moments (20) the one-parameter wave spectrum  $S_{\zeta}(\omega)$ , which depends only on  $H_{1/3}$ . The use of the two-parameter ITTC spectrum, which depends on the characteristic height  $H_{1/3}$  and the average wave period  $T$ , allows us to clarify the position of the boundary of the region of ship nonlocal stability in the mean square in the space of such parameters of the acting excitations as  $\bar{V}, H_{1/3}, T$  [5,6]. The corresponding solution of the system of equations for statistical moments (20) with the definition of the boundary  $\Gamma_2[V, H_{1/3}, T]$  of region  $\Omega_2[V, H_{1/3}, T]$  of ship nonlocal stability in the mean square is shown in Fig. 9.

This solution allows us to clarify also the reliability indicator determined by the formula (15). The result of the refined definition of the boundary of the region of nonlocal stability in the mean square and the interpretation of the use of formula (15) to find the value of the reliability indicator  $P_{kl}$  in the space  $V, H_{1/3}$ , are presented in Fig. 10.

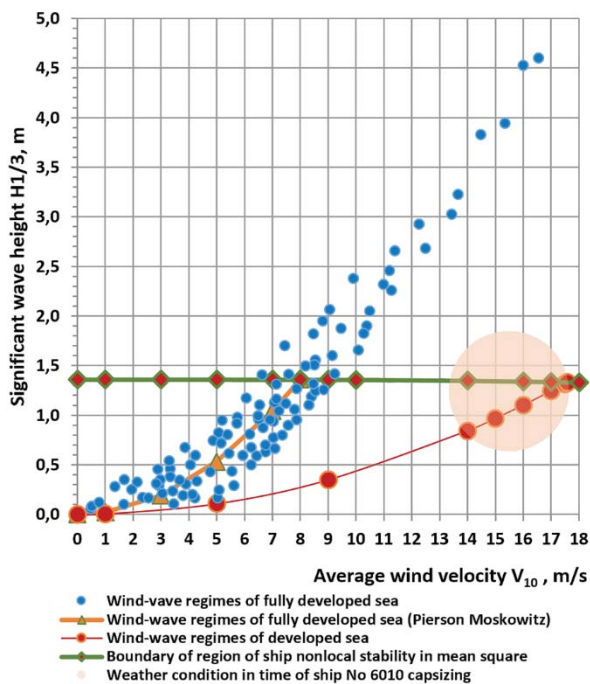


Fig. 8. The determination of the reliability indicator  $P_{kl}(\varphi)$  of the ship in given area of operation, i.e. the probability of its operation without capsizing in accordance with formula (25)

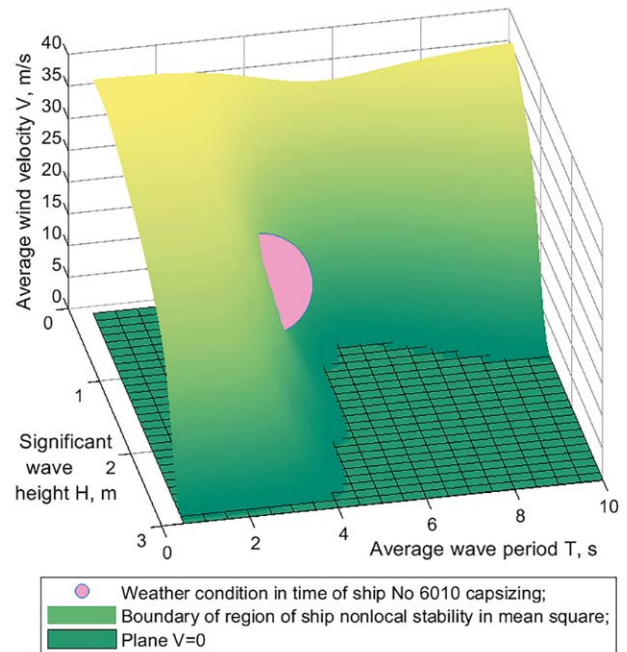


Fig. 9. Boundary  $\Gamma_2[V, H_{1/3}, T]$  of the region  $\Omega_2[V, H_{1/3}, T]$  of nonlocal stability in the mean square and weather conditions for ship No 6010 accident

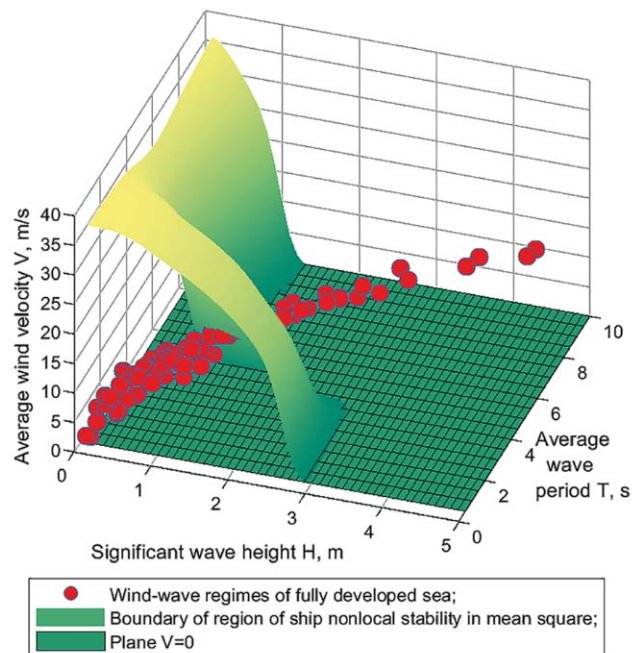


Fig. 10. On determining the reliability indicator of the ship in area of its operation  $P_{kl}(\varphi)$ , i.e. the probability of ship operation without capsizing in accordance with formula (15)

## CONCLUSIONS

1. The proposed complex method of investigating the stochastic nonlocal stability and reliability of the ship in storm conditions of operation has two characteristic features that condition its novelty in ship seakeeping theory. Firstly, it

continues the traditions of the widely known deterministic stability theory of ships at large angles of inclination, both from the point of view of creating new and more realistic approaches for finding the boundaries of areas of nonlocal stability of the ship under actions of wind–waves modes, and from the point of view of improving the physical interpretation of the studied phenomena. Secondly, the method complements the procedure for determining the losses of ship nonlocal stability under the action of different wind–waves modes with an algorithm for calculating the corresponding indicator of ship reliability with the help of the long-term distribution of these modes characteristics for the given area of ship operation.

2. The results of the application of the proposed method of investigating mean-square nonlocal stability are in satisfactory agreement with the results of ship No. 6010 capsizing under the action of the wind–waves mode of the developing sea.

## REFERENCES

1. Himmelblau D. M. (1972): *Applied nonlinear programming*. McGraw Hill, New York.
2. Khasminsky R. Z. (1969): *Stability of systems of differential equations under random perturbations of their parameters*. Fizmatgiz, Moscow.
3. Krasovsky N. N. (1959): *Some problems of the theory of stability of motion*. Fizmatgiz, Moscow.
4. Lyapunov A. M. (1950): *The general problem of motion stability*. GITTL, Moscow, Leningrad.
5. Nekrasov V. A. (1978): *Probabilistic problems of ships seakeeping*. Shipbuilding, Leningrad.
6. Nekrasov V. A. (1985): *Seakeeping and technical stability of the ship. Hydrodynamics of the ship*. Collection of NSI scientific papers. Nikolayev Shipbuilding Institute, Nikolayev.
7. Nekrasov V. A. (1985): *Criteria of seakeeping and reliability indicators for the use of the ship and its technical means in given area of operation. Hydrodynamics of the ship*. Collection of NSI scientific papers. Nikolayev Shipbuilding Institute, Nikolayev.
8. Nekrasov V. A. (2013): *Nonlocal stability of mobile marine objects*. MAST 2013, Gdansk, Poland.
9. Stratonovich R. L. (1961): *Selected issues of the theory of fluctuations in radio techniques*. Soviet Radio, Moscow.

## CONTACT WITH THE AUTHOR

**Valeriy Nekrasov**

*e-mail: valeriy.nekrasov@gmail.com*

Admiral Makarov National University of Shipbuilding,  
Heroiv Ukraine av., 9, 54025 Mykolaiv  
**UKRAINE**

# MANOEUVRING PREDICTION OF KVLCC2 WITH HYDRODYNAMIC DERIVATIVES GENERATED BY A VIRTUAL CAPTIVE MODEL TEST

Kun Dai<sup>1</sup>

Yunbo Li<sup>2</sup>

<sup>1</sup> Harbin Engineering University, Harbin, China

<sup>2</sup> College of Ocean Science and Engineering, Shanghai Maritime University, Shanghai, China

## ABSTRACT

*This paper describes the application of computational fluid dynamics rather than a towing tank test for the prediction of hydrodynamic derivatives using a RANS-based solver. Virtual captive model tests are conducted, including an oblique towing test and circular motion test for a bare model scale KVLCC2 hull, to obtain linear and nonlinear hydrodynamic derivatives in the 3rd-order MMG model. A static drift test is used in a convergence study to verify the numerical accuracy. The computed hydrodynamic forces and derivatives are compared with the available captive model test data, showing good agreement overall. Simulations of standard turning and zigzag manoeuvres are carried out with the computed hydrodynamic derivatives and are compared with available experimental data. The results show an acceptable level of prediction accuracy, indicating that the proposed method is capable of predicting manoeuvring motions.*

**Keywords:** MMG model; KVLCC2; CFD; manoeuvring prediction

## INTRODUCTION

Ship manoeuvrability is an important factor affecting the safety of navigation. In order to comply with the manoeuvring standards developed by the International Maritime Organisation [1, 2] in the design process of a ship, a reliable and accurate estimation of the ship's manoeuvrability is required. According to a statement by the Manoeuvring Committee of the International Towing Tank Conference (ITTC, [3]), free running model tests are considered to be the most reliable method for manoeuvrability predictions. Another widely applied method is to simulate manoeuvring motions based on a mathematical model with hydrodynamic derivatives obtained from captive model tests, such as a planar motion mechanism (PMM) test, an oblique towing test (OTT) and a circular motion test (CMT). However, model tests are confined to researchers and ship designers due to the high cost of experiment facilities and difficulties in optimising manoeuvrability at the design phase.

In recent years, the rapidly developing computational fluid dynamics (CFD) technique has been applied in manoeuvring predictions, and can overcome the disadvantages of model tests. There are two classic types of CFD that can be used in predicting ship manoeuvrability. The first is a fully CFD-based approach that simulates standard manoeuvres with a steering rudder and rotating propeller. Mofidi and Carrica [4] presented a direct simulation of a zigzag manoeuvre for the KRISO Container Ship (KCS) in calm water. Shen et al. [5] implemented a dynamic overset grid technique using the open-source code OpenFOAM and presented free-running manoeuvring simulations for a KCS ship in calm water. Wang et al. [6] further extended the direct simulation of a zigzag manoeuvre for an ONR Tumblehome ship in waves, using the same solver as Shen et al. [5]. These direct CFD simulations are believed to give more accurate predictions, since they can resolve complex flows around the hull and its appendages, and can obtain the details of the local flow during manoeuvres. However,

direct CFD simulation is not sufficiently mature for practical applications due to its huge computational cost and the complex numerical techniques required to deal with the coupled motions of the hull, rudder and propeller.

A more practical alternative is known as a system-based method. This performs manoeuvre simulations by solving mathematical models such as the Abkowitz model [7] and the MMG model [8], in which the manoeuvring hydrodynamic derivatives are generated by conducting virtual captive tests using CFD techniques. The CFD method for predicting hydrodynamic derivatives has drawn increasing amounts of attention in the area of manoeuvrability studies over the past few years. Sakamoto et al. [9] conducted unsteady Reynolds averaged Navier-Stokes (URANS) simulations of static and dynamic PMM tests for a bare surface combatant model 5415 using the CFDShip-Iowa code. Guo et al. [10] have conducted circular motion, static drift and heel test simulations for the ONR Tumblehome model using STAR-CCM+, and have investigated manoeuvring motions in calm water with a four-DOF MMG model that considers surge, sway, roll, and yaw. Liu et al. [11] predicted the manoeuvrability of a KCS ship model using the Abkowitz model, with a full set of linear and nonlinear hydrodynamic derivatives determined by virtual captive model tests using STAR-CCM+. Kim et al. [12] and Islam et al. [13] presented PMM simulation results for a KCS model using an open-source RANS solver in OpenFOAM and an in-house code called SHIP\_Motion, respectively, and predicted hydrodynamic derivatives from the simulation results.

Regardless of the type of mathematical model used, the reliability of manoeuvring prediction depends on the accuracy of the hydrodynamic derivatives. Although manoeuvring simulations based on CFD have gaining attention lately, it is still difficult to acquire accurate hydrodynamic derivatives using the CFD method. More numerical simulations are needed using CFD for captive model tests and systems-based manoeuvring predictions in order to verify the capability of CFD to predict motion related to ship manoeuvring. In this context, the present study aims to investigate ship manoeuvring motion in the horizontal plane via the application of the MMG model, where the hydrodynamic derivatives are determined by a CFD simulation of the captive model tests. A bare KVLCC2 tanker is selected as the study object. Grid and time step dependency studies are performed for a static drift case to estimate the numerical error and uncertainty due to the grid discretisation and time step. An oblique towing test and a circular motion test are simulated in order to obtain the hydrodynamic derivatives for oblique moving and turning motions. Free manoeuvres such as the turning circle and zigzag tests are simulated with the computed hydrodynamic derivatives, and the simulation results for the manoeuvrability parameters for standard manoeuvres are compared with published data for free-running model tests and EFD-based predictions.

## MATHEMATICAL MODEL

### COORDINATE SYSTEMS

Two right-handed coordinate systems are used in this paper, as shown in Fig. 1. The trajectory and heading of the ship are defined in  $o_0-x_0y_0z_0$ , a earth-fixed coordinate system, where the  $x_0-y_0$  plane is fixed on the surface of still water and the  $z_0$  axis points vertically downwards. The hydrodynamic forces acting on the ship are described using a ship-fixed coordinate system  $o-xyz$ , with the origin taken as the mid-ship position. The  $x$ -axis points towards the bow, the  $y$ -axis towards starboard and the  $z$ -axis vertically downwards. The centre of gravity of the ship is located at  $(x_G, 0, 0)$ .  $\Psi$  is the heading angle,  $\delta$  is the rudder angle and  $r$  the yaw rate.  $u$  and  $v$  denote the surge velocity and sway velocity, respectively. The drift angle at the mid-ship position is defined by  $\beta = \tan^{-1}(-v/u)$ , and the total velocity  $U = \sqrt{u^2 + v^2}$ .

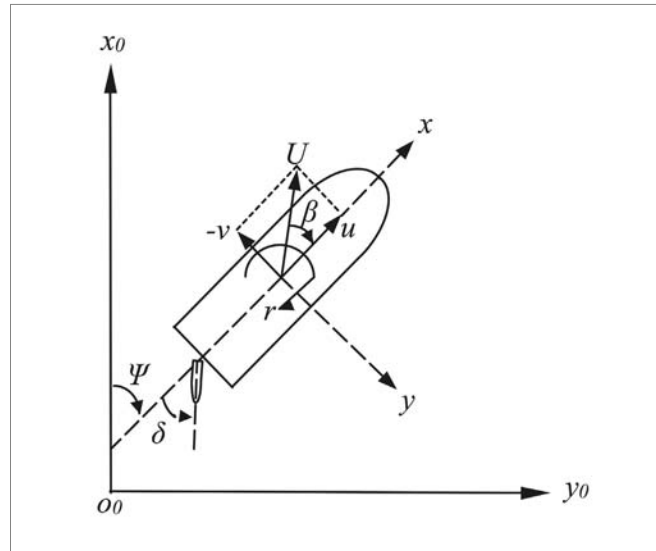


Fig. 1. Coordinate systems used

### MOTION EQUATIONS

The 3-DOF (surge, sway and yaw) ship manoeuvring motion can be described by the following equation:

$$\left. \begin{aligned} (m + m_x)\dot{u} - (m + m_y)vr - x_Gmr^2 &= X \\ (m + m_y)\dot{v} + (m + m_x)ur + x_Gm\dot{r} &= Y \\ (I_{zG} + mx_G^2 + J_z)\dot{r} + x_Gm(v + \dot{u}r) &= N \end{aligned} \right\} \quad (1)$$

where  $m$  is the ship's mass,  $I_{zG}$  is the moment of inertia around the centre of gravity.  $m_x$ ,  $m_y$  and  $J_z$  are the added masses and added moments of inertia.  $\dot{u}$ ,  $\dot{v}$  and  $\dot{r}$  are the corresponding surge acceleration, sway acceleration, and yaw acceleration.  $X$  and  $Y$  are the corresponding force components, and  $N$  is the yaw moment.

$X$ ,  $Y$  and  $N$  on the right-hand side of Eq. (1) are expressed as:

$$\left. \begin{aligned} X &= X_H + X_P + X_R \\ Y &= Y_H + Y_R \\ N &= N_H + N_R \end{aligned} \right\} \quad (2)$$

$$K_T(J_p) = -0.1385J_p^2 - 0.2753J_p + 0.2931 \quad (8)$$

$$10K_Q(J_p) = -0.2045J_p^2 - 0.1856J_p + 0.3071 \quad (9)$$

where the subscripts  $H$ ,  $R$ , and  $P$  denote the force and moment due to the hull, rudder, and propeller, respectively.

### HULL FORCES

The hydrodynamic forces acting on the hull are expressed as follows, following Yasukawa et al. [8]:

$$\left. \begin{aligned} X_H &= -R_0 + X_{vv}v^2 + X_{vr}vr + X_{rr}r^2 + X_{vvv}v^3 \\ Y_H &= Y_vv + Y_r r + Y_{vvv}v^3 + Y_{vvr}v^2r + Y_{vrr}vr^2 + Y_{rrr}r^3 \\ N_H &= N_vv + N_r r + N_{vvv}v^3 + N_{vvr}v^2r + N_{vrr}vr^2 + N_{rrr}r^3 \end{aligned} \right\} \quad (3)$$

where  $R_0$  is the ship's resistance when moving in a straight line, and  $X$ ,  $Y$ ,  $N$  with subscripts  $u$ ,  $v$ ,  $r$  are the hydrodynamic derivatives on manoeuvring.

### PROPELLER FORCE

The longitudinal force of the propeller  $X_p$  is described as follows:

$$X_p = (1 - t_p) \rho n^2 D_p^4 K_T(J_p) \quad (4)$$

$$K_T(J_p) = k_2 J_p^2 + k_1 J_p + k_0 \quad (5)$$

$$J_p = u(1 - w_p) / (n_p D_p) \quad (6)$$

where  $t_p$  is the thrust deduction factor,  $\rho$  is the water density,  $D_p$  is the diameter of the propeller, and  $K_T$  is the thrust coefficient, which can be expressed as a second-order polynomial function of the propeller advance ratio  $J_p$ ,  $n_p$  is the propeller revolution.  $w_p$  is the wake coefficient at the propeller position in manoeuvring motion, and according to [8] can be written as:

$$(1 - w_p) / (1 - w_{p0}) = 1 + [1 - \exp(-C_1 |\beta_p|)] (C_2 - 1) \quad (7)$$

where  $w_{p0}$  is the wake coefficient at the propeller position in straight motion,  $\beta_p$  is the geometric inflow angle to propeller in manoeuvring motion,  $C_1$  denotes the wake change characteristic versus  $\beta_p$  and  $C_2$  represents the value of  $(1 - w_p) / (1 - w_0)$  at large  $\beta_p$ .

For the purposes of the present simulations, the open water characteristics of the corresponding propeller are approximated based on the open water propeller test of the National Maritime Research Institute, Japan [19]:

### RUDDER FORCES

The rudder forces are expressed by a combination of interaction factors and the rudder normal force:

$$\left. \begin{aligned} X_R &= -(1 - t_R) F_N \sin \delta \\ Y_R &= -(1 - a_H) F_N \cos \delta \\ N_R &= -(x_R - a_H x_H) F_N \cos \delta \end{aligned} \right\} \quad (10)$$

where  $F_N$  is the rudder normal force.  $t_R$  is the steering resistance reduction factor, which defines the reduction in rudder resistance during steering.  $a_H$  is the rudder force increase factor, which indicates the additional lateral force acting on the ship by steering.  $x_R$  is the longitudinal position of the rudder, while  $x_H$  denotes the longitudinal acting point of the additional lateral force component. The rudder normal force is expressed as Eqs. (9)–(12).

$$F_N = \frac{1}{2} \rho A_R (u_R^2 + v_R^2) \frac{6.13\lambda}{\lambda + 2.25} \sin a_R \quad (11)$$

$$a_R = \delta - \tan^{-1}(v_R / u_R) \quad (12)$$

$$v_R = U \gamma_R (\beta - l'_R r') \quad (13)$$

$$u_R = \varepsilon u (1 - w_p) \sqrt{\eta \left[ 1 + \kappa \left( \sqrt{1 + \frac{8K_T}{\pi J_p^2}} - 1 \right) \right]^2 + (1 - \eta)} \quad (14)$$

where  $A_R$  is the rudder area,  $\lambda$  is the rudder aspect ratio,  $u_R$  and  $v_R$  are the longitudinal and lateral rudder inflow velocities induced by propeller rotation, respectively;  $\varepsilon$  is the ratio of the wake fraction at the rudder position to that at the propeller position,  $\eta$  is introduced to express the percentage of the rudder area in the propeller race, which is evaluated based on the relative propeller-rudder position;  $\kappa$  is the interaction factor between propeller and rudder;  $U$  is the resultant velocity;  $\gamma_R$  represents the flow straightening coefficients; and  $l'_R$  is the effective longitudinal coordinate of the rudder position.

It should be noted that in the rest of this paper, symbols with the prime symbol ' represent a non-dimensionalised value. Force and moment are non-dimensionalised by  $(1/2) \rho L_{pp} d U^2$  and  $(1/2) \rho L_{pp}^2 d U^2$ , respectively, where  $d$  is the ship draft and  $L_{pp}$  is the length of the ship between perpendiculars. The mass and moment of inertia are non-dimensionalised by  $(1/2) \rho L_{pp}^2 d$  and  $(1/2) \rho L_{pp}^4 d$ , respectively. Lateral velocity  $v$  and yaw rate  $r$  are made non-dimensional as follows:

$$v' = v/U \quad r' = r L_{pp} / U \quad (15)$$



Fig. 2. Geometry of the KVLCC2 tanker

## MODEL SHIP DESCRIPTION

The sample ship studied here is the bare KVLCC2 tanker model. This ship is a very popular test model, and many experimental and CFD test results for this model are open to the public and have been discussed in workshops and conferences [14–16]. Table 1 shows the main particulars. In the table, the parameters of ship models with lengths 2.909 m (L-3 model) and 7.00 m (L-7 model) are shown together with those of a full-scale ship. In this paper, the L-3 model is used for simulation of the captive model tests, while the L-7 model is used for prediction of manoeuvring motions. The geometry of the KVLCC2 tanker is shown in Fig. 2.

Tab. 1. Main particulars of KVLCC2

	Full scale	L-3 model	L-7 model
Scale	1.00	1/110	1/45.7
$L_{pp}$ (m)	320.0	2.909	7.00
$B$ (m)	58.0	0.527	1.27
$D$ (m)	20.8	0.189	0.46
$V$ (m <sup>3</sup> )	312,622	0.235	3.27
$x_G$ (m)	11.2	0.102	0.25
$C_b$	0.810	0.810	0.810
Propeller type	FP	FP	FP
$D_p$	9.86	0.090	0.216
Rudder type	Horn	Horn	Horn
$H_R$	15.8	0.144	0.345
$A_R$	112.5	0.00928	0.0539

## NUMERICAL METHOD

In this study, the CFD software STAR-CCM+ is used in the numerical simulations. This code solves closed RANS equations using the isotropic blended SST  $k-\omega$  turbulence model. The flow domain is discretised using the finite volume method (FVM). The temporal terms are performed with a first-order backwards Euler scheme, and the convection and term diffusion are discretised with a second-order upwind scheme and a second-order scheme, respectively. The pressure-velocity coupling is solved using a SIMPLE algorithm. An all- $y^+$  treatment is employed for near-wall

modelling, which is a hybrid treatment emulating a high  $y^+$  wall treatment with a coarse mesh and low  $y^+$  wall treatment with a fine mesh. The free surface is captured by the two-phase volume of fluid (VOF) technique. In our numerical simulations, three degrees of freedom are considered: surge, sway and yaw. A rotation and translation module is adopted for the simulation of captive model tests in calm and deep water conditions.

## COMPUTATIONAL CASES

In order to obtain the linear and nonlinear hydrodynamic derivatives in the third-order MMG model in Equations (3), simulations of an oblique towing test and a circular motion test are carried out for the KVLCC2 model (L-3 model) without a propeller or rudder. Table 2 presents a summary of the computational conditions. All simulations are performed under static conditions in which all ship motions are restricted. The calculations are conducted on two DELL local workstations (Intel Xeon E5-2670v3 @2.3 GHz, 32 GB) using six processors. The simulations are run for up to 30 s (simulation time) to attain a stable output. The ship speed  $U$  is set to  $Fr = 0.142$ . The Froude number is defined as  $Fr = U / (gL_{pp})^{1/2}$ , where  $g$  is the gravitational acceleration.

Tab. 2. Computational cases for OTT and CMT

Test	$Fr$	$r'$	$\beta(^{\circ})$
OTT	0.142	0	0, $\pm 2$ , $\pm 4$ , $\pm 6$ , $\pm 8$ , $\pm 12$ , $\pm 16$
CMT	0.142	0.2, 0.6, 0.8	0, $\pm 2$ , $\pm 4$ , $\pm 6$ , $\pm 8$ , $\pm 12$ , $\pm 16$

## COMPUTATIONAL DOMAIN AND GRID

An overview of the computational grid and boundary conditions is shown in Figure 3. The inlet is placed at  $1.0L_{pp}$  in front of the bow, the outlet  $3.0L_{pp}$  behind the stern, the top  $0.5L_{pp}$  above the free surface, the bottom  $1.5L_{pp}$  below the still free surface, and each lateral boundary  $1.5L_{pp}$  away from starboard and port sides, respectively. As for the boundary conditions, the outlet plane is specified as pressure outlet, the hull surface is treated as non-slip wall, and the rest of the boundaries are specified as velocity inlet. Wave damping is applied at the outlet and side walls to reduce wave oscillations.

The computational domain is discretised using an unstructured hexahedral grid. In order to capture the flow and wave features during the motion of the ship, the grid around the ship and free surface is refined, as shown in Fig. 3. On the surfaces of the hull, prismatic cells are used to achieve better resolution of the flow near the boundary, and the value

of  $y^+$  is around 40 along the hull. Refinement of the grid near the bow and stern of the hull is employed to resolve the flow, as shown in Fig. 4.

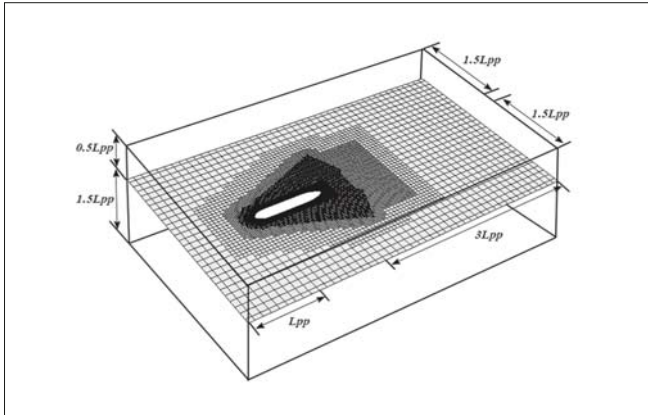


Fig. 3. CFD computational domain and boundary conditions

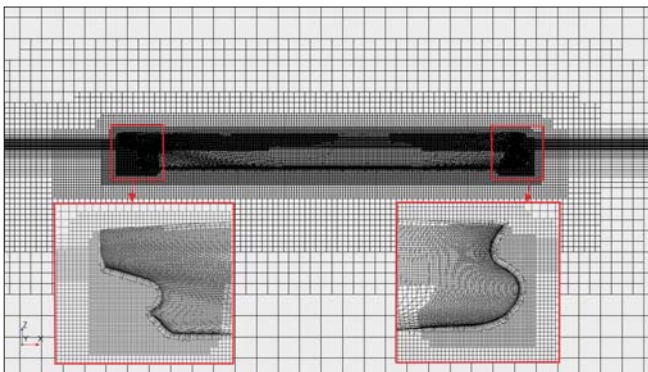


Fig. 4. Grid structure in the regions around the ship

## CONVERGENCE STUDY

Grid size and time step convergence studies are performed for a static drift case with  $\beta = 12^\circ$  at  $Fr = 0.142$ , in order to evaluate the discretisation errors caused by the grid size and time step. A verification study is conducted following the methodology discussed by Stern et al. [17] and Wilson et al. [18].

In the grid spacing convergence study, all grid parameters are given as a percentage of the base size, so that the grid can be refined systematically. A refinement ratio of  $r_G = \sqrt{2}$  is applied for grid refinement. Three sets of grids, referred to here as coarse (S3), medium (S2), and fine (S1), were generated based on a refinement ratio consisting of 1.07 M, 2.38 M and 5.66 M cells, respectively. The time step for the coarse, medium and fine grids was 0.03 s and the computing time was about 10, 24 and 60 hours, respectively. In the time step convergence study, the simulation was performed with a medium grid. Three sets of time steps, referred to here as 0.0424 s (S3), 0.03 s (S2), and 0.0212 s (S1), were used based on the refinement ratio  $r_T = \sqrt{2}$ . The computing times for the coarse, medium and fine time step were about 16, 24 and 31 hours, respectively. The results of the grid convergence and time step convergence studies for simulation of the static drift case are shown in Tables 3

and 4, respectively. It can be observed from Table 3 that  $X'$ ,  $Y'$  and  $N'$  all achieve monotonic convergence with  $0 < R_G < 1$  in the grid convergence study. Similarly,  $X'$ ,  $Y'$  and  $N'$  all achieve monotonic convergence with  $0 < R_T < 1$  in the time step convergence study, as shown in Table 4. Thus, a medium coarse grid with 2.38 M cells and a medium time step of 0.03 s are used in subsequent simulations, in order to balance the computation cost and accuracy.

Tab. 3. Grid convergence of OTT simulation with  $\beta = 12^\circ$

Grid	ID	Grid Size	$X'$	$Y'$	$N'$
Fine	S1	5.66M	-0.02307	0.06952	0.02654
Medium	S2	2.38 M	-0.02309	0.07044	0.02673
Coarse	S3	1.07 M	-0.02333	0.07162	0.02694
RG			0.05674	0.77551	0.92031
PG			8.27886	0.73357	0.23961
UG (%S2)			0.11760	10.89307	23.81957
UGC (%S2)			0.05698	3.19688	7.69665
Convergence			Monotonic	Monotonic	Monotonic

Tab. 4. Time step convergence for the OTT simulation with  $\beta = 12^\circ$

Time-step	ID	Time-step Size	$X'$	$Y'$	$N'$
Fine	S1	0.0212 s	-0.02294	0.07048	0.02688
Medium	S2	0.03 s	-0.02309	0.07044	0.02673
Coarse	S3	0.0424 s	-0.02337	0.07000	0.02655
RT			0.51528	0.08840	0.79220
PT			1.9131	6.9996	0.6721
UT (%S2)			2.3672	0.2606	3.6208
UTC (%S2)			0.8494	0.1277	0.7660
Convergence			Monotonic	Monotonic	Monotonic

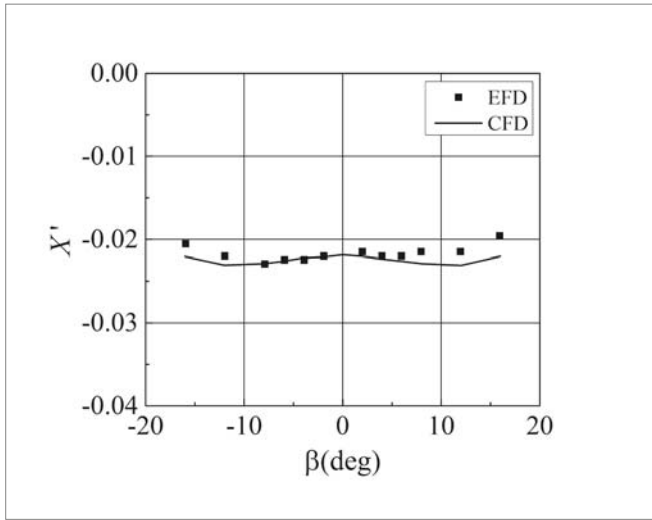
## NUMERICAL RESULTS

### FORCES AND MOMENTS

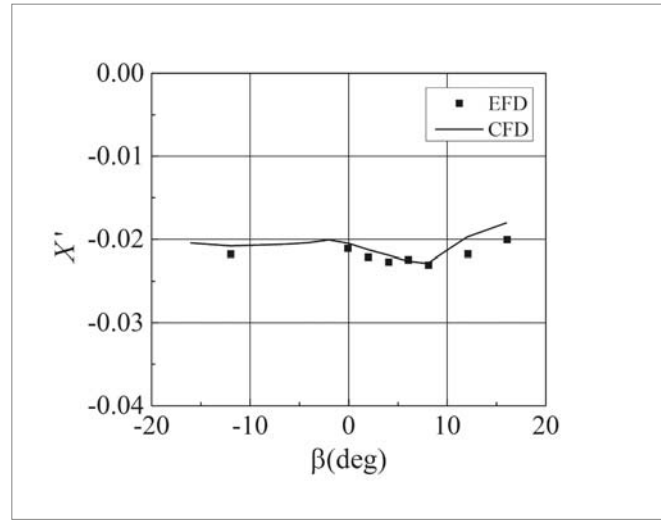
The computed hydrodynamic forces and moments from the simulations of CMT and OTT are compared with EFD data from Yasukawa et al. [8], as plotted in Figs. 5–8. It should be noted that the inertia forces are subtracted from the EFD data. As shown in Fig. 5, the numerical and computational results are in good agreement with the experimental data, although some discrepancies between CFD and EFD can be found at larger drift angles, which are likely to be due to

severe flow separation around the hull. From Figs. 6–8, it can be seen that discrepancies between CFD and EFD become more significant as the yaw rate increases. In general, CFD computation underestimates the sway force but overestimates

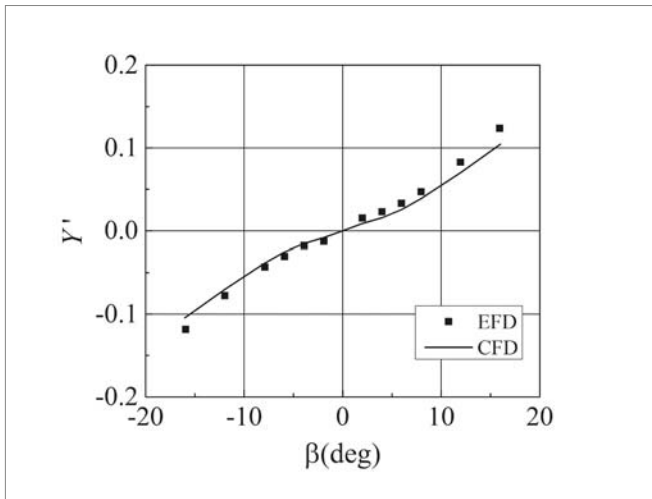
the yaw moment. Moreover, significant deviation occurs at larger negative drift angles under conditions of  $r' = 0.8$ . These discrepancies may be caused by the restriction of ship motion to a large extent.



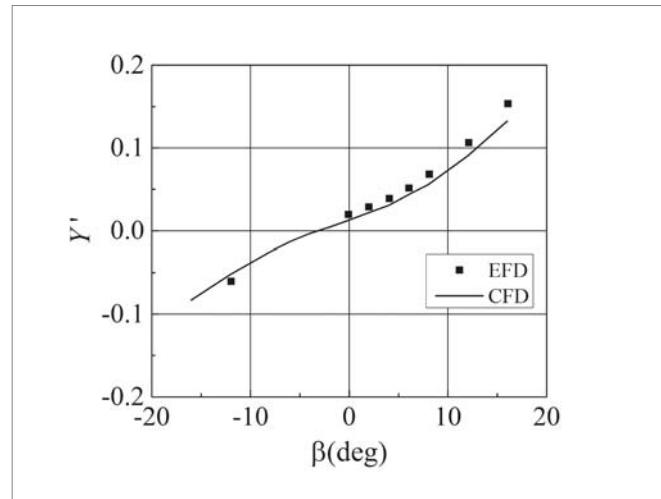
(a1)



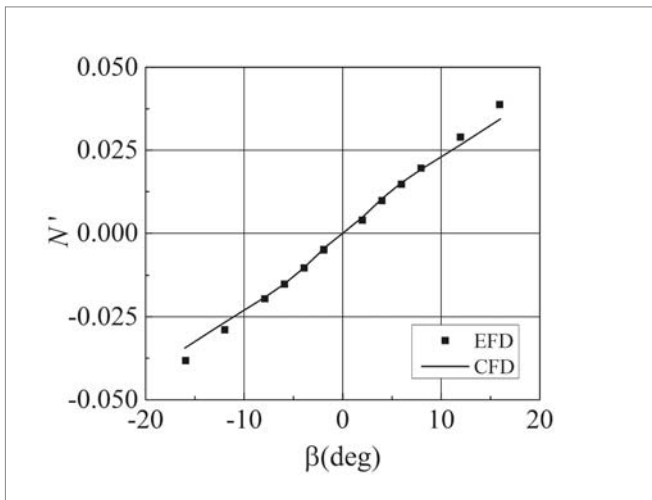
(a2)



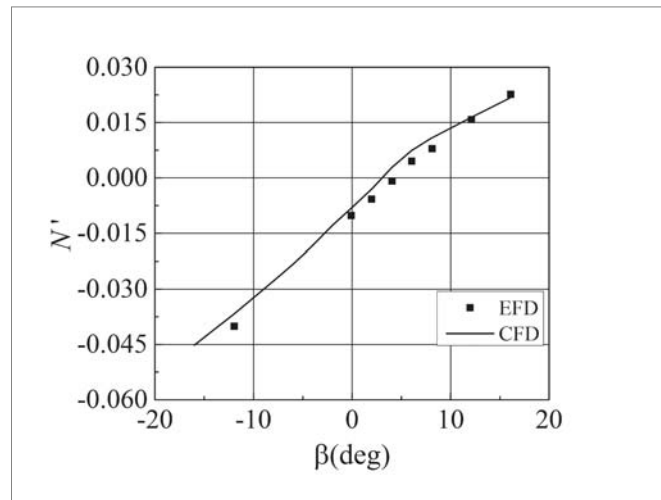
(b1)



(b2)



(c1)



(c2)

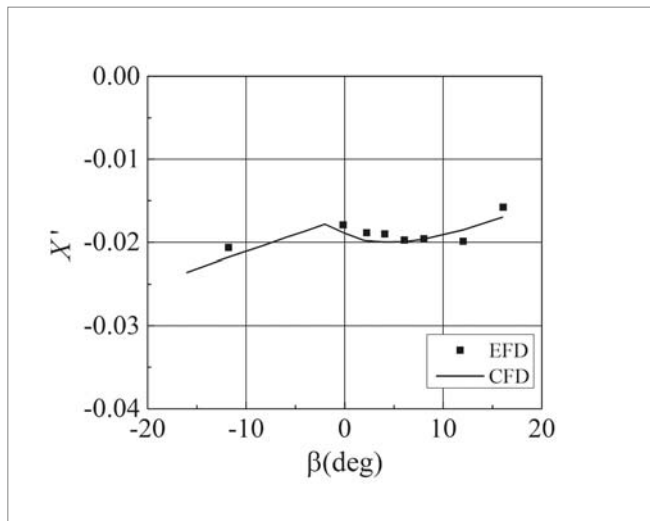
Fig. 5. Comparison of results for OTT: (a1) $X'$ ; (b1) $Y'$ ; (c1) $N'$

Fig. 6. Comparison of results for CMT AT at  $r'=0.2$ : (a2) $X'$ ; (b2) $Y'$ ; (c2) $N'$

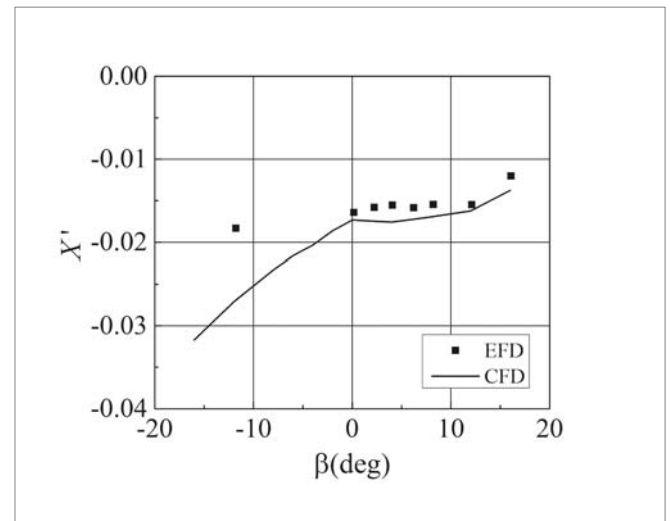
## HYDRODYNAMIC DERIVATIVES

As shown in Eq. (1), the hydrodynamic forces and moment can be expressed by a series of polynomials. The

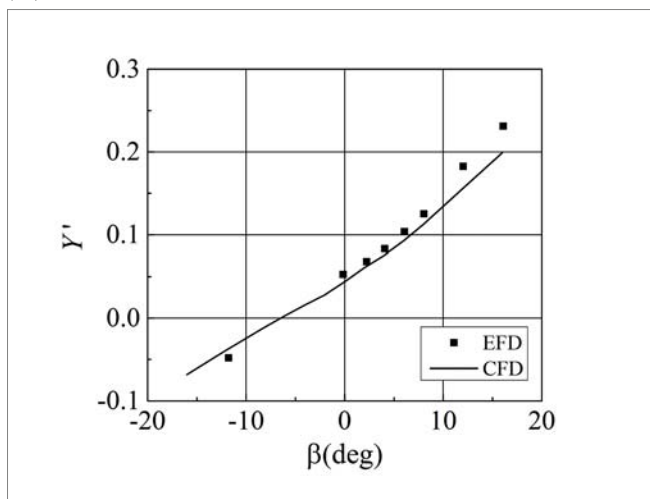
dimensionless hydrodynamic derivatives are determined from the CFD data for captive CMT and OTT, using a least squares method. Fig. 9 presents a comparison of the hydrodynamic derivatives obtained from the EFD and CFD



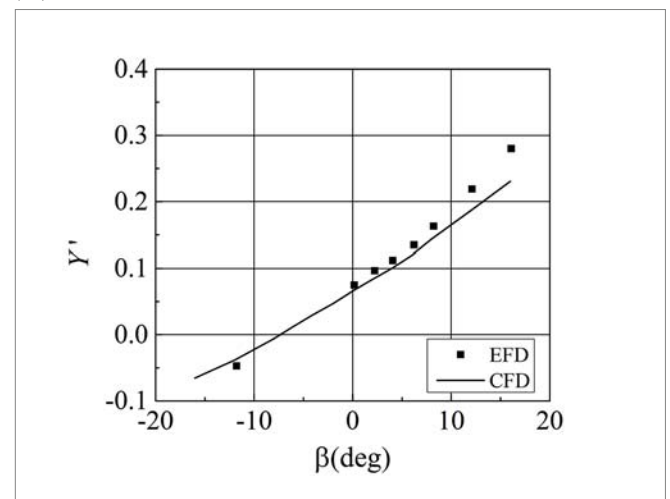
(a3)



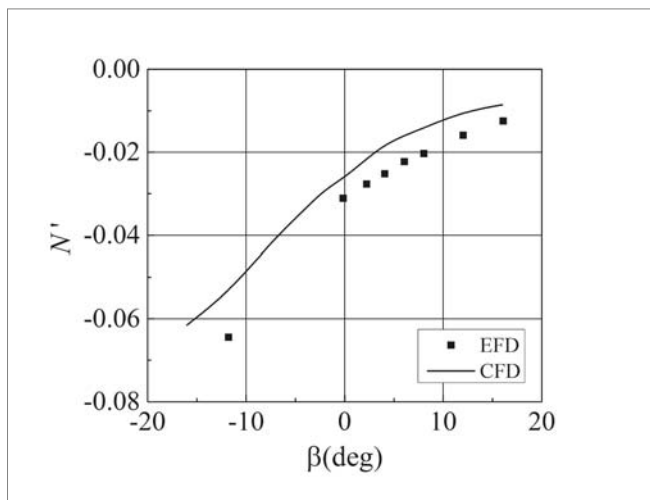
(a4)



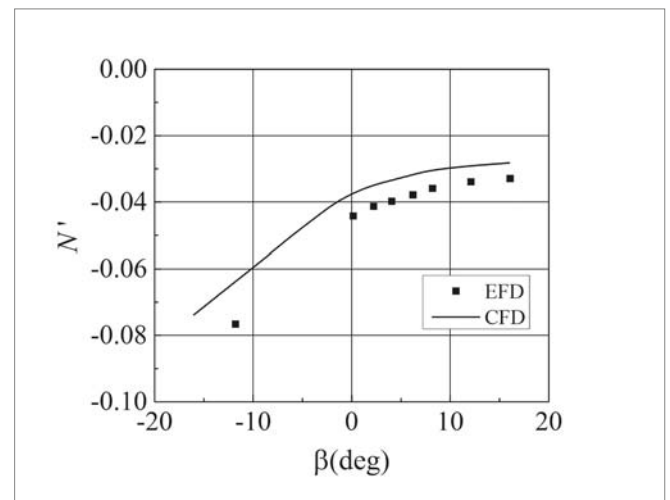
(b3)



(b4)



(c3)



(c4)

Fig. 7. Comparison of results for CMT at  $r'=0.6$ : (a3) $X'$ ; (b3) $Y'$ ; (c3) $N'$

Fig. 8. Comparison of results for CMT at  $r'=0.8$ : (a4) $X'$ ; (b4) $Y'$ ; (c4) $N'$

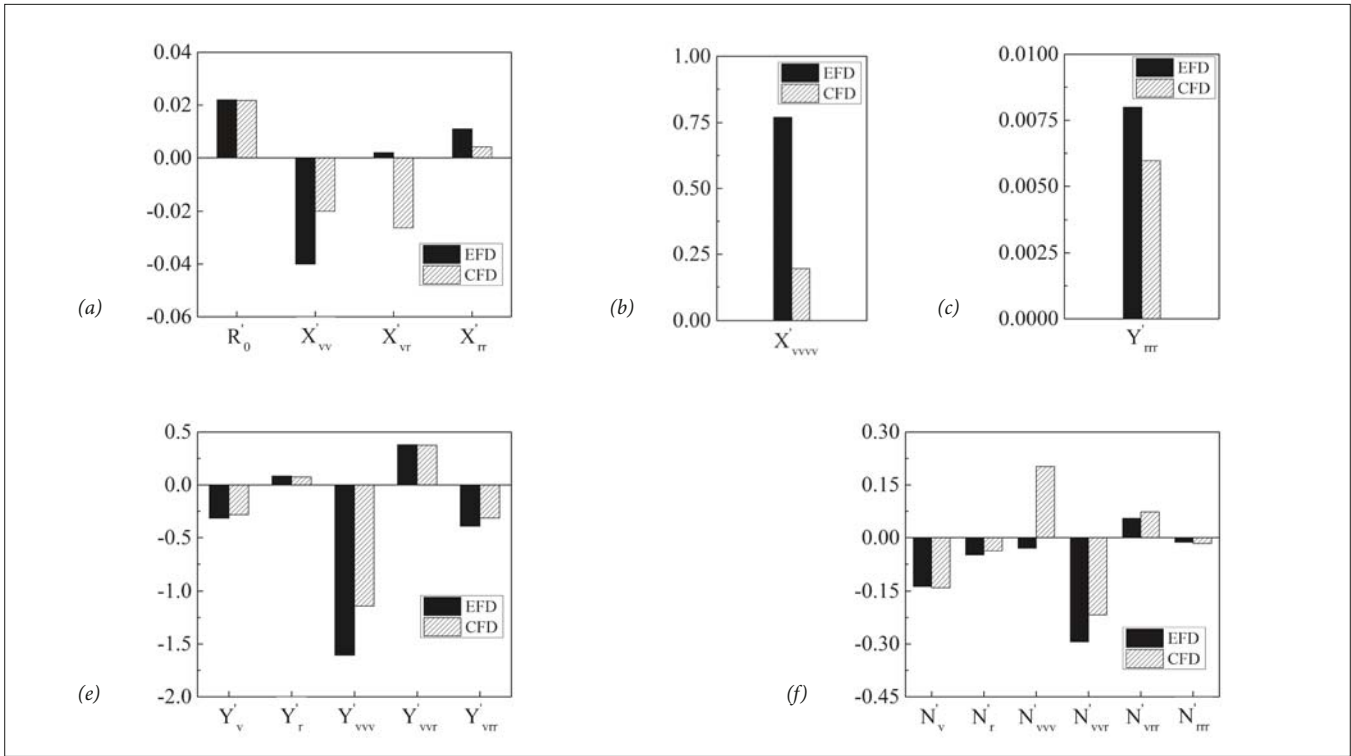


Fig. 9. Comparison of hydrodynamic derivatives

results, where the EFD results are obtained from Yasukawa et al. [8]. The derivatives of  $X'_{vv}$ ,  $X'_{vr}$ ,  $X'_{rr}$ ,  $X'_{vvv}$  obtained by CFD computation show significant deviations from the EFD results. However, the surge force is much less important to the trajectory in manoeuvres as compared with the sway force and yaw moment, meaning that these deviations may have a negligible impact on the manoeuvring simulations. The derivatives of  $Y$  and  $N$  from CFD show good agreement with those from EFD, except for  $Y'_{vvv}$ ,  $Y'_{vrr}$ ,  $N'_{vvv}$  and  $N'_{vrr}$ , indicating that this may result in errors in the sway force and yaw moment in manoeuvring simulations.

## SIMULATION OF STANDARD MANOEUVRES

A turning circle test and zigzag test simulations are carried out for the L-7 model using the derivatives obtained from the CFD data, and are compared with the results of a free-running model test (FRMT) from MARIN [16] and predictions by Yasukawa et al. [8] using derivatives obtained from a captive model test. The inertia terms and parameters for the modules of the propeller and rudder obtained from model tests are listed in Table 5, and are taken from Yasukawa et al. [8]. The trajectory for a turning circle test for  $\delta = \pm 35^\circ$  is presented in Fig. 10. The time histories of the heading angle and rudder angle for  $\pm 10^\circ/\pm 10^\circ$  and  $\pm 20^\circ/\pm 20^\circ$  zigzag manoeuvres are plotted in Fig. 11. A comparison of the manoeuvring parameters of advance ( $A_D$ ), tactical diameter ( $D_T$ ) and overshoot angles (OSAs) is presented in Table 6, and gives a relative comparison error E (%) defined as  $(1 - \text{Cal.}/\text{FRMT}) \times 100\%$ , where 'Cal.' denotes

the parameters predicted by the present method and taken from Yasukawa et al. [8].

As shown in Fig. 10, the trajectory of the turning test matches well in both simulations, although the parameters of advance and tactical diameter are under-predicted by the proposed method and over-predicted by Yasukawa et al. The simulation results of Yasukawa et al. show better accuracy, with a maximum value 5.8% larger than the test results, while the turning indices calculated by the proposed method have a maximum value 9.28% than the EFD data. From Fig. 11, it can be seen that both simulation results roughly agree with the test data and capture the overall trend of the zigzag manoeuvres. In Table 6, a comparison of the errors in the OSAs from a captive model test-based method are positive, except for the second OSA, indicating that Yasukawa et al. under-predict the first and second OSAs compared with FRMT. In contrast, the proposed method over-predicts the OSAs, resulting in negative comparison errors as shown in Table 6. Generally speaking, the captive model test-based method gives worse predictions for zigzag manoeuvres than the proposed method.

Tab. 5. Parameters used in the simulation

$m'_x$	0.022	$t_R$	0.387	$C_1$	2.0
$m'_y$	0.223	$l'_R$	-0.710	$C_2 (\beta_p > 0)$	1.6
$J'_z$	0.011	$w_{p0}$	0.40	$C_2 (\beta_p > 0)$	1.1
$t_p$	0.220	$\varepsilon$	1.09	$\gamma_R (\beta_R > 0)$	0.395
$a_H$	0.312	$\kappa$	0.50	$\gamma_R (\beta_R > 0)$	0.640
$x'_H$	-0.464	$\lambda$	2.747		

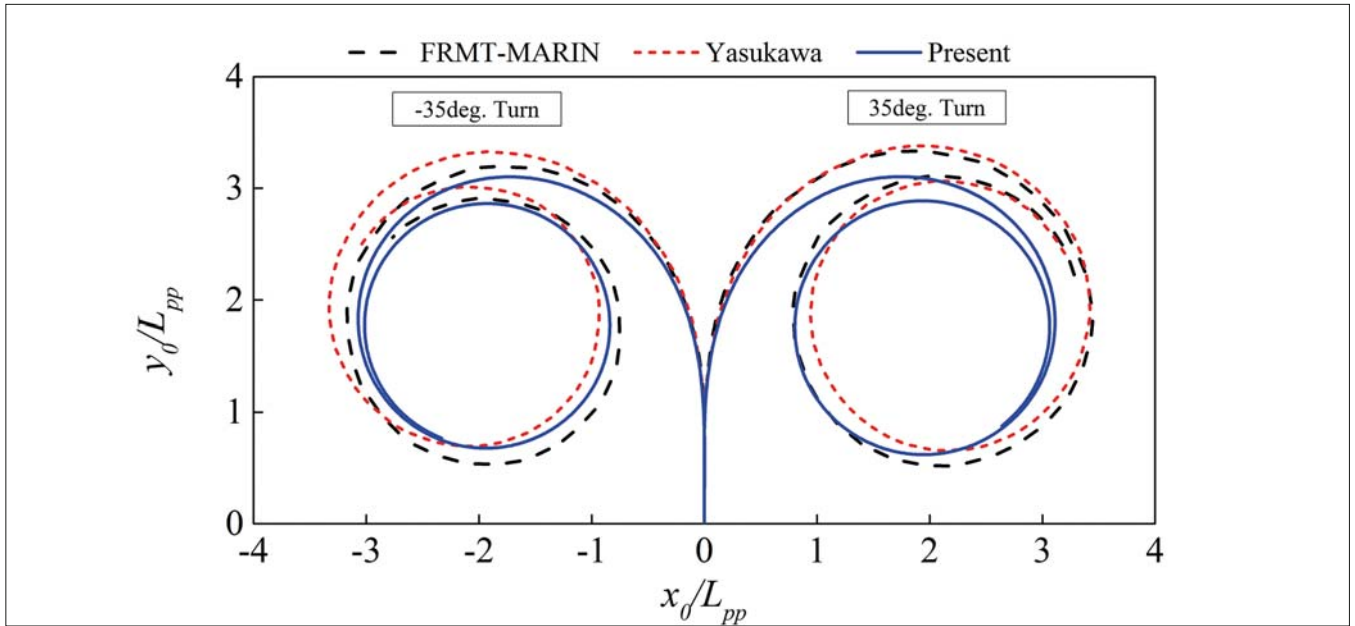
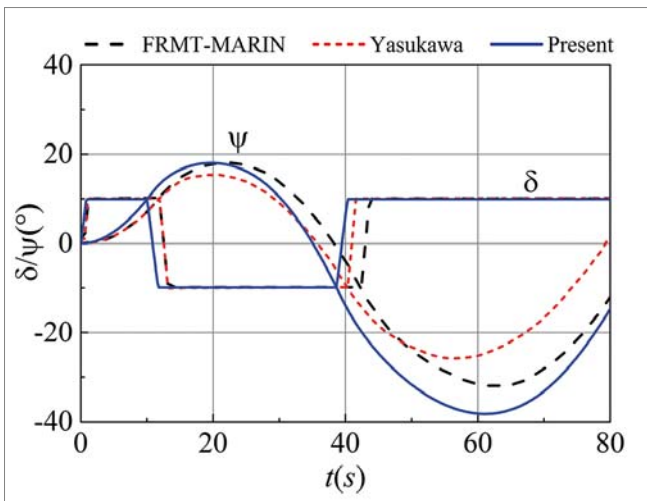
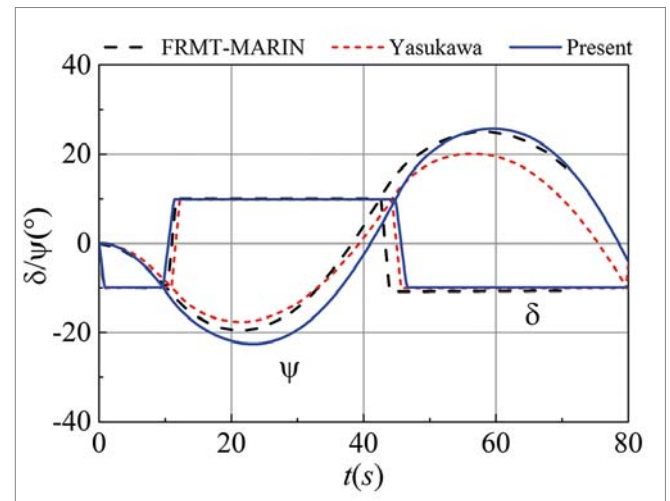


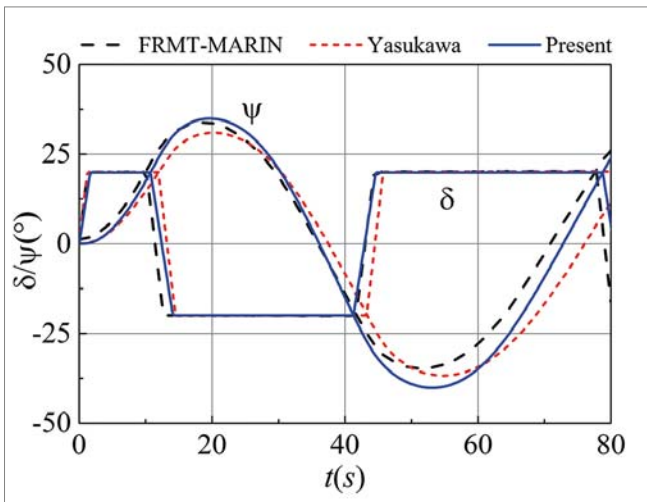
Fig. 10. Comparison of turning trajectory ( $\delta = \pm 35^\circ$ )



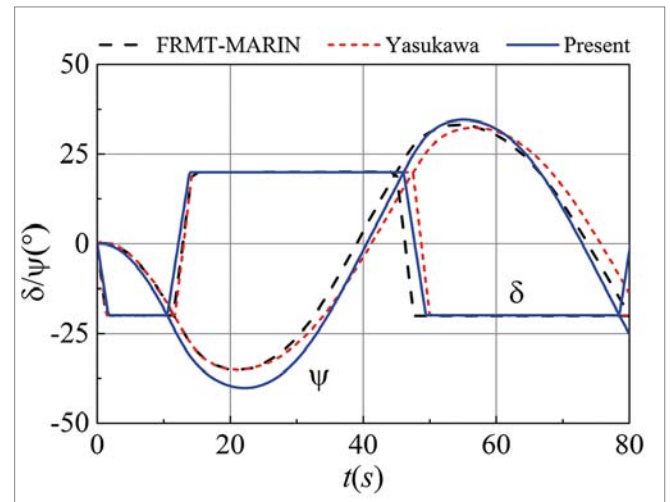
(a)



(b)



(c)



(d)

Fig. 11. Comparison of time histories of the heading angle and rudder angle in zigzag manoeuvres: (a) 10°/10° zigzag; (b) -10°/-10° zigzag; (c) 20°/20° zigzag; (d) -20°/-20° zigzag

Tab. 6. Comparison of manoeuvring parameters

Manoeuvres	Parameters	FRMT-MARIN	Yasukawa	E(%)	Present	E(%)
+35° Turn	$A_D (L_{pp})$	3.25	3.31	-1.85	3.02	7.08
	$D_T (L_{pp})$	3.34	3.36	-0.60	3.03	9.28
-35° Turn	$A_D (L_{pp})$	3.11	3.26	-4.82	3.02	2.89
	$D_T (L_{pp})$	3.08	3.26	-5.84	2.98	3.25
10°/10°	1st OSA (°)	8.2	5.2	36.59	8.3	-1.22
	2nd OSA (°)	21.9	15.8	27.85	28.30	-29.22
-10°/-10°	1st OSA (°)	9.5	7.6	20.00	12.60	-32.63
	2nd OSA (°)	15.0	10.2	32.00	15.7	-4.67
20°/20°	1st OSA (°)	13.7	10.9	20.44	15.3	-11.68
	2nd OSA (°)	14.8	16.8	-13.51	20.2	-36.49
-20°/-20°	1st OSA (°)	15.1	14.5	3.97	20.3	-34.44
	2nd OSA (°)	13.2	12.4	6.061	14.6	-10.61

## CONCLUSION

In this study, CFD-based prediction of 3-DOF ship manoeuvring is implemented for the KVLCC2 model, where the hydrodynamic derivatives of the hull in the 3-DOF MMG model are determined by simulation of a circular motion test and an oblique towing test using CFD. A convergence study is carried out for the simulation of a static drift case. The computed force and moment are validated by comparison with available experimental data. The hydrodynamic derivatives are determined from the computed forces and moments and compared with those from published experimental data, and show satisfactory agreement with experiment except for some high-order terms.

A turning circle test and zigzag manoeuvres are simulated using the computed hydrodynamic derivatives. The numerical results are compared with data from free running model tests and predictions based on a captive model test. From these comparisons, it can be concluded that although prediction based on captive model test shows better performance overall, the present method is effective in determining the hydrodynamic derivatives in the MMG model and predicting ship manoeuvrability.

## ACKNOWLEDGMENT

This work was supported by the National Natural Science Foundation of China (Grant Nos. 51979157) and the Natural Science Foundation of Shanghai, China. (Grant Nos. 19ZR1422500).

## REFERENCES

1. IMO Res MSC (2002): *Standards for Ship Manoeuvrability*, 137 (76).
2. IMO MSC/Circ.1053 (2002): *Explanatory Notes to the Standards for Ship Manoeuvrability*.
3. ITTC, Manoeuvring Committee (2008): *Final Report and Recommendations to the 25th ITTC*. Proceedings of 25th International Towing Tank Conference, Fukuoka, Japan.
4. Mofidi A., Carrica P.M. (2014): *Simulations of Zigzag Maneuvers for a Container Ship with Direct Moving Rudder and Propeller*. *Comput. Fluids*, 96, 191–203.
5. Shen Z., Wan D., Carrica P.M. (2015): *Dynamic Overset Grids in OpenFOAM with Application to KCS Self-Propulsion and Maneuvering*. *Ocean. Eng.*, 108, 287–306.
6. Wang J., Zou L., Wan D. (2018): *Numerical Simulations of Zigzag Maneuver of Free Running Ship in Waves by RANS-Overset Grid Method*. *Ocean. Eng.*, 162, 55–79.
7. Abkowitz, M.A. (1964): *Lectures on Ship Hydrodynamics-Steering and Manoeuvrability*. In: *Hydro- and Aerodynamics Lab, Report No. Hy-5*, Lyngby, Copenhagen, Denmark.
8. Yasukawa H., Yoshimura, Y. (2015): *Introduction of MMG Standard Method for Ship Maneuvering Predictions*. *Journal of Marine Science and Technology*, 20(1), 37–52.
9. Sakamoto N., Carrica P.M., Stern F. (2012): *URANS Simulations of Static and Dynamic Maneuvering for Surface Combatant: Part 1. Verification and Validation for Forces, Moment, and Hydrodynamic Derivatives*. *Journal of Marine Science and Technology*, 17(4), 422–445.

10. Hai-peng G., Zao-jian Z. (2017): *System-Based Investigation on 4-DOF Ship Maneuvering with Hydrodynamic Derivatives Determined by RANS Simulation of Captive Model Tests*. Applied Ocean Research, 68, 11-25.
11. Yi L., Lu Z., Zaojian Z., Haipeng G. (2018): *Predictions of Ship Maneuverability Based on Virtual Captive Model Tests*. Engineering Applications of Computational Fluid Mechanics, 12(1), 334–353.
12. Kim H., Akimoto H., Islam H. (2015): *Estimation of the Hydrodynamic Derivatives by RANS Simulation of Planar Motion Mechanism Test*. Ocean Engineering, 108, 129–139.
13. Islam H., Guedes Soares C. (2018): *Estimation of Hydrodynamic Derivatives of a Container Ship Using PMM Simulation in OpenFOAM*. Ocean Engineering, 108, 164–425.
14. Ueno M., Yoshimura Y., Tsukada Y., Miyazaki H. (2009): *Circular Motion Tests and Uncertainty Analysis for Ship Maneuverability*. Journal of Marine Science and Technology, 14, 469–484.
15. Yoshimura Y., Ueno M., Tsukada Y. (2008): *Analysis of Steady Hydrodynamic Force Components and Prediction of Manoeuvring Ship Motion with KVLCC1, KVLCC2 and KCS*. SIMMAN 2008, Workshop on verification and validation of ship manoeuvring simulation method, Workshop Proceedings, Vol. 1, Copenhagen, pp. E80–E86.
16. SIMMAN (2008): *Part C Captive and Free Model Test Data*. Workshop on verification and validation of ship manoeuvring simulation method, Workshop Proceedings, Vol. 1, Copenhagen.
17. Stern F., Wilson R.V., Coleman H.W., Paterson E.G. (2001): *Comprehensive Approach to Verification and Validation of CFD Simulations Part 1: Methodology and Procedures*. Journal of Fluids Engineering, 123(4), 793–802.
18. Wilson R., Shao J., Stern F. (2004): *Discussion: Criticisms of the “Correction Factor” Verification Method*. Journal of Fluids Engineering, 126(4), 704–706.
19. SIMMAN (2014). Retrieved from <http://simman2014.dk/ship-data/moeri-kvlcc2-tanker/geometry-and-conditions-moeri-kvlcc2-tanker/>.

## CONTACT WITH THE AUTHORS

**Kun Dai**

*e-mail: kundai@hrbeu.edu.cn*

College of Shipbuilding Engineering  
Harbin Engineering University, Harbin  
**CHINA**

**Yunbo Li**

*e-mail: multihull@163.com*

College of Ocean Science and Engineering  
Shanghai Maritime University, Shanghai  
**CHINA**

# A PRACTICAL APPROACH TO THE ASSESSMENT OF WATERJET PROPULSION PERFORMANCE: THE CASE OF A WATERJET-PROPELLED TRIMARAN

**Lei Zhang**

Dalian Maritime University, China

**Jianing Zhang\***

Dalian Maritime University, China

**Yuchen Shang**

Texas A&M University, USA

**Guoxiang Dong**

Shanghai Ship and Shipping Research Institute, China

**Weimin Chen**

Shanghai Ship and Shipping Research Institute, China

\*Corresponding author: 12511951@zjhu.edu.cn (Z.J.)

## ABSTRACT

*To obtain a reasonable evaluation of the performance of waterjet propulsion at the design stage, a semi-theoretical and semi-empirical method is used to calculate the fundamental parameters of waterjet propulsion performance using an iterative approach. To calculate the ship's resistance, a boundary element method based on three-dimensional potential flow theory is used to solve the wave-making resistance, and an empirical approach is used to evaluate the viscous resistance. Finally, the velocity and pressure of the capture area of the waterjet propulsion control volume are solved based on turbulent boundary layer theory. The iteration equation is established based on the waterjet-hull force-balance equation, and the change in the ship's attitude and the local loss of the intake duct are considered. The performance parameters of waterjet propulsion, such as resistance, waterjet thrust, thrust deduction, and the physical quantity of the control volume, are solved by iteration. In addition, a PID-controlled free-running ship model is simulated using the RANS CFD method as a comparison. We apply the proposed approach and the RANS CFD method to a waterjet-propelled trimaran model, and the simulation process and the results are presented and discussed. Although there are some differences between the two methods in terms of the local pressure distribution and thrust deduction, the relative error in the evaluation results for the waterjet propulsion performance is generally reasonable and acceptable. This indicates that the present method can be used at the early stages of ship design without partial information about the waterjet propulsion system, and especially in the absence of a physical model of the pump.*

**Keywords:** waterjet propulsion thrust, pressure jump method, boundary element method, trimaran, negative thrust deduction

## INTRODUCTION

A waterjet-propelled vessel has characteristics such as high efficiency, strong anti-cavitation performance, low noise, and outstanding maneuverability, and waterjet propulsion performance is a significant component of the hydrodynamic performance of the waterjet system. Before the 1990s, waterjet propulsion was mainly adopted in empirical methods and

model tests [1-2]. The 21st ITTC Committee on Waterjets put forward a standard procedure for performance predictions of waterjet-propelled craft, and the momentum flux method and direct thrust measurements for the evaluation of model self-propulsion (SP) tests were recommended [3]. In direct thrust measurements, the impact of the force on the intake duct is difficult to measure, so the momentum flux method is widely used, as it focuses on measurement of the mass flow

in the discharge nozzle, which is more applicable. Meanwhile, based on the above momentum flux method for waterjet propulsion performance, the CFD method is widely used to simulate the detailed flow field and to compute the force components of the system.

Park performed simulations on the intake duct with and without a rotor and stator [4-5], and fully solved the flow details of the intake duct; the results for the simulated momentum flux matched the experimental data to within a relative error of 3.1%. In addition, the streamlines and pressure distribution of the duct were closely captured. The innovative development of overset mesh technology and high-performance computing enabled multi-core parallel CFD computation to be applied to the complex simulation of marine structure interactions. Takai [6-7] used an in-house viscous CFD solver called CFDSHIP-IOWA to perform barehull and self-propulsion simulations for the JHSS WJ model, generating 15 overset blocks to carefully refine the hull surface and near-field, and applied a simplified body-force model to the waterjet pump region to replace the real pump geometry and save on computational cost. The simulation results closely matched the EFD results, and demonstrated the ability to optimize the intake duct shape. Research by Altosole [8] proposed a reliable and effective method of obtaining a preliminary evaluation of the selection of waterjet units and their performance with sufficient accuracy. This method was based on the collection of extensive information about the performance of existing waterjets, and provided a non-dimensional performance diagram, which was beneficial for the prediction of waterjet performance at the design stage. Based on the pressure jump method, Eslamdoost [9-10] used a potential flow calculation module called XSPAN and the double model calculation module XBOUND of the SHIPFLOW software application to study the waterjet-hull interaction problem, and validated the applicability of this method in predicting waterjet thrust and thrust deduction. In recent research, Gong [11] used both experimental and viscous CFD simulations to research the waterjet-hull interaction for a four-waterjet propelled vessel. The differences in the energy/momentum velocity coefficients of the inner and outer waterjets were investigated, and the main causes were found to be the shape of the inlet duct and the presence of stabilizer fins.

The empirical method has an advantage in terms of efficiency, but provides only estimated data on waterjet propulsion performance, and further model tests or CFD based simulations are needed to obtain more details. Viscous CFD tools can simulate the flow field in more detail, but the viscous CFD method is suitable only in cases where there is sufficient physical information about the target, and the efficiency of this technique still needs to be improved. In this paper, semi-theoretical and semi-empirical iterative approaches are used to quickly and effectively predict the hydrodynamic performance of a waterjet-propelled vessel and to provide details of the wave patterns and hull pressure distribution in the partial absence of information, and especially in the absence of a waterjet pump. In the present

study, simulations based on the current method and the RANS CFD method are carried out for a waterjet-propelled trimaran to evaluate the performance of waterjet propulsion, and the differences between the two approaches are analyzed and discussed.

## MATHEMATICAL MODEL

### DEFINITIONS USED IN WATERJET PROPULSION

The global coordinate system satisfies the right-hand rule, and its origin  $O$  is located at the transom on the free surface. The  $X$ -axis points to the bow, along the longitudinal section of the main hull, while the  $Y$ -axis points to the port side and the  $Z$ -axis is perpendicular to the  $XOY$  plane, pointing upwards. The inflow speed is  $U(U_x, U_y)$ , where  $U_x$  points to the negative direction of the  $X$ -axis, and  $U_y$  points to the positive direction of the  $Y$ -axis.

As shown in Fig. 1, the waterjet-hull system includes two parts: the waterjet system, which contains the virtual control volume and the waterjet pump; and the hull system, which contains the remaining hull surface. According to the widely used definitions of van Terwisga [1], the gross thrust ( $T_g$ ) of the waterjet system is calculated based on the flux momentum method in the control volume, which is equal to the horizontal component of the moment flux change. Moreover, the net thrust ( $T_{net}$ ) is defined as the force vector acting on the physical material boundaries of the waterjet system, and is directly passed to the hull.

$$T_g = - \iint_{A_{in}+A_{out}} \rho u_x (u_k n_k) dA = \rho Q u_0 (NVR - \alpha) \quad (1)$$

$$T_{net} = - \iint_{A_{duct}+A_{virtual}} \sigma_x dA - \iiint_{V_{pump}} \rho F_{px} dV \quad (2)$$

where  $\rho$  is the fluid density;  $u_x$  is the fluid velocity vector in the  $x$  component;  $u_k$  and  $n_k$  are the fluid velocity vector and unit normal vector, respectively;  $k=1, 2, 3$  are the surface stresses in the  $x$  direction; and  $F_{px}$  is the unit pump force in the  $x$  direction.  $Q$ ,  $u_0$ ,  $NVR$ , and  $\alpha$  are the mass flow rate, ship speed, nozzle velocity ratio, and momentum velocity coefficient, respectively.  $A_{in}$ ,  $A_{out}$ ,  $A_{duct}$ ,  $A_{virtual}$ , and  $V_{pump}$  correspond to the surface of the capture area, nozzle discharge, duct, virtual surface, and volume of the pump region, respectively.

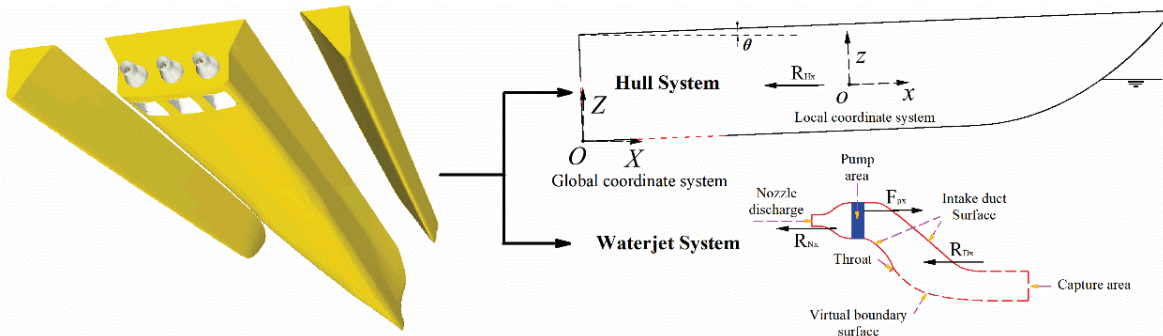


Fig. 1. The waterjet-hull system

During the numerical simulation of self-propulsion to predict the self-propulsion (SP) point of the real ship, the difference in the frictional resistance between the model and the real ship needs to be corrected. The correction force  $F_D$  is the so-called towing force or rope force, and is expressed as:

$$F_D = -\frac{1}{2} \frac{\rho u_0^2 S_w}{\lambda^3} (C_{fm} - C_{fs} + \Delta C_f) \quad (3)$$

where  $S_w$  is the area of the wetted hull surface,  $\lambda$  is the scale ratio, and  $C_{fm}$ ,  $C_{fs}$ , and  $\Delta C_f$  are the frictional coefficients of the ship model and the real ship, and the roughness correction coefficient, respectively.

When the barehull (BH) model test and SP test or simulations have been carried out, and the ship resistance and gross thrust are obtained, the thrust deduction fraction of the waterjet propulsion system can be obtained using the following formula:

$$t = 1 - \frac{R_{BH} - F_D}{T_g} \quad (4)$$

### ITERATIVE SOLUTION MODEL

As shown in Fig.1, the longitudinal force on the hull (with trim and sinkage) is as follows:

$$R_{p,x} = R_H + NR_{D,x} + NR_{N,x} \quad (5)$$

where  $N$  is the number of waterjet units,  $R_H$  is the resistance of the hull except for the intake duct, and  $R_{D,x}$  and  $R_{N,x}$  are the longitudinal forces on the intake duct and the nozzle chamber.

In the present research, the region of the waterjet pump is assumed to be a virtual disk, and the pump force is regarded as the body-force that accelerates the fluid. The circumferential rotation of the waterjet rotor is not accounted for in the simplified body-force method, as the complicated rotational process needed to generate waterjet thrust is not the primary research target here. We therefore simplified the process

and took the final generated axial pump force into account. The pressure difference in the virtual disk is the reason for the variation in the pressure and the velocity of the fluid passing through the pump area. This pressure difference can be written as [9-10]:

$$\Delta p = \frac{R_{RT}}{NA_{out} \cos \theta} \quad (6)$$

$$R_{RT} = R_H + R_{D,x} + N \left( \iint_{S_n} p_c n_x ds + \iint_{S_n} \tau n_x ds \right) \quad (7)$$

where  $\theta$  is the trim angle,  $p_c$  is the constant flow pressure without the waterjet pump,  $\tau$  is the shear stress, and  $S_n$  is the surface of the nozzle chamber.

The Bernoulli equation is applied to the center of the capture area and the nozzle, as follows [12]:

$$\left( \overline{p_m} + \rho g \overline{h_m} + (1/2) \rho g \overline{u_m}^2 \right) + \Delta p = \overline{p_{out}} + \rho g \overline{h_{out}} + (1/2) \rho g \overline{u_{out}}^2 + (1/2) K u_0^2 \quad (8)$$

The ratio between the nozzle velocity and the inlet velocity can be obtained as:

$$k = \frac{\overline{u_{out}}}{u_0} = \sqrt{\frac{2(\overline{p_{in}} - \overline{p_{out}})}{\rho u_0^2} + \frac{2\Delta p}{\rho u_0^2} + \frac{2g(\overline{h_{in}} - \overline{h_{out}})}{u_0^2} + \frac{\overline{u_{in}}^2}{u_0^2} - K} \quad (9)$$

where  $\overline{u_{in}}$  and  $\overline{u_{out}}$ ,  $\overline{p_{in}}$  and  $\overline{p_{out}}$ ,  $\overline{h_{in}}$  and  $\overline{h_{out}}$  represent the average velocities, average pressures and average heights above the baseline of the capture area and above the nozzle, respectively.  $K$  is the local loss due to frictional retardation, changes in the flow direction, and contraction of the duct.

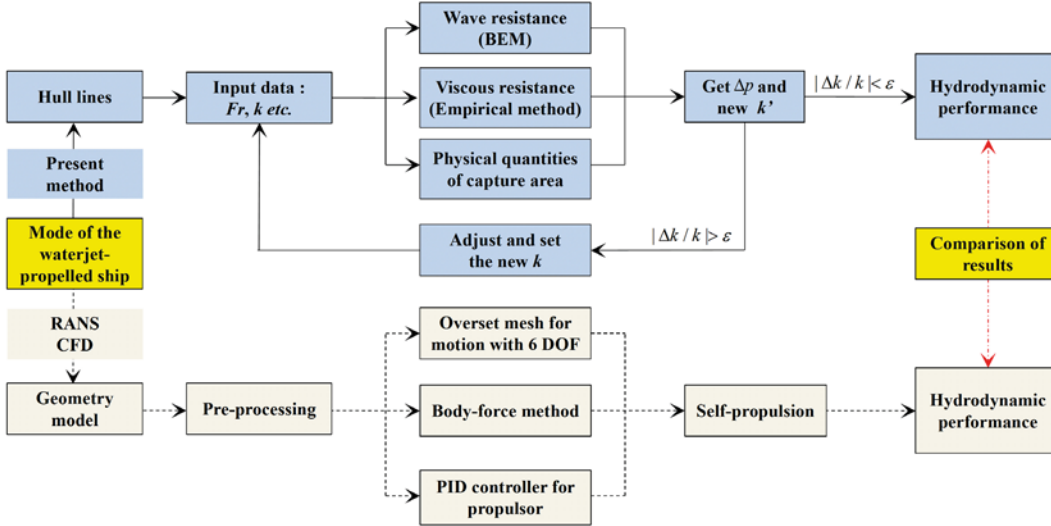


Fig. 2. Flow chart for the proposed method and the RANS CFD method for comparison

Eq. (9) gives the iterative solution model for the waterjet propulsion once the parameters can be calculated. As shown in the upper part of Fig. 2, the present method for calculating the waterjet propulsion performance contains three components that need to be solved: wave-making, viscous resistance, and the physical quantities of the capture area. The velocity ratio  $k$  is the initial input value for the calculation, and after solving the three parts of the equation, a new velocity ratio  $k$  can be obtained from the formula, a process which is iterated until the calculation converges. The waterjet thrust and thrust deduction can then be identified.

## NUMERICAL CALCULATION OF THE RESISTANCE AND CAPTURE AREA

### HULL RESISTANCE

The basic assumptions of potential flow theory are that the fluid is inviscid, incompressible, and ideal. The total velocity potential is expressed as  $\Phi(x, y, z) = -u_0x + \varphi(x, y, z)$ , without considering the unsteady disturbances,  $-u_0x$  represents the velocity potential of uniform flow, and  $\varphi$  is the constant disturbance potential caused by the uniform velocity motion of the ship. We take Zhou's settings [13] as references to set the free surface boundary condition, the hull and duct boundary conditions, the infinite boundary condition, and the transom boundary condition. These boundary conditions are defined in Eqs. (10)–(15), where  $n_x$  is the outward normal component of the hull surface in the  $x$ -direction, and  $k$  is the velocity ratio. In the transom condition,  $h$  is the height of the transom stern edge, and  $x_T$  and  $y$  are the longitudinal and transverse coordinates of the transom stern, respectively.  $\Delta x$  is a finite distance on the free surface after the transom stern, which can be evaluated as the half longitudinal scale of the panel.

$$\nabla^2 \varphi = 0 \quad (\text{In the domain}) \quad (10)$$

$$\frac{\partial \varphi}{\partial n} = u_0 n_x \quad (\text{Hull except nozzle}) \quad (11)$$

$$\frac{\partial \varphi}{\partial n} = k u_0 n_x \quad (\text{At the nozzle}) \quad (12)$$

$$\frac{\partial^2 \varphi}{\partial x^2} + \frac{g}{u_0^2} \frac{\partial \varphi}{\partial z} = 0 \quad (\text{At the free surface}) \quad (13)$$

$$\varphi \rightarrow 0 \quad (\text{At infinity}) \quad (14)$$

$$\varphi_{,xx} - 2\varphi_{,x} / \Delta x = -\frac{g}{u_0} (2h(x_T - y) / \Delta x + \frac{\partial h}{\partial x} (x_T - y)) \quad (\text{Transom}) \quad (15)$$

The boundary element method is used to obtain the perturbation potential  $\varphi$  in the flow field by discretization of the above equations. The wave-making resistance is then obtained in the  $x$ -direction of the hull surface pressure distribution, according to the Bernoulli equation:

$$R_w = \iint_{S_w} P n_x dS = \rho (u_0 \frac{\partial \varphi}{\partial x} - \frac{1}{2} \nabla \varphi \nabla \varphi - g z) \quad (16)$$

Using the balance equations of the hull force and moments, the trim and sinkage are iteratively converged:

$$\iint_S C_p n_z dS = \int_0^L (s - x \tan \theta) y(x, 0) dx \quad (17)$$

$$\iint_S x C_p n_z dS = \int_0^L (s-x \tan \theta) xy(x,0) dx \quad (18)$$

where  $C_p$ ,  $s$ , and  $y(x,0)$  represent the pressure coefficient, the sinkage, and the width of the waterline at position  $x$ .

The hull friction resistance is calculated using the 1957ITTC formula for the friction resistance coefficient, and the final expression is:

$$R_f = \frac{1}{2} \rho u_0^2 (\Delta C_f + \frac{0.075}{(\lg \text{Re} - 2)^2}) \quad (19)$$

where the Reynolds number is  $\text{Re} = u_0 L_{wl} / \nu$ ,  $L_{wl}$  is the waterline length, and  $\nu$  is the kinematic viscosity of water.

The viscous pressure resistance coefficient is based on the approximate formula:

$$C_{pv} = \frac{R_{pv}}{\frac{1}{2} \rho u_0^2 S_w} = 0.09 \frac{A_m}{S_w} = \sqrt{\sqrt{A_m} / 2L_r} \quad (20)$$

and the hull viscous pressure resistance is:

$$R_{pv} = \frac{9 \rho u_0^2 A_m}{200} = \sqrt{\sqrt{A_m} / 2L_r} \quad (21)$$

where  $A_m$  is the midship cross-sectional area, and  $L_r$  is the run length, which should fulfill the condition  $L_r \geq 4.08 \sqrt{A_m}$ .

## CAPTURE AREA

Based on the turbulent boundary layer theory, the velocity distribution at the wall is as follows:

$$u = \begin{cases} u_0 (y / \delta)^{1/n} & (y \leq \delta) \\ u_0 & (y > \delta) \end{cases} \quad (22)$$

where  $y$  is the vertical distance away from the hull surface at the section of the capture area,  $u$  is the velocity of the point, and the value of the index  $n$  is 7 when the model scale is calculated, and 9 in the calculation of the real ship [14].  $\delta$  is the boundary layer thickness, which is calculated by the Weighardt formula at high Reynolds number as  $\delta = 0.27 x (u_0 x / \nu)^{-1/6}$ ; we could also use the plate flow boundary layer formula  $\delta = 0.37 x (u_0 x / \nu)^{-1/5}$ .

In general, a semi-elliptical shape is used to represent the capture area of the control volume, i.e.  $(x / (W / 2))^2 + (y / Y_0)^2 = 1$ , where  $W$  is the width of the capture area, and  $Y_0$  is the effective inflow thickness. The relationship between the hull boundary layer thickness and  $Y_0$  determines the boundary layer influence coefficient, the flow

velocity, and the pressure distribution. The specific formula used to calculate  $Y_0$  is based on Liu's method [14-15].

The momentum velocity coefficient  $\alpha$  is defined as:

$$\alpha = \frac{\int_{A_{in}} u^2 dA}{u_0 \int_{A_{in}} u dA} \quad (23)$$

The average velocity  $u_{in}$  of the capture area can be calculated after determining the relationship between  $\delta$  and  $Y_0$ , and at the scale of the model, the average velocity is determined as follows:

$$u_{in} = \frac{\sum_{i=1}^n u_i S_i}{\sum_{i=1}^n S_i} = 2 \frac{\int_0^{Y_0} x u_y dy}{\int_0^{Y_0} x dy} = \frac{4u_0}{\pi} \left(\frac{Y_0}{\delta}\right)^{1/7} \int_0^1 t^{1/7} (1-t^2)^{1/2} dt \quad Y_0 \leq \delta \quad (24)$$

$$u_{in} = \frac{4u_0}{\pi} \left[ \left(\frac{Y_0}{\delta}\right)^{1/7} \int_0^{\delta/Y_0} t^{1/7} (1-t^2)^{1/2} dt + \int_{\delta/Y_0}^1 (1-t^2)^{1/2} dt \right] \quad Y_0 > \delta \quad (25)$$

The average pressure on the capture area is determined by  $p_{in} = p_d + p_s$ , where  $p_d$  is the average dynamic pressure and  $p_s$  is the average static pressure.

## CASE STUDY: WATERJET-PROPELLED TRIMARAN MODEL

### APPLICATION OF THE PROPOSED METHOD TO A TRIMARAN MODEL

The proposed method for numerical calculation of the waterjet propulsion performance is applied to a model of a waterjet-propelled trimaran [12, 16] with a transom stern, as shown in Fig. 3. Three sets of waterjet units are installed at the stern. The main dimensions are listed in Table 1.

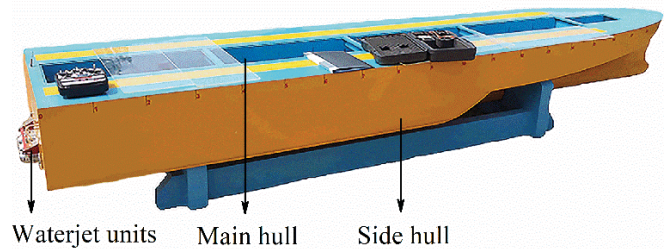


Fig. 3. The waterjet-propelled trimaran model

Tab. 1. Main data used in the trimaran model

Length $L_{pp}$ (m)	4.00	Displacement $\Delta(t)$	0.0648
Width $B$ (m)	0.867	Length of side hull $L_s$ (m)	2.23
Draft $T$ (m)	0.12	Longitudinal distance between the main hull and side hull (m)	0.00
Scale ratio	1:30	Transverse distance between the main hull and side hull (m)	0.411

## HULL MODIFICATION AND MESH DISTRIBUTION

Since the physical surface area of the waterjets exceeds the hull transom area in the waterjet-propelled vessel, if the free surface panel and hull panels are directly generated for the wave-making resistance calculation, numerical errors will be obtained in the influence coefficient matrix in the potential flow calculation, due to the penetration between the duct panel and the free surface panel. To avoid this situation, while maintaining the duct model unmodified, the main hull of the trimaran should be lengthened appropriately to ensure that the calculation is correct. As shown in Fig. 4, the stern is extended by two amounts,  $1.25\%L_{pp}$ , and  $2.5\%L_{pp}$ . Since the  $1.25\%L_{pp}$  lengthened model is still partly outside of the transom, the  $2.5\%L_{pp}$  lengthened trimaran model is more suitable and is therefore applied in the remaining calculations. The increase in the total resistance due to the lengthened part is corrected, and this is expressed as  $\Delta R = -0.5\rho u_0^2 S_{add} C_t$ , where  $S_{add}$  is the wetted surface area of the lengthened part and  $C_t$  is the calculated total resistance coefficient.

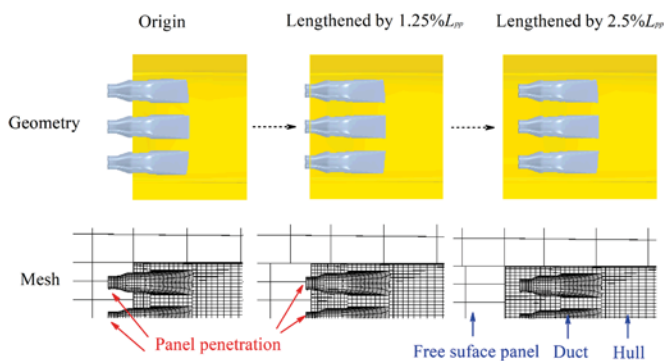


Fig. 4. Geometry and mesh of the original and lengthened models when calculating the wave-making resistance

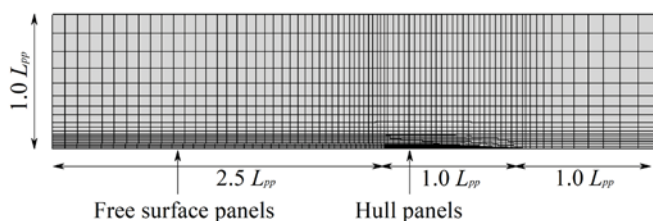


Fig. 5. Panels of the free surface and wetted hull

Due to symmetry characteristics, a half mesh is generated for the free surface and the trimaran. The wetted modified hull is divided into 1520 panels, and a local mesh refinement approach is applied. The free surface is divided into 1430 panels (Fig. 5).

## THE ITERATIVE CONVERGENCE PROCESS

In the iterative calculation used in the present approach, there are two iterative processes. One is the inner iteration of attitude, based on Eq. (17) and Eq. (18), when calculating the wave resistance, and the other is the outer iteration of

the nozzle velocity ratio, based on Eq. (9). Fig. 6 shows the inner iterative convergence process for the trim and sinkage for  $Fr = 0.30, 0.45,$  and  $0.60$  (the trim at the stern is positive). At speeds of  $Fr = 0.30$  and  $0.45$ , the hull motion converges within four to five iterations, and the convergence criterion is that the difference between the last two iterations is less than 1.5%. When  $Fr=0.60$  at high speed, the convergence criterion is satisfied after seven iterations.

It can be seen that as the speed increases, the numerical fluctuations in the calculation process also become larger, and the number of iterations needed gradually increases. In the outer iteration, substantial convergence for the nozzle velocity ratio can be achieved after four or five iterations. When using a 3.6 GHz processor for single-core computing, each iteration takes about 1.5 minutes; it therefore takes about half an hour to calculate a low-speed point, and several hours to calculate a series of speed points. If multi-threaded parallel computing is used, the time cost will be greatly reduced.

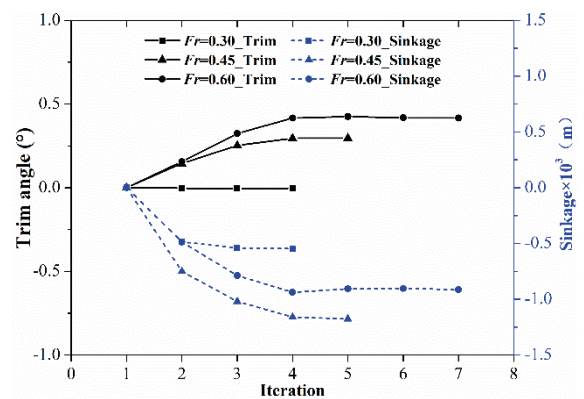


Fig. 6. Convergence of attitudes in one inner iteration

## RANS CFD MODEL

Fig. 7 shows the fully-appended geometric model of the trimaran, including the main hull, side hulls, intake duct, nozzle, rotor, and stator.

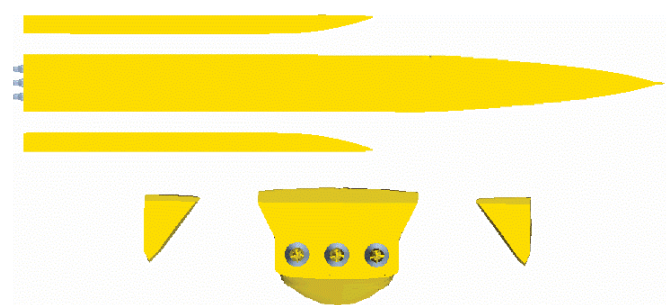


Fig. 7. Geometry of the trimaran model

## PID CONTROLLER AND BODY-FORCE METHOD

For the SP problem, the traditional method in viscous CFD is to fix the ship model in the longitudinal position to encounter the water flow at a specified speed; then, the speed of the propulsor is gradually increased with a fixed step size, and the calculated resistance and thrust curves are finally interpolated to obtain the SP point. In the present RANS CFD comparison simulation, a free-running model is used that can travel freely in real space, rather than using the conventional CFD self-propelled method to encounter water flow in a fixed position. To maintain the required hull speed in self-propulsion, the PID controller [17] is used to automatically adjust the rotating speed of the waterjet rotor. The PID-controlled rotor revolution is as follows:

$$RPM = Pe + I \int_0^t e dt + D \frac{de}{dt} = P(u_0 - u_M) + I \sum_{i=2}^M (u_0 - u_i / 2 - u_{i-1} / 2) \Delta t - Da \quad (26)$$

where  $e = u_0 - u_M$  is the error term,  $u_0$ , and  $u_i$  are the target hull speed, the hull speed at simulated time  $t$ , and the hull speed at the iteration  $i$ , respectively.  $M$  is the total simulated iteration number,  $\Delta t$  is the time step, and  $a$  is the hull acceleration.  $P$ ,  $I$ , and  $D$  are the coefficients of the proportion, integration, and differentiation terms, respectively.

A widely used propulsion approach, the body-force method uses the concept of an actuator disk rather than a real propeller, and has been shown to be a reasonable approach to the simulation of maneuvering and self-propulsion [18-19]. In the current viscous CFD model, the waterjet rotor is used to simulate the open water performance and obtain convergent KT and KQ curves. These performance curves are applied to the body-force region. As shown in Fig. 8, the original rotor is replaced by a virtual disk of the same radius.

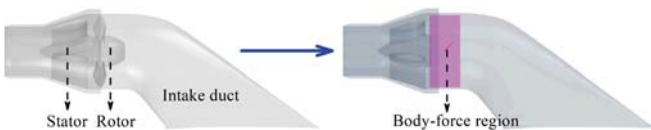


Fig. 8. The body-force region in the intake duct

## GRID CONVERGENCE ANALYSIS

The computational domain is cuboid, with a size of  $4.5L_{pp} \times 3.0L_{pp} \times 1.5L_{pp}$ . The prism layer grid is 2.0 cm thick and contains six layers, the growth factor is 1.414, and the  $y^+$  value of the hull surface mesh is less than 100. The volume mesh is generated using prism and trimming volume techniques. To carry out the unstructured mesh convergence analysis, Baek [20] and Gong [11] used the total number of grids to define the refinement ratio, and the mesh independence of the RANS CFD was validated using the following equations:

$$r = \left( \frac{N_{finer}}{N_{coarser}} \right)^{1/3} \quad (27)$$

$$E = \left( \frac{S_{coarser} - S_{finer}}{1 - r^2} \right) \quad (28)$$

$$U_N = F_s |E| \quad (29)$$

where  $N$  is the total number of the grids,  $r$  represents the refinement ratio,  $S$  is the solution to the corresponding mesh density, and  $F_s$  is the safety factor, which is equal to three.

To carry out a grid convergence analysis for the RANS CFD contrast model, three different mesh densities are applied to simulate the BH model and the SP performance for  $Fr=0.30$ . The total resistance for the BH model and the total resistance and RPM for the SP model are validated as shown in Tables 2 and 3, where *Extr.* is the linear extrapolated predicted value of the finer mesh adopting the same refinement ratio. The final uncertainty is normalized by *Extr.* The results show that with an increase in the mesh density, the uncertainty in the total resistance drops from 16.72% to 4.56% and from 6.53% to 1.05% for the BH and SP models, respectively, and the uncertainty in the RPM for the SP model drops from 8.93% to 4.65%. The uncertainty results for the fine mesh are reasonable and reliable, and thus the fine mesh density is applied to the comparison models. The final mesh and the computational region used are shown in Fig. 9.

Tab. 2. Mesh convergence for the BH model

Barehull model	Coarse (0.65 M)	Medium (1.30 M)	$E$	$U_N$	<i>Extr.</i>	$U_N\%$ ( <i>Extr.</i> %)
$R_{BH}$	12.65	12.26	0.66	1.99	11.88	16.72%
Barehull model	Medium (1.30 M)	Fine (2.73 M)	$E$	$U_N$	<i>Extr.</i>	$U_N\%$ ( <i>Extr.</i> %)
$R_{BH}$	12.26	12.14	0.18	0.55	12.03	4.56%

Tab. 3. Mesh convergence for the SP model

SP Model	Coarse (0.69 M)	Medium (1.34 M)	$E$	$U_N$	<i>Extr.</i>	$U_N\%$ ( <i>Extr.</i> %)
$RPM$	7400	7275	204	613	7162	8.93%
$R_H$	14.43	14.25	0.306	0.919	14.07	6.53%
SP Model	Medium (1.34 M)	Fine (2.85 M)	$E$	$U_N$	<i>Extr.</i>	$U_N\%$ ( <i>Extr.</i> %)
$RPM$	7275	7200	118	353	7121	4.65%
$R_H$	14.25	14.28	-0.050	0.150	14.32	1.05%

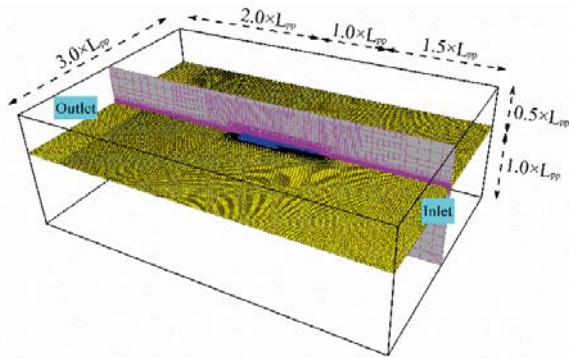
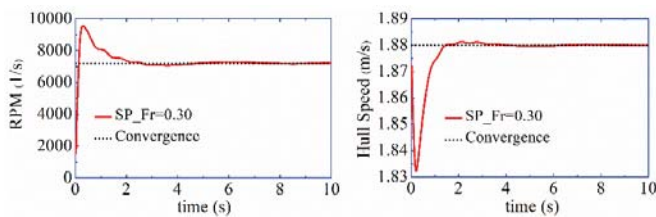


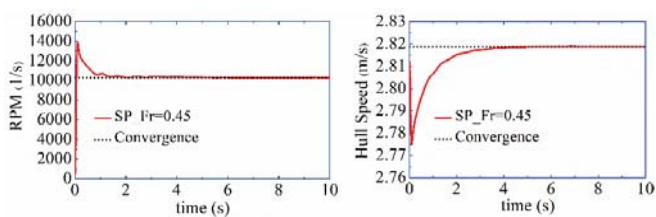
Fig. 9. Computational domain and mesh for the RANS CFD model

Three different speed inputs ( $Fr=0.30, 0.45$  and  $0.60$ ) are used in the comparison models. The towing force at different speeds is also added to the hull. Fig. 10 shows the convergence process for the rotor and hull speeds at different Froude numbers. We can see that the increased resistance rapidly reduces the hull speed at all three values of  $Fr$  after starting the simulations. Through the PID control, the rotor RPM is automatically adjusted to the maximum speed within a simulation time of  $0.2\text{--}0.3$  s; the RPM is then gradually reduced, and the hull speed is gradually increased. The rotor RPM, hull speed, thrust, resistance, and attitudes all start to fluctuate slightly, and converge steadily within  $2\text{--}4$  s of simulation time. The traveling wave of the ship converges slowly compared to the above physical quantities, and the simulation time needed for stabilization of the wave pattern is at least 10 s.

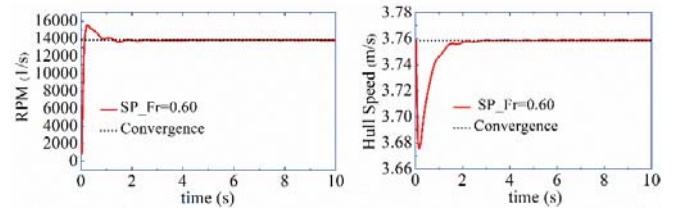
The PID controller technique used in the rapid response of the ship's speed apparently reduces the fluctuations in the physical quantities, which is beneficial for convergence of the simulation. The body-force method used for the propulsion also contributes to the time saving. Although the above techniques are used in the RANS CFD simulations, for the self-propulsion simulation at the specified speed, the time required for a convincing simulation result is still several tens of hours using parallel computing.



a.  $Fr=0.30$



b.  $Fr=0.45$



c.  $Fr=0.60$

Fig. 10. Time history of RPM and hull speed in RANS CFD

## RESULTS AND DISCUSSION

### PHYSICAL QUANTITIES OF THE CAPTURE AREA

Fig. 11 shows the boundary layer velocity distribution for the hull, the capture area, and the control volume streamlines for the three waterjet propulsion ducts in the RANS CFD simulation at  $Fr=0.30$ . The thickness of the boundary layer reaches a maximum in the middle bottom of the hull, while it reaches a minimum in the bilge. The capture area varies with the hull surface curvature, and the shape of the middle duct capture area is a regular semi-ellipse, as it is located at the flat hull bottom, while the shapes of the other two ducts are inclined semi-ellipses as they are located close to the bilge area where the curvature is considerably changed.

In this paper, the results of the capture area calculation obtained from the turbulent boundary layer method are compared with the results from the RANS CFD method, as shown in Table 4. The width used in the present method is fixed at  $W=1.2D$ , where  $D=0.06$  m is the maximum diameter of the intake duct. The RANS CFD results show that the width  $W$  and height  $Y_0$  decrease with an increase in  $Fr$ . The results of the proposed method give a similar trend for the variation in  $Y_0$ , while the value of  $Y_0$  is 29% larger than the viscous results on average, and the maximum difference in the width  $W$  is 8.9%. The velocity distribution of the capture area determines the momentum velocity coefficient  $\hat{a}$ . Different computed values of  $\hat{a}$  are observed at the three capture areas of the left, center, and right intake duct. Since the outer waterjets are affected by the inlet shape of the bilge, the momentum velocity coefficients are both reduced compared with that of the center waterjet, but this difference is reduced with an increase in  $Fr$ . The maximum difference between the present approach and the viscous CFD method is 3.9%. In the range  $Fr=0.30\text{--}0.60$ , the range of  $\hat{a}$  is  $0.782\text{--}0.795$ , and this increases gradually with  $Fr$ .

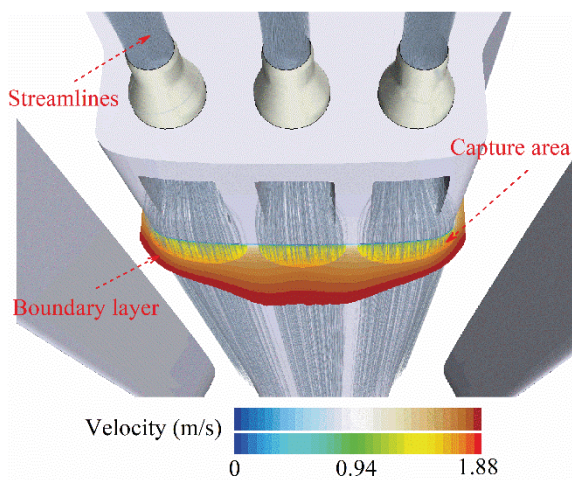


Fig. 11. Capture area, boundary layer, and streamlines in RANS CFD ( $Fr=0.30$ )

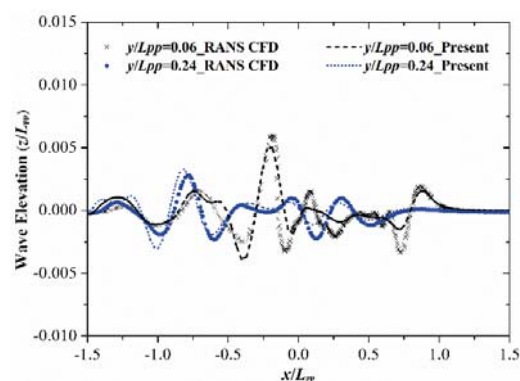
Table 4. Comparison of the parameters of the capture area

$Fr$	RANS CFD method				Present method	Relative error
	$\alpha_L$	$\alpha_C$	$\alpha_R$	$\alpha_{ave}$		
0.30	0.812	0.816	0.812	0.813	0.782	-3.9%
0.45	0.809	0.822	0.807	0.813	0.790	-2.8%
0.60	0.820	0.825	0.822	0.822	0.795	-3.3%
$Fr$	$Y_0$ (m)			$W$ (m)		
	RANS CFD	Present	Relative error	RANS CFD	Present	Relative error
0.30	0.0219	0.0272	24.2%	0.0790	0.072	-8.9%
0.45	0.0214	0.0278	29.9%	0.0788	0.072	-8.6%
0.60	0.0210	0.0280	33.3%	0.0784	0.072	-8.2%

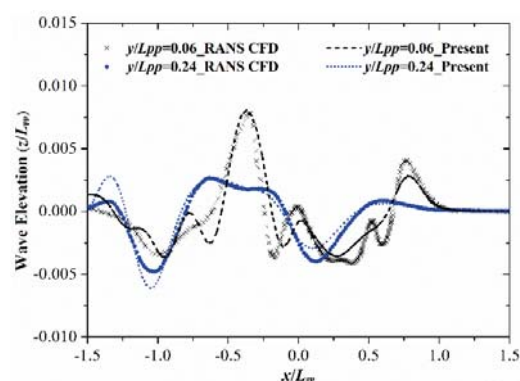
## WAVE PATTERNS

Fig. 12 shows a comparison of the wave patterns in the present approach and the RANS CFD method, where the  $y/L_{pp}=0.06$  wave-cut profile lies between the main body and the side hull of the trimaran, and the  $y/L_{pp}=0.24$  wave-cut profile is located outside of the side hull. In general, the ship traveling wave has an obvious speed effect. The wave peak of the bow increases by nearly a factor of two between  $Fr=0.3$  and  $Fr=0.6$ . The wave crest at the stern increases and moves backwards, and the wave trough formed between the main hull and the side hull also moves backwards and becomes deeper. A comparison of the two methods shows that except for the first wave trough at the rear of the ship with  $Fr=0.6$ , the value calculated using the present method is smaller, and the result for  $y/L_{pp}=0.24$  far from the hull shows good agreement with the RANS CFD method, including the small fluctuations in the wave patterns and the amplitude of the peak and troughs.

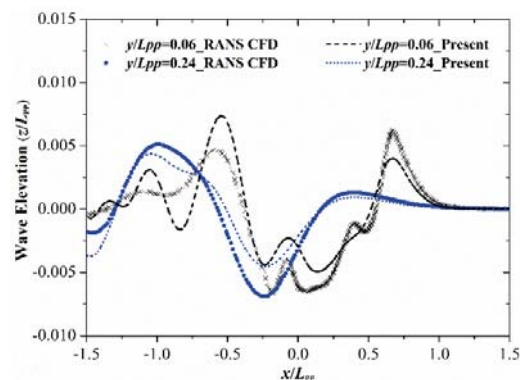
The main reason for the differences in the wave patterns between the two methods is that since the potential flow theory is based on the boundary element method, it cannot simulate the physical phenomenon of the actual water spray from the nozzle discharge at the stern, so the interaction between the flow field and water flow from the waterjets cannot be modeled. This effect is not apparent while the nozzle velocity is small at low speeds ( $Fr=0.30$ ), but when the nozzle velocity is increased sufficiently at high speeds ( $Fr=0.60$ ), a more direct effect occurs, and the flow field around the stern is changed. This is also the reason why the two wave-cut profiles show a relatively large difference at the stern and rear of the ship when  $Fr=0.60$ , which gradually decreases with the spread of the wave patterns (from  $y/L_{pp}=0.06$  to  $y/L_{pp}=0.24$ ).



a.  $Fr=0.30$



b.  $Fr=0.45$



c.  $Fr=0.60$

Fig. 12. Elevation of wave-cut profiles for the present approach and the RANS CFD method

## PRESSURE DISTRIBUTION AT THE INTAKE DUCT

Since a lengthened hull is used in the calculation of wave-making resistance to avoid numerical error, and the viscous CFD contrast model uses the actual model without modification, the pressure distribution on the intake duct surface between the above two methods will show some differences, as illustrated in Fig. 13. The pressure coefficient near the nozzle is negative ( $C_p = -0.5$  to  $-1.0$ ) in the present method, while the pressure coefficient in viscous CFD is close to zero. The above phenomenon is mainly due to the adoption of the velocity exit boundary condition in the calculation of potential flow, which implies a negative pressure distribution at the nozzle and means that the peripheral surface element pressure distribution is also negative.

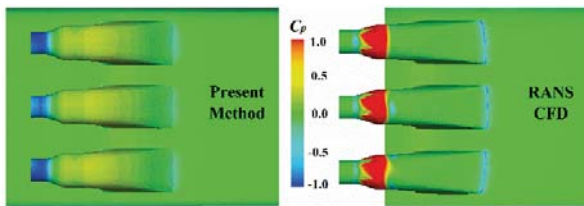


Fig. 13. Pressure distribution around the intake duct ( $Fr=0.60$ )

Another area with an apparent pressure difference is the stator region in viscous CFD, where the stator model is retained due to the need to eliminate the rotational energy of the accelerated fluid in the actual waterjet propulsion system. When the fluid passes through the stator after rotational acceleration, the circumferential rotating energy of the fluid is eliminated by the rectification of the stator, leaving only the axial velocity to eject. Hence, in the stator region, due to the impact of the rotating fluid, a sizeable local pressure coefficient (up to a maximum of 2.5) will occur. At the same time, a simplified body-force method is adopted in the pump area (compared with the body-force method used in RANS CFD, the simplified method neglects the circumferential rotation of the rotor and only considers the axial force). The stator is not set, so the pressure coefficient distribution in the stator area is lower, but the discrepancy between them is relatively small in the pump area.

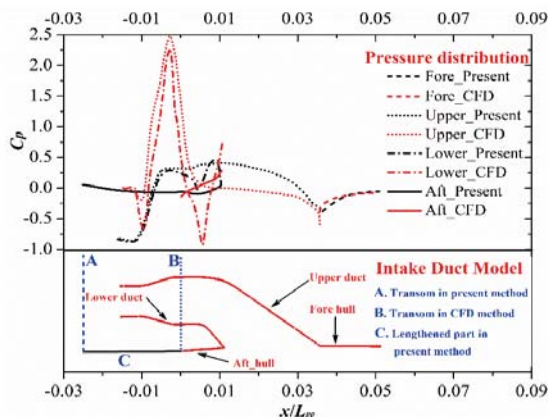


Fig. 14. Pressure coefficient contrast curves ( $Fr=0.60$ )

Fig. 14 shows the pressure coefficient curves on the longitudinal section, in the center plane of the intake duct and the nearby hull. The difference in the pressure distribution between the two methods can be intuitively observed. For the waterjet propulsion system, the value of the pressure coefficient in the viscous CFD method is close to zero, and the value for the present method is near  $-0.9$ , while for the stator region, the value in the present method is between  $-0.9$  and  $0.3$ , and that in the viscous CFD method ranges from  $-0.7$  to  $2.5$ ; for the oblique ascending part of the duct, the values of pressure coefficients in both methods are relatively small, and are between  $-0.3$  and  $0.4$ . For the hull system area, the pressure distribution on the hull surface in front of the intake duct is kept the same (Fore\_hull area). The part of the hull that is below the lower surface of the duct has a longer distribution curve, due to the 2.5% lengthening of the hull in the proposed method, and value from the viscous CFD method is slightly higher in the Aft\_hull region, where the pressure coefficients tend to be close to each other. In general, the pressure distribution on the intake duct of the waterjet propulsion system in the two methods is different due to the different physical models used, while the pressure distribution on the hull surface of the hull system tends to be the same.

## WATERJET THRUST AND THRUST DEDUCTION

The distribution of the gross waterjet thrust and the hull resistance of the trimaran are shown in Fig. 15. The difference between the barehull resistance in the present method and the RANS CFD method is less than 3%, and the difference percentage in the gross thrust is less than 5%. The difference in the maximum hull resistance between the present approach and the viscous CFD method is 4.2% at  $Fr=0.3$  for the waterjet hull. The hull resistance and waterjet thrust obtained via the proposed approach are in good agreement with the RANS CFD results.

The variation curve for the nozzle velocity ratio with  $Fr$ , as calculated by the iterative method, is shown in Fig. 16. For  $Fr=0.30-0.60$ , the trend in  $k$  is downward, while the calculated values are distributed around the value of 1.5. Compared with the results of the RANS CFD method, the difference in  $k$  between the two methods is less than 3%.

The total thrust deduction fraction (shown in Fig. 16) can be calculated using Eq. (4). Both methods show a positive thrust deduction within a range of Froude numbers of  $0.30-0.60$ , and the general trend in  $t$  is downward with an increase in the Froude number, except for the peak value (marked in red in Fig. 16) at  $Fr=0.375$  for the proposed method. We can find the reason for this inflection point in Eq. (4), as the fraction of total thrust deduction is determined by the difference between  $T_g$  and the  $R_{BH}-F_D$  term. If the difference is negative, a negative thrust deduction is obtained, and contrary positive thrust deduction is obtained for a positive difference. For the present calculated positive value of  $t$ , the thrust deduction curve follows the same trend as the difference term variation curve. The difference term reaches a maximum at  $Fr=0.375$ ,

as shown in Fig. 15, and thus the maximum thrust deduction fraction is obtained as shown in Fig. 16.

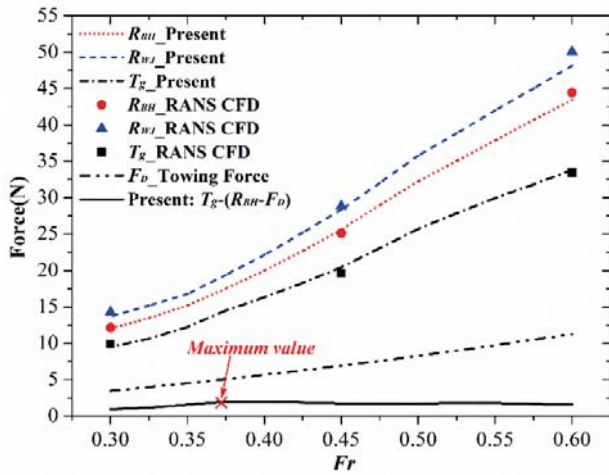


Fig. 15. Hull resistance and waterjet thrust

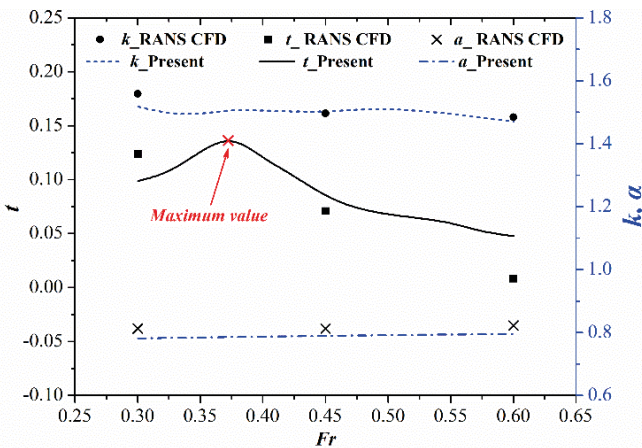


Fig. 16. Comparison of momentum velocity coefficient  $a$ , velocity ratio  $k$  and thrust deduction fraction  $t$

## CONCLUSIONS

The applicability of the present approach to the prediction and evaluation of the performance of waterjet propulsion was confirmed by comparing simulation results with the widely used viscous CFD method. For both of these methods, the mathematical and physical models used, the convergence process, and the results were described and discussed in detail, and the following conclusions can be drawn:

1) Although there were some differences in the local pressure distribution and the results of thrust deduction between the proposed method and the CFD method, based on a comparison between the capture area quantities, wave patterns, hull surface pressure distribution, resistance, thrust and thrust deduction, it can be seen that the calculated results for waterjet propulsion are in good

agreement with the results of the converged RANS CFD method.

- 2) The time-saving advantage of the present approach to the assessment of waterjet propulsion performance compared with the viscous CFD method is very large, and is generally a factor of a few tens in terms of efficiency.
- 3) In the proposed numerical approach, the boundary element method used in the calculation of wave-making resistance can provide more details of the wave patterns and hull pressure distribution, and offers significant time savings. The simplified body-force model is used in the area of the waterjet pump to extend the applicability of the present method, especially in the absence of details about the waterjet pump; an empirical approach is used to calculate the viscous resistance; and the boundary layer theory method is used to calculate the physical quantities of the capture area. This saves on resource costs while giving reasonable accuracy. A comparison indicates that the present research provides a practical approach to the assessment of waterjet propulsion performance.

## ACKNOWLEDGMENTS

We would like to thank Editor-in-Chief Prof. Wieslaw Tarelko and the reviewers for their helpful comments. This work was financially supported the High-Tech Ship Research Project of the Ministry of Industry and Information Technology of China, National and International Scientific and Technological Cooperation Special Projects of China (2013DFA80760) and the Fundamental Research Funds for the Central University of China (3132019320, 3132019001).

## REFERENCES

1. Van T.T. (1991): *The Effect of Waterjet-Hull Interaction on Thrust and Propulsive Efficiency*. Proceedings of 1st International Conference on Fast Sea Transportation Conference, Trondheim, Norway, 1991, 1149-1167.
2. Alexander K., Coop H., Van T.T. (1993): *Waterjet-Hull Interaction: Recent Experimental Results*. SNAME Transactions, Vol. 102, 275-335.
3. ITTC (1996): *The Specialist Committee on Waterjets: Final Report and Recommendations to the 21st ITTC*. Proceedings of the 21st International Towing Tank Conference, Trondheim.
4. Park W.G., Jin H.J., Chun H.H., Kim M.C. (2005): *Numerical Flow and Performance Analysis of Waterjet Propulsion System*. Ocean Engineering, Vol. 32(14-15), 1740-1761.
5. Park W.G., Yun H.S., Chun H.H., Kim M.C. (2005): *Numerical Flow Simulation of Flush Type Intake Duct of Waterjet*. Ocean Engineering, Vol. 32(17), 2107-2120.

6. Takai T. (2010): *Simulation Based Design for High Speed Sea Lift with Waterjets by High Fidelity URANS Approach*. Master's thesis, University of Iowa.
7. Takai T., Kandasamy M., Stern F. (2011): *Verification and Validation Study of URANS Simulations for an Axial Waterjet Propelled Large High-Speed Ship*. Journal of Marine Science and Technology, Vol. 16(4), 434-447.
8. Altosole M., Benvenuto G., Figari M., Campora U. (2012): *Dimensionless Numerical Approaches for the Performance Prediction of Marine Waterjet Propulsion Units*. International Journal of Rotating Machinery, Vol. 2012, 1-12.
9. Eslamdoost A. (2014): *The Hydrodynamics of Waterjet/Hull Interaction*. PhD thesis, Chalmers University of Technology.
10. Eslamdoost A., Larsson L., Bensow R. (2014): *A Pressure Jump Method for Modeling Waterjet/Hull Interaction*. Ocean Engineering, Vol. 88, 120-130.
11. Gong J., Guo C.Y., Wang C., Wu T.C., Song K.W. (2019): *Analysis of Waterjet-Hull Interaction and its Impact on the Propulsion Performance of a Four-Waterjet-Propelled Ship*. Ocean Engineering, Vol. 180, 211-222.
12. Zhang L., Zhang J.N., Shang Y.C. (2019): *A Potential Flow Theory and Boundary Layer Theory Based Hybrid Method for Waterjet Propulsion*. Journal of Marine Science and Engineering, Vol. 7(4), 113.
13. Zhou L.L. (2012): *Numerical Study of High Speed Ship Tail Wave*. PhD thesis, Wuhan University of Technology.
14. Liu Z.L., Yu R.T., Zhu Q.D. (2012): *Study of a Method for Calculation Boundary Layer Influence Coefficients of Ship and Boat Propelled by Water-Jet*. Journal of Ship Mechanics, Vol. 16(10), 1115-1121.
15. Gong J., Guo C.Y., Song K.W. (2016): *Experimental Study of Boundary Effect Coefficients of Waterjet Propelled Ship Model*. 2016 Meeting of the Technical Committee on Ship Mechanics, 313-319.
16. Zhang L., Zhang J.N., Shang Y.C. (2019): *Stern Flap-Waterjet-Hull Interactions and Mechanism: a Case of Waterjet-propelled Trimaran with Stern Flap*. Journal of Offshore Mechanics and Arctic Engineering, DOI: <https://doi.org/10.1115/1.4045498>.
17. Wang J.H., Wan D.C. (2018): *CFD Investigations of Ship Maneuvering in Waves Using naoe-FOAM-SJTU Solver*. Journal of Marine Science and Application, Vol. 17(3), 443-458.
18. Broglia R., Dubbioso G., Durante D., Mascio A.D. (2013): *Simulation of Turning Circle by CFD: Analysis of Different Propeller Models and their Effect on Manoeuvring Prediction*. Applied Ocean Research, Vol. 39, 1-10.
19. Jin Y.T., Duffy J., Chai S.H., Magee A.R. (2019): *DTMB 5415M Dynamic Manoeuvres with URANS Computation Using Body-Force and Discretised Propeller Models*. Ocean Engineering, Vol. 182, 305-317.
20. Baek D.G., Yoon H.S., Jung J.H., Kim K.S., Paik B.G. (2015): *Effects of the Advance Ratio on the Evolution of a Propeller Wake*. Computers and Fluids, Vol. 118, 32-43.

## CONTACT WITH THE AUTHORS

**Lei Zhang**

*e-mail: csylzl@163.com*

Dalian Maritime University,  
1 Linghai Road, 116026 Dalian,

**CHINA**

**Jianing Zhang**

*e-mail: zhangjianing@dlnu.edu.cn*

Dalian Maritime University,  
1 Linghai Road, 116026 Dalian,

**CHINA**

**Yuchen Shang**

*e-mail: 2060293657@qq.com*

Texas A&M University, 400 Bizzell Street,  
77843 College Station,

**USA**

**Guoxiang Dong**

*e-mail: dongguoxiang@sssri.com*

Shanghai Ship and Shipping Research Institute,  
600 Minsheng Road in Pudong New Area, 200135 Shanghai,

**CHINA**

**Weimin Chen**

*e-mail: chenweimin@sssri.com*

Shanghai Ship and Shipping Research Institute,  
600 Minsheng Road in Pudong New Area, 200135 Shanghai,

**CHINA**

# STRUCTURAL ASSESSMENT OF THE HULL RESPONSE OF AN FPSO UNIT TO DROPPED OBJECTS: A CASE STUDY

**Ozgur Ozguc**

Istanbul Technical University, Dept. of Naval Architecture and Ocean Eng., Turkey

## ABSTRACT

*Offshore structures are exposed to the risk of damage caused by various types of extreme and accidental events, such as fire, explosion, collision, and dropped objects. These events cause structural damage in the impact area, including yielding of materials, local buckling, and in some cases local failure and penetration. The structural response of an FPSO hull subjected to events involving dropped objects is investigated in this study, and non-linear finite element analyses are carried out using an explicit dynamic code written LS-DYNA software. The scenarios involving dropped objects are based on the impact from the fall of a container and rigid mechanical equipment. Impact analyses of the dropped objects demonstrated that even though some structural members were permanently deformed by drop loads, no failure took place in accordance with the plastic strain criteria, as per NORSOK standards. The findings and insights derived from the present study may be informative in the safe design of floating offshore structures.*

**Keywords:** Drop object, Hull response, Impact analysis, Offshore structures

## INTRODUCTION

Offshore structures are exposed to the risk of damage caused by vessel impacts or dropped objects. Accidents involving dropped objects often occur during operations on offshore units. Dropped objects generally have relatively high velocities in the most critical cases, and the influence of inertia forces on the response of the impacted structure is large.

The load from a dropped object is described by its kinetic energy, which is governed by the mass of the object, including the hydrodynamic added mass, and the speed of the object at the immediate point of impact [3]. Under most conditions, the major part of the kinetic energy must be dissipated as strain energy within the impacted component, and possibly within the dropped object. The most significant threat to global structural integrity is likely to be damage to the tanks, which could impair the intactness and stability of the floating offshore facilities [4].

The structural members of the deck need to be designed so that the load bearing capacity of the whole ship is intact after an accidental load occurs. The impact resistance of a deck

depends on the plate thickness and the size and spacing of the supporting stringers. The structural integrity of the whole ship is normally not compromised due to dropped loads, but local damage and the consequences of this damage may lead to catastrophic results [5].

Jung et al. [11] focused on grated-steel deck structures subjected to dropped objects. An experimental study was undertaken in a dropped object test facility, and nonlinear finite element computations using LS-DYNA were also performed for the corresponding test models.

Sun et al. [14] studied items dropped on offshore units in order to investigate the overall falling process using nonlinear FEM software. The geometry of the dropped items, the horizontal speed of the dropped items, whether they were dropped into water, and various boundary conditions were accounted for.

Ingve [10] performed impact analyses for dropped objects in accordance with the typical NOKSOK N-004 standards for accidental actions. Different shapes, sizes and weights and various impact positions were used to simulate the dropped object, and analyses were carried out using the nonlinear finite element program USFOS.

Ahn et al. [1] investigated the effect of the conditions under which an object is dropped, using a parametric study. This study examined the methodology, conditions, and design aspects of dropped object calculations using a non-linear dynamics FEM analysis. Based on a comparison of the findings from direct FEM analyses with those from a simplified energy method using the Offshore Code DNVGL-RP-C204 [4], the findings were affected by the application of failure criteria in accordance with the requirements of the Code, the application of material properties, the location of the dropped object, and the condition of the object.

Moan [12] described the lessons learnt from accidents on offshore structures, and then gave a brief outline of general principles for safety management based on these experiences. Emphasis was placed on the Accidental Limit State (ALS) criteria.

Bergstad [3] evaluated the resistance of the deck structures in ship hulls to impacts from objects, with particular application to falling containers, and found that the energy absorption and the deformation of the deck structure needed to be analyzed. In general, nonlinear finite element methods were required in addition to procedures for the estimation of absorbed energy.

The present paper aims to investigate the structural response of an FPSO hull exposed to dropped object events. This is achieved using the critical energy absorption and localized deformation to penetration of the deck structure exposed to impacts from falling containers and rigid equipment. The scope of this work includes all possible FPSO locations affected by dropped accidental loads. The effects of different types of material are also accounted for. Critical areas for dropped object events are determined based on a minimum drop direction of within 10° to the vertical direction, as per DNVGL-OS-C102 [7] requirements.

In order to assess the strength versus dropped objects, nonlinear finite element analyses are performed using an explicit nonlinear software code in LS-DYNA. With respect to the hull structure of the FPSO, areas such as the main lay-down located on the poop deck, the galley and infill deck and cargo deck are included in the strength assessments.

## FPSO DESIGN

A double-sided, single-bottom hull is designed. Three thrusters are provided for heading control, although not for propulsion, and these thrusters are not used to assist the natural weathervaning of the vessel, as shown in Fig. 1. Topside modules are installed onto module support stools that are fabricated and erected on the cargo deck. A moon pool is located between the cargo area and the fore part of the vessel for integration of the turret.

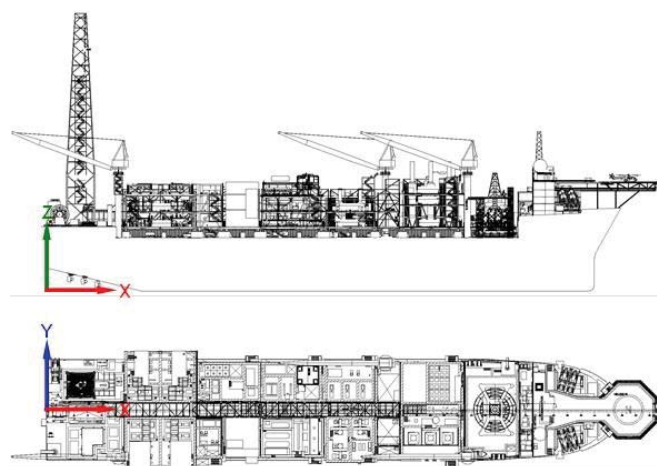


Fig. 1. General arrangement of the FPSO vessel

The principal dimensions of the FPSO are as follows:

- Length O.A.                    335.6 m
- Length B.P.                    320.0 m
- Breadth                            58.8 m
- Depth                             31.0 m
- Design Draft                    21.5 m
- Scantling Draft                22.5 m
- Frame Spacing                 0.8 m
- Web Frame Spacing         4.0 m

## DROPPED OBJECT SCENARIOS

The dropping of objects during crane operations can cause damage to equipment and structural members such as the deck plating and walls. It is therefore necessary to check and validate the strength of structures for vulnerable areas against impact from dropping objects when the probability level is greater than  $10^{-4}$  per year.

When modeling the worst case scenario of a dropped object load, the impact angle is essential. Zhang [16] performed extensive analyses to study the effect of impact angle in cases of ship collisions and dropped objects (the latter are of course more relevant in the present study). An object was dropped onto a plate at different impact angles, and the critical impact energy was found. As expected, a perpendicular impact was the most critical, as shown below in Fig. 2.

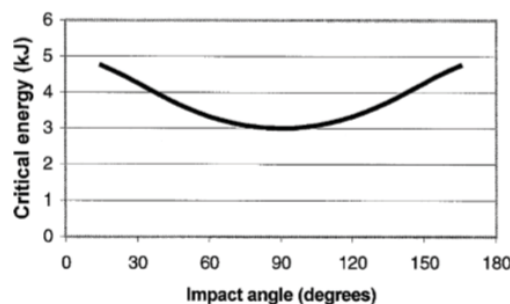


Fig. 2. Critical energy vs. impact angle of dropped object [16]

The rules applicable to the structural design of an impact load were reviewed, and specifically those rules relevant to dropped objects. DNV GL Offshore Standards and Recommended Practices are relevant and contain rules for the structural design of offshore ships and ALS design. According to these standards, all accidental loads that are relevant and have an annual frequency of occurrence greater than  $10^{-4}$  need to be taken into account in the safety design [6]. The specific requirements concerning accidental loads are given in DNV GL-OS-A101 [6].

In this study, the design of the FPSO contains three main pedestal cranes and one knuckle boom crane. Pedestal crane 1 is the forward crane on the starboard side, while pedestal crane 2 is the forward crane on the port side and pedestal crane 3 is the aft crane on the starboard side. A knuckle boom crane is located on the infill deck, on the starboard side. Based on the design loads, drop height and swinging radii (defined by the characteristics and capacities of the cranes), the present study will assess the impact loads from dropped objects acting on the main lay-down area located on the poop deck. The crane layout, including the maximum and minimum reach of each crane, is shown in Fig. 3.

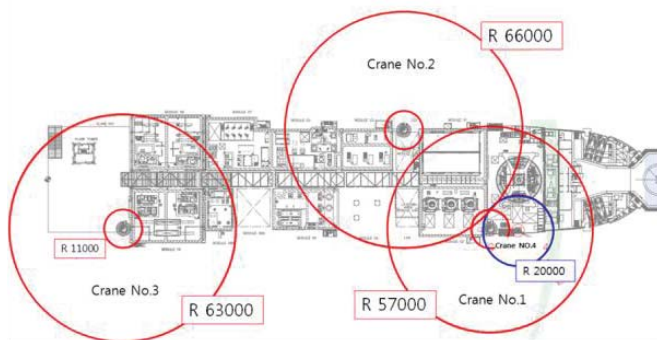


Fig. 3. General arrangement of the FPSO with crane layout

The acceptance criteria are that the structural areas around the impact locations of the dropped object may suffer plastic deformation, but no penetration is allowed. In other words, the critical failure strain should not be exceeded. For the other neighboring structures, the residual stress should be less than the allowable stress as per the DNV GL Class Rules [8], and deformation of the structure should not cause global collapse. In addition, the pillars must not be collapsed by buckling. In all cases, no collapse is allowed and the integrity of structures should be preserved.

To model the worst-case impact scenario, the container was dropped edge-first onto the deck at an impact angle of  $90^\circ$ . In the main analyses, the container was defined as an infinitely rigid shell, meaning that the impact energy was absorbed exclusively by the deck.

Dropping scenarios with regard to the impact of the container edge, such as large and small contact areas and one-corner contact are also examined. Information about the dropped objects and dropping heights considered here is summarized in Table 1. These impact locations are illustrated

in Figs. 4 to 7. In all cases, a weak structure is assumed and a drop analysis is carried out.

Tab. 1. Design impact loads

Target area	Dropped object & condition	Impact area			Impact energy (KJ)	Height	Weight
Main lay-down area Poop deck	20 foot ISO container (rigid)	D1	6.1 × 0.6 m	Small	518	2 m	26 ton
		D2	6.1 × 2.4 m	Large	765	3 m	26 ton
		D3	1.1 × 0.9 m	One corner	264	2 m	26 ton

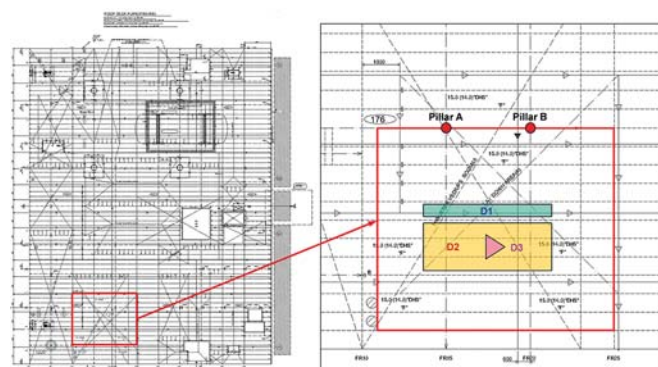


Fig. 4. Contact locations of the poop deck area - D1, D2 and D3 zones

Information on the structural scantling, such as the thicknesses and material grades of the plate, girder and stiffener, is given in detail in Tables 2 to 5.

Tab. 3. Poop deck area - D1, D2 and D3 zones

Gross plate thickness	15 mm
Longitudinal girder	800 × 12 + 200x20 (T-bar)
Longitudinal stiffener	250 × 90x10/15 (angle bar)
Material grade for plate	HT36
Material grade for longitudinal girder	HT36
Material grade for longitudinal stiffener	HT36

## DESIGN CRITERIA

DNV GL and NORSOK give several recommendations concerning loads and the consequences of dropped objects. NORSOK N-004 [13] presents formulae for the determination of the impact velocity (in air and in water), as well as formulae for strain energy dissipation, associated damage (indentation or failure) and critical plastic strain with respect to typical steel material grades. The critical plastic strain adopted in the NORSOK Standards [13] will be used in the design acceptance check from the point of view of plastic strain. The value of the critical plastic strain for each steel grade is shown in Table 6. However, in this study, puncture of the deck plate is not

acceptable over the full extent of the hull deck in the cargo area and above any hydrocarbon tank which may be outside of the cargo area, and the poop deck should not undergo more than 5% strain. Higher deformations can be specified for the lay-down areas or similar working decks, up to the following limits;

- Primary structures should not undergo more than 5% plastic strain; and
- The plastic deformation of secondary stiffeners should be limited to 10% strain.

For hull areas such as the hull deck, local details at the areas of interest can be modeled with an element mesh size of  $100 \times 100$  mm in the analysis model. For a fine mesh FE model, the requirements given in DNV GL-OS-C102 [7] may be applicable. Usage factors are defined according to the mesh size, and the calculated usage factor based on the von Mises equivalent membrane stress at the centre of a shell element should not exceed the permissible peak usage factor, as shown in Table 6. Permissible peak usage factors ( $\eta_{peak}$ ) given in DNV GL-OS-C102 [7] are defined based on the structural components, design method, load combination and applied mesh size.

The calculated usage factor based on the von Mises equivalent membrane stress at the centre of a plane element (shell or membrane) shall not exceed the permissible peak usage factor given in DNV GL-OS-C102 [7].

Tab. 6. Permissible peak usage factor for fine mesh FE analysis:

$$\sigma_{peak} = \eta_{peak} \cdot \sigma_{material\_yield\_stress} [7]$$

Permissible peak usage factors ( $\eta_{peak}$ ) for fine mesh FE analysis	Mesh size		
	50 × 50 mm	100 × 100 mm	200 × 200 m
	1.7	1.48	1.25

A buckling capacity check is performed in accordance with the requirements given in the DNV GL Rules for Classification of Ships (Pt. 3, Ch. 1, Sec.13) [8]. The ideal elastic buckling strength without accepting any local distribution of the loads is used as a basis, together with the acceptance criteria given in the DNV GL Rules for Classification of Ships [8].

A buckling strength check is implemented to confirm the stability of the columns underneath the lay-down area with regard to catastrophic collapse under the impact load. Pillars under an impact load are subjected to two kinds of failure modes: buckling and yielding. Yielding does not lead to a catastrophic collapse of the pillars, since structural integrity will remain until rupture occurs. Thus, in order to avoid catastrophic pillar collapse from the impact load, buckling is checked using the Euler formula [8].

## ASSESSMENT METHOD

In this study, we use FE analyses to assess the multitude of possible scenarios involving dropped objects and the structural configurations to be analyzed. An FE analysis is the most flexible method for this problem, as it can account for the possible effects that occur and assess the relevant factors

such as impact energy, boundary conditions, material, and the different shapes and stiffnesses of indenters and the location of the indentation. An assessment of nonlinear material behavior is essential when determining the response of a structure.

To check whether the hull structures of an FPSO have sufficient strength to withstand dropped object events, nonlinear FE analyses are performed, including events involving large deformations of structures and elasto-plastic material properties. The strain hardening effect and the ultimate stress are considered in these analyses as a bi-linear strain-stress curve according to material grades, as shown in Fig. 5. Fracturing is determined on the basis of the critical plastic strain of the material used, as per the NORSOK Standard [13]. Fig. 6 shows the material properties used in the nonlinear simulations. The ultimate stress data are average values taken from online material information resources [6], and the critical strain data are taken from the NORSOK Standards [13].

For mild steel, these coefficients were originally determined experimentally by Paik [15] as  $C = 40.4 \text{ s}^{-1}$  and  $q = 5$ . Alsos and Amdahl [2] suggested that the values of  $C$  would be greater for cases with large plastic deformations and high strain rates, and obtained better results when the coefficients had values of  $C = 4000 \text{ s}^{-1}$  and  $q = 5$ .

DNV GL [4] recommends the same values ( $C = 4000 \text{ s}^{-1}$  and  $q = 5$ ) for typical offshore steels, if no other values are specified. Paik [17] also reports the coefficients for high tensile steel as  $C = 3200 \text{ s}^{-1}$  and  $q = 5$ . As an initial configuration, the coefficients used in the ABAQUS model for mild and HT-36 steel were defined as  $C = 40.4 \text{ s}^{-1}$  and  $q = 5$ . The Cowper-Symonds rate enhancement formula was used to model the effect of strain rate on the material properties, as shown in Fig. 6.

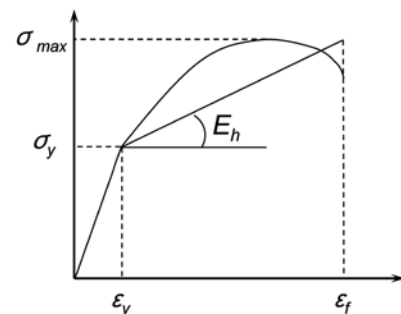


Fig. 5. Stress-strain curve for a bi-linear material

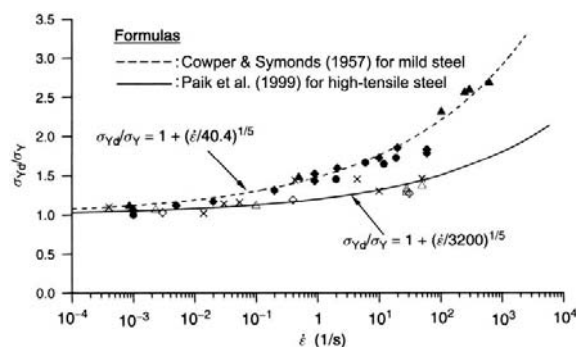


Fig. 6. Strain rate effect

$$\sigma_p = \sigma_y + \frac{EE_h}{E - E_h} \varepsilon_p \quad (1)$$

$$E_h = \frac{\sigma_{\max} - \sigma_y}{\varepsilon_f - \varepsilon_y} \quad (2)$$

where

$\sigma_y$  = yield stress

$E_h$  = Young's modulus

$E_h$  = hardening modulus

$\sigma_p, \varepsilon_p$  = plastic stress and plastic strain

$$\frac{\sigma_{yd}}{\sigma_y} = 1 + \left\{ \frac{\varepsilon}{D} \right\}^{1/q} \quad (3)$$

Mild steel:  $D = 40.4, \quad q = 5$

HT steel:  $D = 3200, \quad q = 5$

Here,  $\sigma_{yd}$  is the dynamic yield stress, and  $\sigma_y$  is the static yield stress.

The material properties used in the initial configuration are based on the quality of the steel used for the decks of the FPSO. This includes mild, HT32 and HT36 grades of steel, as per the DNV GL code [5], which proposes engineering and true stress-strain parameters for these steel grades based on tests of different plate thicknesses. They recommend using the true stress-strain properties as input for FE analysis. Values for the plate thickness of  $t < 16$  mm are applied in the material definition, as listed in Table 7.

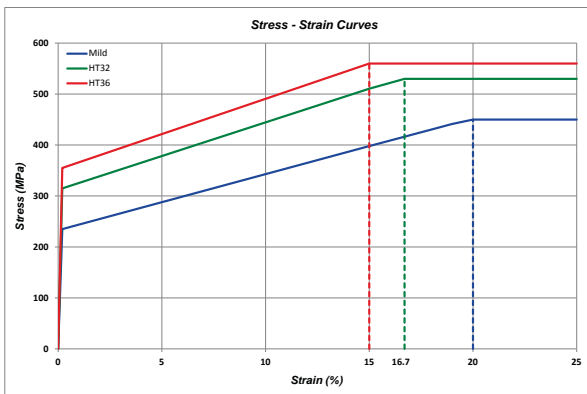


Fig. 7. Stress-strain curves for different steel grades

Tab. 7. Material properties used in the non-linear FE analyses [5]

Steel grade	Mild	HT 32	HT 36
Yield stress	235 MPa	315 MPa	355 MPa
Elastic strain	0.20%	0.20%	0.20%
Ultimate stress	450 MPa	530 MPa	560 MPa
Critical strain	20.0%	16.7%	15.0%
Density	7850 kg/m <sup>3</sup>	7850 kg/m <sup>3</sup>	7850 kg/m <sup>3</sup>

Steel grade	Mild	HT 32	HT 36
Young's modulus	$2.06 \times 10^{11}$ N/m <sup>2</sup>	$2.06 \times 10^{11}$ N/m <sup>2</sup>	$2.06 \times 10^{11}$ N/m <sup>2</sup>
Poisson's ratio	0.3	0.3	0.3
Tangent modulus	1085 MPa	1303 MPa	1385 MPa
Hardening parameter	1.0	1.0	1.0
Strain rate (C)	$40.4 \text{ s}^{-1}$	$3200 \text{ s}^{-1}$	$3200 \text{ s}^{-1}$
Strain rate (P)	$5.0 \text{ s}^{-1}$	$5.0 \text{ s}^{-1}$	$5.0 \text{ s}^{-1}$

## FINITE ELEMENT MODELS

The mesh size of the FE model should fit with nonlinear FE analysis according to engineering judgment and nonlinear FE assumptions. For example, the areas of interest are modeled using very fine mesh size of around  $100 \times 100$  mm, while the other areas have meshes of longitudinal stiffener spaced size. The dropped objects in all scenarios are assumed to be infinitely rigid, and all energies are therefore absorbed by the FPSO hull structure. FE models for each target area with rigid dropped objects are shown in Fig. 8.

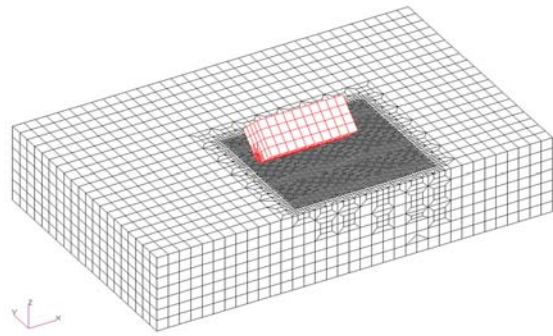


Fig. 8. FE model for drop impact analysis of the poop deck area

It is assumed that the FPSO vessel does not move during the drop events, which gives conservative results in terms of safety. The boundary conditions of the FPSO hull structure are therefore fixed. The boundary conditions applied to each area in the FE models are shown in Fig. 9.

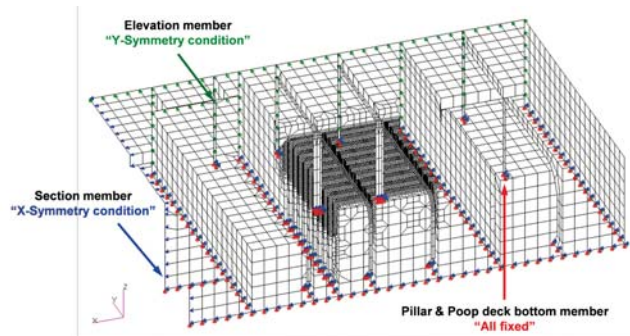


Fig. 9. Boundary conditions for the poop deck area

## FINITE ELEMENT SIMULATIONS

Drop events are simulated by assigning various energy levels to the rigid body representing the dropped object, such as a container, and the equipment. During these drop events, the surface contact between the dropped objects and FPSO hull structure is taken into consideration. The contact is defined using an automatic single surface contact in LS-DYNA. Automatic contact, which may occur due to a large deformation of the FPSO structure, is also considered, and the initial shell thickness offset is always included. Impact energy is defined as the energy that a dropped object possesses just prior to impact. This is determined by conservation of energy, where it is assumed that all of the potential energy of the dropped object is converted to kinetic energy on impact, i.e. impact energy (J) = mass (kg) x acceleration due to gravity (m/s<sup>2</sup>) x height (m). This analysis considers the heavier lifts and compares these against the impact resistance strength of the target zone (TZ) decking. The decks in the identified TZs should be able to resist the impact energies associated with a dropped ISO container (with assumed mass 15 tons) from 3 m (442 kJ). This will significantly reduce the predicted frequency of deck failure, bringing it to below 10<sup>-4</sup> per year. Contact areas are divided into three types: small, large and one-corner contact). A small contact area means that an inclined container is dropped, while a large contact area means the flat bottom of container. A small contact area can occur when the wires of the two cranes are disconnected and the drop height is changed, as shown in

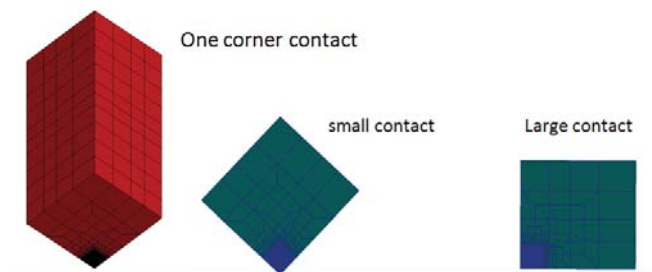


Fig. 10. Small, large and one-corner contact areas of the drop object

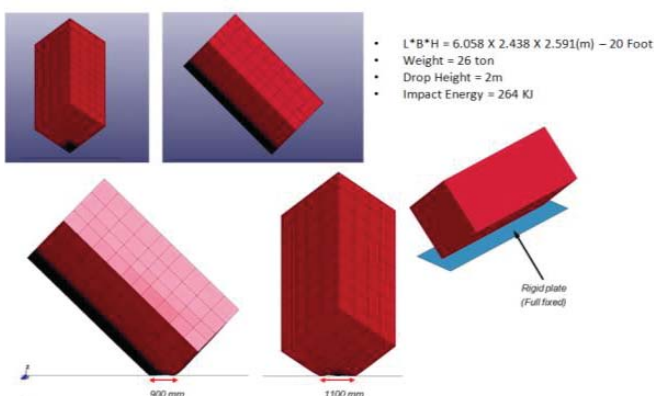


Fig. 12. Calculation of the contact area for one-corner contact

Fig. 10. In a small contact area scenario, the sharp corner of the container will cause more conservative deformation and stress. The container also has a larger relative deformation energy, because it is less weak than the structural members. It is therefore important to calculate an appropriately small contact area. A one-corner contact means that one wire is disconnected in the small contact scenario. The one-corner and small contact areas can be calculated from the container deformation of dry drop simulation using the commercial analysis tool LS-DYNA.

Tab. 9. FE analysis results for drop impact events

	Target area		Dropped object	Load Case	Maximum plastic strain (%)			Max. reaction force			
					Primary member	Criterion	Second member	Criterion	Result	Location	Tons
Dropped object	Main lay-down area	Poop deck	Container	D1	3.1	5%	1.68	10%	Satisfied	Pillar B	405.4
				D2	2.91	5%	2.78	10%	Satisfied	Pillar B	391.1
				D3	2.41	5%	5.55	10%	Satisfied	Pillar A	151.7

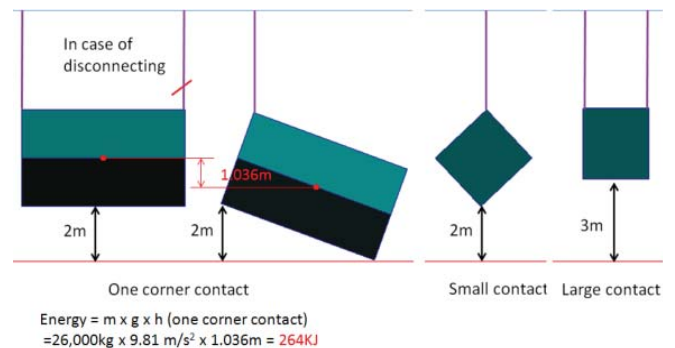


Fig. 11. Drop heights for small, large and one-corner contact scenarios

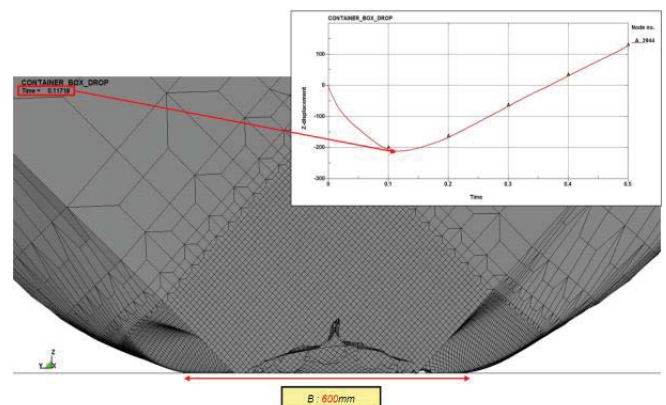


Fig. 13. Results of drop test for small contact area (deformation)

The findings of our calculations are shown in Figs. 14–19 for all cases studied, including plots of the deformed shape

and plastic strain contours, and graphs of the penetration depth of the dropped object.

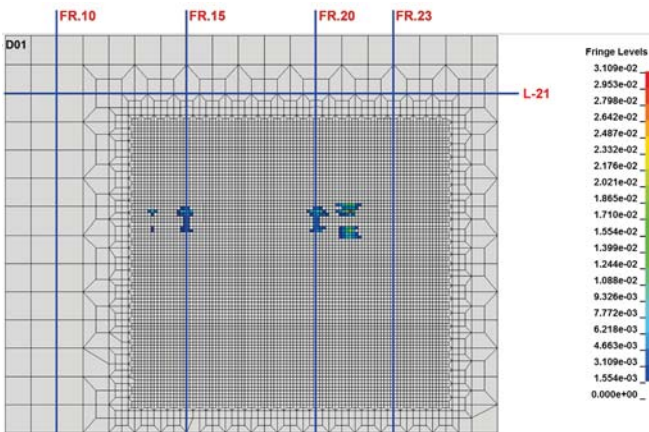


Fig. 14. Deformed shape and plastic strain contour – D1

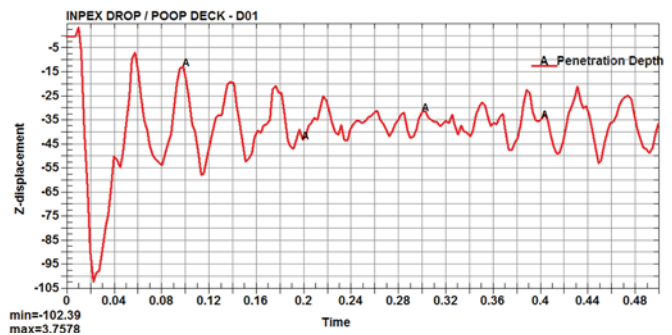


Fig. 15. Graph of penetration depth – D1

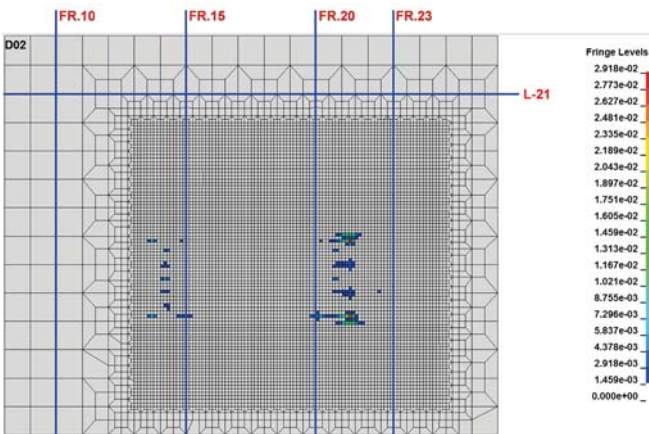


Fig. 16. Deformed shape and plastic strain contour – D2

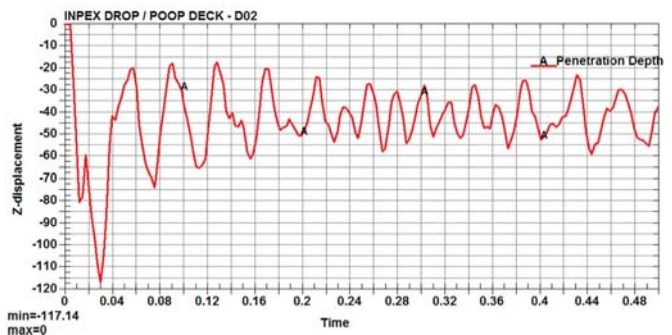


Fig. 17. Graph of penetration depth – D2

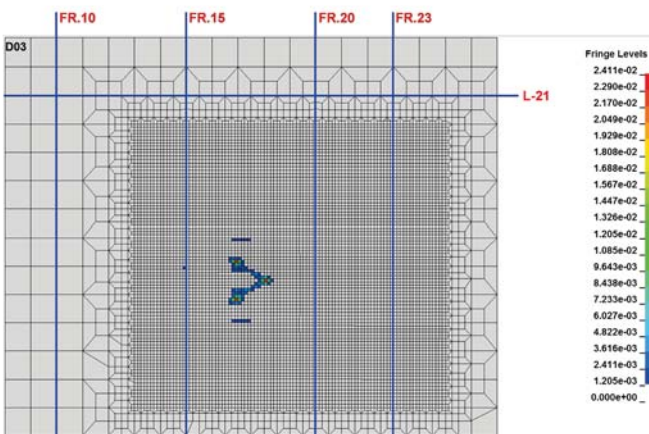


Fig. 18. Deformed shape and plastic strain contour – D3

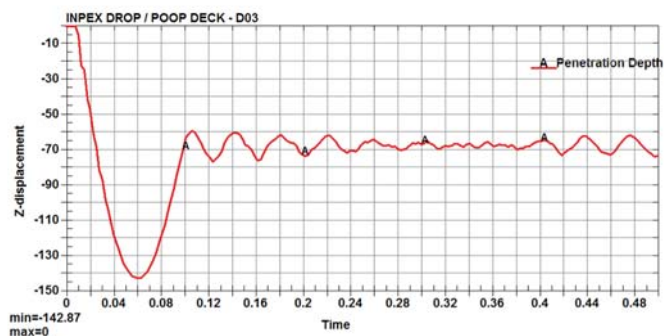


Fig. 19. Graph of penetration depth – D3

## CONCLUSIONS

Drop impact analyses based on numerical impact simulations were carried out to investigate the safety of a FPSO hull structure during dropped object events. In all cases, the impacted structures suffered significant plastic deformation, but no failure occurred using the plastic strain criteria of the NORSOK Standards and the DNV GL Class Rule. Some structures were permanently deformed at the location of the drop event. However, the dropped objects did not breach the primary member. The maximum plastic strain of the cargo hull deck occurred at D11 and was 4.98%, i.e. within the allowable criteria of 5.0%. For the other neighboring structures, the equivalent stresses were less than the allowable stress set out in the DNV GL Class Rules, and structural deformation did not cause global collapse. Furthermore, the pillars supporting the main lay-down area did not suffer from buckling under the reaction forces. Finally, the findings and insights of the present study can be informative in the safety design of floating offshore structures. This article is useful from a practical engineering viewpoint, as containers are handled above FPSO units and an understanding of the effects of dropping one onto different types of deck is important from the point of view of safety assessment. The undertaken scope proves to be larger with all possible FPSO locations affected by dropped accidental loads. The effects of different material types are also accounted for. This study provides a technical basis for reducing the damage to FPSO deck structures and for taking reasonable protective actions based on the FE analyses carried out here.

## REFERENCES

1. Ahn K., Chun M., Han S., Jang K., Suh Y. (2014): Dropped Object Analysis Using Non-linear Dynamic FE Analysis. 33rd International Conference on Ocean, Offshore and Arctic Engineering, Volume 4A, Structures, Safety and Reliability, San Francisco, California, USA.
2. Alsos H.S., Amdahl J. (2009): On the Resistance to Penetration of Stiffened Plates, Part I - Experiments. International Journal of Impact Engineering, Vol. 36, No. 6, 799-807.
3. Bergstad A. (2014): Assessment of Hull Response Due to Impact from Falling Object, MSc thesis, Department of Marine Technology, Norwegian University of Science and Technology, Norway.
4. DNV GL-RP-C204 (2018): Design Against Accidental Loads. Recommended Practice, Høvik, Det Norske Veritas, Norway.
5. DNV GL-RP-C208 (2018): Determination of Structural Capacity by Non-linear FE Analysis Methods. Recommended Practice, Høvik, Det Norske Veritas, Norway.
6. DNV GL-OS-A101 (2019): Safety Principles and Arrangements. Høvik, Det Norske Veritas, Norway.
7. DNV GL-OS-C102 (2019): Structural Design of Offshore Ship-Shaped Units. Høvik, Det Norske Veritas, Norway.
8. DNV GL Rules for Classification. (2019): Hull Structural Design Ships with Length 100 Meters and Above. Part 3, Chapter 1.
9. Ehlers S. (2010): Strain and Stress Relation until Fracture for Finite Element Simulations of a Thin Circular Plate. Thin-Walled Structures, Vol. 48, No. 1, 1-8.
10. Ingve N. (2014): Dropped Object Protection Analyses, Master's thesis, University of Stavanger, Norway.
11. Jung B.G., Jo S.W., Paik J.K., Seo J.K., Kim Y.H. (2016): Experimental and Numerical Studies on Non-linear Impact Response of Deck Structures Subjected to Dropped Objects. 35th International Conference on Ocean, Offshore and Arctic Engineering, Vol. 3, Structures, Safety and Reliability, Busan, South Korea.
12. Moan T. (2009): Development of Accidental Collapse Limit State Criteria for Offshore Structures. Structural Safety, Vol. 31, 124-135.
13. NORSOK Standard (2004): Design of Steel Structures, N-004, Rev. 2.
14. Sun L.P., Ma G, Nie C.Y., Wang Z.H. (2011): The Simulation of Dropped Objects on the Offshore Structure. Advanced Materials Research, Vol. 339, 553-556.
15. Paik J.K. (2007): Practical Techniques for Finite Element Modeling to Simulate Structural Crashworthiness in Ship Collisions and Grounding (Part I: Theory). Ships and Offshore Structures, Vol. 2, No. 1, pp. 69-80.
16. Zhang S. (1999): The Mechanics of Ship Collision, PhD Thesis, Lyngby, Technical University of Denmark.

## CONTACT WITH THE AUTHOR

**Ozgur Ozguc**

*e-mail: ozguco@yahoo.com.sg*

Istanbul Technical University,

Dept. of Naval Architecture and Ocean Eng.,

Maslak, 34469 Istanbul,

**TURKEY**

## A METHOD TO DETERMINE THE TIGHTENING SEQUENCE FOR STANDING RIGGING OF A MAST

**Leszek Samson**

Gdańsk University of Technology, Poland

**Maciej Kahsin**

Gdańsk University of Technology, Poland

### ABSTRACT

*The article proposes an alternative method to determine the sequence of generation of pre-tension forces in standing rigging of a mast. The proposed approach has been verified on both a virtual simulation experiment and laboratory tests. In this method, the desired tension values are obtained using the influence matrix which allows to calculate the effect of tension change in an individual rope on the tension distribution in the remaining ropes in the system. Unlike the presently used method, in which the desired tension distribution is obtained in a long-lasting iterative process burdened with relatively large errors of final values, the proposed method makes it possible to achieve the final tension distribution in a finite number of steps. In the case of FEM analyses, the new method can be a useful tool for determining an arbitrary distribution of tension forces in ropes via solving a system of linear equations.*

**Keywords:** pre-tension, standing rigging, rig, tightening sequence, initial tension

### INTRODUCTION

Guy rope systems are used in numerous technical objects in which achieving an appropriate force distribution is of high importance. A sample list of such objects may include: suspension bridges, drawbridges, and guyed masts and chimneys. This paper analyses the tension distribution issue for a guyed mast.

Classification societies require that the pre-tension in standing rigging is periodically controlled and that the tension forces in ropes are equal to those predicted by the designer [1, 2, 14].

The tightening sequence for a standing rigging should be properly planned, as an incorrect sequence of tightening may lead to damage, or even total deterioration of the object [3, 10, 19].

The requirements of classification societies do not provide recommendations concerning proper selection of tension force generation sequence. Also, there are no literature publications which would study and attempt to optimise the above task in maritime applications.

The presently used method consists in achieving the desired tension in a rope via tightening individually each element of the rigging, each time adapting the tension force

to the desired value, until the satisfactory force distribution is obtained [7, 9]. In this article, the above approach is referred to as the standard method.

Due to mutual interaction between the ropes and with the remaining elements of the structure, the above method takes, as a rule, an iterative course, which makes achieving the predicted tension distribution practically impossible [4, 5, 6, 8, 11, 15, 18].

The new method proposed in the article makes use of the influence matrix [16, 17] and the initial tension distribution in the ropes. This approach makes it possible to achieve the desired force distribution in a limited number of steps.

The above two methods are compared in the article based on the results of simulation studies and experimental tests.

The new method is based on a system of linear equations, the coefficients of which are the elements of the influence matrix. It is assumed that the ropes are rectilinear before and during the tightening process and, consequently, the matrix elements do not change their values.

## TESTED OBJECT

The object used for comparing the standard method and the new method is a mast with three guy ropes. Fig. 1 shows a sketch of the structure, where elements 1 through 3 represent the ropes and element 4 is the mast.

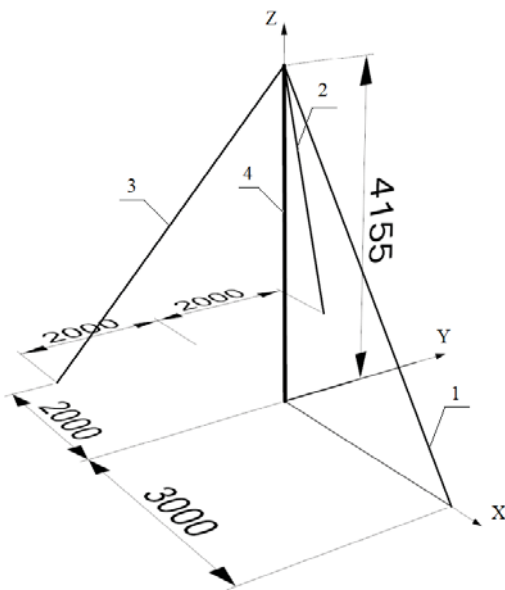


Fig. 1. Sketch of mast with three guy ropes, dimensions in [mm]

## TEST RIG

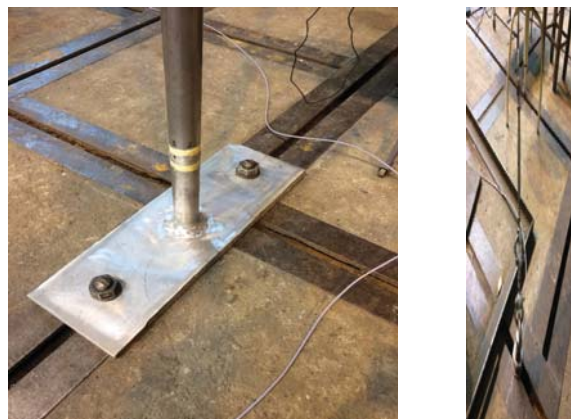
The mast is made of aluminium alloy. Its cross-section has the shape of circular ring with outer diameter of 60 mm and wall thickness of 2.5 mm. The mast was welded to a plate of

25 mm in thickness, made of aluminium alloy, and then the entire structure was screwed to the base.



Fig. 2. Test rig: 1,2,3 – guy ropes, 4 – mast

Galvanised steel ropes 6x19+FC with diameter of 5 mm were fastened with hooks to the masthead and with anchor bolts to the floor. Between each hook and anchor bolt there were: the rope, a tightener, a dynamometer, and shackles. Details of the test rig are shown in Fig. 3 and Fig. 5. The prepared test rig made it possible to measure the tension force in a rope with the accuracy of up to 4 N.



a) mast base

b) anchor bolt

Fig. 3. Details of mast attachment

## FEM MODEL

To verify qualitative advantages of the new method over the standard method, a numerical simulation study was performed. The model of the real mast structure was discretised using the Final Element Method (FEM). In the further step of the study, the results of the simulation were compared with those measured on the real test rig.

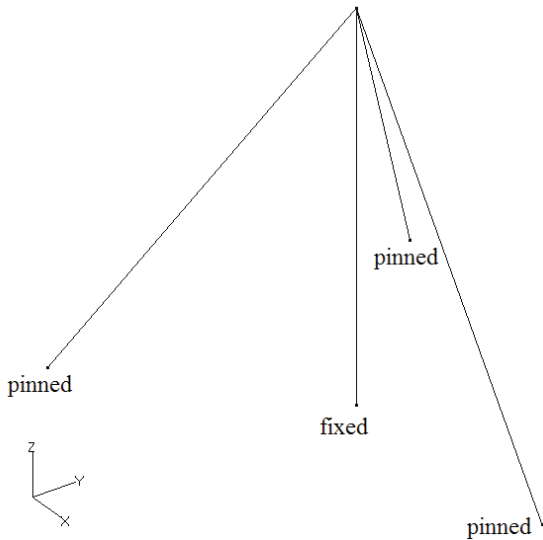


Fig. 4. The applied discrete model and boundary conditions

In the numerical model, the ropes and the mast were modelled as one-dimensional elements: rods and beam, respectively. The parameters of the discrete elements reflected the characteristics of the real object.

The material characteristics were determined experimentally using a testing machine. For aluminium alloy, the obtained longitudinal modulus of elasticity was equal to 67 GPa. The equivalent stiffness assumed for the rope-tightener-dynamometer-shackle unit corresponded to the circular cross-section of 5 mm in diameter and the longitudinal modulus of elasticity equal to 50 GPa. This representation of stiffnesses made it possible to model the entire guy rope unit as one finite element.

The numerical model consists of four finite elements. As the boundary conditions, all degrees of freedom were removed at the mast base, along with all linear displacements of the ropes fastened to the floor. The numerical model is shown in Fig. 4.

The masthead model was simplified: the node was situated at the intersection of straight lines between the rope attachment points and the mast axis.

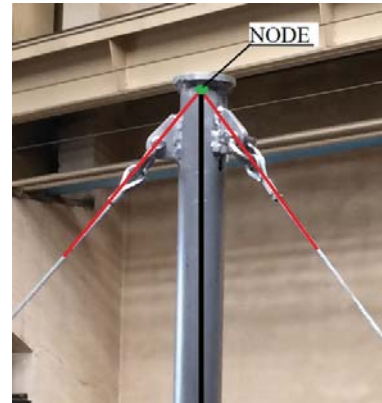


Fig. 5. Fastening of guy ropes to the masthead

The tension forces in the ropes were generated by shortening of the rod element modelling the real rope [12, 13]. Equivalent rope shortening and force generation was achieved via a temperature change and the resulting response of the structure. The desired force value in the element was achieved in two steps. In the first step, the force change in the element which resulted from the temperature change by 1 degree was generated and recorded. Then, in the second step, assuming structural linearity, the temperature increase was calculated which was necessary to achieve the desired total force change in the element.

## STANDARD METHOD

In the standard method, the process starts from an arbitrary rope in which the tension force is tuned to the desired value via shortening, or lengthening, of the rope with the tightener. In the next step, the tension force in the next rope is tuned, and so on, until the desired tension distribution is achieved in the entire rigging.

The set of the desired tension forces can have the following vector form:

$$\mathbf{S}_{\text{des}} = \begin{Bmatrix} 700 \\ 514 \\ 514 \end{Bmatrix} N \quad (1)$$

This vector, the same for all cases, was assumed in the analysis presented in the article.

To illustrate the method, the rope tightening process was simulated numerically and studied experimentally in the test rig. The process started from rope 1 (acc. to Fig.1), in which the tension force was tuned to 700N, then the force of 514N was generated in rope 2, and finally, the force in rope 3 was corrected to 514N. In the next iterations, these actions were repeated.

The initial distribution of tension forces in the ropes can be given as the following vector (with the row number corresponding to the rope number):

$$S_{init} = \begin{Bmatrix} 208 \\ 142 \\ 125 \end{Bmatrix} N \quad (2)$$

In the standard method, the information on the initial force distribution in the ropes is not necessary. The method starts with an arbitrary rope. Therefore, the initial force distribution does not affect the sequence of actions when tightening the structure.

Fig. 6 shows force changes in the ropes which were recorded experimentally after each of 12 tightening steps (which in total corresponded to 4 iterations). Step 0 represents the initial force distribution.

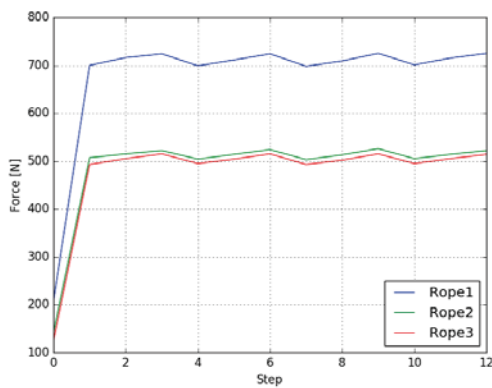


Fig. 6. Changes of forces in ropes: experiment, standard method, 12 tightening steps

The results obtained after the last tightening step (step 12) are given in Table 1.

Tab. 1. Force values in ropes recorded experimentally after 12 tightening steps: standard method

Rope	Desired value [N]	Obtained value [N]	Difference [%]
1	700	725	3.6
2	514	522	1.8
3	514	514	0.0

The course of the tightening process simulated using the FEM model is shown in Fig. 7.

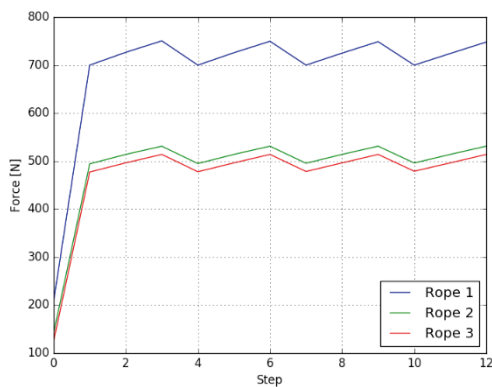


Fig. 7. Changes of forces in ropes: FEM simulation, standard method, 12 tightening steps

The results of simulation after tightening step 12 are given in Table 2.

Tab. 2. Force values in ropes obtained from FEM simulation after 12 tightening steps: standard method

Rope	Desired value [N]	Obtained value [N]	Difference [%]
1	700	748	6.9
2	514	531	3.3
3	514	514	0.0

Fig. 8 shows the result of the simulation for the standard method, when the tightening sequence was extended to 82 steps. It is clearly visible that, even for such a long time of tightening, the desired tension distribution has not been obtained. The final force values in individual ropes after step 82 are given in Tab. 3.

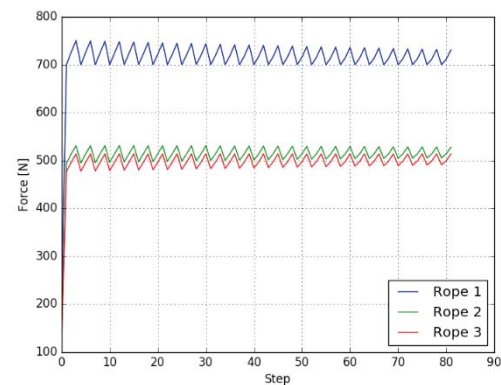


Fig. 8. Changes of forces in ropes: FEM simulation, standard method, 82 iterations,

Tab. 3. Force values in ropes obtained from FEM simulation after 82 iterations: standard method

Rope	Desired value [N]	Obtained value [N]	Difference [%]
1	700	731	4.5
2	514	528	2.8
3	514	514	0.0

## METHOD MAKING USE OF INFLUENCE MATRIX

The method proposed in this article makes use of the influence matrix  $A$ , the initial force vector  $S_{init}$ , and the desired force vector  $S_{des}$ .

Matrix  $A$  is a square matrix with the dimension equal to the number of ropes. In each row, the matrix elements represent force changes in ropes generated by the elementary force increase in the rope corresponding to the row number. For instance, row 1 is created as a result of elementary force increase in rope 1, therefore the first element is equal to 1

and the remaining elements correspond to the resulting force changes in the other ropes.

The desired force vector can be calculated from Eq. (3):

$$\mathbf{S}_{des} = \mathbf{S}_{init} + \mathbf{A} \Delta \mathbf{S} \quad (3)$$

where  $\Delta \mathbf{S}$  is the force increase vector, in which successive rows correspond to rope numbers.

Transforming this equation gives Eq. (4):

$$\Delta \mathbf{S} = \mathbf{A}^{-1} (\mathbf{S}_{des} - \mathbf{S}_{init}) \quad (4)$$

The obtained vector  $\Delta \mathbf{S}$  contains the force increase values which should be generated to achieve vector  $\mathbf{S}_{des}$ .

Solving Eq. (4) requires that the influence matrix  $\mathbf{A}$  is a nonsingular matrix, which is fulfilled for statically indeterminate systems.

## EXECUTION OF NEW METHOD

The influence matrices have been determined separately for the examined real object and the simulation model.

The experimentally obtained influence matrix is given as:

$$\mathbf{A}_{eks} = \begin{bmatrix} 1.0 & 1.349 & 1.326 \\ 0.723 & 1.0 & 0.962 \\ 0.732 & 0.986 & 1.0 \end{bmatrix} \quad (5)$$

while the influence matrix for the discrete model is:

$$\mathbf{A}_{MES} = \begin{bmatrix} 1.0 & 1.352 & 1.352 \\ 0.716 & 1.0 & 0.968 \\ 0.716 & 0.968 & 1.0 \end{bmatrix} \quad (6)$$

The initial force vector was:

$$\mathbf{S}_{init} = \begin{Bmatrix} 245 \\ 173 \\ 196 \end{Bmatrix} N \quad (7)$$

Based on the experiment, the force increase vector  $\Delta \mathbf{S}$  was calculated from Eq. (4) as:

$$\Delta \mathbf{S} = \begin{Bmatrix} 362 \\ 572 \\ -512 \end{Bmatrix} N \quad (8)$$

The following tightening sequence was assumed:

- in rope 1: tension force was increased by 362 N,
- in rope 2, tension force was increased by 572 N,
- in rope 3, tension force was decreased by 512 N.

Fig. 9 illustrates the force values obtained when executing the force increase vector (8).

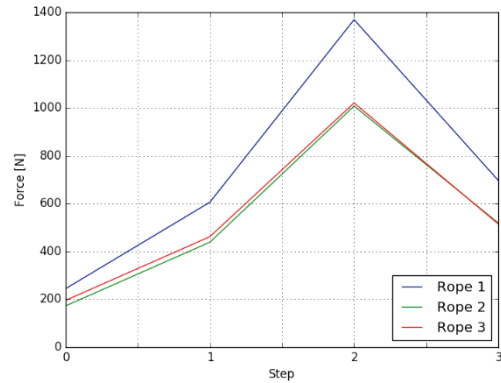


Fig. 9. Changes of forces in ropes: experiment, new method, 3 tightening steps

Table 4 collates the force values in the ropes, which were achieved after tightening step 3.

Tab. 4. Absolute rope tension force error experimentally recorded after 3 tightening steps: new method

Rope	Desired value [N]	Obtained value [N]	Difference [%]
1	700	697	-0.4
2	514	519	1.0
3	514	514	0.0

The vector  $\Delta \mathbf{S}$  was calculated using Eq. (4) and the influence matrix (6) obtained from FEM simulation:

$$\Delta \mathbf{S} = \begin{Bmatrix} 159.3 \\ 484.7 \\ -265.3 \end{Bmatrix} N \quad (9)$$

Fig. 10 illustrates changes of forces in ropes after successive tightening steps.

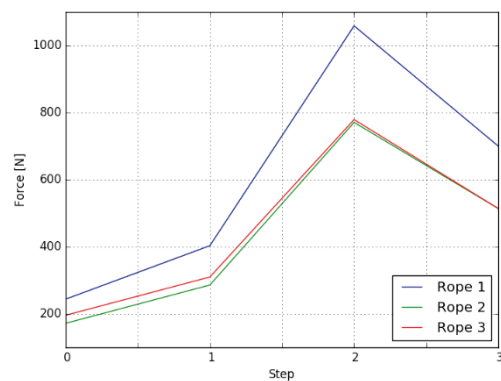


Fig. 10. Changes of forces in ropes: FEM simulation, new method, 3 tightening steps

Table 5 collates the force values in the ropes, which were achieved after 3 tightening steps.

Tab. 5. Force values in ropes after 3 tightening steps: FEM simulation, new method

Rope	Desired value [N]	Obtained value [N]	Difference [%]
1	700	700	0.0
2	514	514	0.0
3	514	514	0.0

## LIMITS IN APPLICATION OF NEW METHOD

The new method is based on linear relationships between loads, displacements, and deformations. To ensure preservation of constant values of the influence matrix elements, certain limits were introduced with respect to minimal and maximal forces in ropes during the tightening process.

### MINIMUM FORCE LIMIT

To limit possible effects caused by rope loosening, the tension forces in ropes should not drop below zero. In the present analysis, the intransgressible minimum limit for forces in ropes was assumed equal to 150 N.

Based on the numerical analysis, the initial force vector for the examined rope system was selected as:

$$S_{\text{init}} = \begin{Bmatrix} 250 \\ 180 \\ 180 \end{Bmatrix} N \quad (10)$$

The force increase vector was calculated from Eq. (4) as:

$$\Delta S = \begin{Bmatrix} -549 \\ 369 \\ 369 \end{Bmatrix} N \quad (11)$$

Fig. 11 shows the predicted tightening sequence for which the forces in all ropes drop below the assumed limit in the first iteration step.

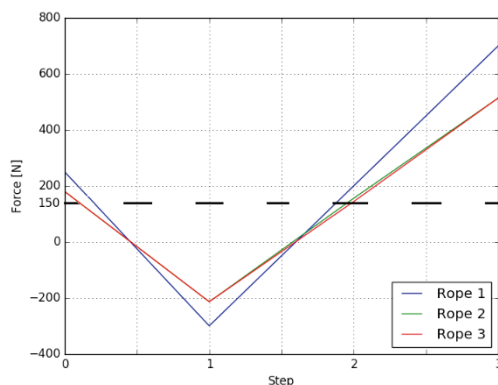


Fig. 11. Unacceptable tightening sequence due to force drop in all ropes below the assumed limit

In such a case, it is necessary to terminate the tightening step before the tension force in any rope drops below the assumed limit.

To execute the force increase vector (11), in the first step, the force drop by 42 N was generated in rope 1, which led to force increase by 150 N in ropes 2 and 3. Then, in the second and third steps, the forces in rope 2 and rope 3 were increased by 369 N, respectively. In the final, fourth step, the force in rope 1 was decreased by 507 N, (being the difference between the desired force of -549 N and the force -42 N applied in the first step).

The tightening executed in accordance with the above sequence does not lead to force dropping below the assumed low limit in any rope. The corrected tightening sequence is illustrated in Fig. 12.

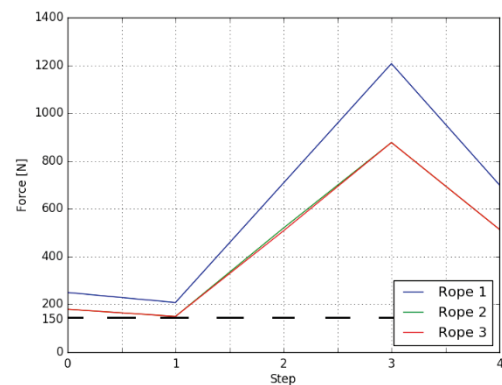


Fig. 12. Rope tightening sequence taking into account the minimum force criterion

### MAXIMUM FORCE LIMIT

To ensure a safe sequence of rope tightening, it is necessary to introduce a maximum limit for forces in ropes which must not be exceeded during the tightening. This limit can be determined by a maximum permissible load of the rope, or some equipment elements, and/or by the carrying capacity limit of the used measuring sensors. The maximum limit for tension forces in ropes assumed in the present analysis was equal to 1300 N.

The effect of exceeding this limit was tested on the case with the initial force vector:

$$S_{\text{init}} = \begin{Bmatrix} 210 \\ 175 \\ 175 \end{Bmatrix} N \quad (12)$$

The force increase vector  $\Delta S$  was calculated using Eq. (4) and the influence matrix (6) obtained from FEM simulation:

$$\Delta S = \begin{Bmatrix} 1492 \\ -371 \\ -371 \end{Bmatrix} N \quad (13)$$

Fig. 13 shows the predicted tightening sequence, for which the tension force in rope 1 exceeds the assumed limit in the first iteration step.

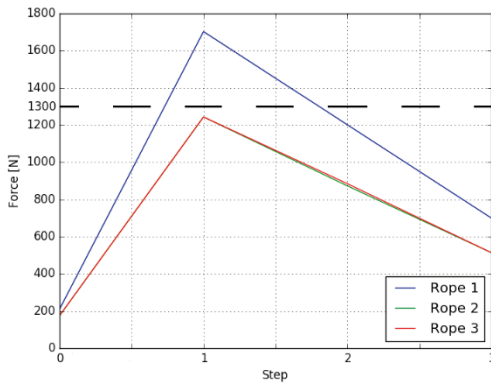


Fig. 13. Unacceptable tightening sequence due to exceeding maximum force limit in rope 1

Analogously to the case of minimum force in rope, the tightening step should be terminated before the maximum force limit is exceeded in any rope.

For the analysed case, in the first step, the force in rope 1 should be increased by 1492 N, but this would lead to exceeding the assumed force limit of 1300 N. Therefore, the force in this rope can only be increased by 1090 N to reach the limit. In the second and third steps, the tension forces were decreased by 371 N in rope 2 and rope 3, respectively. In the final step, the force in rope 1 was increased again, this time by 402 N, being the difference between the desired force value of 1492 N and the previously applied force increase of 1090 N. Using the above tightening sequence, the desired tension force distribution was obtained after four steps, without exceeding the assumed maximum force limit. The course of force changes in ropes for this case is illustrated in Fig. 14.

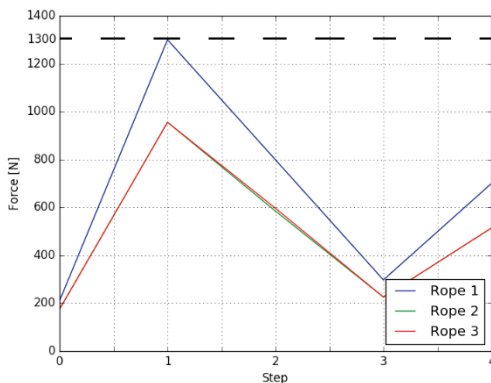


Fig. 14. Corrected tightening sequence taking into account the maximum force limit

## TESTING MINIMUM AND MAXIMUM FORCE LIMITS IN ROPES

An experiment was performed on a test rig to check the effect of minimum and maximum limits imposed on tension forces in ropes. The exact values of these limits were equal to 150 N and 1300 N, respectively.

The initial force distribution in ropes was:

$$S_{init} = \begin{Bmatrix} 315 \\ 240 \\ 247 \end{Bmatrix} N \quad (14)$$

Using Eq. (4), the vector  $\Delta S$  was calculated for the influence matrix (5) and the initial force distribution (14):

$$\Delta S = \begin{Bmatrix} 1984 \\ -559 \\ -638 \end{Bmatrix} N \quad (15)$$

Generating the force increase of 1984 N in rope 1 is not possible, as it would lead to exceeding the maximum force limit. Therefore, in the first step, the tension force in rope 1 was increased by 985 N to reach the limit of 1300 N in this rope. In the second step, the force in rope 2 was decreased by 559 N. Then, in the third step, the force in rope 3 was decreased by 253 N, as the tension force in rope 2 reached the minimum limit of 150 N. In the fourth step, the force in rope 1 was increased by 999 N, being the difference between 1984 N (the desired final value) and 985 N (the force change applied in the first step). In the fifth step, no action was taken in rope 2, as the entire force change was already generated in the second step. In the final, sixth step, the tension force in rope 3 was decreased by 385 N, being the difference between the desired final value of -638 N and the force decrease by 253 N executed in the third step.

The above tightening sequence is shown in Fig. 15.

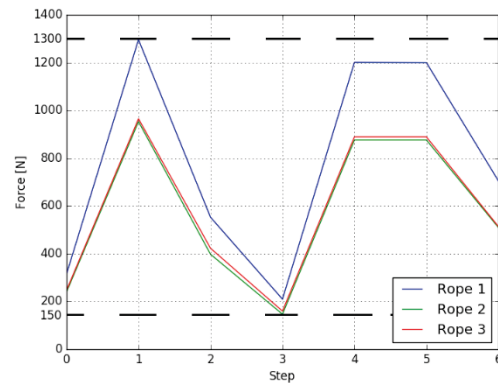


Fig. 15. Changes of forces in ropes taking into account assumed force limits: experiment, new method, 6 tightening steps

The values of forces in individual ropes obtained after 6 tightening steps are collated in Table 6.

Tab. 6. Force values in ropes experimentally recorded after 6 tightening steps: new method

Rope	Desired value [N]	Obtained value [N]	Difference [%]
1	700	705	0.7
2	514	510	-0.8
3	514	514	0.0

## CONCLUSIONS

The article compares two methods of structure tightening applied to a guyed mast, namely: the currently used standard method, and the new method proposed by the authors. Laboratory tests and FEM simulations were performed to assess the number of steps needed to achieve the desired force distribution in the ropes composing the examined rigging structure.

The proposed method radically simplifies the optimal tightening procedure for a given rigging to obtain the desired tension distribution in ropes. It makes it possible to obtain, in a small number of steps, accurate values of pre-tension forces using a numerical model. In the conventional iterative approach, this task was extremely time and labour consuming.

The differences between the values of influence matrix elements for the numerical model (5) and the real physical object (6) amount to 2.5% of absolute error. Possible causes of these differences will be analysed to create a more accurate numerical representation of the real object, and thus to allow direct application of the influence matrix obtained from FEM simulation to real objects.

The obtained results have shown that the proposed method makes it possible to control tension forces in ropes, and to obtain the desired tension distribution in a given rigging. Practical implementation of this method requires taking into account real limits concerning the stability of the structure and intransgressible minimum and maximum tension limits in its elements. These two aspects are the object of current studies performed by the authors.

## BIBLIOGRAPHY

1. DNV GL, Rules for Classification.: *Design and construction of large modern yacht rigs*, 2016.
2. Lloyd's Register., Rules and Regulations for the Classification of Ships.: *Masts and standing rigging*, Part 4, Section 10, 2017.
3. Ślęczka D., Ziemiański L.,: *Dynamic response of the mast to rapid break of guy rope (in Polish)*, *Budownictwo i Inżynieria Środowiska*, 45, 2007.
4. Grabe G.: *The Rig of the "UCA" - Finite element Analysis*, University of Applied Sciences, Amsterdam 2004.
5. Grabe G.: *The Carbon and PBO Rig for the "sailOvation" - Finite element Analysis*, University of Applied Sciences, Kiel.
6. Grabe G.: *The Rig of the research sailing yacht "Dyna" Measurements of Forces and FEA*, High Performance Yacht Design Conference, Auckland-New Zealand 2002.
7. Rizzo C., Boote D., *Scantling of mast and rigging of sail boats: A few hints from a test case to develop improved design procedures*, 11th International Symposium on Practical Design of Ships and Other Floating Structures, Brazil 2010.
8. Bentes J., Menezes R., Riera J.: *Dynamic response of guyed towers in transmission lines submitted to broken conductors*, 9th International Conference on Structural Dynamics, Portugal 2014.
9. Nelofer A., Kumar S.: *Finite Element Analysis of Guyed Masts under Seismic Excitation*, International Journal of Science and Research 2015.
10. Cuomo A., Zucker H., Dreslin S.: *Tower Technician Killed When Guyed Tower Collapsed, Case Report 09NY095*, Fatality Assessment and Control Evaluation, New York-USA 2017.
11. Hensley G., Plaut R.: *Three-dimensional analysis of the seismic response of guyed masts*, *Engineering Structures* 29, 2006.
12. ADINA R&D Inc. *Theory and Modeling Guide*, Watertown, MA, USA, 2009
13. NX Nastran, *Theoretical Manual*, 2016.
14. Bureau Veritas, *Rules for the Classification and the Certification of Yachts*, NR500, 2016
15. Kozioł K., *Guyed bar structures: the analysis of dynamic response to exceptional loads (in Polish)*, Politechnika Krakowska, Kraków 2007.
16. Coria I., Abasolo M., Olaskoaga I., Etxezarreta A., Aguirrebeitia J.: *A new methodology for the optimization of bolt tightening sequences for ring type joints*, *Ocean Engineering* 129, 2017, pp.441–450.
17. Yu-wen D., You-yuan W.: *A Research to Cable Force Optimizing Calculation of Cable-stayed Arch Bridge*, *Procedia Engineering* 37, 2012, pp.155 – 160.
18. Bradon J., Chaplin C., Ermolaeva N.: *Modelling the cabling of rope systems*, *Engineering Failure Analysis* 14, 2007, pp.920–934.
19. Kozak J., Tarełko W.: *Case study of masts damage of the sail training vessel POGORIA*. *Engineering Failure Analysis*, Volume 18, Issue 3, 2011, pp.819-827.

## CONTACT WITH THE AUTHORS

**Leszek Samson**

*e-mail: leszek.samson@pg.edu.pl*

Gdańsk University of Technology,  
Gabriela Narutowicza Street 11/12 , 80-233

**POLAND**

**Maciej Kahsin**

*e-mail: mkahsin@pg.edu.pl*

Gdańsk University of Technology,  
Gabriela Narutowicza Street 11/12 , 80-233

**POLAND**

## SELECTED ISSUES OF HYBRID OUTBOARD MOTORS

Wojciech Leśniewski

Gdańsk University of Technology, Poland

### ABSTRACT

*The aim of the research reported in the article was designing a hybrid drive system based on an outboard internal combustion engine offered by a selected producer and testing its operating characteristics. The article presents different designs of this type of drive which can be found in the literature and are available in the market. The designed hybrid outboard drive system was tested both on the laboratory test rig and in real operating conditions. The results of these tests are included.*

**Keywords:** boat drive, outboard motors, hybrid drive, emission-free drive, electric drive

### IDEA OF HYBRID OUTBOARD DRIVE

Enormous progress in technology and attempts to increase the operating efficiency of drive systems are the reasons why watercraft drives with electric motors gain in interest and popularity. On some boats, where possible, a conventional internal combustion drive can be fully replaced by electric drive, while for the watercraft on which the nature and potential of operation require leaving the internal combustion engine, a hybrid system seems the most suitable solution. As long as typical stationary drive systems are concerned, the matter seems trivial. The electric motor is very often mounted at the shaft axis or parallel to it, depending on the type of hybrid system to be installed: parallel or serial, and how much place is available for system expansion. However, in the case of boats with outboard motors, the hybridisation problem becomes more complex. While a serial hybrid system enables using a power generator with a set of batteries and an electric outboard propeller, a parallel system requires a special design of the outboard motor. Possible solutions based on two independent drives: electric and with internal combustion engine, should be excluded and the searched hybrid system should have a shared propeller, as otherwise,

the system could only act as two independent drives, with no profits resulting from hybridisation.

### GENESIS OF THE PROJECT

Since 2006, the author of the article was a member of a team of research workers and students of Gdansk University of Technology involved in building and testing the operation of solar energy fed watercrafts. Actively participating for over 10 years in international racings and other events related with unconventional methods of watercraft feeding, the author had an opportunity to observe a huge development in available technologies. Miniaturisation of control systems, increase in power density of electric motors, and improvement in operational safety of newest battery types are the reason why the electric drive is becoming more and more available and cheaper in both installation and operation terms.

A research project which provided opportunities to learn about principles and conditions of operation of hybrid drive systems was related with designing a drive system for watercraft intended to operate in the Zulawy Loop [1]. Within the framework of this project, a special test rig was

built, along with a complete drive system based on 100 kW Diesel engine and 15 kW electric motor. The tests of this drive system, performed in conditions close to its real operation, have made it possible to study its behaviour in given operating conditions. Considerations on possible concepts of hybrid systems were the motivation for searching for solutions applicable on boats on which the use of a stationary drive was not possible.

## EXISTING DESIGNS OF OUTBOARD DRIVES

Despite the existence of a number of patents, hybrid drives are not available in the market. However, at a time of increasing focus on improving the drive efficiency, and concern about the purity of exhaust gas leaving the boat drive engine, the need for designing and production of hybrid systems for small boats with outboard drives seems inevitable. An internal combustion engine offers great opportunities concerning the navigation range and power of the given watercraft, while the electric drive is quiet and does not emit exhaust gases. Unfortunately, installing large batteries is very expensive and takes much more space than a fuel tank needed for feeding conventional drive systems with internal combustion engines. That is why full elimination of internal combustion drive is not always possible, and in those cases a combination of both drive types is necessary. A hybrid drive system should be simple in maintenance and should expand the range of operation of the conventional drive system.

Installing an additional electric module involves some new requirements. The watercraft with this drive should be more versatile in terms of accessible water areas and navigation

restrictions. Current patents, which have been developed in recent years, offer different concepts of hybrid drive systems. They are based on new designs of complete drives or very complex modifications of existing ones (Fig. 1).

In the designs published in the literature, the electric motor is placed under the internal combustion engine and in this case these two systems drive a shared vertical shaft, or the electric motor is installed in the propeller base casing and drives the propeller shaft. Another, simpler method of installing an additional electric drive is shown in Fig. 2 and consists in mounting the electric system with a separate propeller on the anti-cavitation plate. This case is considered a combination of two independent systems, and its only advantage is the possibility to navigate using an electric drive, while the remaining advantages resulting from the use of a hybrid system are lost. In general, the solutions proposed in the literature do not include concepts of modernisation of existing drives owned by boat users or offered for sale.

## MODERNISATION CONCEPT OF EXISTING DRIVE

The existing patents and designs of hybrid outboard drives assume that a completely new drive system will be built. However, drive hybridisation refers not only to newly built systems, but also to those offered in the market or already used on boats. The replacement of these systems is usually unnecessary and unjustified from the economic and ecological point of view. For those cases, a solution which turned out most suitable after performing numerous tests and analyses is a concept of an additional module hybridising the existing outboard drive (Fig. 3).

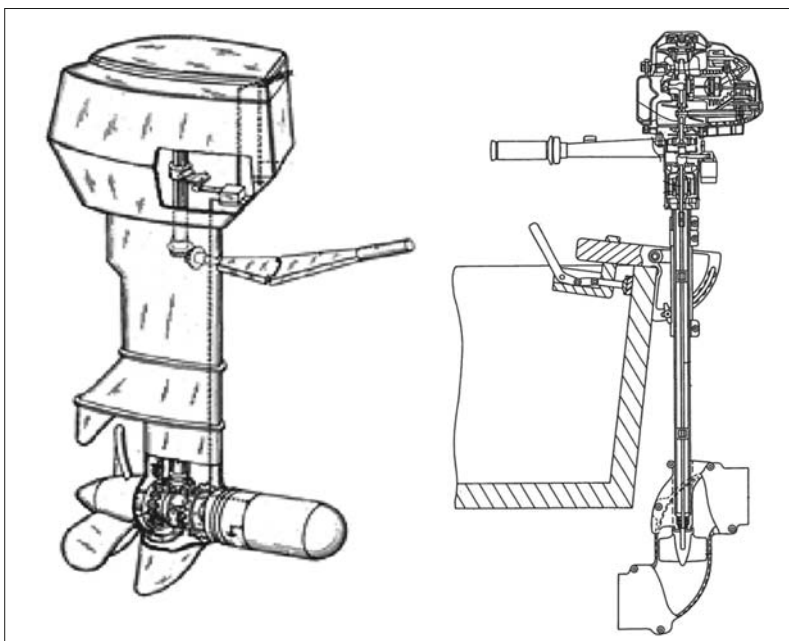


Fig. 1. Different solutions of outboard drives: electric motor mounted at the propeller shaft axis (left); electric motor mounted at the vertical shaft axis, under the internal combustion engine (right) [2],[3]



Fig. 2. Electric motor installed on anti-cavitation plate

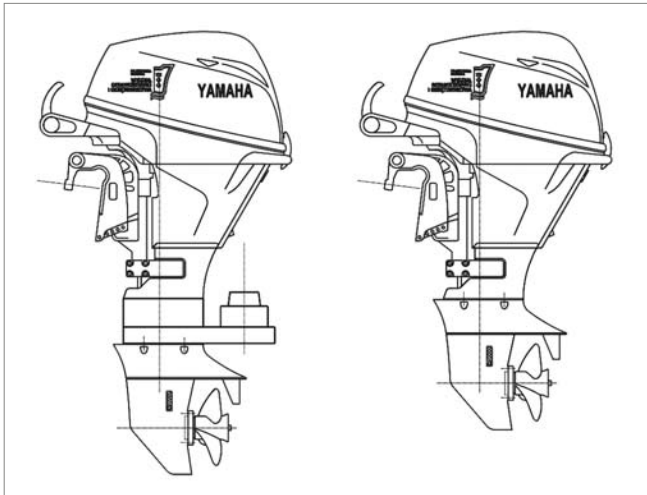


Fig. 3. Hybrid outboard drive (left) and drive before modernisation (right)



Fig. 4. Electric module installed on the outboard motor base

There are some important factors which affect the selection of a proper place for delivering additional power to the propeller shaft. The currently built outboard drives are frequently based on similar elements for a given type series of propellers, which makes it possible to use one electric system for all these propellers.

The engine selected for design and test purposes was 15 KM YAMAHA F15CES with short base, the outboard engine of a leading producer which has some margin of permissible power transmitted to the bevel gear. A 20 KM engine of the same type is also offered for sale. Before modification, the engine was expected to work faultlessly during the performed tests and generate no errors and doubtful data. The engine is equipped with a reversing reduction gear with ratio of 2.08:1, mounted in the column base. When using an electric motor for driving, it is noteworthy that the amount of energy stored in the battery is limited. The electric motor used for expanding the drive system was an air cooled 3 kW DC motor. This motor was also used by the author in other projects, which made it possible to assess the effect of configuration of the drive system on its operation. The electric motor was installed above the propeller base division plane (Fig. 4) and connected to the vertical shaft via a belt transmission. During the operation of the electric drive, the water pump and the upper part of the vertical shaft are inactive. A one-way clutch was used to disconnect the internal combustion part when the electric system was active. For this purpose, the original shaft, available in producer's service as a replaceable element, had to be modernised.

The electrical energy in the battery is very valuable, as the batteries are most expensive components when investing in electric drive. Their capacity affects directly the time of watercraft operation in electric mode. Considering the amount of stored energy, the drive system should be designed and modified in such a way that its total efficiency is as high as possible. When designing the electric system, all mechanisms which do not participate in its operation should be disconnected. This mostly refers to the internal combustion engine crankshaft and the cooling water pump.

The electric motor has much smaller power, therefore its rotational speed should be properly adjusted when driving the same propeller as the internal combustion engine. Propellers for drive systems with internal combustion engines are selected such that the engine can reach its nominal rotational speed. In this situation, the belt transmission ratio for the electric motor should be selected in such a way that both drives can work at their nominal powers and rotational speeds, thus ensuring long lasting and faultless operation of the hybrid drive.

## TEST RIG

Modifying an outboard motor involves some new requirements and limitations. The drive system intended for use on watercraft should undergo a very thorough inspection and testing. Of high importance is maintaining relevant reliability of the modified motor. If the object of modification is a brand-new engine, its modification may cause loss of manufacturer's warranty, therefore the introduced modifications should receive approval from the engine producer. First of all, they should not affect the correctness of operation of internal combustion engine components, which is a precondition for maintaining warranty for unmodified parts. The remaining components should be manufactured with utmost accuracy to ensure proper operation of the system.

The test rig was designed and manufactured in such a way as to provide opportunities for measuring operating parameters of the hybrid system in the entire range of electric motor operation. A complete motor was mounted on a specially prepared frame and connected to a hydraulic pump via flexible couplings and torque meter (Fig. 5). The hydraulic oil pressure in the pump circuit was controlled using a throttling valve, which made it possible to adjust the torque and rotational speed to nominal operating parameters of the electric motor.



Fig. 5. Hybrid outboard drive on test rig

Changing the rotational speed of the electric motor simultaneously adjusted the motor load. This is the situation which also occurs during a real operation of the outboard motor. The parameters recorded during the tests included: rotational speed, propeller shaft torque, voltage and current delivered to the complete system (including measuring systems for batteries and the cooling system for electric motor). The measuring system used for recording mechanical power consisted of a torque meter with measuring range of 0–20 Nm, and an in-house optical sensor of rotational speed which generated one voltage pulse per one shaft revolution. This system also included terminals for measuring the voltage supplied to the controller and the current transformer LEM LAH 100-P 100A / 50mA used for measuring the current in the supply cable to the controller. The recorded parameters were used for calculating electric and mechanical power of the drive system without propeller.

## RESULTS OF MEASUREMENTS AND THEIR DISCUSSION

The nominal point of system operation was defined by the settings at which the motor consumed 75 A current at 48 V voltage. These values were specified by the producer as nominal operating parameters. For those settings the motor reached the rotational speed of 41,22 rps on propeller shaft. The remaining operating points were obtained by reducing rotational speed via changing the setting of the hydraulic pump throttling valve. The characteristics obtained in this way are shown in Fig. 6 and Fig. 7. For each point of electric motor operation, the temperature was measured until thermal equilibrium was reached. During the operation, the motor was heated up to 65°C in time depending on the applied load. The intensity of electric motor air cooling depended only on the current speed, as the air exchange in the motor casing did not depend on the applied load. The obtained maximum total efficiency of the electric drive without propeller was equal to 67%.

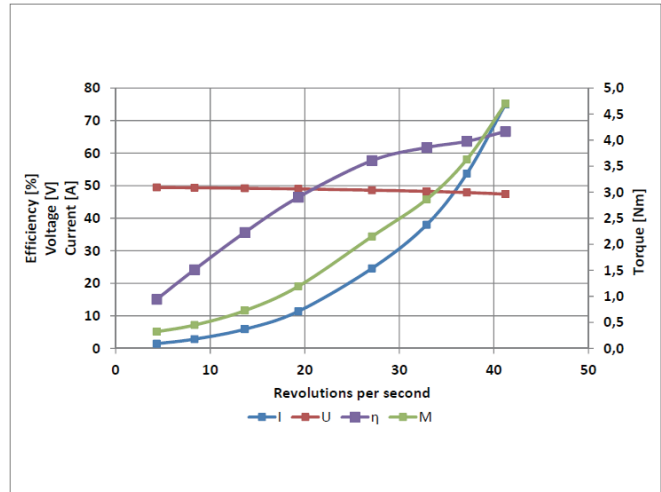


Fig. 6. Experimentally recorded operating parameters and efficiency of hybrid outboard drive system working in electric mode

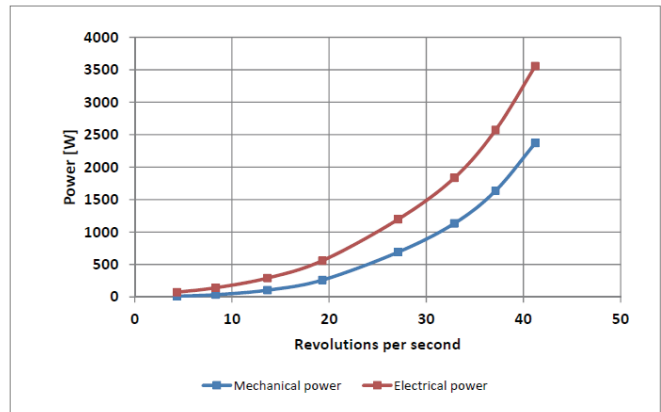


Fig. 6. Mechanical and electric power calculated from experimentally recorded operating parameters of hybrid outboard drive system working in electric mode

According to the data delivered by the producer, the maximum efficiency of the selected electric motor is 88%. However, in the examined drive system, a number of additional power loss sources can be named, such as the bevel gear, for instance, which is adapted to operate at power nearly three times as high as that delivered in electric mode. When designing the electric system, sealing of the vertical shaft and belt transmission at a number of additional points was assumed. The electric power measurement referred to the entire drive system, therefore losses generated in cables, controller, and the electric motor cooling system (with two blowers) had also to be taken into consideration. Each of these elements is a potential source of losses and affects the total system operation efficiency. Taking account of these additional power loss sources, the total efficiency of the drive system without propeller should range within 60–70%, which were the values obtained from the tests.

## CONCLUSIONS

In present days, increasing the use of hybrid drive systems on watercraft and in widely understood sea transport seems imminent. Hybrid systems offer many possibilities. The use of a hybrid system with one propeller enables parallel operation of both drives, or only sole operation of one (electric) drive. Moreover, it makes it possible to additionally load the internal combustion engine, which its advantage over conventional systems. As a rule, the internal combustion engine can work effectively when its load exceeds 60% of nominal load. Therefore, when its basic load drops below that level, it is profitable to additionally load the engine with the electric motor, thus recovering part of energy and improving total efficiency of the system. The recovered energy can be stored in batteries and then used for supplying the electric drive. This issue will be studied at the next stage of the research of the presented hybrid drive system.

Electric motors used in hybrid drives of boats usually reach about 30% of power of the main drive, which usually is the internal combustion engine. This proportion is justified economically. The electric motor allows the boat to sail with smaller resistance and does not require installation of large batteries. One hour of operation of the 3-kW electric motor used in the tested drive system required installation of about 25 kg of modern lithium batteries, which is equivalent in volume with a portable fuel tank used for outboard engines. Boats which seem ideal for this type of drive are so-called houseboats, which usually make use of engines with long base. The use of hybrid drive on those boats (Fig. 8) allows them to enter water areas on which the watercraft with zero emission is only allowed to sail.

The tests with the designed hybrid motor, performed on the laboratory test rig, confirmed the correctness of the adopted design assumptions. Optimal parameters of electric motor cooling were properly selected, and the efficiency of its operation was checked. In field conditions, the system underwent leakage tests and other measurements which allowed to determine parameters of cooperation of electric motor with internal engine.

A significant conclusion from the performed test is the existence of three states of operation of the hybrid system, which are characterised by different rotational speeds of electric motor. The motor can work parallel with the internal combustion engine at engine's rotational speed, or, after switching the engine off, decrease the rotational speed of the propeller to adapt it to the power available in this configuration. This rotational speed depends on the propeller characteristic and in the examined case, was about twice as low as that of the internal combustion engine.

## REFERENCES

1. J. Kowalski, W. Leśniewski, and W. Litwin, "Multi-source supplied parallel hybrid propulsion of the inland passenger ship STA.H. Research work on energy efficiency of a hybrid propulsion system operating in the electric motor drive mode," *Polish Maritime Res.*, vol. 20, pp. 20–27, 2013.
2. Rodolfo Rodriguez Balaguer, Patent *Outboard motor unit*, US3703642A 1971-10-28.
3. Hiroyuki Kitani, Kazumi Miyashita, Shigeo Terada, Tadafumi Hirose, Patent: *Outboard motor* US20060025025A1 2004-07-28.
4. <https://www.boatownersworld.com/navigator-35-electric-boat-motor-35lb-thrust-sku-653501-stainless-steel.html> 20.10.2018.

## CONTACT WITH THE AUTHORS

**Wojciech Leśniewski**

*e-mail: wojciech.lesniewski@pg.edu.pl*

Gdańsk University of Technology  
Narutowicza 11/12, 80-233 Gdańsk  
**POLAND**

# AERODYNAMIC PERFORMANCE OF A NEW DOUBLE-FLAP WING SAIL

**Dongqin Li**

School of Naval Architecture & Ocean Engineering, Jiangsu University of Science and Technology, China

**Yili Zhang**

Jiangsu University of Science and Technology, China

**Peng Li**

Jiangsu University of Science and Technology, China

**Jingjing Dai**

Jiangsu University of Science and Technology, China

**Guohuan Li**

Jiangsu University of Science and Technology, China

## ABSTRACT

*As a type of natural energy resource, wind power is used in the modern implementation of wind-assisted technologies as a method for reducing the fuel consumption and environmental pollution of ocean-going ships. In order to promote the full usage of ocean wind energy for cargo ships, an innovative type of ship propulsion-assisted wing sail is proposed in this paper. The propulsion efficiency of this new wing sail can be increased by enlarging its area in both the transverse and vertical directions in good weather conditions, and it can be folded up automatically in poor weather conditions, improving the sailing safety of the ship. The sail parameters relating to the gaps and rotation angles between different parts of the wing sail are compared, and the values giving the best aerodynamic performance are identified using CFD simulation technology. The results for the lift and drag coefficients for the new wing sail at different attack angles are also compared with those of traditional aerofoil sails, including an arc-shaped rigid sail and a variable-camber sail proposed in 2015. From the viewpoint of the sailing performance of the vessel, our results demonstrate that this new type of wing sail has good aerodynamic performance and can reduce fuel costs for commercial vessels.*

**Keywords:** double-flap wing sail, aerodynamic performance, Computational Fluid Dynamics (CFD), parameter optimization

## INTRODUCTION

Cargo shipping is an inexpensive and convenient way of transporting goods around the world. However, a negative impact has been observed in the shipping transport industry in terms of greenhouse gas emissions and harmful liquid substances. Many different kinds of measures and technologies have already been adopted on board ships for the purposes of energy saving and emission reduction [1].

As it is a renewable energy source and offers the possibility of environmental sustainability, wind power has been used for centuries to provide the main thrust through sail technology. Although sail-assisted propulsion is not currently considered to provide sufficient main thrust for large maritime shipping, it can offer considerable economic and environmental

advantages by reducing fuel consumption when coupled with conventional propulsion [2, 3]. Sails can produce the aerodynamic forces of drag  $D$  and lift  $L$  [4], both of which can be harnessed for towing, as illustrated in the coordinate system in Fig. 1. Here,  $\alpha$  means the attack angle,  $\beta$  the wind angle,  $X$  the forward force and  $Y$  the side force.

The issue of how to design new types of sail that can produce higher thrust and more reliable aerodynamic performance has become a research topic of considerable interest. The objective of this study is to investigate the aerodynamic performance of a proposed collapsible double-flap wing sail. Attention is paid to the design of the shapes of the three parts of the new wing sail, using a comparison of different mesh structures, mesh sizes and turbulence models, and the optimum combination of parameters under specific wind conditions is sought. In

terms of its automatic and flexible structural features, this new type of collapsible double-flap wing sail is designed to increase the propulsion efficiency by enlarging the area of the sail in the transverse and vertical directions when suitable wind conditions become available. It can also be folded up automatically in poor weather conditions to reduce the sail area in the transverse section and improve the sailing safety of the ship. This new wing sail is composed of three parts, the main, front and back wings. Using computational fluid dynamics (CFD), the sail parameters are investigated, including the gaps and rotation angles between its component parts, and the best parameters for excellent aerodynamic performance are determined.

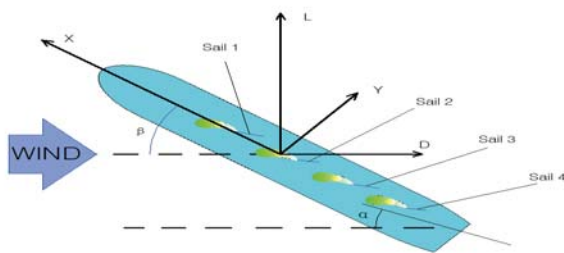


Fig. 1. Coordinate system of the cascade sails for an imaginary ship

## DEVELOPMENT OF SAIL-ASSISTED TECHNOLOGY

Although sails have been utilized for ship propulsion since ancient times, modern sail-assisted technology was put into use only in the 1970s, due to the first global oil crisis. It is well-known that high-performance modern sails with large wing areas can be efficient on these vessels, and that the type of sail greatly affects the aerodynamic performance and its application on board vessels.

A comparison of the maximum lift coefficients for various types of soft, hard and rotor sails, based on wind tunnel tests, was carried out by Bergeson and Greensward [5]. In 1985, Walker wing sails with an airfoil shape were proposed by John Walker; these were first used on a 3000-ton freighter called “MV Ashington” and can provide fuel savings of 15–25% [6]. In 1991, a wind-assisted ship propulsion device (WASP) consisting of a cylinder-flap wing was developed [7], and in 2005, a new hybrid sail [8] consisting of a slat, a hard sail and a oft sail was designed for advanced sail-assisted bulk carriers. Ouchi et al. [9] proposed a telescopic structure for hard sails in 2011, and in 2013, the same authors presented the “Wind Challenger” project [10], which investigated the use of wing sails for an 180,000 deadweight tonnage (DWT) bulk carrier. Li [4] proposed a type of hard sail called variable-camber sail in 2015, and investigated the performance of cascade sails.

From the above references, it is clear that the use of sail-assisted technologies can increase the ratio of the wind thrust to the thrust generated by the conventional engines, and can therefore decrease fuel consumption.

## SAIL TYPES AND SELECTION OF TARGET SHIPS

### SELECTION OF THE SAIL TYPE

The issue of how to choose a sail type to improve the ship’s propulsion efficiency is a major concern in the application of sail-assisted technology. Traditional soft sail propulsion can no longer be used in modern cargo shipping, due to the insufficient propulsion power generated and restrictions on deck space. Flettner rotors are used to provide auxiliary propulsion force by rotating with the aid of electric motors, but these may cause extra energy consumption. There are also some deficiencies when using kite devices, such as difficulties in launching and retrieving them. An investigation of the existing typical and innovative sail systems was undertaken [11], and the aerodynamic performance of different types of sail rig was compared. As a result of this investigation, a wing sail with flaps was chosen as our research target, based on its superior drag/lift ratio performance, and new design style was used that allows it to be folded in bad weather conditions.

### SELECTION OF THE TARGET SHIP

The particulars of the ship were used to define the initial dimensions and location of the wing sail. The candidate type of ship must have an open deck area, without extensive superstructure or deck machinery. The mounting site should also be carefully chosen to ensure that forces can be safely transferred to the ship’s structure.

Tab. 1. Characteristics of the target vessel

Characteristic	Dimension
Overall length	~199.99 m
Length between perpendiculars	192.00 m
Moulded breadth	32.26 m
Depth designed	15.40 m
Draft in full load	10.50 m
Speed design	13.0 kn
Deadweight	46,000 t

Tab. 2. Main dimensions of the wing sail

Characteristic	Dimension
Chord of the main wing	10 m
Chord of the front wing	6 m
Chord of the back wing	4 m
Total width	20 m
Height	24 m
Aspect ratio	1.2
Camber ratio	0.12

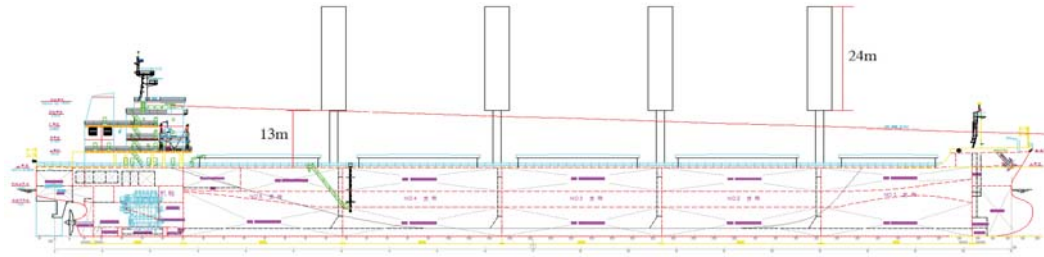
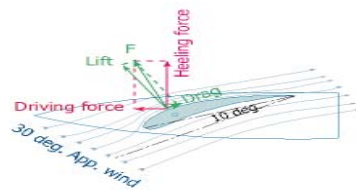


Fig. 2. General arrangement of the target vessel

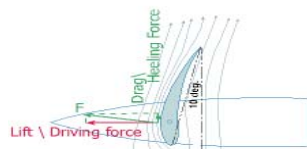
A 45000DWT bulk carrier with five cargo holds was chosen as the target ship, with a distance between adjacent hatches of about 8 m. The characteristics of the target vessel are listed in Table 1, and the general arrangement is shown in Fig. 2. Based on the ship's characteristics, four sets of wing sails 20 m wide and 24 m high were installed on the target ship; the aspect ratio of the wing sails was 1.2 and the camber ratio 0.12. The main dimensions of the wing sails are shown in Table 2.

## ANALYSIS OF FORCES ON THE WING SAIL

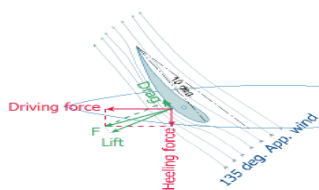
As suggested by its name, a wing sail is similar to the wing of an aircraft. A force analysis at different wing angles is shown in Fig. 3. The forces acting on the ship are the thrust  $T$  and drift  $H$ , which can be derived from the lifting force  $F_L$  and drag force  $F_D$  of the sail. In the form of dimensionless indexes, these forces can be expressed as the lifting coefficient  $C_L$ , the drag coefficient  $C_D$ , the thrust coefficient  $C_T$  and the drift coefficient  $C_H$ .



(a) 30° apparent wind



(b) 90° apparent wind



(c) 135° apparent wind

Fig. 3. Force analysis at different wind angles

The forces acting on the wing sail are shown in Fig. 4. The thrust and drift forces acting on the ship are as follows:

$$\begin{aligned} T &= F_L \cos \alpha + F_D \sin \alpha \\ H &= F_D \cos \alpha - F_L \sin \alpha \end{aligned} \quad (1)$$

The thrust and drift force coefficients can be expressed in the form of dimensionless indexes as

$$\begin{aligned} C_T &= C_L \sin \beta - C_D \cos \beta \\ C_H &= C_L \cos \beta + C_D \sin \beta \end{aligned} \quad (2)$$

where

$$\begin{aligned} C_L &= F_L / (0.5 \rho_a V_r^2 S) \\ C_D &= F_D / (0.5 \rho_a V_r^2 S) \\ C_T &= T / (0.5 \rho_a V_r^2 S) \\ C_H &= H / (0.5 \rho_a V_r^2 S) \end{aligned} \quad (3)$$

Here,  $C_T$ ,  $C_H$  and  $C_L$  and  $C_D$  are the thrust, drift, lift and drag force coefficients, respectively;  $\rho_a$  is the density of air ( $\text{kg}/\text{m}^3$ );  $S$  represents the total sail area ( $\text{m}^2$ );  $V_r$ ,  $V_s$  and  $V$  are the apparent wind velocity, ship velocity and absolute wind velocity ( $\text{m}/\text{s}$ );  $\beta$  is the apparent angle of wind (degrees);  $\alpha$  is the angle of attack (degrees);  $\gamma$  is the true wind angle (degrees);  $\delta$  is the angle between the center line of the ship and the chord of the sail; and  $b$  is the chord length of the whole wing ( $\text{m}$ ).

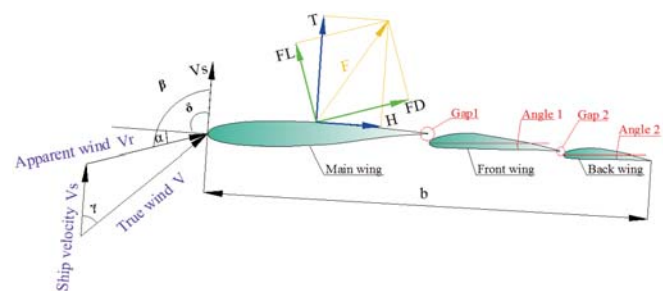


Fig. 4. Forces acting on the wing sail

## NEW DESIGN OF A DOUBLE-FLAP WING SAIL

Based on a comprehensive analysis of the main types of sail in the literature [11], a wing sail was demonstrated

to have advantages such as good performance in assisted propulsion, a simple structure and convenient operation. From the literature [12], it can be seen that the use of flaps in a wing sail can enlarge the overall wind area of the sail and change its camber to increase the lift force. Based on our research, a new type of collapsible wing sail with double flaps is proposed in this paper, using additional flaps. The profile of double-flap wing sail is shown in Fig. 4.

Our proposed wing sail has three components: the main, front and back wings. These wings were designed separately in order to enable the sail to fold in a retractable way. The area of the wing sail can be increased in the transverse and vertical directions when suitable wind conditions become available, and it can be folded up automatically poor weather conditions to reduce the wind area in the transverse section and improve the sailing safety of the ship.

### OPTIMIZATION OF THE MAIN WING

The front shape of the main wing maintains symmetry while the afterbody part has a certain arc degree, so the shape of the main wing needs to be designed separately. Two types of airfoils are used to form a new shape of wing sail. In general, a large camber ratio for the sail is advantageous; however, the transverse force and the yaw angle will be increased when the camber ratio is too large, meaning that the camber ratio is usually between 0.1 and 0.18 [13]. A camber ratio of 0.12 was selected for the main wing in our design. A NACA 0012 airfoil, one of the most widely used low-speed airfoils, was used as the symmetrical head of the main wing. Since the front and back wings need to be folded back into the main wing, the tail of the main wing has a certain degree of curvature. Thus, a low-speed GOE413 airfoil was selected as the shape of the tail of the main wing, with a high lifting coefficient. These two airfoils are combined to form a novel shape for the head and tail, as shown in Fig. 5.

### OPTIMIZATION OF THE DOUBLE-FLAP WING

A double-flap arrangement effectively increases the wind area of the wing sail and the camber of the wing, and improves the loading capacity of the main wing, thus enhancing the lift force. A low-speed airfoil is used in the design of the shape of the front wing, which is an integrated airfoil combining the NACA4412 and GOE413. The NACA4412 airfoil has a higher lift coefficient, while the airfoil of GOE413 has a certain degree of curvature in the back area, so this combined airfoil can be used as an alternative wing flap which can be easily folded back and fitted closely with the main wing. An integrated optimized section of the front wing is shown in Fig. 6.

Here, the back wing is designed in a similar way to the front wing, which is also a type of low-speed airfoil. The NACA 4412 airfoil is chosen for this section. The front shape of the back wing has the same curvature as the back shape of the front wing, so that the back wing can be folded back to the front wing. The optimized section of the back wing is shown in Fig. 7.



Fig. 5. Optimized sectional view of the main wing

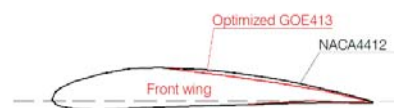


Fig. 6. Optimized sectional view of the front wing

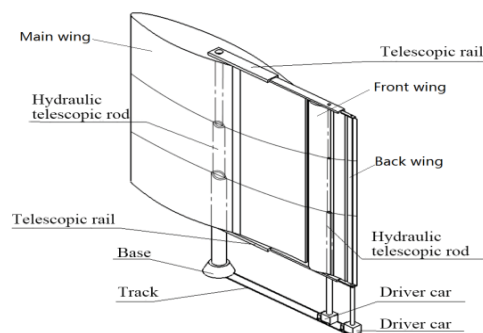


Fig. 7. Optimized sectional view of the back wing

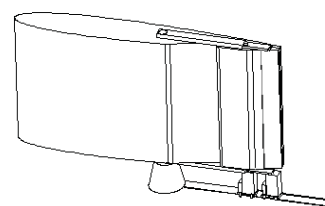
### EXPANSION AND FOLDING MECHANISMS

This new type of collapsible wing sail is based on a rotating frame mast. The two flap wings can be folded back together with the main wing to reduce the area in bad weather or near a harbor. All three wings can be slid up and down the mast together. The frame structure and folding status of the wing sail are shown in Fig. 8.

Depending on the available deck space and other restrictions, multiple sets of this new wingsail may be deployed on the target vessel. The lift force can be maximized by rotating the sail to the optimum angle of attack. Wing sails can also be used as 'brakes' to slow down the vessel, if needed, instead of using the engine astern.



(a) Frame structure (expanded status)



(b) Folded status (side view)



(c) Folded status (top view)

Fig. 8. Expansion and folding of the wing sail

## CFD SIMULATION AND PARAMETER OPTIMIZATION

In our research, a computational fluid dynamics (CFD) numerical simulation method was used to evaluate the aerodynamic performance of our new type of wing sail, as this approach has been demonstrated as being accurate and efficient. First, we used the professional CFD software STAR CCM+ for the aerodynamics calculations for the normal NACA0012 wing type, in order to test and verify the accuracy of the simulation. This software was then used to simulate the aerodynamic forces on our new type of wing sail, with different parameter combinations and attack angles. The NACA0012 airfoil was chosen as the calculation object, and the results for the lifting and drag coefficients at an angle of attack of 15°, using different turbulence models, mesh topology structures and mesh sizes, were compared with experimental data. The results are listed in Table 3 and illustrated in Fig. 9.

Tab. 3. Lift and drag forces under different conditions

Turbulence model	$F_L$	$F_D$	Mesh topology	$F_L$	$F_D$	Mesh size	$F_L$	$F_D$
SST	1.41	0.23	Structured mesh	1.51	0.32	Small mesh size (130,000)	1.25	0.37
SA	1.46	0.22	Unstructured mesh	1.58	0.37	Medium mesh size (500,000)	1.41	0.22
Standard k-ε	1.61	0.48	Hybrid mesh	1.47	0.29	Large mesh size (750,000)	1.42	0.23
Experimental values	1.43	0.23	Experimental values	1.43	0.23	Experimental values	1.43	0.23

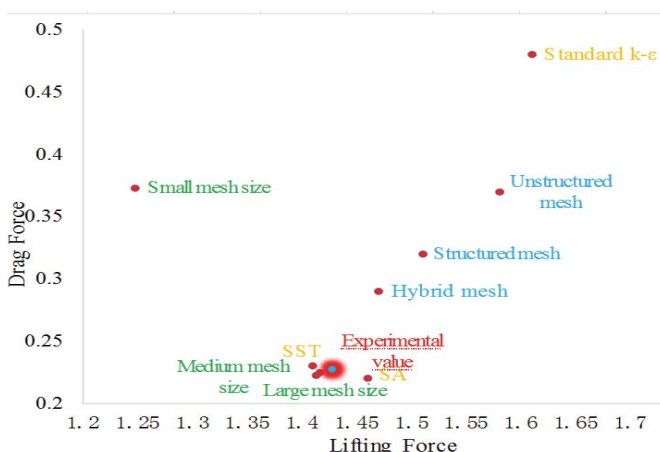


Fig. 9. Comparison of different grid settings and turbulence models



(a) Structured mesh (b) Unstructured mesh (c) Hybrid mesh

Fig. 10. Mesh structure using different topologies

In order to determine the influence of the turbulence model on the accuracy of the results, the SA, SST and standard k- $\omega$  turbulence models were chosen for comparison. The topological structure of the mesh also has a very important influence on the accuracy of the CFD calculation results. As shown in Fig. 10, structural, unstructured and hybrid meshes were used, in order to explore their effects on the CFD calculation, and the SST turbulence model was used to calculate the lift and drag coefficients of NACA0012 for different mesh topology structures.

From Table 3, we can see that the lift and drag forces calculated by the SST turbulence model are closer to the experimental values, and are more accurate than the other two turbulence models. Furthermore, the double-flap wing sail proposed in this paper is a complicated object with multi-section airfoils; a hybrid mesh was therefore adopted in which the key areas were filled with structured meshes and the other

regions with unstructured mesh. A suitable mesh size was then chosen for simulation of the new wing sail.

## PARAMETER OPTIMIZATION FOR THE WING SAIL

Since different combinations of parameters can greatly affect the aerodynamic performance of the double-flap wing sail, the control variable method [12] was used to solve this multi-parameter optimization problem, in which each parameter was changed individually while the others remained unchanged.

The parameters of the new wing sail include the front wing angle (Angle 1), the back wing angle (Angle 2), the gap (Gap 1) between the main and front wings, and the gap (Gap 2) between the front and back wings, as shown in Fig. 4. In this section, the influence of each parameter on the total aerodynamic performance of the wing sails is discussed

using the control variable method. The numerical model of the wing sail used in this paper is based on a scale ratio of 1:50. Computations were run in the STAR CCM+ CFD software for an incoming wind speed of 10 m/s. The lift and drag coefficients with different parameters and angles of attack were simulated in this CFD software, and an optimized parameter combination was obtained.

Using Eqs. (1), (2) and (3), the maximum thrust coefficient and the corresponding drift force coefficient of the sail model were calculated for different apparent wind angles  $\theta$ . As in reference [12], the front wing angle (Angle 1) and the back wing angle (Angle 2) were both set to 0°, 2°, 4° and 6°, while the gap between the main and front wings (Gap 1) and the gap between the front and back wings (Gap 2) were set to 3% C, 5% C and 8% C, where C is the chord length of the main wing (m). Different combinations of these parameters will result in different aerodynamic performance of the wing sail. Since space was limited, the range of the wind angle was kept between 40° and 140°, with a measuring interval of 10°, and the thrust and drift force coefficients for certain parameter combinations are shown in Fig. 11. As can be seen from the figure, the change in the thrust force coefficient is significant when the wind angle is 40°–120°, while thrust force coefficient is greatly improved when the wind angle is above 80° with sail gaps 5% C, and reaches maximum value when the wind angle is 110° with Angle 1 set to 2° and Angle 2 set to zero. With an increase in the wind angle, the drift force coefficients for different gaps are reduced accordingly.

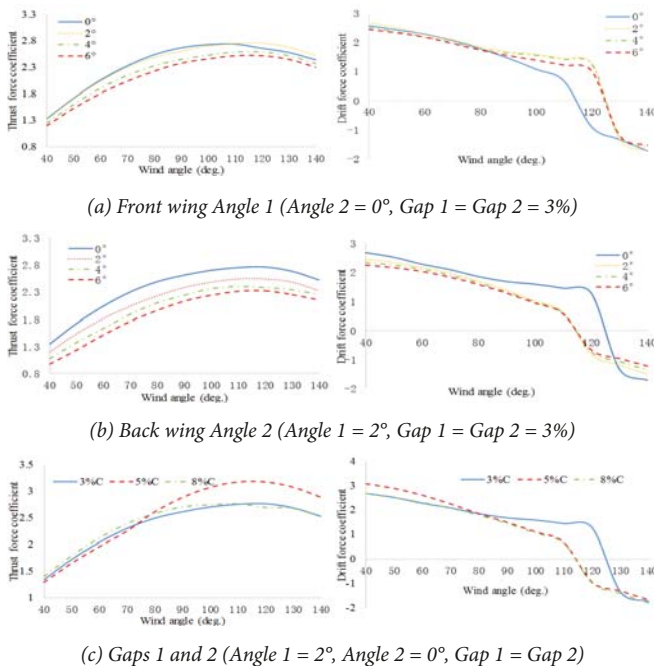


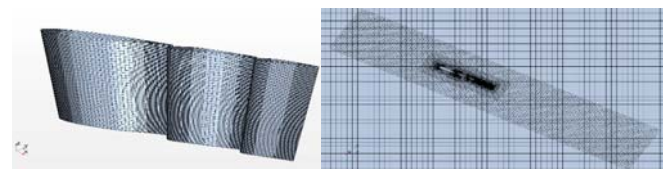
Fig. 11. Thrust and drift force coefficients for different parameters

Tab. 4. Simulation results for optimum coefficients

Wind angle (°)	Lift coefficient $C_L$	Drag coefficient $C_D$
0	-0.30	0
5	0.80	0.04
10	0.55	0.07

Wind angle (°)	Lift coefficient $C_L$	Drag coefficient $C_D$
15	0.57	0.13
20	0.70	0.23
25	1.27	0.40
30	1.60	0.60
35	1.68	0.80
40	1.33	1.00
50	0.88	1.38
60	0.72	1.64
70	0.44	1.85
80	0.18	2.24
90	-0.12	2.32

After comparing the simulation results for different parameters, the optimal combination of sail parameters (Angle 1 = 2°, Angle 2 = 0°, Gap 1 = Gap 2 = 3% C) was chosen for the specific condition of apparent wind speed. The results for the optimum lift and drag coefficients are listed in Table 4, while a mesh model of our proposed wing sail is shown in Fig.12.



(a) Geometric model of the sail (b) Computational domain mesh

Fig. 12. Mesh model of the new wing sail

## COMPARISON AND ANALYSIS

In order to evaluate the performance of our new wing sail, the calculation results were compared with those for traditional sail types (NACA0012 and arc sail) and a variable-camber sail [4]. The aerodynamic performance results are shown in Fig. 13. It is worth mentioning that the variable-camber sail is the most recent sail type in the literature, and was proposed by Japanese researchers in 2015 [4].

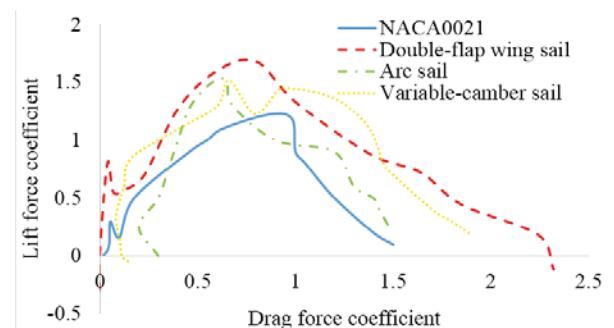
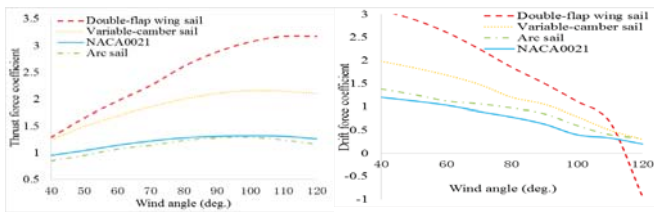


Fig.13. Lift and drag coefficients for the four sails

As can be seen from the above figure, the lift and drag force coefficients are superior to other traditional types of sails

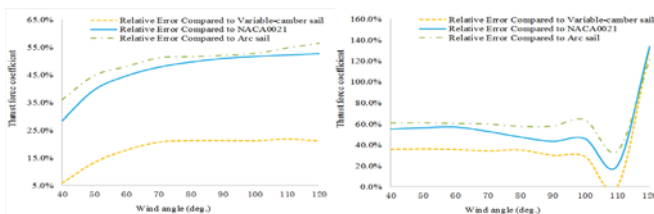
and the recently designed variable-camber sail. Especially in downwind conditions, the drag force may also form part of the propulsion force for the ship. In order to further verify the thrust performance of the new sail, the lift and drag force coefficients were converted to the thrust and drift coefficients using Eqs. (1), (2) and (3). When the wind angle was between 40° and 120°, the thrust from the wing sail was conducive to propulsion of the ship. The values of the thrust and drift coefficient values at wind angles of 40°–120° are shown in Fig. 14. It can be seen that the thrust coefficient of the new wing sail can reach 3.17 when the wind angle is 110°, which is much higher than the values for the traditional and variable-camber sails.



(a) Thrust force coefficient (b) Drift force coefficient

Fig. 14. Comparison of thrust and drift force coefficients

We also compared the results for the proposed double-flap wing sail with those of the variable-camber, NACA0021 and arc sails, and the results are shown in Fig. 15. The relative error (RE) is calculated as  $RE = (y_i - y_i^*)/y_i$ , where  $y_i$  represents the results for the proposed double-flap wing sail and  $y_i^*$  the comparable results for the variable-camber, NACA0021 and arc sails.



(a) Relative error in the thrust force coefficient (b) Relative error in the drift force coefficient

Fig. 15. Comparison of relative error for thrust and drift force coefficients

From the results of this comparison, we can see that our new type of wing sail is aerodynamically efficient and has a higher aspect ratio and performance, with a relatively small sail area. The two wing flaps increase the total area of the wing sail, and change the curvature of the airfoil, while the apparent angle between the wind and the whole wing sail can be changed and more force can be gained. There are small gaps between the three parts of the wing sail through which the wind can flow easily, and the wind velocity can be increased together with the air pressure decreased, giving a greater lifting force in a stable way.

## CONCLUSIONS

As a technology that has been already adopted on board ships for the purposes of energy saving and emission reduction, sail-assisted propulsion has made remarkable achievements in recent years. In this paper, a new collapsible wing sail with double flaps was proposed, and its aerodynamic performance was studied. The authors investigated the best configuration of parameters and analyzed the aerodynamic performance of the new wing sail using a numerical simulation method. The following results were obtained:

(1) A collapsible wing sail with double flaps was proposed. The maximum lift coefficient of the wing sail reached about 1.68 with the expansion of the two flaps.

(2) The proposed double-flap wing sail gives better performance than the variable-camber, NACA0021 and arc sails.

(3) In order to achieve high performance from the wing sail in most wind directions, it is necessary to consider the best configuration of the parameters for the wing sail.

(4) The thrust coefficient of the wing sail increased with the angle of attack, between 40° and 120°.

From the simulation results, it is clear that the use of our proposed wing sail can easily save energy in terms of ship propulsion, and in future work, we will focus on wind tunnel tests and development of a control system.

## ACKNOWLEDGMENTS

The authors wish to thank the National Natural Science Foundation of China (Grant No. 5150911) and the Natural Science Foundation of Jiangsu Province of China (Grant No. BK2012696) for financial support.

## REFERENCES

- Scupi A., Avital E. J., Dinu D., et al. (2015): *Large Eddy Simulation of Flows around a Kite Used as an Auxiliary Propulsion System*. Journal of Fluids Engineering, Vol. 137(10),1-8.
- Naaijen P., Koster V., Dallinga V.(2006): *On the Power Savings by an Auxiliary Kite Propulsion System*. International Shipbuilding Progress, Vol. 53(4), 255-279.
- Grosan N., Dinu D. (2010): *Considerations Regarding Kite Towed Ship's Manoeuvring*. Proceedings of the 3rd International Conference on Maritime and Naval Science and Engineering, 28-33, WSEAS, Constanta, Romania.
- Li Q., Nihei Y., Nakashima T., Ikeda Y. (2015): *A Study on the Performance of Cascade Hard Sails and Sail-Equipped Vessels*. Ocean Engineering, Vol. 98, 23-31.
- Bergeson L., Greenwald K.C. (1985): *Sail Assists Developments 1979-1985*. Journal of Wind Engineering and Industrial Aerodynamics, Vol. 19(1-3), 45-114.

6. Scott D. (1985): *Sail-Assist for Cargo Ships: Computer Controlled*. Popular Science, Vol. 226, 68(3).
7. Low H. T., Luo S. C., Winoto S. H. (1991): *Flow Past a Wind-assisted Ship Propulsion Device*. Ocean Engineering, Vol. 18(6), 555-565.
8. Ueno M., Tsujimoto M., Takekawa M., Fujita H., et al. (2005): *Fundamental Research for Development of an Advanced Sail-Assisted Ship*. IEEE Techno-Ocean '05, Vol. 2, 1102-1109.
9. Ouchi K., Uzawa K., Kanai A. (2011): *Huge Hard Wing Sails for the Propulsor of Next Generation Sailing Vessel*. The Second International Symposium on Marine Propulsors, Hamburg, Germany, June 2011 .
10. Ouchi K., Uzawa K., Kanai A., Katori M. (2013): "Wind Challenger": *The Next Generation Hybrid Sailing Vessel*. The Third International Symposium on Marine Propulsors, Launceston, Tasmania, Australia, May 2013, 562-567.
11. Burden A., Lloyd T., Mockler S., et al. (2010): *Concept Design of a Fast Sail Assisted Feeder Container Ship*. Main Report of Group Design Project, University of Southampton, School of Engineering Sciences, 58-59.
12. Lin Y.(2013): *Design and Research on a Flap-Wing Sail for a Wind-Assisted Vessel*. Master's thesis, Dalian Marine University, Dalian, China (in Chinese).
13. Guo S.(2012): *Optimized Design of a Wingsail and Study of Energy-Saving Applications for a Sail-Assisted Ship*. Master's thesis, Dalian Marine University, Dalian, China (in Chinese).

## CONTACT WITH THE AUTHORS

### Dongqin Li

*e-mail: mandy\_ldq@163.com*

School of Naval Architecture & Ocean Engineering,  
Jiangsu University of Science and Technology,  
NO.2 Mengxi Road, Jingkou District, 212003 Zhenjiang

**CHINA**

### Yili Zhang

*e-mail: 435356064@qq.com*

Jiangsu University of Science and Technology,  
NO.2 Mengxi Road, Jingkou District, 212003 Zhenjiang,

**CHINA**

### Peng Li

*e-mail: 596293695@qq.com*

Afilicja: Jiangsu University of Science and Technology,  
NO.2 Mengxi Road, Jingkou District, 212003 Zhenjiang,

**CHINA**

### Jingjing Dai

*e-mail: 270397934@qq.com*

Jiangsu University of Science and Technology,  
NO.2 Mengxi Road, Jingkou District, 212003 Zhenjiang,

**CHINA**

### Guohuan Li

*e-mail: 2272658340@qq.com*

Jiangsu University of Science and Technology,  
NO.2 Mengxi Road, Jingkou District, 212003 Zhenjiang,

**CHINA**

# FRAMEWORK OF AN EVOLUTIONARY MULTI-OBJECTIVE OPTIMISATION METHOD FOR PLANNING A SAFE TRAJECTORY FOR A MARINE AUTONOMOUS SURFACE SHIP

Rafał Szłapczyński  
Hossein Ghaemi  
Gdańsk University of Technology, Poland

## ABSTRACT

*This paper represents the first stage of research into a multi-objective method of planning safe trajectories for marine autonomous surface ships (MASSs) involved in encounter situations. Our method applies an evolutionary multi-objective optimisation (EMO) approach to pursue three objectives: minimisation of the risk of collision, minimisation of fuel consumption due to collision avoidance manoeuvres, and minimisation of the extra time spent on collision avoidance manoeuvres. Until now, a fully multi-objective optimisation has not been applied to the real-time problem of planning safe trajectories; instead, this optimisation problem has usually been reduced to a single aggregated cost function covering all objectives. The aim is to develop a method of planning safe trajectories for MASSs that is able to simultaneously pursue the three abovementioned objectives, make decisions in real time and without interaction with a human operator, handle basic types of encounters (in open or restricted waters, and in good or restricted visibility) and guarantee compliance with the International Regulations for Preventing Collisions at Sea. It should also be mentioned that optimisation of the system based on each criterion may occur at the cost of the others, so a reasonable balance is applied here by means of a configurable trade-off. This is done throughout the EMO process by means of modified Pareto dominance rules and by using a multi-criteria decision-making phase to filter the output Pareto set and choose the final solution*

**Keywords:** Maritime autonomous surface ships; evolutionary multi-objective optimisation; ship manoeuvres; fuel consumption; ship collision avoidance

## INTRODUCTION

The concepts of the 'green ship' and autonomous vessels are two fundamental issues discussed in the Blue Growth strategy developed by the EU. This study addresses both of these simultaneously. Many solutions related to unmanned or autonomous ships have already been presented by researchers, including basic control and steering [21, 22, 28] and automatic obstacle detection [9, 30]. Some of these are relatively new, e.g. USV-dedicated risk analysis [43, 44], human factors in the remote control of maritime autonomous surface ships (MASSs) or unmanned surface vehicles (USV) [23]. There are also a number of issues that are not completely novel

but which have been redefined in the context of MASS/USV, such as optimising collision avoidance manoeuvres [28, 31] in compliance with International Regulations for Preventing Collisions at Sea (COLREGS) [2, 5, 7, 24, 27], which is the topic of this paper.

The International Maritime Organisation (IMO) specifies four degrees of autonomy for MASS:

1. *Ship with automated processes and decision support: Seafarers are on board to operate and control shipboard systems and functions. Some operations may be automated.*
2. *Remotely controlled ship with seafarers on board: The ship is controlled and operated from another location, but seafarers are on board.*

3. *Remotely controlled ship without seafarers on board: The ship is controlled and operated from another location. There are no seafarers on board.*
4. *Fully autonomous ship: The operating system of the ship is able to make decisions and determine actions by itself.*

As can be seen, the role of human operators is expected to be reduced in the development of MASSs. It may also be expected that these ships will combine two or more degrees of autonomy. A common feature of all these degrees of autonomy is that a reduction in the role of a human operator means a larger role for the decision-making system on board, which will replace the older concept of a decision support system. Human navigators heavily rely on experience and an intuitive understanding of the ship's behaviour and environmental conditions; in the case of a MASS, all information must be provided and taken into account in a more direct and formal manner. This gives rise to new needs related to data access and processing, and optimisation methods. The required data include at least:

- hydro-meteorological conditions [4],
- ship manoeuvrability and stability-related issues,
- fuel consumption.

Similarly, in terms of optimisation, it is necessary to focus on:

- robust, adaptive and time-efficient methods and algorithms that are adjusted to the needs of MASS,
- modelling and taking into account multiple constraints, including:
  - COLREGS,
  - the limitations of a waterway.

Of these constraints, COLREGS are of particular note. While there are many publications on this topic, the majority of them deal with a limited subset of COLREGS. The exceptions include research [42] done at Massachusetts Institute of Technology that aims to quantify compliance with COLREGS in terms of collision avoidance. However, these researchers omit the issues of navigation within traffic separation schemes (TSSs) or in restricted visibility [35]. It should also be noted that COLREGS will need to be partly revised for use with MASSs. Since the future form of COLREGS remains unspecified, any related method that is developed should be flexible enough to enable configuration and updating with the implemented COLREGS rules.

In terms of optimisation methods, a single-objective approach is largely used in works on collision avoidance [20, 39, 48]. Another approach is to aggregate many criteria into a single cost function by applying weight factors. Both of these techniques have certain limitations, and may be insufficient for collision avoidance applications. Time and fuel consumption are important objectives, and the risk of collision needs to be addressed more fully than it has been in the past. Handling the risk of collision as a single optimisation constraint is an outdated approach, resulting in solutions that are not fully acceptable or applicable. Instead, the risk of collision should be minimised, especially if it can be done at a marginal cost in terms of extra

time and fuel consumption. A true multi-objective approach is therefore considered here. However, the application of this approach to collision avoidance is a scientific challenge due to:

- the longer processing time of this approach compared with single-objective or simplified (aggregated) multi-objective methods,
- the high complexity of the optimisation problem itself (discussed in detail in the following sections),
- the real-time limitations of the computational process in encounter situations (depending on the particular situation, a safe solution needs to be found within one to three minutes).

In view of the above, the aim of the present research is to design and develop a multi-objective method of planning safe trajectories for a MASS involved in encounter situations at sea. Our method will apply an evolutionary multi-objective optimisation (EMO) [1] algorithm to pursue three objectives:

- minimisation of extra time spent on collision avoidance manoeuvres,
- minimisation of fuel consumption due to collision avoidance manoeuvres,
- minimisation of the risk of collision.

The developed method should be able to:

- model a ship's behaviour with a sufficient accuracy for collision avoidance purposes,
- carry out optimisation taking into account three objectives simultaneously (minimisation of time spent on manoeuvring, minimisation of fuel consumption and minimisation of the risk of collision),
- be fast enough for real-time MASS applications and to handle encounters with multiple targets,
- make decisions without interaction with a human operator,
- handle all basic types and circumstances related to ship encounters (including open or restricted waters and good or restricted visibility),
- be compliant with COLREGS in their current form,
- include future updates of COLREGS.

## OUTLINE OF THE PROPOSED METHOD

The proposed method will include modelling part necessary for the correct development and verification of the main optimisation method. A set of mathematical models is needed, since the performance of our multi-objective method must be tested in a near-real computer simulation environment. Unrealistic simplifications are undesirable, as these can reduce the method's computational complexity and computational time, making it unrepresentative. In order to avoid an overly optimistic assessment of the performance of the method, it should also cover the full functional scope of the part of the MASS that is responsible for autonomous decision making in encounter situations. Hence, it must cover:

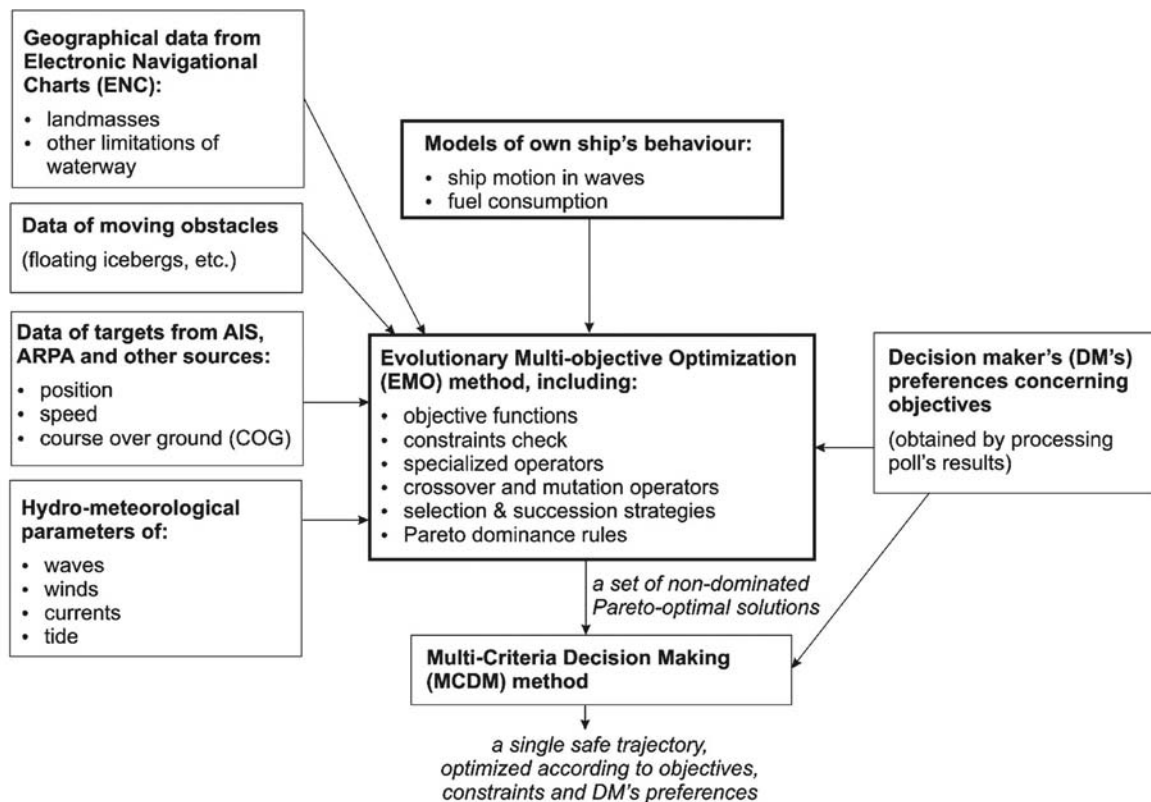


Fig. 1. Outline of the proposed method

1. Mathematical and simulation models of a ship's motion and fuel consumption,
2. An efficient EMO method including multiple problem-driven enhancements and mechanisms,
3. A set of objective functions, constraint-handling functions and various operators that can boost the performance of the EMO method,
4. An application integrating all of the developed elements of the method as a simulation environment software tool.

The proposed method is summarised in Fig. 1.

It is assumed here that the proposed method will cover a lower layer of the integrated navigation system (INS), according to the IMO resolution [10] on avoiding collisions with targets encountered while following a pre-determined route. The routing for the MASS should be done in such a way that heavy traffic areas are avoided as far as possible, in order to reduce the number of encounters. The MASS should also stick to the traffic flow direction within a TSS. If a TSS cannot be avoided, the MASS should cross it in such a way that the existing traffic flow is not affected (keeping safe distances from ships navigating within traffic lanes). An example of this is shown in Fig. 2, which was generated by our prototype software using EasyMap components (the distances in the latitudinal and longitudinal directions are not equal in Fig. 2, due to the geographical projection used by EasyMap).

The remainder of the paper is structured based on the above scheme (Fig. 1) and the assumptions made. Sections 3 and 4 are dedicated to models of the ship's behaviour and the EMO method.

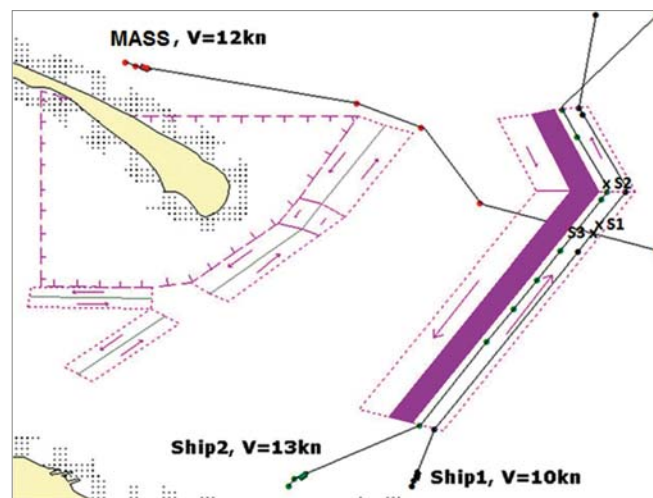


Fig. 2. A MASS crosses lanes of traffic without affecting traffic flow (keeping safe distances from ships within the traffic lanes)

## MATHEMATICAL AND SIMULATION MODELS OF THE SHIP'S MOTION

The development of the model includes several sub-models that allow for unsteady-state analysis under different sea conditions and in different modes of operation.

### MODEL OF THE SHIP'S HULL AND PROPELLER

The functions of the model include determining the longitudinal linear velocity of the ship (surge velocity) with respect to the ship's hull resistance [25], and address the following issues:

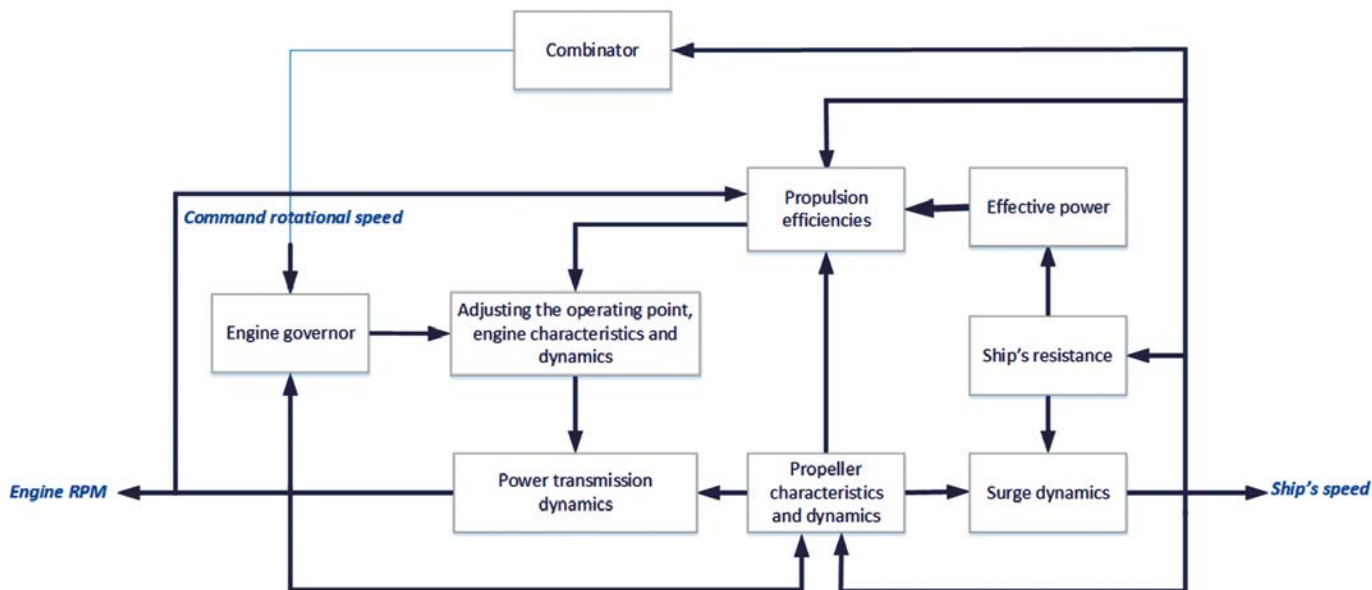


Fig. 3. Block diagram of the models from Tasks 1 and 2: the hull-propeller-engine model

- The resistance of the ship's hull in calm water
- The resistance of the ship's hull in rough sea, including added resistance,
- The characteristics of the propeller, including the advance number, torque and thrust coefficients, wake coefficient and thrust deduction factor,
- The ship's propulsion efficiencies, and the effective and required power,
- The speed of the ship (surge).

The model is summarised in Fig. 3.

### MODEL OF SHIP'S DIESEL ENGINE, GOVERNOR AND PROPELLER PITCH ADJUSTMENT

The unsteady-state behaviour of a diesel engine is considered, particularly in the case where the influence of the governor has significant impact on the ship's motion, and when its interaction with propeller is considered. This model can be applied if a controllable pitch propeller is included in the propulsion system and also when a detailed description of the engine behaviour is required. The main output of this model is the time variation of the torque generated by the engine in response to changes in the command rotational speed. This includes modelling:

- The dynamics of the diesel engine (engine torque),
- The dynamics of the governor (fuel rate into the engine).

A mathematical model of the diesel engine can be constructed based on a quasi-steady concept, and if necessary can then be improved to take into account the thermodynamics and flow regime characteristics of each cylinder, exhaust gas receiver, turbocharger, inlet air manifold, air and exhaust gas valves or ports, and the mechanical parts and shaft dynamics.

The propeller pitch adjustment mechanism is a hydraulic system that is modelled by a full mathematical model of an electro-hydraulic servomechanism. The lower part of Fig. 3 shows a block diagram of modules 1 and 2, while Fig. 4 shows a detailed block diagram of the diesel engine in combination with the propeller, propeller pitch and ship hull dynamics, and their related interactions. To model the crash-stopping test, the time required to reverse the engine shaft rotation and adjust the governor setting should be also considered, although this is not included in the present model.

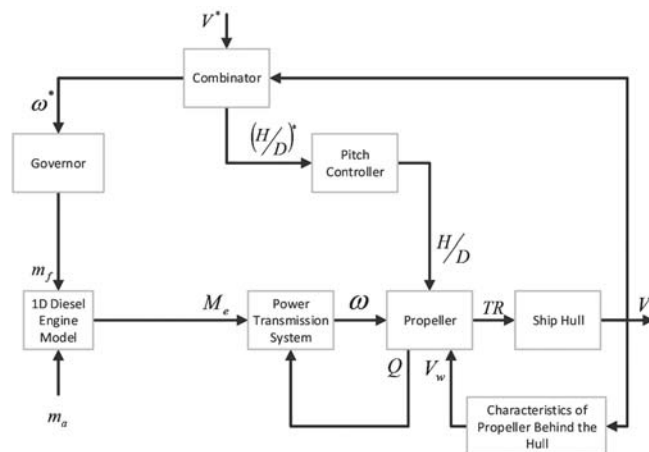


Fig. 4. Combined diesel engine model with the mathematical models of the propeller, hull and propeller pitch adjustment

To ensure that the mathematical model is applicable to a vessel, it was checked by simulating the behaviour of a merchant ship equipped with a slow-speed diesel engine with fixed-pitch propeller, as the command engine rotational speed is changed from 100% to 80% of the normal continuous rating (NCR). The results are presented in Figs. 5–10.

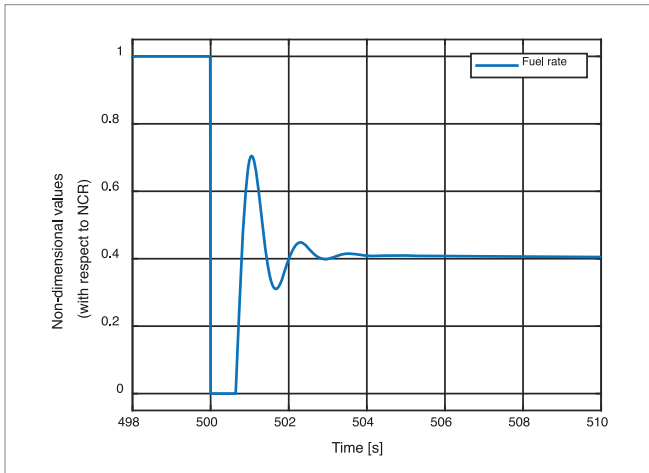


Fig. 5. Fuel rate time series

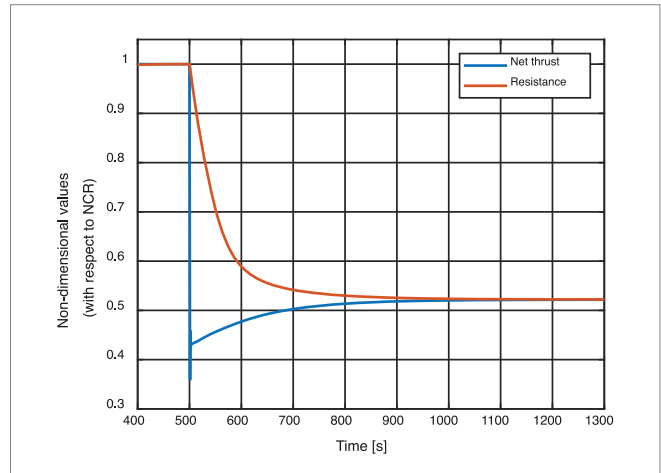


Fig. 8. Time series for net thrust generated by propeller and resistance of the ship

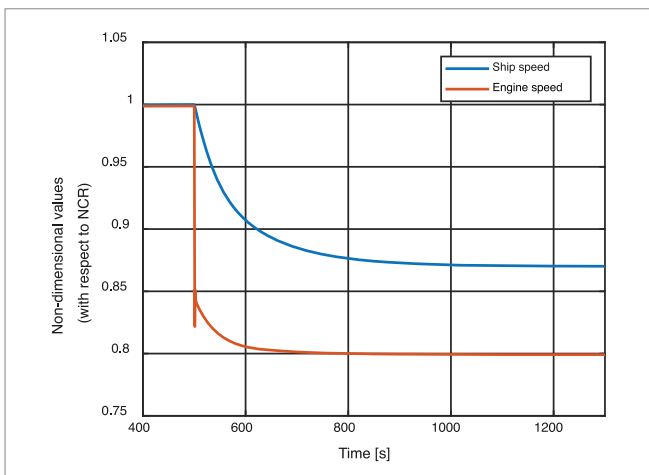


Fig. 6. Time series for the speed of the ship and the rotational speed of the engine

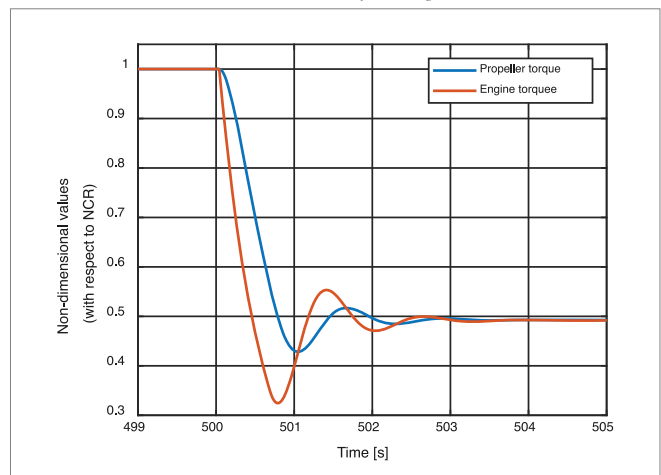


Fig. 9. Time series for propeller and engine torque

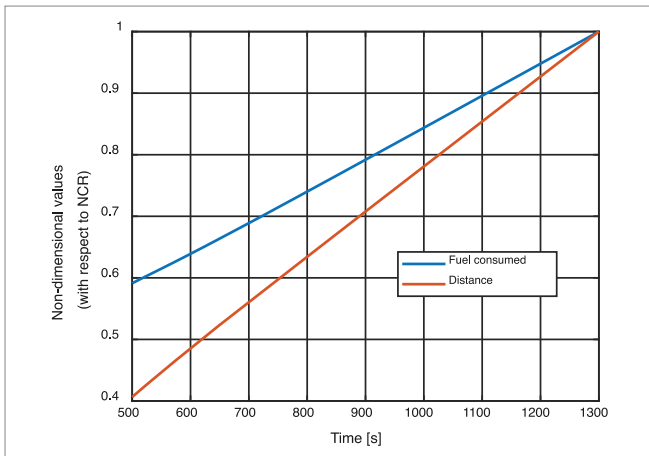


Fig. 7. Time series for fuel consumed and distance covered

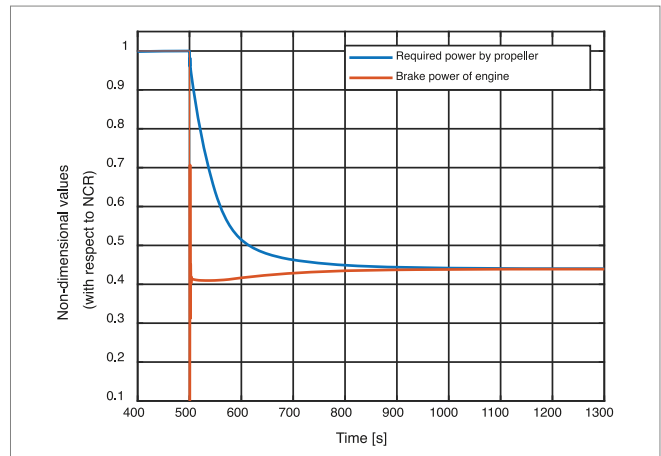


Fig. 10. Time series for power required by propeller and brake power generated by engine

From these results, it is obvious that the propeller and engine need only a few tens of seconds to approach a steady mode, while the ship needs several hundred seconds to come to a steady state. This is due to the very high inertia of the ship in comparison to the engine shaft and propeller. In general, the results seem to be rational and acceptable. For instance, the behaviour of the following pairs:

- net generated thrust by propeller and ship's resistance (Fig. 8),
  - propeller torque and engine torque (Fig. 9),
  - required power by propeller and generated brake power by engine (Fig. 10),
- which become equal in the steady-state condition, confirm the correctness of the calculations and permit the use of this model for further investigations.

## MODEL OF SHIP MANOEUVRES

The previous two sub-sections discussed a mathematical model for the vessel when the rudder angle is fixed and does not change over time. In the case where the rudder angle changes, a manoeuvring model will be conducted and integrated with the previous sub-models, based on which the sway and yaw variables can be coupled to the surge variables. In general, this part includes the modelling of:

- the ship's dynamics and motion for the coupled surge-sway-yaw system,
- the hydrodynamic forces on the ship and their moments,
- motion stability checking of the ship.

The mathematical model of the ship's manoeuvres is nonlinear, and an outline of this model is given in Fig. 11.

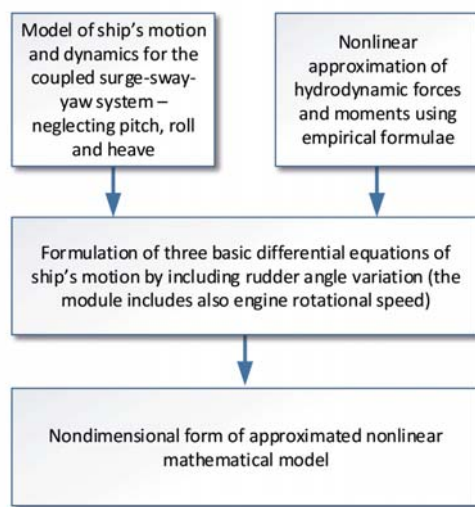


Fig. 11. Outline of the mathematical model of ship manoeuvres

The first module of the model in Fig. 10 (upper left) provides a general nonlinear mathematical model of the ship's motion in the  $xy$ -plane. The second module (upper right) is the most problematic part, particularly when ship is not in calm water. There are several different empirical methods that can be used to model the ship's manoeuvres in calm water, using the so-called hydrodynamic coefficients. For example, Kijima, Fossen, Ankudinov or Lewandowski coefficients can be used [18]. However, in a rough sea, seakeeping analysis should also be provided, and the drift and heading angles should be included. As a result, the position, course and trajectory of the ship will be determined. Alternatively, the simplified model described in [6, 26] can be applied. The model can be verified based on the typical procedures and requirements delivered by ITTC in relation to the manoeuvring tests. The applied mathematical model has the following general form:

$$\begin{aligned}
 m(\dot{u} - vr - r^2x_g) &= X_h + X_r + X_p \\
 m(\dot{v} + ur + x_g\dot{r}) &= Y_h + Y_r + Y_p \\
 I_{zz}\dot{r} + mx_g(\dot{v} + ur) &= N_h + N_r + N_p
 \end{aligned}$$

$$Y_p = 0$$

$$N_p = 0$$

$$X_h + X_r = u \frac{\partial X}{\partial u} + \dot{u} \frac{\partial X}{\partial \dot{u}} + v \frac{\partial X}{\partial v} + \dots$$

$$Y_h + Y_r = u \frac{\partial Y}{\partial u} + \dot{u} \frac{\partial Y}{\partial \dot{u}} + v \frac{\partial Y}{\partial v} + \dots$$

where  $u$  and  $v$  represent the surge and sway velocities, respectively, and  $r$  is the angular velocity around the  $z$ -axis (yaw);  $m$  is the total mass of the ship (including added masses);  $I_{zz}$  is the mass moment of inertia;  $x_g$  is the position of the centre of gravity;  $X$  and  $Y$  are the longitudinal and horizontal hydrodynamic forces;  $N$  is the hydrodynamic moment around the  $z$ -axis; and the indexes  $h$ ,  $r$  and  $p$  denote the hull, rudder and propeller, respectively. The last three variables are functions of the abovementioned velocities and their derivatives (accelerations), as well as the rudder angle  $\delta$ .

These relationships permit to indicate the last but one module in Fig. 11. They are supported and completed using the empirical hydrodynamic coefficients. An approximation is applied when items higher than second order are neglected in the equations. To construct the last module, the forces and moment are non-dimensionalised by dividing by  $\rho L_{pp} Tu/2$  and  $\rho L_{pp}^2 Tu^2/2$ , respectively, and the mass and moment of inertia are non-dimensionalised by dividing by  $\rho L_{pp}^3 T/2$  and  $\rho L_{pp}^4 T/2$ , respectively [8] (where  $T$  is the net thrust,  $\rho$  is the water density and  $L_{pp}$  is the ship's length between perpendiculars).

The propeller rotational speed varies over time and directly influences the change in the surge speed, and should therefore be considered an additional state variable. In this regard, the differential equations in the model of the ship's motion include also changes in the rotational speed of the propeller,  $\omega_p$ , as follows:

$$\dot{\omega}_p(t) = \frac{1}{J_p} [Q_e(t) - Q_p(t) - Q_l(t)]$$

where  $Q_e$ ,  $Q_p$  and  $Q_l$  stand for the engine torque, propeller torque and equivalent torque losses, respectively, and  $J_p$  is the moment of inertia of the propeller, shaft and power transmission elements connected to the propeller.

$Q_p$  can be calculated by the following formula:

$$Q_p(t) = k_Q \rho n(t) |n(t)| D^5$$

in which  $k_Q$  is the propeller torque coefficient (which is given by the manufacturer or determined based on model tests, and depends on the number of blades, advance number, Reynold's number, propeller area coefficient and pitch ratio),  $\rho$  is the density of sea water [ $\text{kg/m}^3$ ],  $D$  is the diameter of the propeller and  $n(t)$  is the rotational speed of the propeller [rps].

$Q_l(t)$  can be determined in relation to the mechanical efficiency of the elements of the power transmission system, including the bearings, coupling, connecting shafts, clutch

and gears, if applied.  $Q_i(t)$  is typically a function of propeller rotational speed, but in a simplified model can be considered to be constant.

The mathematical model of the engine is added to the whole model. The engine model used in this study is the same as that presented in [45], and is therefore not repeated here.

Again, to ensure the viability and accuracy of the model, it is checked using some conventional manoeuvrability tests. An example is the turning circle test [11]. The validity of the manoeuvring models was checked by taking into account the possibility of correcting the hydrodynamic coefficients. The mathematical model was tested for an offshore supply vessel, and the results confirmed the validation of the model (see Fig. 12). The application of the model will allow the manoeuvrability to be taken into account more accurately for all modes of operation, rather than simply the basic mode that has been used in the past to determine a ship's manoeuvrability [47].

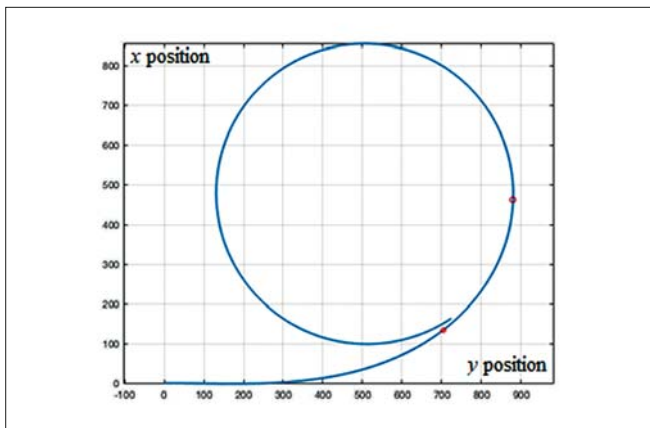


Fig. 12. Characteristics of the turning circle manoeuvre, when the rudder angle is changed by  $35^\circ$

## AN EVOLUTIONARY MULTI-OBJECTIVE OPTIMISATION METHOD FOR PLANNING SAFE SHIP TRAJECTORIES

The fully functional, problem-oriented EMO method will include:

1. A backbone EMO method, which must allow for multiple custom enhancements,
2. A module that is responsible for handling various optimisation constraints by:
  - a. Determining the degree to which they are met by a given ship's trajectory,
  - c. Applying specialised operators that amend unacceptable trajectories so that they satisfy the constraints.

Both of the elements listed above are briefly described in the following sub-sections.

### BACKBONE EMO METHOD

The design of the proposed optimisation is roughly based on the classic Strength Pareto Evolutionary Algorithm 2 (SPEA 2) [49]. To improve the performance of SPEA 2, the

proposed method will include a number of modifications and enhancements. Choosing EMO as the base for the optimisation method makes it possible to find a good representation of a Pareto-optimal set [41], including potential non-convexities [12]. This is a significant advantage compared to aggregated objective evolutionary algorithms, which are unable to find solutions from the non-convex parts of a Pareto set, even when multi-started with modified weights. EMO methods have therefore recently been applied to numerous marine optimisation problems [46]. Another of their advantages is that they make it possible to include the decision maker's (DM's) preferences [19], which allows the designers to focus on the most important part of the objective space, thus reducing the number of analysed solutions while still returning a good representation of a Pareto optimal set as the end result. Multiple approaches to applying the DM's preferences are known, including interaction with the DM or specifying a reference solution; however, most of these are impractical in a collision avoidance context. Interaction during the optimisation process is impossible because of time limits, while a reference solution would require a database of collision avoidance scenarios covering all possible situations; this is practically impossible, and even if available would be flawed due to overestimation or underestimation errors. In the present research, we have developed our own approach based on a trade-off that includes the DM's preferences. This approach is loosely based on the one introduced in [3], but is generalised to cover a given number of objectives. The exact values of the trade-off factors used here can be configured to reflect the voyage mission defined by the ship owners. In practice, this trade-off is of particular importance in collision-avoidance situations, since safety and economy are usually contradictory objectives. Optimising one may occur at the cost of the other, so a reasonable balance by means of a configurable trade-off is essential. The trade-off is applied throughout the EMO process by means of modified Pareto dominance rules as well as in the multi-criteria decision-making (MCDM) phase to filter the output Pareto set and choose the final solution.

The EMO method developed here will cover the three objectives specified in the earlier sections. Of these, particular emphasis must be put here on safety. Traditionally, safety has been taken into account solely as a constraint; for example, solutions that exceed a certain threshold (which is set for a particular type of threat) cannot be accepted, and are thus eliminated from the process. Alternatively, safety can be considered an optimisation criterion and the risk index can be minimised. In the proposed multi-objective approach, this is handled both as a constraint and as one of three criteria. We search for solutions with the lowest possible risk index as well as for solutions that optimise the other two criteria. However, solutions whose risk index exceeds a certain threshold are eliminated, regardless of the values for the other objectives (e.g. fuel consumption), even if they are not Pareto-dominated. This involves quantifying the risk of collision with other ships, and a robust method of determining safe manoeuvres for a specified ship safety domain [36] has been

proposed in [38]. Using this method, safe combinations of course and speed can be found without affecting the method's computational complexity, resulting in a shortening of the overall computational time. The abovementioned approach can be directly applied in the proposed EMO method.

### SHIP TRAJECTORY CODING IN THE EMO METHOD

In this method, each candidate trajectory is represented by an individual in the EMO population. Each individual is defined by a sequence of course changes accompanied by a sequence of times at which the manoeuvre is initiated. This representation allows for a significant reduction in the variable space. Each change in course is a discrete value (in degrees) from the predefined set. By default, the set is:  $\{-60, -55, -50, -45, -40, -35, -30, -25, -20, -15, 0, 15, 20, 25, 30, 35, 40, 45, 50, 55, 60\}$ , and this default 21-element set can be conditionally extended to cover course changes of up to 90° on each side. Limiting each course change to one of 21 possible discrete values can greatly reduce the number of poor quality offspring generated in the evolutionary process. In addition to course changes, the current values of the ship's course are also computed (they are needed for the evaluation of solutions). However, course changes (rather than course values) are used for mutation and crossover operators, in order to ensure that each newly created or modified trajectory is in the format used for acceptable course changes. In this way, we can reduce the probability of generating solutions that are of no practical value. Using discrete course changes throughout the EMO process enables us to reduce the crowding problem and avoid multiple solutions that are too close to each other, and allows redundant solutions to be easily identified and eliminated.

### HANDLING OPTIMISATION CONSTRAINTS

To make sure that the method returns acceptable solutions, we need to check that the optimisation constraints are satisfied. To ensure reasonable progress of the method, we also need to determine the degree to which they are met by a given trajectory for the ship. The most important constraints here are related to:

- avoiding running aground,
- avoiding collisions with stationary obstacles,
- taking into account other limitations of a waterway in restricted areas,
- avoiding collisions with other moving objects,
- compliance with COLREGS.

The first three of these constraints are handled by use of electronic navigational charts (ENCs). This has already been done in EMO methods applied to optimisation problems in marine navigation, such as weather routing [16, 29, 33]. In general, the problem of handling ENC-derived constraints in Evolutionary Algorithms (EA) can be considered solved [40], including in coastal waters [39]. Possible approaches to

this include the direct use of ENCs as vector maps or converting them to bitmaps for use in the optimisation process. We have developed a solution based on the second approach and apply this in the proposed EMO method.

For collision avoidance, it has been shown that both radar and AIS data on targets can be integrated with ENC [14]. In autonomous ships, the accuracy of target tracking is essential, and multiple methods of increasing this accuracy have been proposed [15]. In the proposed method, dealing with collision avoidance as a constraint is done in the same way as for safety as an optimisation objective, as described in Section 4.1. A special problem that is related to collision avoidance is compliance with COLREGS. Some of COLREGS rules that need to be taken into account include the majority of rules from Part B (Steering and Sailing), as listed below.

1. Conduct of a vessel in any visibility conditions:
  - a. Rule 6. Safe speed
  - b. Rule 7. Risk of collision
  - c. Rule 8. Action to avoid collision
  - d. Rule 9. Narrow channels
  - e. Rule 10. Traffic Separation Schemes
2. Conduct of vessels in sight of one another:
  - a. Rule 13. Overtaking
  - b. Rule 14. Head-on situations
  - c. Rule 15. Crossing situations
  - d. Rule 16. The give-way vessel
  - e. Rule 17. The stand-on vessel
  - f. Rule 18. Responsibilities between vessels
3. Conduct of vessel in restricted visibility – Rule 19.

As mentioned in the Introduction, COLREGS will be re-written in the next few years to include MASS. While the exact form of the new rules is unknown, it is reasonable to assume that changes will be made to minimise the impact of new rules on conventional vessels (otherwise, all navigators would have to be retrained to comply with the new regulations). Consequently, we can assume that a MASS will be obliged to act in a similar way to conventional vessels when engaged in an encounter; thus, the current COLREGS will be applied in the proposed method, and these can be updated as soon as the new rules for a MASS are introduced. As of now, there are no current COLREGS rules that would regulate the negotiation of collision avoidance manoeuvres between ships. We therefore assume that a MASS will manoeuvre with no direct ship-to-ship communication other than broadcast and received AIS messages. Another issue is the possibility that a MASS may encounter a conventional (manned) ship that is obliged to give way, but does not do so. An unexpected manoeuvre (noncompliant with COLREGS) by a manned ship may drastically change the navigational situation and result in an immediate collision threat. In both cases, the MASS will need to react quickly, within a shorter time than usually allowed for planning and executing evasive action. In such cases, a multi-objective optimisation of the trajectory of the MASS may not be possible, and a simple evasive action may need to be applied that can be determined automatically by the algorithm used in [37].

To speed up convergence to the optimal Pareto set, a vast array of specialised operators designed to eliminate particular types of problems is used. These operators have previously been designed for the purposes of research by the present authors [35] although this involved a single-objective optimisation problem rather than a multi-objective one. The abovementioned extensions to the EMO method include:

- operators avoiding collisions with other ships,
- operators avoiding grounding, collisions with stationary obstacles and violations of various limitations of a waterway,
- operators avoiding violations of selected COLREGS rules (listed above).

The problem of complying with basic COLREGS rules related to collision avoidance (Rules 6 to 9 and 13 to 18 of COLREGS) [17] was addressed by the main author in [34], and the problem of collision avoidance in restricted visibility (Rule 19 of COLREGS) was addressed in [35]. Navigating within traffic separation schemes (Rule 10 of COLREGS) was examined, and the developed method automatically generated traffic patterns for compliance with particular rules (used at the pre-processing stage of the evolutionary process). Other optimisation techniques have included:

- semi-deterministic operators dedicated to eliminating specified problems of an evolutionarily planned ship trajectory,
- modifications to the traditional scheme of evolutionary operations that can reduce the number of most time-consuming operations.

All of the above result in much greater progress within each generation, and consequently a much faster convergence of the optimisation process. These elements will also be applied in the proposed method. The expected effect is convergence to an acceptable solution within one minute, and further refining of this solution is possible if the situation allows (i.e. there is no immediate danger). In the case of a dangerous situation that has already developed, as observed in [13], a simplified approach referred to as ‘fast reasoning’ is recommended. In this case, fast reasoning can be carried out by reducing the optimisation problem to the single-objective one of minimising collision risk. It is worth noting that the approach proposed here is considered sufficient for successful collision avoidance actions of the ship, although it obviously cannot be applied to the multi-objective synchronisation of multiple ships supervised via a Vessel Traffic Service(VTS) centre.

## SUMMARY AND CONCLUSIONS

The design of a MASS and MASS-related features is one of the most important and challenging topics in today’s marine engineering. It is only a question of time before MASSs are exploited on a large scale, and it is therefore crucial to develop methods that minimise the risk of collision and reduce costs and pollution, which both depend strongly on fuel consumption.

At present, published works on collision avoidance methods (for both manned vessels and MASSs) almost exclusively use a single-objective optimisation approach, making it practically impossible to successfully achieve safety- and economy-related goals at the same time and in parallel. The method presented in this paper represents an attempt to develop such solutions. By applying this method, it is possible to reduce the collision threat as far as possible without a significant increase in the abovementioned costs, which are incurred by the ship-owners and the natural environment alike. The proposed method proves that it is possible and desirable to replace the predominant single-objective optimisation approach to collision avoidance with a truly multi-objective one. Additional research into the modelling of the motion of ships will help in understanding the influence of manoeuvring conditions and sea states on fuel consumption, as well as the interactions induced by the motion of the ship and the environmental variables.

## REFERENCES

1. Bechikh, S., M. Kessentini, L. Ben Said, K. Ghédira: *Preference Incorporation in Evolutionary Multiobjective Optimization: A Survey of the State-of-the-Art*, Adv. Comput. 98 (2015) 141–207.
2. Bertaska, I.R., B. Shah, K. Von Ellenrieder, P. Švec, W. Klinger, A.J. Sinisterra, M. Dhanak, S.K. Gupta: *Experimental evaluation of automatically-generated behaviors for USV operations*, Ocean Eng. 106 (2015) 496–514.
3. Branke, J., T. Kaußler, H. Schmeck: *Guidance in evolutionary multi-objective optimization*, Adv. Eng. Softw. 32 (2001) 499–507.
4. Burmeister, H.-C., W. Bruhn, Ø.J. Rødseth, T. Porathe: *Autonomous Unmanned Merchant Vessel and its Contribution towards the e-Navigation Implementation: The MUNIN Perspective*, Int. J. e-Navigation Marit. Econ. 1 (2014) 1–13.
5. Campbell, S., W. Naeem, G.W. Irwin: *A review on improving the autonomy of unmanned surface vehicles through intelligent collision avoidance manoeuvres*, Annu. Rev. Control. 36 (2012) 267–283.
6. Chroni, Dionysia & Liu, Shukui & Plessas, Timoleon & Papanikolaou, Apostolos. (2015). *Simulation of the maneuvering behavior of ships under the influence of environmental forces*. (2015) 111–120. DOI: 10.1201/b18855-16.
7. Cockcroft, A.N., Lameijer J.N.F.: *A guide to the collision avoidance rules: international regulations for preventing collisions at sea*, Elsevier, 2012.
8. Fossen, T.I.: *Handbook of Marine Craft Hydrodynamics and Motion Control*, John Wiley & Sons, Ltd, Chichester, UK, 2011.

9. Hermann, D., R. Galeazzi, J.C. Andersen, M. Blanke: *Smart sensor based obstacle detection for high-speed unmanned surface vehicle*, IFAC-PapersOnLine. 28 (2015) 190–197.
10. IMO: Resolution MSC.252(83) *Adoption of the Revised Performance Standards for Integrated Navigation Systems (INS)*, Imo - Msc. 252 (2007) 1–49.
11. ITTC: *Final Report and Recommendations to the 24th ITTC*. 24th International Towing Tank Conference, 2005.
12. Jakob, W., C. Blume: *Pareto optimization or cascaded weighted sum: A comparison of concepts*, Algorithms. 7 (2014) 166–185.
13. Jingsong, Z., W. Price: *Automatic collision avoidance systems: Towards 21st century*, in: Dep. Sh. Sci., 2008: pp. 1–10.
14. Kazimierski, W., A. Stateczny: *Radar and Automatic Identification System Track Fusion in an Electronic Chart Display and Information System*, J. Navig. 68 (2015) 1141–1154.
15. Kazimierski, W., G. Zaniewicz, A. Stateczny: *Verification of multiple model neural tracking filter with ship's radar*, in: 2012 13th Int. Radar Symp., IEEE, 2012: pp. 549–553.
16. Krata, P., J. Szlapczynska: *Ship weather routing optimization with dynamic constraints based on reliable synchronous roll prediction*, Ocean Eng. 150 (2018) 124–137.
17. Lazarowska, A.: *A new deterministic approach in a decision support system for ship's trajectory planning*, Expert Systems with Applications, Volume 71, 2017, Pages 469-478, ISSN 0957-4174
18. Lee, H.-Y., S.-S. Shin: *The Prediction of ship's manoeuvring performance In initial design stage*, PRADS Pr. Design Ships Mob. Units. (1998) 666–639.
19. Li, K., K. Deb, X. Yao: *R-Metric: Evaluating the Performance of Preference-Based Evolutionary Multi-Objective Optimization Using Reference Points*, IEEE Trans. Evol. Comput. 22 (2017) 821–835.
20. Li, W., W. Ma: *SIMULATION ON VESSEL INTELLIGENT COLLISION AVOIDANCE*, Polish Marit. Res. 23 (2016) 138–143.
21. Lisowski, J.: *Optimization-Supported Decision-Making in the Marine Game Environment*, in: Mechatron. Syst. Mech. Mater. II, Trans Tech Publications, 2014: pp. 215–222.
22. Lisowski, J.: *Analysis of Methods of Determining the Safe Ship Trajectory*, TransNav, Int. J. Mar. Navig. Saf. Sea Transp. 10 (2016) 223–228.
23. Man, Y., M. Lundh, T. Porathe, S. MacKinnon: *From Desk to Field – Human Factor Issues in Remote Monitoring and Controlling of Autonomous Unmanned Vessels*, Procedia Manuf. 3 (2015) 2674–2681.
24. Naeem, W., S.C. Henrique, L. Hu: *A Reactive COLREGs-Compliant Navigation Strategy for Autonomous Maritime Navigation*, IFAC-PapersOnLine. 49 (2016) 207–213.
25. Olszewski, H., H. Ghaemi: *New concept of numerical ship motion modelling for total ship operability analysis by integrating ship and Environment Under One Overall System*, Polish Marit. Res. 25 (2018) 36–41.
26. Papanikolaou, A., N. Fournarakis, D. Chroni, S. Liu: *Simulation of the Maneuvering Behavior of Ships in Adverse Weather Conditions*, 212 (2016) 11–16.
27. Perera, L.P., J.P. Carvalho, C. Guedes Soares: *Autonomous guidance and navigation based on the COLREGs rules and regulations of collision avoidance*, Adv. Sh. Des. Pollut. Prev. (2010) 205–216.
28. Perera, L.P., L. Moreira, F.P. Santos, V. Ferrari, S. Sutulo, C. Guedes Soares: *A navigation and control platform for real-time manoeuvring of autonomous ship models*, IFAC, 2012.
29. Perera, L.P., C.G. Soares: *Weather routing and safe ship handling in the future of shipping*, Ocean Eng. 130 (2017) 684–695.
30. Polvara, R., S. Sharma, J. Wan, A. Manning, R. Sutton: *Obstacle Avoidance Approaches for Autonomous Navigation of Unmanned Surface Vehicles*, J. Navig. (2017) 1–16.
31. Praczyk, T.: *Neural anti-collision system for Autonomous Surface Vehicle*, Neurocomputing. 149 (2015) 559–572.
32. Stateczny, A.: *Neural Manoeuvre Detection of the Tracked Target in ARPA Systems*, IFAC Proc. Vol. 34 (2001) 209–214.
33. Szlapczynska, J.: *Multi-objective Weather Routing with Customised Criteria and Constraints*, J. Navig. 68 (2015) 338–354.
34. Szlapczynski, R.: *A new method of planning collision avoidance manoeuvres for multi-target encounter situations*, J. Navig. 61 (2008) 307–321.
35. Szlapczynski, R.: *Evolutionary planning of safe ship tracks in restricted visibility*, J. Navig. 68 (2015) 39–51.
36. Szlapczynski, R., J. Szlapczynska: *A Simulative Comparison of Ship Domains and Their Polygonal Approximations*, TransNav, Int. J. Mar. Navig. Saf. Sea Transp. 9 (2015) 135–141.
37. Szlapczynski, R., J. Szlapczynska: *A Target Information Display for Visualising Collision Avoidance Manoeuvres in Various Visibility Conditions*, J. Navig. 68 (2015) 1041–1055.

38. Szlapczynski, R., J. Szlapczynska: *A method of determining and visualizing safe motion parameters of a ship navigating in restricted waters*, Ocean Eng. 129 (2017) 363–373.
39. Tsou, M.C.: *Integration of a geographic information system and evolutionary computation for automatic routing in coastal navigation*, J. Navig. 63 (2010) 323–341.
40. Tsou, M.C.: *Multi-target collision avoidance route planning under an ECDIS framework*, Ocean Eng. 121 (2016) 268–278.
41. Utyuzhnikov, S. V., P. Fantini, M.D. Guenov: *A method for generating a well-distributed Pareto set in nonlinear multiobjective optimization*, J. Comput. Appl. Math. 223 (2009) 820–841.
42. Woerner, K., M.R. Benjamin, M. Novitzky, J.J. Leonard: *Quantifying protocol evaluation for autonomous collision avoidance: Toward establishing COLREGS compliance metrics*, Auton. Robots. (2018) 1–25.
43. Wrobel, K., P. Krata, J. Montewka, T. Hinz: *Towards the Development of a Risk Model for Unmanned Vessels Design and Operations*, Int. J. Mar. Navig. Saf. Sea Transp. 10 (2016) 267–274.
44. Wróbel, K., J. Montewka, P. Kujala: *Towards the assessment of potential impact of unmanned vessels on maritime transportation safety*, Reliab. Eng. Syst. Saf. 165 (2017) 155–169.
45. Zeraatgar, H., M.H. Ghaemi: *The Analysis of Overall Ship Fuel Consumption in Acceleration Manoeuvre Using Hull-Propeller-Engine Interaction Principles and Governor Features*, Polish Marit. Res. 26 (2019) 162–173.
46. Zhang, Z., C. Lee: *Multiobjective Approaches for the Ship Stowage Planning Problem Considering Ship Stability and Container Rehandles*, IEEE Trans. Syst. Man, Cybern. Syst. 46 (2016) 1374–1389.
47. Zhao-Lin, W.: *Quantification of Action to Avoid Collision*, J. Navig. 37 (1984) 420–430.
48. Zhou, K., J. Chen, X. Liu: *Optimal Collision-Avoidance Manoeuvres to Minimise Bunker Consumption under the Two-Ship Crossing Situation*, J. Navig. (2019) 151–168.
49. Zitzler, E., M. Laumanns, L. Thiele: *{SPEA2}: Improving the {Strength} {Pareto} {Evolutionary} {Algorithm}*, EUROGEN 2001. Evol. Methods Des. Optim. Control with Appl. to Ind. Probl. (2002) 95–100.

## CONTACT WITH THE AUTHORS

**Rafał Szlapczyński**

*e-mail: rafal.szlapczynski@pg.edu.pl*

Gdańsk University of Technology  
Narutowicza 11/12, 80-233 Gdańsk  
**POLAND**

**Hossein Ghaemi**

*e-mail: ghaemi@pg.edu.pl*

Gdańsk University of Technology  
Narutowicza 11/12, 80-233 Gdańsk  
**POLAND**

# REVIEW OF WEATHER FORECAST SERVICES FOR SHIP ROUTING PURPOSES

Marcin Życzkowski<sup>1</sup>

Joanna Szłapczyńska<sup>2</sup>

Rafał Szłapczyński<sup>1</sup>

<sup>1</sup> Gdańsk University of Technology, Poland

<sup>2</sup> Gdynia Maritime University, Poland

## ABSTRACT

*Weather data is nowadays used in a variety of navigational and ocean engineering research problems: from the obvious ones like voyage planning and routing of sea-going vessels, through the analysis of stability-related phenomena, to detailed modelling of ships' manoeuvrability for collision avoidance purposes. Apart from that, weather forecasts are essential for passenger cruises and fishing vessels that want to avoid the risk associated with severe hydro-meteorological conditions. Currently, there is a wide array of services that offer weather predictions. These services include the original sources – services that make use of their own infrastructure and research models – as well as those that further post-process the data obtained from the original sources. The existing services also differ in their update frequency, area coverage, geographical resolution, natural phenomena taken into account and finally – output file formats. In the course of the ROUTING project, primarily addressing ship weather routing accounting for changeable weather conditions, the necessity arose to prepare a report on the state-of-the-art in numerical weather prediction (NWP) modelling. Based on the report, this paper offers a thorough review of the existing weather services and detailed information on how to access the data offered by these services. While this review has been done with transoceanic ship routing in mind, hopefully it will also be useful for a number of other applications, including the already mentioned collision avoidance solutions.*

**Keywords:** marine gas turbine, inlet air fogging, applicability

## INTRODUCTION

Weather conditions have been taken into account in route planning since the very beginning of marine navigation. Already in the mid-XIXth century, for the first time in history a large compilation of climatology data in the form of weather and currents of the world was made public to the marine community. The data was combined from ships' log books into the "Wind and Current Chart of the North Atlantic" by Matthew F. Maury in 1847. At that time, in many cases seasonally recommended routes from Maury's charts allowed for significant passage reductions. His achievement has been further continued by other researchers and more recently, in the XXth century, taken over by the British Admiralty, US Navy and some meteorological groups. Publications such as Admiralty Ocean Passages for the World or the Navy's

Pilot Charts accompanied by historical weather data were the first and basic resources for route planning in the last century. Since the mid-XXth century, route planning taking into account weather conditions, nowadays also known as weather routing (especially for long-distance such as trans-Atlantic routes), has been additionally supported by numerical weather predictions. These days such predictions are made available via the internet in the form of special file formats (GRIB1, GRIB2 or netCDF). Meanwhile, special tools and methods have been created to support route optimisation (originally single-objective ones in terms of passage time or fuel consumption minimisation) by using numerical predictions.

The first methodological approach to weather routing, initially proposed for manual use, was the isochrone method [9]. It was based on geometrically determined and recursively defined time fronts (isochrones) to find time-optimal routes.

## RESEARCH BACKGROUND – SHIP WEATHER ROUTING ACCOUNTING FOR CHANGEABLE WEATHER CONDITIONS

In the next decades, computer implementations of the method were developed, as in [7]. There are also other approaches to weather routing: dynamic programming for a grid of points has been proposed in [14,29] and in a 3D version in [5,28]. As presented in [2], solving a specified optimal control problem allows for finding the time-optimal path. Another approach using the extended single-objective Dijkstra algorithm was presented in [11,12]. A multi-objective approach brings new qualities to weather routing by making it possible to optimise more than one criterion at a time. A simplified multi-objective approach to route planning with aggregation to a single criterion has been proposed in [24]. However, a purely mathematical approach to such optimisation with Pareto-optimal sets has been proposed so far by [8,13,20,21,25,30,31].

The importance of numerical weather predictions is increasing lately due to significant changes in seasonal weather trends on the one hand and the improved ability to predict weather dynamics on the other. Modelling of ship and environment interaction is becoming more realistic due to the use of sophisticated numerical tools. Dealing with severe weather conditions has been addressed by many authors. More accurate weather forecasts for marine purposes have been described in [15, 17], among others. Research on the wave climate along the North Atlantic routes has been provided in [27]. A related work on weather conditions for the European coast has been done in [26]. Harsh weather and its impact on ship routing and navigation has been discussed in [3, 4, 6, 16]. Similarly, the impact on ships' behaviour and safety was researched in [1, 10, 19], the application to collision avoidance in [22] and routing of sailing vessels in [23, 30, 31]. In general, it might be safely stated that weather data is nowadays used in a majority of navigational and ocean engineering research problems.

Apart from that, weather forecasts are essential for passenger cruises and fishing vessels that want to avoid the risk associated with severe hydro-meteorological conditions. Currently, there is a wide array of services that offer weather forecasts. They include the original sources – which make use of their own infrastructure and research models – as well as those that further post-process the data obtained from the original sources. The existing services also differ in their update frequency, area coverage, geographical resolution, natural phenomena taken into account and finally – output file formats. The paper offers a thorough review of the existing weather services and detailed information on how to access the data offered by those services.

The rest of the paper is organised as follows. The background of the research, including a brief description of a current weather routing project, has been provided in Section 2. A classification of weather services is presented in Section 3, followed by a discussion on the optimal choice of weather data for ship routing in Section 4. The details of the selected data sources and data formats are given in Section 5 and finally the summary and conclusions are presented in Section 6.

The project entitled “Ship Routing Accounting for Changeable Sea Conditions” (acronym ROUTING, funding schema: ERA-NET Cofund MarTERA-1, call 2017) [32] aims at developing a new type of ship weather routing, based on the research presented in [21]. In this project state-of-the-art robust route optimisation methods are to be applied, and selected sources of uncertainty related to weather predictions are also taken into account. What is more, live ship and weather parameter measurements provided by on-board installed instruments are to be utilised to improve both ship modelling and weather predictions (by means of data assimilation). The primary goal of the ROUTING project is to design, develop and test on-board a prototype of such weather routing system during a 6-month voyage.

The system is to comprise of three key elements:

- Ship handling DSS (decision support system),
- Weather routing DSS, Transmission module supporting ship–shore–ship data transmission (via cost-optimised Wi-Fi/GSM/satellite connection, where applicable).

The ship handling DSS is to be responsible for continuous on-board measurements and generating alerts in case of dangerous operations. The DSS will include devices for:

registering the motions in the six-degrees of freedom (6 DoF),

- estimating fuel consumption,
- monitoring hull stresses,
- monitoring current weather conditions,
- associating the measurements with a specific ship position and speed.

The DSS will introduce also its own, separate GPS measurements in order to improve the position accuracy [18] of stored information.

The weather routing DSS will in turn optimise the routes while taking into account the previous DSS data and weather predictions. The DSS will allow the exploitation of the information provided by the ship handling DSS in terms of improved ship modelling and accuracy of the weather forecast. The DSS will implement a state-of-the-art evolutionary multi-objective method (EMO) for robust route optimisation. Three optimisation criteria (passage delay, fuel consumption and safety of passage) will be constrained by eight optimisation constraints addressing ship stability and the safety of crew and cargo, among others.

It has been decided that, among various sources of uncertainties in the process of ship route optimisation, the key weather forecasted wave parameter, namely significant wave height, will be considered during optimisation as an ensemble forecast (i.e. a vector of forecasts). Such ensemble is a vector of the forecasted values of the same weather parameter created by a stochastic approach with the adoption of random model perturbation. The ensemble forecast approach means that the predicted weather conditions are described, instead of a single predicted value, by a vector of such values, usually equally

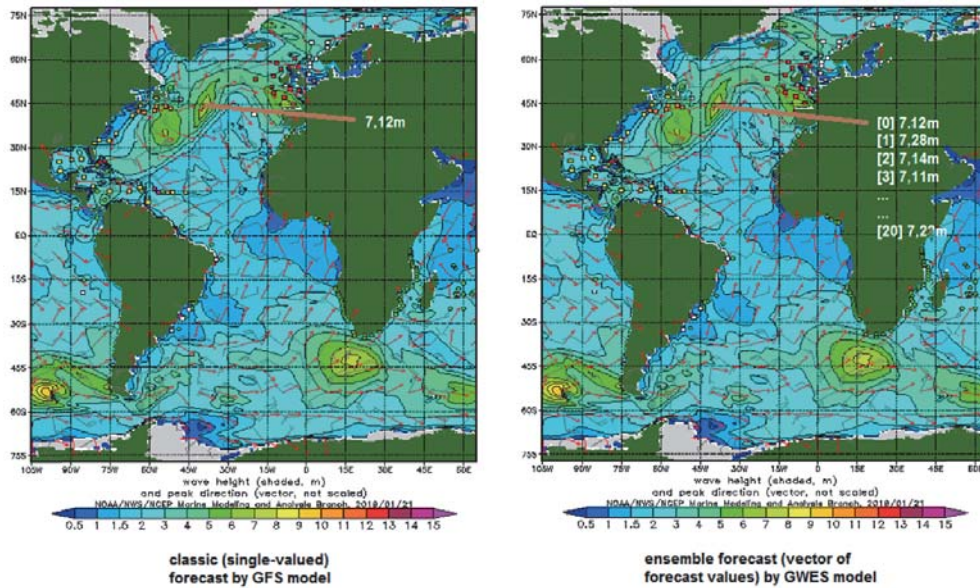


Fig. 1. Illustrative comparison of a single forecast (source: NOAA GFS model data) and ensemble forecast (source: NOAA GWES model data) for significant wave height  $H_s$

probable. It is worth noting that so far there is no robust method available for incorporating ensemble forecasts into the ship weather routing process. Designing and developing such a method will be one of the key challenges in the course of this project.

During the initial phase of the ROUTING project, research on the available weather forecast services, providing forecasts of the assumed weather parameters, accuracy and covering the area of the expected sea trial of the prototype (North Atlantic) was conducted. The following weather parameters are expected to be gathered on the project's weather server:

- wave forecasts:
  - significant wave height (as ensemble forecast),
  - peak wave period,
  - mean wave direction;
- wind forecasts: U- and V- speed components;
- ocean currents: U- and V- speed components.

The next sections provide details on the available weather services and their suitability for the needs of the ROUTING project.

## OVERVIEW OF WEATHER SERVICES

Meteorological services deal with archiving, but also the analysis of received meteorological measurements. The services can provide various hydro-meteorological data and forecasts, with wind, sea waves and sea currents, among others. The main task of the services includes creating and disseminating forecasts or reports on the current state of the meteorological situation in a commercial or non-profit way. Some meteorological services use their own data sourced from measuring buoys and stations or from satellite images, while others use external data sources. The weather forecasting process nowadays is realised based on numerical weather prediction (NWP) models. With this approach, the weather

situation can be described using a mathematical description provided with a digital file. NWP models are constantly being developed by significant weather services. This mathematical description of the weather situation can be saved in various digital formats (GRiB1, GRiB2 or netCDF), provided they are acceptable to WMO (the World Meteorological Organisation). The metadata of this digital file contains information on the originating centre defined in accordance with WMO standards.

Some of the meteorological services are originating centres, meaning that they use their own measurement sources to broadcast weather forecasts. There are also services that modify existing numerical models, increasing their accuracy and resolution. Another important factor is the range of meteorological services: global (covering the entire world) and local ones. It is worth emphasising that local description usually presents the weather situation using numerical models with a denser description grid, thus offering higher accuracy. Some of the weather services specialise in offering various meteorological and hydrological products. These products can be extracted as forecasts, archive data and current data. Forecasts can be of varying duration, with different transmission and updating frequencies. They are usually created in a deterministic fashion (one forecast value to describe the meteorological situation at a given point in space and time), although ensemble forecasts are becoming increasingly popular. As an illustration between the classic and ensemble approach, a comparison of a single-valued (classic) forecast by the NOAA GFS model and an ensemble approach by the NOAA GWES model for significant wave height ( $H_s$ ) forecasts is provided in Fig. 1.

## WEATHER FORECASTS FOR SHIP ROUTING

The meteorological services disseminate the necessary weather information for many sectors of the economy to carry out specialised tasks. In this paper we will discuss weather services that disseminate information about current and forecasted meteorological conditions needed in shipping, with a focus on ship routing. Ship routing and monitoring is carried out on the basis of ships' manoeuvring data and sea conditions. In this case, it is assumed that the sea conditions are determined by the parameters of wind (speed and direction given directly or via U- and V- components of speed), wave (period, height and direction) and sea currents (speed and direction given directly or via U- and V- components of speed). What is more, the wave parameters such as significant wave height can be determined based on the ensemble approach. The research area covered here (for the purpose of the ROUTING project) is limited to the North Atlantic.

The factors taken into account when selecting a particular weather service include:

- geographical coverage,
- availability of particular hydro-meteorological data (wind, waves, sea currents) for the considered basin (North Atlantic),
- data access costs (where applicable),
- resolution of data occurrence,
- length and frequency of issuing forecasts,
- data formats,
- origin of the provided data, and,
- the experience and overall esteem of a meteorological service.

The aforementioned factors were noted on the basis of available information on the websites and metadata of the forecast description files (GRiB2) of selected weather services. Below we list the characteristics of a few selected weather services, including the organisation, its structure experience,

the role it plays in the World Meteorological Organisation and what type of meteorological data is available.

### THE NATIONAL OCEANIC AND ATMOSPHERIC ADMINISTRATION (NOAA), [HTTP://POLAR.NCEP.NOAA.GOV/](http://polar.ncep.noaa.gov/)

NOAA is an agency, under the US Department of Commerce, involved in daily weather forecasts, severe storm warnings, and climate monitoring for fisheries management, coastal restoration and supporting marine commerce. The National Centers for Environmental Prediction (NCEP) within NOAA are responsible for providing weather, hydrologic and climate forecasts. This service belongs to WMO, officially identified there under the number 7. NCEP contains nine distinct centres, which are characterised by a large variety of services and products. There are special sub-centres specialising in predicting meteorological conditions for the sea (Ocean Prediction Center and the Aviation Weather Center), but also in space (Space Weather Prediction Center). The Storm Prediction Center (SPS) and Tropical Hurricane Resort in Miami, Florida (NHPC) predict meteorological threats such as tornadoes, strong storms, lightning and fires. The Environmental Modeling Center (EMC) develops and improves numerical weather, climate, hydrological and ocean prediction. This centre operates and maintains more than 20 numerical prediction systems, including GFS, GEFS, SREF and CFS. The Central Operations NCEP manages the flow of data and meteorological products in the organisation. This centre is responsible for preparing NCEP products for dissemination. Products include traditional deterministic forecasts, as well as ensemble forecasts. The models of particular interest in this service include: GFS, Multi-grid Wave, GWES and RTFOS model. All data sources are produced by NOAA. The file format is GRiB2 except for the currents data, which is stored in netCDF format.

Tab. 1. The National Oceanic and Atmospheric Administration (NOAA), <http://polar.ncep.noaa.gov/>

Model	Data type	Resolution	Forecast runs	Forecast time step / interval	Forecast length	Area
GFS	wind	0.25° x 0.25	4 times a day: 0000, 0600, 1200, 1800 UTC	1h / <120h, 3h / 120h-180h 12h / 180h-384h	384 h	Latitude max: 90° Latitude min: -90° Longitude min: -180° Longitude max: 180°
Multi-grid Wave	waves	0.5° x 0.5°	4 times a day: 0000, 0600, 1200, 1800 UTC	1h / <120h, 3h / 120h-180h	240 h	Latitude max: 90° Latitude min: -77.5° Longitude min: -180° Longitude max: 180°
GWES	waves (ensemble)	0.5° x 0.5°	4 times a day: 0000, 0600, 1200, 1800 UTC	240h ensemble forecast: 1 control + 20 perturbed members	240 h	Latitude max: 90° Latitude min: -77.5° Longitude min: -180° Longitude max: 180°
RTFOS	currents	(1/12)° x (1/12)°	once a day		72h	Global

**THE EUROPEAN CENTRE FOR MEDIUM-RANGE WEATHER FORECASTS (ECMWF), [HTTPS://WWW.ECMWF.INT/EN/FORECASTS](https://www.ecmwf.int/en/forecasts)**

ECMWF is an organisation that coordinates two services from the EU's Copernicus Earth observation programme: the Copernicus Atmosphere Monitoring Service (CAMS) and the Copernicus Climate Change Service (C3S). ECMWF belongs to WMO, where it is identified with the number 98. ECMWF is based in Reading, UK, has 22 Member States and 12

Tab. 2. The European Centre for Medium-Range Weather Forecasts (ECMWF), <https://www.ecmwf.int/en/forecasts>

Model	Data type	Resolution	Forecast runs	Forecast time step / interval	Forecast length	Area
HRES	wind	0.125° x 0.125°	4 times a day 0000, 0600, 1200, 1800 UTC	1h / <90h 3h / 90h - 144h 6h / 144h - 240h	240h	Global
HRES-WAM	waves	0.125° x 0.125°	4 times a day 0000, 0600, 1200, 1800 UTC	1h / <90h 3h / 90h - 144h 6h / 144h - 240h	240h	Global
ENS-WAM	waves (ensemble)	0.25° x 0.25°	2 times a day 0000, 1200 UTC	3h / <144h 6h / 144h - 360h	360h	Global

Co-operating States (Poland is not included). It is one of six members of the Co-ordinated Organisations (NATO, CoE, ESA, OECD, EUMETSAT). Primarily, this is a research institute and an operational service, producing and disseminating global numerical weather predictions and other data. The tasks also include the archiving of meteorological data and carrying out scientific and technical research to improve forecasting skills. When considering global forecasts, ECMWF takes into account ensemble-based analyses and predictions. There is free access to all services provided and output data is stored in GRIB2 format.

Tab. 4. The German Weather Service (DWD), <https://www.dwd.de/en>

Model	Data type	Resolution	Forecast runs	Forecast time step / interval	Forecast length	Area
ICON	wind	7km x 7km	2 times a day 0000, 1200 UTC	1h / <78h 3h / 78h-120 h	120h	Local: Europe
WAM	waves	7km x 7km	2 times a day 0000, 1200 UTC	1h / <78h 3h / 78h-120 h	120h	Local: North Europe
Cosmo	wind	2.8km x 2.8km	2 times a day 0000, 1200 UTC	1h / <27h	27h	Local: North Europe

**EU COPERNICUS, [HTTP://MARINE.COPERNICUS.EU/SERVICES-PORTFOLIO/ACCESS-TO-PRODUCTS/](http://marine.copernicus.eu/services-portfolio/access-to-products/)**

Copernicus is the European Union's Earth Observation Programme based on satellite Earth observation (6 satellites). The organisation includes, among others, a marine service that provides its own archive and prediction of marine data. The marine service includes two different types of centres. The first one – Thematic Data Assembly Centres, collect marine data using satellite and in situ observations in real time. The second one – Monitoring and Forecasting Centres (MFC), generate reanalyses (20 years back), analyses (current) and 10-day forecasts of the ocean. The Copernicus Programme receives data, products and support services from EUMETSAT. EUMETSAT manages the EU space segment and belongs to the originating centre WMO list, where it is listed as number 254. There is free access to all services using own source data. Data is stored in netCDF format.

Tab. 3. EU Copernicus, <http://marine.copernicus.eu/services-portfolio/access-to-products/>

Model	Data type	Resolution	Forecast runs	Forecast time step / interval	Forecast length	Area
NEMO	waves, currents	.083° x .083°	daily 1200 UTC	1h / <120h	120h	89°S-90°N
NEMO	waves, currents	.25° x .25°	daily 1200 UTC	1h / <120h	120h	83oS-89.75oN

**THE GERMAN WEATHER SERVICE (DWD), [HTTPS://WWW.DWD.DE/EN](https://www.dwd.de/en)**

Germany's National Meteorological Service, with headquarters located in Offenbach, belongs to the WMO originating centre list as number 78. The numerical weather prediction (NWP) model developed by this organisation is

called ICON. DWD is one of only fourteen weather services in the world running a global numerical weather prediction (NWP) model. DWD belongs to COSMO (the Consortium for Small-scale Modelling). Its general goal is to develop, improve and maintain a non-hydrostatic limited-area weather data model, called COSMO. DWD marine services produce both deterministic and probabilistic ocean data predictions. There is free access to all services using its own source data. Data is stored in GRiB2 format.

**JAPANESE METEOROLOGICAL AGENCY,  
[HTTPS://WWW.JMA.GO.JP](https://www.jma.go.jp)**

The Japanese Meteorological Agency is the national weather service of Japan. It includes the Meteorological Research Institute, Meteorological Satellite Center, Aerological Observatory, Kakioka Magnetic Observatory, and Meteorological College. It belongs to WMO under number 34. This service produces and disseminates meteorological deterministic and ensemble forecast data. It develops its own numerical weather prediction models, as follows: GSM, MSM, LFM and GEPS. This service mainly distributes meteorological products for Asia. There is free access to all services using its own source data. Data is stored in GRiB2 format.

**ATMOSPHERIC MODELING AND  
 WEATHER FORECASTING GROUP -  
 AM&WFG (NATIONAL & KAPODISTRIAN  
 UNIVERSITY OF ATHENS), [HTTP://  
 FORECAST.UOA.GR/WAMINFO.PHP](http://forecast.uoa.gr/waminfo.php)**

A group of scientists from the Kapodistrian University of Athens have been operating for 25 years on the development of their own models of weather description. This service mainly provides forecasts for the Mediterranean Sea. The meteorological service participates in the creation of numerical model predictions: SKIRON and RAMS, based on the data received from NCEP. There is free access to all services using NOAA source data. Data is stored in GRiB2 format.

**THEYR PRECISION WEATHER PLANNER,  
[HTTPS://WWW.THEYR.COM/INDEX.ASP](https://www.theyr.com/index.asp)**

This company is responsible for the commercial delivery of high-precision weather and ocean forecasts. It produces its forecasts using the WRF system model using NOAA data. There is payable access to all services using NOAA source data. Data is stored in GRiB2 format.

Tab. 5. Japanese Meteorological Agency, <https://www.jma.go.jp>

Model	Data type	Resolution	Forecast runs	Forecast time step / intrval	Forecast length	Area
GSM	wind, waves	0.1875 x 0.1875	3 times a day 0000, 0600, 1800 UTC	-	134h	Global
GEPS	waves (ensemble: 13 members)	0.5625 x 0.5625	2 times a day 0000, 1200 UTC	Twice a week / <34 days	34 days	Global

Tab. 6. Atmospheric Modeling and Weather Forecasting Group - AM&WFG (National & Kapodistrian University of Athens), <http://forecast.uoa.gr/waminfo.php>

Model	Data type	Resolution	Forecast runs	Forecast time step/ interval	Forecast length	Area
SKIRON	wind, waves	0.1° x 0.1°	-	3h / <120h	120h	Local: Europe

Tab. 7. Theyr Precision weather planner, <https://www.theyr.com/index.asp>

Model	Data type	Resolution	Forecast runs	Forecast time step	Forecast length	Area
NOAA-WRF	wind, waves	0.01° x 0.01°	-	1, 3 or 6 hours	6 days	Local

**METEO CONSULT, [HTTPS://MARINE.METEOCONSULT.CO.UK/](https://marine.meteoconsult.co.uk/)**

The METEO CONSULT service disseminates meteorological data using NOAA data sources. It is a private company providing services in forecasting the weather for the maritime sector. There is mostly free access to all services using NOAA source data. Data is stored in GRiB2 format.

**EXPEDITION 10, [HTTP://WWW.EXPEDITIONMARINE.COM/EGRIB.HTML](http://www.expeditionmarine.com/egrrib.html)**

This organisation offers tactical and navigation software, which is dedicated to well-known regattas. Expedition has been in development since the mid-1990s by veteran Volvo Ocean Race navigator and Whitbread winner Nick White. It offers WRF weather models mainly for the Australian coast. There is free access to all services using NOAA source data. Data is stored in GRiB2 format.

**THE TIDETECH GROUP, [HTTPS://TIDETECHMARINEDATA.COM/](https://tidetechmarinedata.com/)**

This is a private weather service, which disseminates data from NOAA and Copernicus, but also disseminates sources of the Sri Lankan meteorological centre (<http://www.meteo.slt.lk>), centre 131 of WMO. This service provides free access in a demo version and full functionality as commercial services. All of its services use NOAA source data. Data is stored in GRiB2 format.

When selecting the appropriate weather service for the purposes of the ROUTING project, the content of the abovementioned tables was verified in the context of the credibility of the organisation and the usefulness of specific data sources. In addition, the ease of access to individual data sources was verified. After the analysis, the following choices have been made.

- Wind: GFS model from NOAA,
- Waves: from NOAA sources
  - mean wave direction and wave period between peaks from the Multi-grid Wave model,
  - ensemble forecast significant wave height from the GWES model,
- Sea currents: Real Time Ocean Forecast System from NOAA.

It must be mentioned here that, when it comes to data sources on ocean currents, some services offer historical archive data instead of forecasts. One such archive-based source is Ocean Surface Current Analysis Real-time (OSCAR), developed by NASA. In practice, such data is useful for estimating seasonal changes of sea currents, but it might not be sufficient as a source for weather routing (where accurate long-term forecasts are needed) or for collision avoidance (where up-to-date data or short-term forecasts are necessary).

**SELECTED WEATHER DATA MODELS**

The selected weather data models (GFS, Multi-grid Wave and GWES from NOAA) are presented in detail in the following sub-sections.

*Tab. 8. Meteo Consult, <https://marine.meteoconsult.co.uk/>*

Model	Data type	Resolution	Forecast runs	Forecast time step / intrval	Forecast length	Area
GFS	wind	4km x 4km	-	-	-	Local: Europe

*Tab. 9. Expedition 10, <http://www.expeditionmarine.com/egrrib.html>*

Model	Data type	Resolution	Forecast runs	Forecast time step / intrval	Forecast length	Area
NOAA-WRF	wind, waves	0.1° x 0.1° 0.03° x 0.03°	-	1h / <72h 0.5h / <36h	72h 36h	Local: coast of Australia, Europe, China

*Tab. 10. The Tidetech Group, <https://tidetechmarinedata.com/>*

Model	Data type	Resolution	Forecast runs	Forecast time step / intrval	Forecast length	Area
NOAA-WRF	wind, waves, currents	0.1-0.02°	2 times a day	3h / <120h	120h	Global

## THE GFS MODEL FROM NOAA

The GFS model provides wind data and is available on the Nomads server (administrated by NOAA), under the access link:

<http://nomads.ncep.noaa.gov/pub/data/nccf/com/gfs/prod/>.

The data provided there are organised as follows:

- In the above location, there are folders named according to the rule: gfs.YYYYMMDDHH, where YYYY is the year, MM is the month, DD day, HH hour of the forecast issue.
- In the selected folder, the GFS model files for the given date and time are named according to the following rule: Gfs.tHHz.pgrb2.0p25.FFF, where HH is the time of the weather forecast issue, and FFF is the forecast for the FFF's forecast hour counted from the HH release forecast.
- In the selected file, wind parameters are defined by U- and V- components. The U- component is defined by the ugrd10m variable, and the V- component by the vgrd10m variable.

## THE GWES MODEL FROM NOAA

The GWES model provides the significant wave height as one main control forecast and 20 equally probable accompanying forecasts – various variants of the control forecast.

The model is available on the Nomads server, under the access link: <http://nomads.ncep.noaa.gov:9090/pub/data/nccf/com/wave/prod/>. The data provided there are organised as follows:

- GWES is located in folders named according to the rule: gwes.RRRRMMDD, where YYYY is the year, MM is the month, DD is the day of issue of the GWES model forecast set.
- There are 84 GRiB2 files in the GWES model folder, as well as other files in different formats. The GWES GRiB2 files are marked as follows: gwesPP.glo\_30m.tHHz.grib2, where PP is the sequence number in the given set of projections (00 to 20), HH the time of the edition of the forecast data set.
- In the selected files, the significant wave height is defined by the HTSGW variable.

## MULTI-GRID WAVE MODEL FROM NOAA

The Multi-grid Wave model provides the data on:

- significant wave height,
- wave period between the peaks,
- mean wave direction.

The model is available on the Nomads server, under the access link: <http://nomads.ncep.noaa.gov:9090/pub/data/nccf/com/wave/prod/>. The data provided there are organised as follows:

- The Multi-grid Wave model is located in folders named according to the rule:

multi\_1.RRRRMMDD, where RRRR is the year, MM is the month, DD is the day of the forecast issue.

- There are many GRiB2 files in the folder of this model, including files for local areas.
- GRiB2 files of the Multi-grid Wave model for global coverage are marked as *Multi\_1.glo\_30m.tHHz.FFF.grib2*, where HH is the time of the weather forecast issue, and FFF is the forecast for FFF - the hour of the forecast calculated from the HH release forecast.
- The height of the significant wave in the above GRiB2 file is marked in the full version (long name) as “Significant height of combined wind waves and swell& Ground or water surface”, and in the abbreviation “HTSGW”. The given HTSGW is expressed in meters [m].
- The wave period between the peaks is named in the full version (long name) “Primary wave mean period & Ground or water surface”, with the abbreviation “PERPW”. The value of the data is expressed in seconds [s].
- The mean wave direction is named in the full version (long name “Primary wave direction” or “abbreviation”), the value of the data is expressed in degrees, where 0° means the movement towards the real north, 90° towards the east, and 180° towards the south (according to oceanographic convention).

## REAL TIME OCEAN FORECAST SYSTEM FROM NOAA

The model is offered by NOAA / NCEP and provides, among others, forecasts of sea currents. Forecasts are available in netCDF and GRiB2 file formats, though the latter covers only selected areas, mainly the Pacific (Fig. 2), so the netCDF files are recommended for worldwide applications, including transatlantic weather routing.

RTOFS data (including global netCDF files) are available under the link:

<http://nomads.ncep.noaa.gov:9090/pub/data/nccf/com/rtofs/prod/>.

The above location contains folders named according to the rtofs.YYYYMMDD convention, where YYYY is the year, MM is the month and DD is the day of the forecast issue. netCDF (\*.nc) files in those folders are named according to the rule: rtofs\_glo\_2ds\_XNNN\_PERIOD\_MODE.nc, where X equals 'f' (forecast) or 'n' (nowcast – a short-term forecast), NNN is the time in hours that the forecast covers, UPDATE indicates how often the forecast is issued: (“daily”, “3hrly” or “1hrly”), MODE means a forecast done for either diagnostic (“diag”) or prognostic (“prog”) variables.

In the case of weather routing, the recommended files are:

rtofs\_glo\_2ds\_fNNN\_daily\_prog.nc (NNN: 000, 024, 048 and 072).

## SUMMARY AND CONCLUSIONS

As has been shown in the paper, the multitude of weather data services might actually be misleading. When it comes to the detailed needs (here: for the purpose of weather routing in the North Atlantic), it turns out that the majority of available sources are lacking area coverage, update frequency, resolution or completeness. In the paper a number of weather data services have been presented and the ones that are optimal for the specified needs have been chosen. Following this, their functionality, as well as data access and data formats, has been researched and the results are provided in the current paper. While this review has been prepared with oceanic ship routing in mind, hopefully it will also be useful for a number of other applications, including collision avoidance.

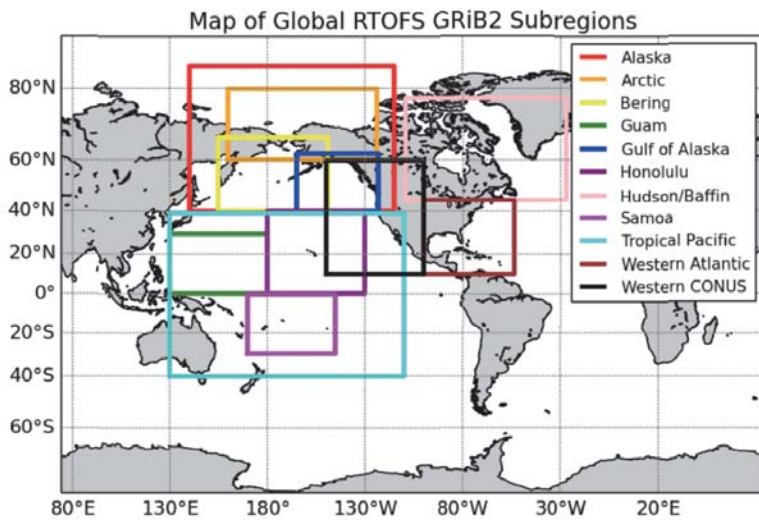


Fig. 2. Geographical regions covered by GRIB2 files of Real Time Ocean Forecast System (image taken from: [https://polar.ncep.noaa.gov/global/about/grib\\_description.shtml](https://polar.ncep.noaa.gov/global/about/grib_description.shtml)).

The files contain, among others, the velocity of a sea current given by the parameters “u\_velocity” (velocity towards east) and “v\_velocity” (velocity towards north).

It is worth noting that the grid (4500 x 3298 points) in the RTOFS global model files has an Arctic bi-polar patch (above 47°N) and a Mercator projection between 47°N and 78.6°S, as presented in Fig. 3.

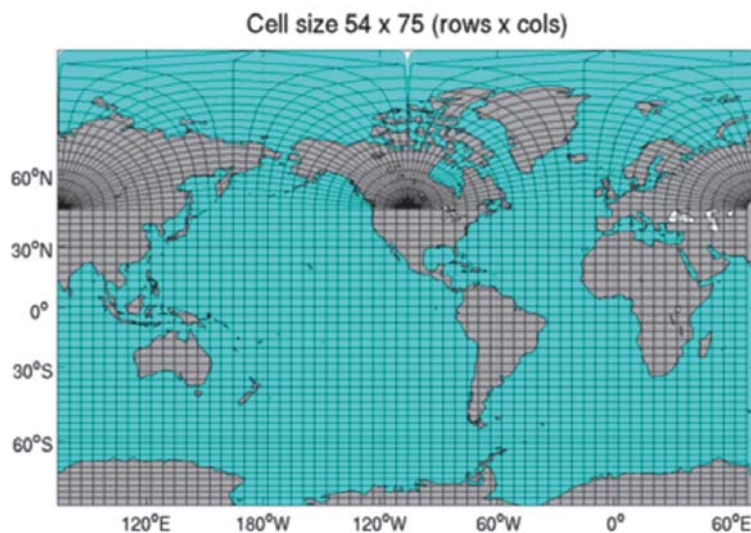


Fig. 3. Grid of the global Real Time Ocean Forecast System (image taken from: <https://polar.ncep.noaa.gov/global/about/images/large/pic1.png>).

## ACKNOWLEDGEMENTS

This research was supported by The National Centre for Research and Development in Poland under the grant on the ROUTING research project (MARTERA-1/ROUTING/3/2018) in the ERA-NET COFUND MarTERA-1 programme (2018-2021).

## REFERENCES

1. Acanfora M., Montewka J., Hinz T., Matusiak J. (2017): Towards realistic estimation of ship excessive motions in heavy weather. A case study of a containership in the Pacific Ocean. *Ocean Eng.*, Vol. 138, 140–150.
2. Bijlsma S. J. (2008): Minimal Time Route Computation for Ships with Pre-Specified Voyage Fuel Consumption. *J. Navig.*, Vol. 61, 723–733.
3. Chang Y., Tseng R., Chen G., Chu P. C. (2013): Ship Routing Utilizing Strong Ocean Currents. *J. Navig.*, Vol. 66, 825–835.
4. Chen C., Shiotani S., Sasa K. (2013): Numerical ship navigation based on weather and ocean simulation. *Ocean Eng.*, Vol. 69, 44–53.
5. Chen H. (2013): Weather routing versus voyage optimisation. *Digit. Sh.*, 26–27.
6. Decò A., Frangopol D. M. (2015): Real-time risk of ship structures integrating structural health monitoring data: Application to multi-objective optimal ship routing. *Ocean Eng.*, Vol. 96, 312–329.

7. Hagiwara H., Spaans J. A. (1987): Practical Weather Routing of Sail-assisted Motor Vessels. *J. Navig.*, Vol. 40, 96–119.
8. Hinnenthal J., Clauss G. (2010): Robust Pareto-optimum routing of ships utilising deterministic and ensemble weather forecasts. *Ships Offshore Struct.*, Vol. 5, 105–114.
9. James R.W. (1957): Application of wave forecast to marine navigation. US Naval Oceanographic Office, Washington.
10. Krata P., Szlapczynska J. (2018): Ship weather routing optimization with dynamic constraints based on reliable synchronous roll prediction. *Ocean Eng.*, Vol. 150, 124–137.
11. Mannarini G., Coppini G., Oddo P., Pinardi N. (2013): A Prototype of Ship Routing Decision Support System for an Operational Oceanographic Service. *TransNav, Int. J. Mar. Navig. Saf. Sea Transp.*, Vol. 7, 53–59.
12. Mannarini G., Pinardi N., Coppini G., Oddo P., Iafrazi A., Nazionale I., Creti V. D. (2016): VISIR-I : small vessels – least-time nautical routes using wave forecasts. *Geosci. Model Dev.*, Vol. 9, 1597–1625.
13. Marie S., Courteille E. (2013): Multi-Objective Optimization of Motor Vessel Route. *Int. J. Mar. Navig. Saf. Seas Transp.*, Vol. 3, 133–141.
14. Motte R. H., Calvert S. (1990): On The Selection of Discrete Grid Systems for On-Board Micro-based Weather Routeing. *J. Navig.*, Vol. 43, 104–117.
15. Natskår A., Moan T., Alvær P. O. (2015): Uncertainty in forecasted environmental conditions for reliability analyses of marine operations. *Ocean Eng.*, Vol. 108, 636–647.
16. Perera L. P., Soares C. G. (2017): Weather routing and safe ship handling in the future of shipping. *Ocean Eng.*, Vol. 130, 684–695.
17. Roulston M. S., Ellepola, J., von Hardenberg J., Smith L. A. (2005): Forecasting wave height probabilities with numerical weather prediction models. *Ocean Eng.*, Vol. 32, 1841–1863.
18. Specht C., Rudnicki J. (2016): A Method for the Assessing of Reliability Characteristics Relevant to an Assumed Position-Fixing Accuracy in Navigational Positioning Systems. *Polish Marit. Res.*, Vol. 23, 20–27.
19. Suzuki R., Tsukada Y., Tsujimoto M., Muraoka E., Ueno M. (2017): A study on high-lift rudder performance in adverse weather based on model tests under high propeller load. *Ocean Eng.*, Vol. 136, 152–167.
20. Szlapczynska J. (2007): Multiobjective Approach to Weather Routing. *TransNav - Int. J. Mar. Navig. Saf. Sea Transp.*, Vol. 1, 273–278.
21. Szlapczynska J. (2015): Multi-objective weather routing with customised criteria and constraints. *J. Navig.*, Vol. 68.
22. Szlapczynski R., Krata P. (2018): Determining and visualizing safe motion parameters of a ship navigating in severe weather conditions. *Ocean Eng.*, Vol. 158, 263–274.
23. Tagliaferri F., Viola I. M. (2017): A real-time strategy-decision program for sailing yacht races. *Ocean Eng.*, Vol. 134, 129–139.
24. Tsou M.-C. (2010): Integration of a Geographic Information System and Evolutionary Computation for Automatic Routing in Coastal Navigation. *J. Navig.*, Vol. 63, 323–341.
25. Vettor R., Guedes Soares C. (2015): Multi-objective Route Optimization for Onboard Decision Support System. 99–106.
26. Vettor R., Guedes Soares C. (2017): Characterisation of the expected weather conditions in the main European coastal traffic routes. *Ocean Eng.*, Vol. 140, 244–257.
27. Vettor R., Soares C. G., Wo Y. (2017): Assessment of the Storm Avoidance Effect on the Wave Climate along the Main North Atlantic Routes. *J. Navig.*, Vol. 69, 127–144.
28. Wei S., Zhou P. (2012): Development of a 3D Dynamic Programming Method for Weather Routing. *Int. J. Mar. Navig. Saf. Sea Transp.*, Vol. 6, 79–85.
29. de Wit C. (1990): Proposal for Low Cost Ocean Weather Routeing. *J. Navig.*, Vol. 43, 428–439.
30. Życzkowski M., Krata P., Szłapczyński R. (2018): Multi-objective weather routing of sailboats considering wave resistance. *Polish Marit. Res.*, Vol. 25, 4–12.
31. Życzkowski M., Szłapczyński R. (2017): Multi-Objective Weather Routing of Sailing Vessels. *Polish Marit. Res.*, Vol. 24.
32. ROUTING project web-page, (n.d.).

## CONTACT WITH THE AUTHORS

**Marcin Życzkowski**

*e-mail: marzyczk@pg.edu.pl*

Gdańsk University of Technology

Narutowicza 11/12, 80-233 Gdańsk

**POLAND**

# HYBRID FINITE ELEMENT METHOD DEVELOPMENT FOR OFFSHORE STRUCTURES' CALCULATION WITH THE IMPLEMENTATION OF INDUSTRY STANDARDS

**Jacek Łubiński**

Gdansk University of Technology, Poland

**Henryk Olszewski**

Gdansk University of Technology, Poland

## ABSTRACT

*In the design process of offshore steel structures, it is typical to employ commercial calculation codes in which simulation and evaluation of results are performed on the basis of the available standards (e.g. API, DNV, Lloyds). The modeling and solution rely on finite element methods and cover the simulation of the structure's properties along with the influence of the marine environment – sea currents, wave and wind loading, as well as the influence of vibrations, buoyancy and accompanying mass of water. Both commercial and open source mathematical modeling software which is available nowadays allows for cost effective and flexible implementation of advanced models for offshore industrial structures with high level of credibility and safety. The models can be built to suit task-specific requirements and evaluated on the basis of the selected criterial system best suited to the needs of the customer. Examples of methodology for environmental and structural model development are presented, along with simulation results covering a wide scope of data, ranging from stress and deformation to resonant characteristics and issues of technological feasibility.*

**Keywords:** offshore structures, design calculations, sea loading, stress evaluation, FEM

## INTRODUCTION

Correct designing of steel offshore structures is a responsible task due to numerous threats to human life and health, as well as to their possessions and natural environment which may result from possible failure of such a structure. The report prepared for UK Health & Safety Executive [28] reveals that in exploitation practice of drilling and production platforms with human crew, about 10 % of accidents involving bodily injury result from constructional errors, i.e. errors made at early project implementation stages.

One of basic issues related with designing a drilling rig is identifying environmental conditions to be faced on the route of its transportation and final foundation. These conditions include environmental loads acting on the rig during its

transportation, foundation, and operation in extreme sea states. The information on parameters determining environmental conditions for the offshore structure can be found in standards and regulations of classification societies [1–3, 13, 16]. Taking into consideration extreme environmental conditions is necessary when calculating the strength of the structure. There are a number of methods to assess the extreme sea state parameters. These methods fall into two categories: short-term and long-term. The parameters considered in the model of structure's load include sea currents and waves, sea liches, forced vibrations, or even the action of sea ice cap [4, 5, 7, 9, 22]. For structures with long exploitation lifetime, a very important factor is its fatigue life assessment. This refers to both stationary [1 – 3, 13, 16] and floating structures [6, 7].

For economic reasons, the entire methodology of marine structure design calculations should be time- and cost-efficient,

at the same preserving acceptable representativeness. As a rule, commercial computer codes make use of beam models of steel structures, with shell models additionally introduced at nodes exposed to stress concentration and fatigue. This model architecture makes it possible to minimise computing power demand (simplicity of beam model) and to analyse maximum stresses (shell model). However, it requires combined use two types of finite elements, and offers only simplified analysis of interaction between the fluid and slender elements of the designed structure.

As an alternative to that approach, a methodology is proposed in the article which consists in developing a model entirely based on shell elements, with complete representation of the geometry of the load bearing structure, but with simplification of passive elements (risers, for instance) and the deck module to a single equivalent inertia, the action of which is passed in the way reflecting the real action of those elements. The advantages of this method include increased accuracy in specifying marine environment load application points and complete information on stress distributions in walls of pipe elements and profiles composing the supporting structure of the entire offshore structure, all this achieved at comparable demand for computing power and memory of the used computer. To improve further the economy of computations, a detailed analysis of the model of wave motion was performed and a simplified model was selected which had similar accuracy to that resulting from the theory [4, 5].

The discrete structure was modelled using a hybrid finite element method [15], which is a combination of the method of deformable finite elements and the concentrated mass method. This method is based on the assumption that parts of the marine structure which are responsible for its response to the applied load are modelled using deformable finite elements. In the supporting structure for the stationary platform, these are the shell elements which ensure complete representation of its geometry and provide opportunities for analysing stress concentrations at model nodes. The remaining parts of the structure, which are not involved in generating response to the applied load, are modelled using concentrated mass elements. These elements are not simply mass points, but masses with attributed tensors of inertia. The geometric representation of a mass point is a point, while concentrated masses can be connected with each other, and with deformable elements, elastic-damping constraint elements (like in the finite element method [24, 25, 26, 27]), elastic elements, and/or massless rigid elements. External loads can be applied directly to mass points, or via elastic-damping elements, elastic elements, or massless rigid elements. The above method of digitisation makes it possible to increase the accuracy of modelling in regions with greatest impact on the results of calculations, at the same time reducing the dimensions of the matrix describing the model of the entire structure and thus shortening the computing time, which is of high importance when performing long-lasting analyses with iterations [15].

## ENVIRONMENTAL LOADS OF MARINE STRUCTURE

According to the standard API RP 2A-WSD [2], when calculating both floating marine structures and those founded on the seabed, the loads generated by the following environmental phenomena should be taken into account:

- 1) wind,
- 2) sea current,
- 3) sea wave,
- 4) ice cap,
- 5) waves generated by earthquakes,
- 6) earthquakes.

Additionally, accidental loads generated, for instance, by fire or explosion, or when the structure is hit by a ship, should also be taken into account.

In the case of slender marine structures, such as production platforms of jacket type, production pipe casings (risers), pipelines, or ropes anchoring the structure, of high importance is the flow of fluid in the vicinity of the structure. In those cases, the wave generated loads can be calculated using the Morison equation [3, 7, 29, 30], which is based on the assumption that the load of the structure coming from the fluid flowing around it is equal to the sum of forces of inertia and flow resistance.

In a slender marine structure, vortex induced vibrations (VIV) can appear when the frequency of changes of the vortex motion of the fluid (caused by waves or sea current) is in resonance with the free-vibration frequency of the structure. Therefore, pipe calculations should also include the analysis of fatigue loads coming from waves and water vortices.

## WEIGHT OF STRUCTURE

The weight of the structure is calculated directly from the FEM model, based on material density and volumes of finite elements. The FEM codes automatically attribute concentrated forces and continuous loads coming from structure's weight to particular finite elements. The weight of the marine structure equipment is represented in the model by pressures and concentrated forces applied at selected nodes.

## FUNCTIONAL LOADS

When analysing structure's elements, the use of variable loads provides opportunities for studying loads coming from different configurations of the transported cargo, and thus determining extreme load values. Variable loads are taken into account in FEM models as pressures applied to selected decks and tank walls.

## WIND CAUSED LOADS

It is assumed that the marine structure loads caused by wind are static in nature [1, 2]. The wind thrust force is a function of wind pressure and wind thrust area [1]:

$$F_w = P_w \cdot A_w \quad (1)$$

where:

$P_w$  – wind thrust pressure:

$$P_w = V^2 \cdot C_h \cdot C_s \quad (2)$$

$V$  – wind speed,

$C_h$  – height coefficient,

$C_s$  – shape coefficient,

$A_w$  – wind thrust area.

The definitions of height and shape coefficients are given in regulations of classification societies. The wind thrust pressure (2) is calculated based on the Bernoulli theory of fluid flow, according to which the fluid acts with the following dynamic pressure on the motionless body [1]:

$$P_w = \frac{1}{2} \rho V^2 \quad (3)$$

where:

$\rho$  – fluid density.

In the majority of cases, the wind generated loads are applied to the structure's model in the form of concentrated horizontal forces acting at certain heights above sea level.

## LOADS CAUSED BY WAVES AND SEA CURRENT

Hydrodynamic loads caused by waves, and forces of inertia caused by structure's rolling are low-frequency dynamic loads. To assess them, simplified quasi-static models can be used [1, 2, 30]. It is noteworthy that these calculations should be performed taking into account further fatigue analysis, in which the main load component is the action of waves, due to its cyclic nature.

In the case of floating marine structures, the calculations should be performed for extreme sea state parameters. These calculations take also into account forces of inertia coming from averaged motion of the structure.

In the case of stationary marine structures, the calculations are usually performed for a series of cases to:

- 1) accurately model the wave motion in the marine structure foundation place,
- 2) accurately describe the transmittance and load amplification factors.

The response of the marine structure is obtained as a result of the analysis of regular, design, and stochastic waves.

The load of the marine structure caused by the action of extreme wave [1, 2, 30] can be calculated using commercial computer codes, such as AQUA, WAMIT, etc. [7]. These calculations should take into account different wave directions, in order to assess maximum stresses related to those directions.

The force distributions over marine structure beams caused by the flow of water particles in their vicinity is calculated from Morrison's equation (4). This approach is widely used in standards [1, 2, 3, 7, 16]. It makes it possible to obtain results close to reality, provided that the dimensions of the beam's cross section are several times smaller than both the wave length and the characteristic distance between neighbouring beams [1, 2, 30]. These conditions are met for typical stationary marine structures. The continuous load per unit length of the cylinder with diameter  $D$  consist of two components [1]:

$$\bar{F} = \bar{F}_n + \bar{F}_t \quad (4)$$

where:

$\bar{F}_n$  – continuous load perpendicular to cylinder surface,

$\bar{F}_t$  – continuous load tangential to cylinder surface (parallel to cylinder axis).

Each component can be presented as a function of water particle velocity and calculated from Morrison's equation. In the direction perpendicular to the cylinder surface, the continuous load is given as [1]:

$$\bar{F}_n = \bar{F}_{Dn} + \bar{F}_{In} \quad (5)$$

where:

$\bar{F}_{Dn}$  – resistance force of normal flow:

$$\bar{F}_{Dn} = \frac{1}{2} C_{Dn} D \rho \bar{V}_n |\bar{V}_n| \quad (6)$$

$\bar{F}_{In}$  – force of inertia of normal flow [1]:

$$\bar{F}_{In} = \frac{1}{4} \pi C_{Mn} D^2 \rho \bar{V}_n \quad (7)$$

$C_{Dn}$  – resistance coefficient of the flow normal to the beam surface,

$C_{Mn}$  – inertia coefficient of the flow normal to the beam surface,

$\rho$  – water density,

$\bar{V}_n$  – normal component of the relative velocity of water particles with respect to the beam element.

In the direction tangential to the beam surface, it is assumed that the effect of the forces of inertia of the flow is negligibly small and the continuous load in this direction depends only on flow resistance [1]:

$$\bar{F}_t = \bar{F}_{Dt} = \frac{1}{2} \pi C_{Dt} D \rho \bar{V}_t |\bar{V}_t| \quad (8)$$

where:

$C_{Dt}$  – resistance coefficient of the flow tangential to the beam surface,

$\bar{V}_t$  – tangential component of the relative velocity of water particles.

These forces can be expressed in the local coordinate system  $x, y, z$ , in which the  $x$ -axis coincides with the beam axis, while the  $y$ - and  $z$ -axes are perpendicular to the beam axis [1]:

$$\begin{aligned} \bar{F}_x &= \frac{1}{2} \pi C_{Dt} D \rho |\bar{V}_t| \bar{V}_t \\ \bar{F}_y &= \frac{1}{2} C_{Dn} D \rho |\bar{V}_n| \bar{V}_y + \frac{1}{4} \pi C_{Mn} D^2 \rho \bar{V}_y \\ \bar{F}_z &= \frac{1}{2} C_{Dn} D \rho |\bar{V}_n| \bar{V}_z + \frac{1}{4} \pi C_{Mn} D^2 \rho \bar{V}_z \end{aligned} \quad (9)$$

where:  $x, y, z$  are the axes of the local coordinate system fixed to the beam.

For non-cylindrical beams, the above equations consider differences in hydrodynamic behaviour of the beam in two directions:  $y$  and  $z$ , perpendicular to the beam axis. In this case, the continuous loads of the beam in the local coordinate system are given as [1]:

$$\begin{aligned} \bar{F}_x &= \frac{1}{2} \pi C_{Dt} (D_y + D_z) \rho |\bar{V}_t| \bar{V}_t \\ \bar{F}_y &= \frac{1}{2} C_{Dy} D_y \rho |\bar{V}_n| \bar{V}_y + \frac{1}{4} \pi C_{My} D_y^2 \rho \bar{V}_y \\ \bar{F}_z &= \frac{1}{2} C_{Dz} D_z \rho |\bar{V}_n| \bar{V}_z + \frac{1}{4} \pi C_{Mz} D_z^2 \rho \bar{V}_z \end{aligned} \quad (10)$$

where:

$C_{Dy}, C_{Dz}$  – flow resistance coefficients in the direction of  $y$ - and  $z$ -axis, respectively, in the local coordinate system fixed to the beam,

$D_y, D_z$  – effective dimensions of the beam's cross section in the directions of  $y$ - and  $z$ -axis, respectively, in the local coordinate system fixed to the beam.

## MODELLING OF WIND WAVE

Wave is the deformation of the sea free surface, which moves from one point to the other in the given water region. For instance, after dropping a stone into the water, the free surface deformation propagates around the point at which the stone hit the water (circular wave). It is the free surface deformation which propagates, and not the water mass itself. Currently, the surface wave in water can be described using one of five theories [2, 7, 34]:

- 1) gravitational wind wave (linear model),
- 2) fifth-order Stokes wave,
- 3) stream function,

- 5) trochoidal (cnoidal) wave,
- 6) solitary wave.

Each of these theories enables obtaining an approximate solution to equations of flow motion within certain ranges of wave amplitudes and periods, and water depths. Fig. 1 presents parameters describing the sea wave [34].

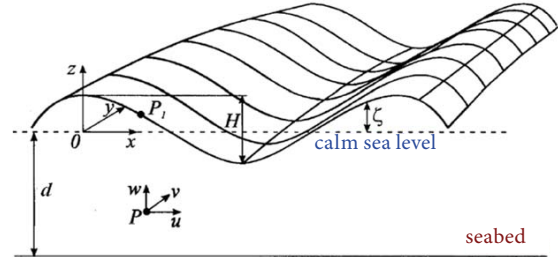


Fig. 1. Parameters describing the sea wave:  $H$  – wave height,  $d$  – water depth,  $\zeta$  – free surface deflection,  $x$ - $y$ - $z$  – global coordinate system,  $u$ - $v$ - $w$  – local coordinate system fixed to fluid element  $P$ ,  $P1$  – fluid element situated on the free surface [34]

For gravitational wind waves, it is assumed that [7, 9, 34]:

- 1) at large water depths, the effect of surface wave action is limited to a small surface layer,
- 2) water displacements, velocities and accelerations in the horizontal and vertical directions are of the same order,
- 3) accelerations in the vertical direction are of the order of acceleration due to gravity,  $g$ ,
- 4) the Coriolis acceleration is negligibly small due to short period of motion,
- 5) the motion is unsteady, i.e. [7, 9, 34]:

$$\frac{\partial}{\partial t} \neq 0 \quad (11)$$

- 6) the mass of water does not travel with the deformed wave (linear wave model)

The issues of water motion in wind wave can be analysed as a special case of the boundary value problem of partial differential equations [34]. The boundary conditions defined for the free surface of the wave include kinematic and dynamic conditions. For the seabed, the kinematic boundary condition is defined. Additionally, side boundary conditions can be defined, along with the condition for wave motion damping. It is assumed in the calculations that the fluid is incompressible, and the water motion is irrotational. Consequently, it can be assumed that the water flow is potential [34].

Let us consider the case of wave travelling in the direction of decreasing  $x$  values. The value of the potential is given by its real part:

$$\Phi = a \frac{\omega \cosh[k(z+d)]}{k \sinh(kd)} \sin(-kx - \omega t + \theta) \quad (12)$$

The free surface deflection is affected by the real part of the potential (with the imaginary part omitted):

$$\zeta = a \cdot \cos(-kx - \omega t + \theta) \quad (13)$$

where:

$a$  – wave amplitude,

$\omega$  – circular frequency, pulsation,

$k$  – wave number [7]:  $k = \frac{2\pi}{L}$ ,

$t$  – time,

$\Theta$  – constant.

Under the sea surface, the fluid elements make orbital motions. These motions can have different orbits, depending on water depth, see Fig. 2. The water is considered deep when the water depth  $d$  is larger than half of the wave length  $L$ .

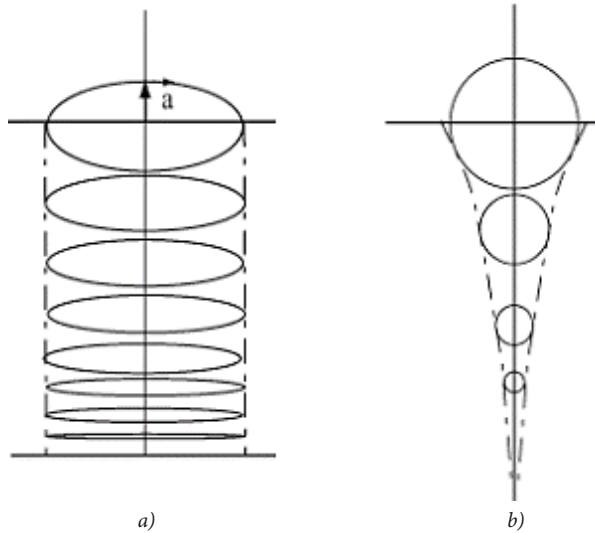


Fig. 2. Orbital motions of fluid elements: a) shallow water, b) deep water [34]

The velocity components of the fluid element in orbital motion are (Fig. 1):

$$u = -\frac{\partial \Phi}{\partial x} = a\omega \frac{\cosh[k(z+d)]}{\sinh(kd)} \cos(-kx - \omega t + \theta) \quad (14)$$

$$w = -\frac{\partial \Phi}{\partial z} = -a\omega \frac{\sinh[k(z+d)]}{\sinh(kd)} \sin(kx - \omega t + \theta) \quad (15)$$

The acceleration components of the fluid element in orbital motion are given by:

$$a_x = \frac{\partial u}{\partial t} = -a\omega^2 \frac{\cosh[k(z+d)]}{\sinh(kd)} \sin(kx - \omega t + \theta) \quad (16)$$

$$a_z = \frac{\partial w}{\partial t} = -a\omega^2 \frac{\sinh[k(z+d)]}{\sinh(kd)} \cos(kx - \omega t + \theta) \quad (17)$$

Let us assume that the constant  $\theta$  for the wave with height  $H$  several times smaller than both wave length  $L$  and water depth  $d$  is equal to zero. Then, with the use of Eq. (12), the velocity potential can be written as:

$$\Phi \approx a \frac{\omega}{k} \frac{\cosh[k(z+d)]}{\sinh(kd)} \sin(-kx - \omega t) \quad (18)$$

Taking into consideration the definitions of wave circular frequency and wave number, the velocity potential takes the following form:

$$\Phi \approx a \frac{2\pi}{L} \frac{\cosh\left[\frac{2\pi}{L}(z+d)\right]}{\sinh\left(\frac{2\pi d}{L}\right)} \sin\left(-\frac{2\pi}{L}x - \frac{2\pi}{T}t\right) \quad (19)$$

Then, assuming that the wave shape is close to a sine wave, for which the amplitude  $a$  is equal to half of its height  $H$ , we arrive at:

$$\Phi \approx \frac{HL}{2T} \frac{\cosh\left[\frac{2\pi}{L}(z+d)\right]}{\sinh\left(\frac{2\pi d}{L}\right)} \sin\left[2\pi\left(-\frac{x}{L} - \frac{t}{T}\right)\right] \quad (20)$$

Finally, the free surface deflection in the simplified free-surface model is given as:

$$\zeta \approx \frac{H}{2} \cos\left[2\pi\left(-\frac{x}{L} - \frac{t}{T}\right)\right] \quad (21)$$

Eq. (21) does not depend on sea depth  $d$ . The shape of the wave surface, which in fact depends on the sea depth, can be determined directly from the dynamic boundary condition for the free surface (full free surface model):

$$\zeta = \frac{1}{g} \frac{\partial \Phi}{\partial t} \Big|_{z=0} = -\frac{\pi HL}{gT^2} \operatorname{ctgh}\left(\frac{2\pi d}{L}\right) \cos\left[2\pi\left(-\frac{x}{L} - \frac{t}{T}\right)\right] \quad (22)$$

In this case, the velocity components of the fluid element in orbital motion are given by the following equations:

$$u = -\frac{\partial \Phi}{\partial x} = \frac{H\omega}{2} \frac{\cosh\left[\frac{2\pi}{L}(z+d)\right]}{\sinh\left(\frac{2\pi d}{L}\right)} \cos\left[2\pi\left(-\frac{x}{L} - \frac{t}{T}\right)\right] \quad (23)$$

$$w = -\frac{\partial \Phi}{\partial z} = -\frac{H\omega}{2} \frac{\sinh\left[\frac{2\pi}{L}(z+d)\right]}{\sinh\left(\frac{2\pi d}{L}\right)} \sin\left[2\pi\left(-\frac{x}{L} - \frac{t}{T}\right)\right] \quad (24)$$

and the acceleration components take the following form:

$$a_x = \frac{\partial u}{\partial t} = \frac{H\omega^2}{2} \frac{\cosh\left[\frac{2\pi}{L}(z+d)\right]}{\sinh\left(\frac{2\pi d}{L}\right)} \sin\left[2\pi\left(-\frac{x}{L} - \frac{t}{T}\right)\right] \quad (25)$$

$$a_z = \frac{\partial w}{\partial t} = \frac{H\omega^2}{2} \frac{\sinh\left[\frac{2\pi}{L}(z+d)\right]}{\sinh\left(\frac{2\pi d}{L}\right)} \cos\left[2\pi\left(-\frac{x}{L} - \frac{t}{T}\right)\right] \quad (26)$$

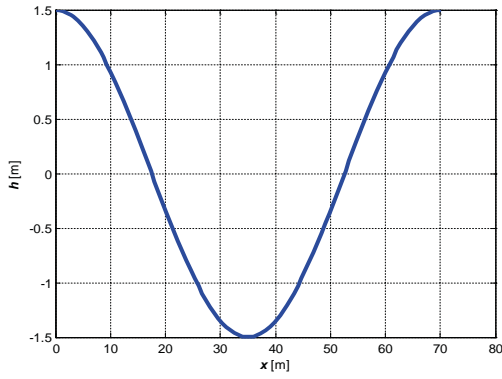


Fig. 3. Sea free surface deflection given by the simplified model, Eq. (21)

The wave models were implemented in Matlab environment with the following arbitrarily assumed parameter values:

- 1) wave height:  $H = 3$  m,
- 2) sea depth:  $d = 80$  m,
- 3) wave period:  $T = 6.69$  s,
- 4) wave length:  $L = 70.06$  m.

Fig. 3 presents the shape of wind wave free surface deflection which was determined using the simplified model given by Eq. (21). Differences between the wind wave free surface deflection shapes determined using the full model (22) and the simplified model (21) do not exceed  $\pm 2$  mm, which confirms correctness of the assumptions adopted when developing the simplified model (21).

Fig. 4 shows the limiting shape of the wave velocity potential (for  $\frac{1}{4}$  cycle of orbital motion of fluid element) determined for:

$$\sin \left[ 2\pi \left( -\frac{x}{L} - \frac{t}{T} \right) \right] = 1$$

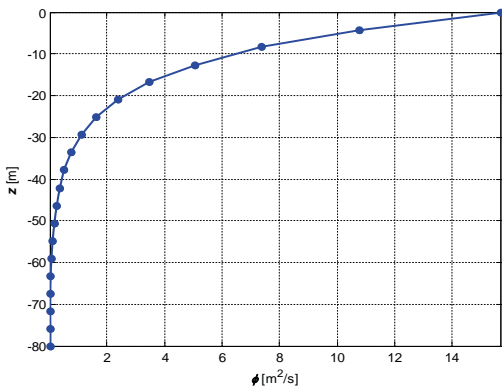


Fig. 4. Wave velocity potential for  $\frac{1}{4}$  cycle of rotational motion of fluid element

Fig. 5 shows the limiting shape of velocity component  $u$  in orbital motion of fluid element (beginning of motion) determined for:

$$\cos \left[ 2\pi \left( -\frac{x}{L} - \frac{t}{T} \right) \right] = 1$$

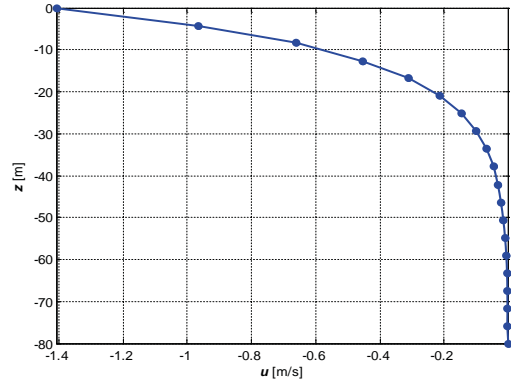


Fig. 5. Velocity component  $u$  in orbital motion of fluid

Fig. 6 shows the limiting shape of velocity component  $w$  in orbital motion of fluid element determined for:

$$\sin \left[ 2\pi \left( -\frac{x}{L} - \frac{t}{T} \right) \right] = 1$$

Fig. 7 illustrates the phenomenon of height increase of the wave with the assumed initial height  $L$  and period  $T$  when the sea depth decreases (wave passing through the shallows).

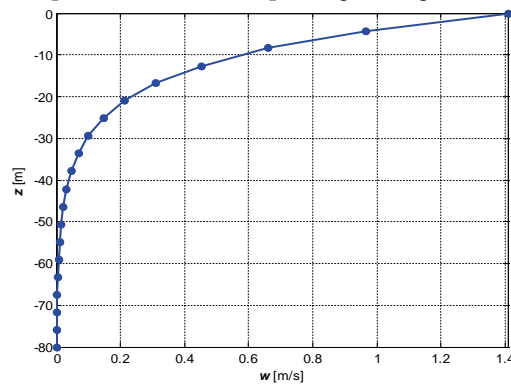


Fig. 6. Velocity component  $w$  in orbital motion of fluid for  $\frac{1}{4}$  cycle of rotational motion of fluid element

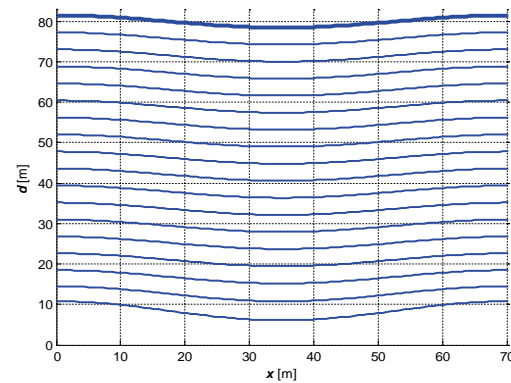


Fig. 7. Wave profile changes related with sea depth decrease

Fig. 8 shows the limiting shape of acceleration component  $a_x$  in orbital motion of fluid element determined for:

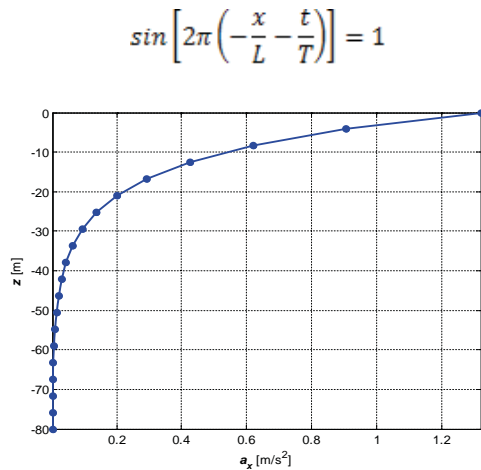


Fig. 8. Acceleration component  $a_x$  in orbital motion of fluid for  $\frac{1}{4}$  cycle of rotational motion of fluid element

Fig. 9 shows the limiting shape of acceleration component  $a_z$  in orbital motion of fluid element determined for the beginning of motion:

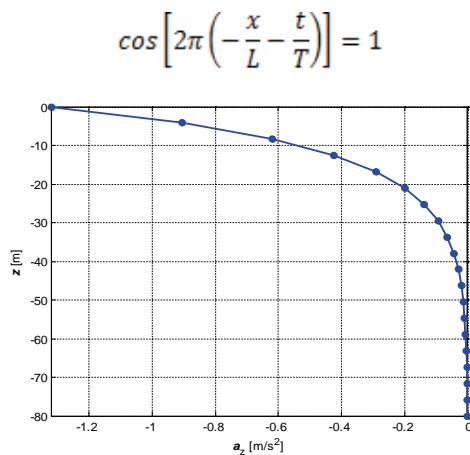


Fig. 9. Acceleration component  $a_z$  in orbital motion of fluid (beginning of rotational motion)

The motion trajectory of fluid element at depth of 37.9 m, with velocity and acceleration vectors for each element position, is shown in Fig 10, while Fig. 11 shows the trajectories at selected sea depths, starting from seabed up to free surface.

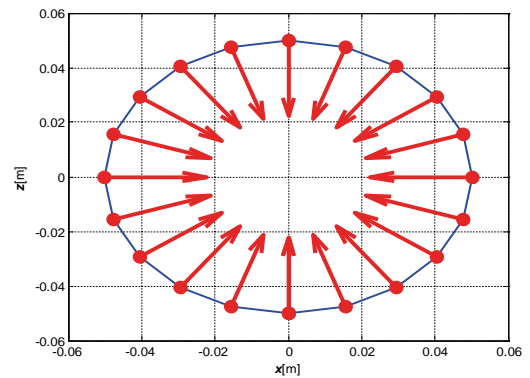
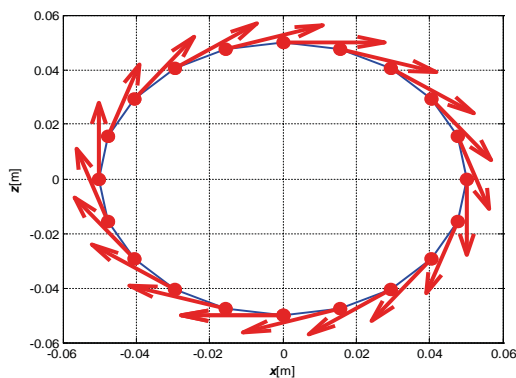


Fig. 10. Trajectory of rotational motion of fluid element at depth of 37.8947 m, with marked velocity vectors (top) and acceleration vectors (bottom)

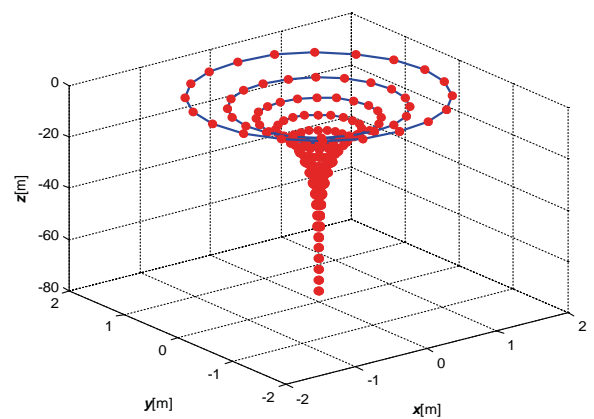


Fig. 11. Trajectories of fluid elements at selected depths

## MODELLING OF MARINE STRUCTURES

Stationary marine structures are, as a rule, welded pipe structures with vertical or inclined legs connected with each other by stiffeners. The marine structure creates a support for upper, surface parts, such as pipelines, risers, and other equipment. The stages of marine structure modelling include [2, 29]:

- 1) determining needs of the project,
- 2) modelling conditions of marine environment and structure foundation,
- 3) working out preliminary design offers, with predicted possible places of installation, as well as conditions and costs of their execution,
- 4) selecting dimensions of the structure which will allow determining its load in each operating phase: well drilling, production, and well cleaning,
- 5) assessing the project with respect to erection technology and costs,
- 6) performing the analysis of load and stress distributions in the structure during its construction, transportation, and assembly in the foundation place,
- 7) analysing possibilities of structure's closing after termination of its operating lifetime.

The analyses of a stationary marine structure begin with determining geometric and material parameters of elements composing the structure, as well as parameters of its foundation and operation, and environmental and accidental loads.

Two basic types of analyses can be named:

- 1) linear analyses which aim at checking static and fatigue load limits based on regulations of classification societies (API RP2A [2], ABS [1], etc.);
- 2) nonlinear finite element method-based analyses which make it possible to determine the structure's response to accidental loads (such as collisions with other floating marine structures, fires, explosions, and earthquakes), and extreme environmental loads. These analyses are also performed for existing stationary marine structures.

The FEM analysis of a marine structure includes:

- 1) the analysis of the abovenamed environmental loads. Here, an additional factor taken into consideration is the effect of sea lichens which manifests itself in the increase of hydrodynamic load and total weight of the structure. The hydrodynamic model of the structure should include such equipment elements as drainage pipes, risers, vertical pipelines, caissons, ladders, stairs, etc. Depending on the type and amount of equipment elements, the action of waves on them should be considered. It is assumed that the equipment which is not permanently connected with the main frame of the marine structure (welded to the structure) is not a structure's element, and is only taken into account as additional load acting on the structure, a so-called non-structural member;
- 2) the foundation analysis, taking into consideration the interaction between the seabed soil and structure's elements;
- 3) the analysis of the load bearing structure and working decks.

The acting loads should be determined for each operating stage: well drilling, production, well cleaning, and their combinations. According to the standard NTS [23], the analyses of marine structures should allow to determine:

- 1) maximum shearing forces generated by waves and sea currents – needed for calculating dimensions of structure's reinforcements,
- 2) maximum restoring moments – needed for calculating dimensions of load bearing columns and the foundation,
- 3) maximum local forces acting on particular elements of the structure, which may occur at wave positions different than that generating the maximum global load for the entire structure.

The fatigue analysis of the marine structure should include all actions which are cyclic in nature and have relatively large frequency. This includes waves and other local phenomena caused by wave hitting against the structure, and by formation of vortices in water close to the structure.

According to the regulations of classification societies [1, 2], when the marine structure is founded on shallow water, the nonlinear wave theory should be applied. In those cases, deterministic fatigue analyses are also used. On the other hand, in cases of deep-water marine structures, the significance of dynamic phenomena is much higher than for shallow-water founded structures. In those cases, the fatigue analyses are performed for some frequency range (stochastic dynamic analyses). They require linearization of non-linear soil models. The stiffness matrix, which describes the structure's cooperation with the soil, is determined for the sea wave (with given parameters), the effect of which on the fatigue damage of the structure is most significant.

## SAMPLE CALCULATIONS

The geometric model of the selected offshore structure, founded at depth of 80 m, is shown in Fig. 12. The object of the analysis was the stationary steel production platform consisting of the load bearing structure and the deck module. The geometric model for this structure was prepared and the strength calculations were performed in FEMAP environment.

The load bearing structure consists of three modules with four legs, between which a number of beams are extended in X-arrangement to increase the platform stiffness. On the upper plane of each module, guides for six production risers are mounted. The load bearing structure is the support for the deck module. The upper surface of the deck module is the production deck, below which the main technological deck is situated, with three mounted risers. Further below, there is the encased transportation deck.

The geometric model of the production platform was discretised using the earlier described hybrid finite element method, being a combination of the classic method of deformable finite elements and the concentrated mass method. The static and dynamic strength of the entire platform depends mostly on that of the load bearing structure. Therefore, this part was discretised using deformable finite elements, while the deck module and production risers were modelled using the concentrated mass method. The hybrid method was adapted for offshore structures based on the experience gained when developing models of large inland structures exposed to vibrations [15]. In Fig. 12, the structure discretised using deformable finite elements is marked green, while the deck and the production risers were reduced to concentrated masses marked yellow.

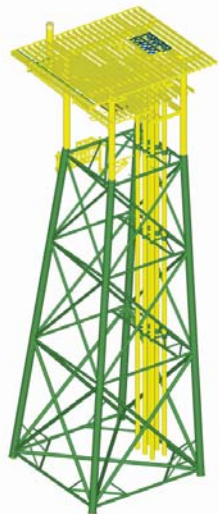


Fig. 12. Geometric model of production platform – isometric view

The deck module and the production risers were discretised using one concentrated mass, connected via two-dimensional rigid elements with the load bearing structure's legs and risers' guides. The parameters of inertia of this concentrated mass were determined by discretising the geometric model of the deck module and production risers with deformable finite elements. As a result, a complete model of the production platform was obtained, as shown in Fig. 13 presenting a net of finite elements, a symbolic representation of equivalent loads for the deck module, and constraints applied to supports of load bearing columns.

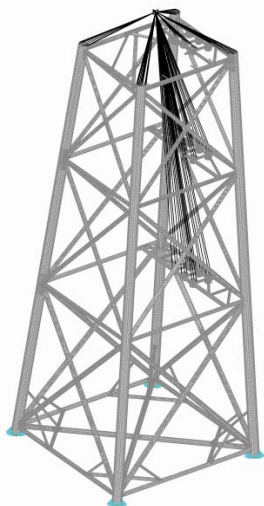


Fig. 13. Complete model of production platform

The model of marine environment was developed for the following parameters:

- wave height:  $H = 3$  m,
- sea depth:  $d = 80$  m,
- wave period:  $T = 6.69$  s,
- wave length:  $L = 70.06$  m.

The above described wave model was used for calculating the water thrust pressure acting on the production platform. The calculations took into consideration the self-weight of the structure. It was assumed that the structure's part situated under water surface is sunken, and, consequently, the buoyance force is negligibly small compared to the remaining loads of the structure. Fig. 14 shows the loads acting on the platform structure model.

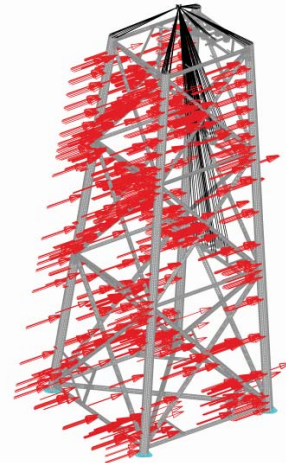


Fig. 14. Loads acting on the production platform structure model

As a result of calculations performed in FEMAP environment, the structure's deformations were obtained (Fig. 15) along with reduced stresses in deformable elements (Fig. 16, Fig. 17).

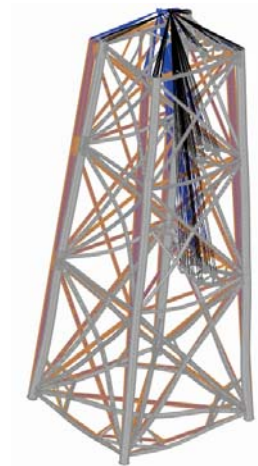


Fig. 15. Deformations of the production platform structure model

The use of deformable finite elements for discretising the load bearing structure has made it possible to calculate local stress concentrations at structure's nodes, with maximum values reaching up to 192 MPa. These stress concentrations were recorded at nodes situated close to the seabed, in the connection places of X-arranged beams with structure's legs (Fig. 17). Those places are the areas with the highest values of bending moments and forces shearing the entire load bearing

structure, at simultaneous presence of notches caused by close vicinity of beams linked together at a given node.

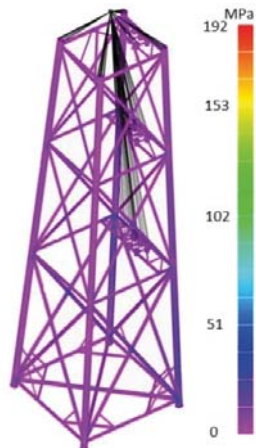


Fig. 16. Reduced stresses in deformable finite elements

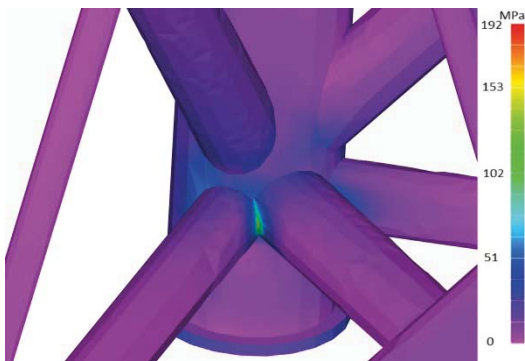


Fig. 17. Local stress concentrations at structure's node

## CONCLUSIONS

The hybrid method combines together the advantages of the method of deformable finite elements and the concentrated mass method. It provides an opportunity for modelling complex structures, such as the production platform studied in the article. Deformable finite elements make it possible to analyse in detail the main part of the platform, which is the load bearing structure. In the analysed case, it allowed to determine local stress concentrations at structure's nodes. The remaining, complex platform parts, being the source of load for the load bearing structure, were discretised using the concentrated mass method, which resulted in substantial reduction in the number of finite elements used to discretise the geometric model of the deck module and production risers. In the analysed case, this reduction amounted to about 35%, while simultaneously preserving the same stress and deformation values in the model (difference by 2%).

The use of recommendations on modelling of structures and loads applied to them which are available in industry-recognisable standards and manuals makes that the obtained results can be interpreted as valuable design calculations which

can be used for making responsible decisions concerning real marine platform designs. A considerable advantage of the proposed method is the possibility of its implementation in an arbitrary computing environment, (the case reported in the article was analysed in Matlab® environment), depending on the software and hardware owned by the potential user. This property would be extremely valuable in possible parallel verification of calculations performed at different marine industry centres with different computing systems to increase the safety of designed or already existing structures.

## BIBLIOGRAPHY

1. American Bureau of Shipping (ABS), *Rules for Building and Classing Offshore Installations, Special Committee on Offshore Installations*, New York, 1997.
2. American Petroleum Institute, *RP 2A-WSD Planning, Designing, and Constructing Fixed Offshore Platforms – Working Stress Design*, 2015.
3. Bureau Veritas, Marine & Offshore Division, *Rules for the Classification of Offshore Units PART B – Structural Safety, Chapters 1 – 2 – 3, NR 445.B1 DT R05 E*, Neuilly sur Seine, France, December 2016
4. Chakrabarti S.K., *Hydrodynamics of offshore Structures*, Computational Mechanics Publications, 1987.
5. Chakrabarti, S. K. (ed) 2005. *Handbook of Offshore Engineering*, San Francisco: Elsevier.
6. CMPT, *Floating Structures: A Guide for Design and Analysis*, editor: N. Baltrop, Oilfield Publications, Inc., 1998.
7. Faltinsen O.M., *Sea Loads on Ships and offshore Structures*, Cambridge Ocean Technology Series, Cambridge University Press, 1990.
8. Hare J., Johnson M., *Underlying Causes of Offshore Incidents FP/09/21*, Health & Safety Laboratory UK, 2009
9. Jensen J.J., *Dynamic Amplification of Offshore Steel Platform Response due to Non-Gaussian Wave Loads*, Marine Structures, tom 7, str. 91÷105, 1994.
10. Kruszewski J., Wittbrodt E., Walczyk Z., *Vibrations of mechanical systems in computer approach (in Polish)*, Volume 1 and 2, WNT, Warsaw 1996.
11. Kruszewski J., Sawiak S., Wittbrodt E.: *Rigid finite element method in dynamics of structures (in Polish)*. Warsaw: WTN, 1999.
12. Kruszewski J., Gawroński W., Wittbrodt E., Najbor F., Grabowski S., *Rigid finite element method (in Polish)*, Warsaw: Arkady, 1975.

13. Lloyds Register of Shipping. 1988. *LRS Code for Offshore Platforms*, London.
14. *Norsok Standard, Subsea Structures and Piping System*, Rev. 2, June 1998
15. Olszewski H.: *The effect of foundation on dynamic characteristics of power turbine set (in Polish)*. Ph.D. thesis. Gdansk: PG, 2001
16. Polish Register of Shipping, Publication No. 105/P *Rules for Construction and Survey of Fixed Offshore Platforms*, 2014
17. Sarpkaya T., Isaacson M., *Mechanics of Wave Forces on offshore Structures*, Van Nostrand Reinhold Co., 1981.
18. Uhl T.: *Computer-aided identification of models of mechanical constructions (in Polish)*. Warsaw: WNT, 1997.
19. Wittbrodt E., *Dynamics of systems with time-dependent configuration: Finite Element Method (in Polish)*. Gdansk: Zeszyty Naukowe Politechniki Gdanskiej, nr 364, Mechanika XLVI, 1983.
20. Wittbrodt E., Adamiec-Wójcik I., Wojciech S., *Dynamics of flexible multibody systems: Rigid finite element method*, Berlin, Heidelberg, New York, Springer Verl., 2006.
21. Zhao C.T., Bai Y., Shin Y., *Extreme Response and Fatigue Damages for FPSO Structural Analysis*, Proc. of ISOPE'2001, 2001.
22. Zhang D., Yu S., Wang Y., Yue Q, *Sea ice management for oil and gas platforms in the Bohai sea*, Dalian University of Technology, China, Polish Maritime Research S.I. 2017 S2 (94) 2017 Vol. 24; pp. 195-204
23. Wang Z., Zhang B., Wang T., *Analysis and experiments on sea load and fastened mechanics on pipe clamps*, Polish Maritime Research S.I. 2017 S2 (94) 2017 Vol. 24; pp. 74-80
24. Kruszewski J., Wittbrodt E., Sawiak S.: *Computer Aided Design (CAD): Rigid finite element method in dynamics of structures (in Polish)*, WNT, Warsaw 1999.
25. Kruszewski J., Wittbrodt E.: *Vibrations of mechanical systems in computer approach. Volume I; Linear issues (in Polish)*, WNT, Warsaw 1992.
26. Kruszewski J., Wittbrodt E., Walczyk Z.: *Vibrations of mechanical systems in computer approach. Volume II; Selected issues (in Polish)*, WNT, Warsaw 1993.
27. Kruszewski J., Gawroński W., Wittbrodt E., Najbar F., Grabowski S.: *Rigid finite element method (in Polish)*, Wydawnictwo Arkady, Warsaw 1975.
28. UK Health & Safety Executive: *Offshore workforce involvement and consultation. Offshore Installations (Safety Representatives and Safety Committees) Regulations*, 1989.
29. DNV-RP-H103: *Modelling and Analysis of Marine Operations*
30. DNV-RP-C205: *ENVIRONMENTAL CONDITIONS AND ENVIRONMENTAL LOADS*
31. NORSOK N-003:2017: *Actions and action effects*
32. NORSOK N-006:2015: *Assessment of structural integrity for existing offshore load-bearing structures.*
33. NORSOK N-004:2013: *Design of steel structures.*
34. Massel S.R.: *Ocean Surface Waves: Their Physics and Prediction*, Advanced Series on Ocean Engineering – Volume 86, 2nd Edition, World Scientific, 1996.

#### **CONTACT WITH THE AUTHORS**

**Jacek Łubiński**

*e-mail: jacek.lubinski@pg.edu.pl*  
Gdansk University of Technology,  
ul. G.Narutowicza 11/12, 80-233 Gdańsk,  
**POLAND**

**Henryk Olszewski**

*e-mail: h.olszewski1@wp.pl*  
Gdansk University of Technology,  
ul. G.Narutowicza 11/12, 80-233 Gdańsk,  
**POLAND**

# AUTONOMOUS PLATFORM TO PROTECT MARITIME INFRASTRUCTURE FACILITIES

Eugeniusz Kozaczka

Grażyna Grelowska

Gdańsk University of Technology, Poland

## ABSTRACT

*Problems regarding the security of maritime infrastructure, especially harbours and offshore infrastructure, are currently a very hot topic. Due to these problems, there are some research projects in which the main goal is to decrease the gap and improve the methods of observation in the chosen area, for both in-air and underwater areas. The main goal of the paper is to show a new complex system for improving the security of the maritime infrastructure by means of many methods of observation – such as thermovision, optical devices, and radar systems – generally by means of an electromagnetic wave as a carrier of information in the air and acoustical methods in water. The system can be applied to the protection of maritime infrastructure as well as the coastal zone.*

**Keywords:** maritime infrastructure protection, offshore facilities, systems of surface and underwater observation

## INTRODUCTION

The problem of the protection of military and civilian ports against terrorist attacks from the sea, as well as the security of other critical maritime infrastructure facilities is gaining more and more interest in recent years. Offshore areas may represent the best type of environment to conduct clandestine operations, especially from the sea: the features of such an environment weaken the detection and identification processes carried out by defenders, while allowing the covert execution of illegal activities.

The most significant illegal activities conducted in such an environment include infiltration, drugs/weapons smuggling, sabotage/disruption of infrastructures, and even terrorist acts [10].

The danger of terrorist attacks exists also during peacetime, and naval forces are not always ready to counter unexpected terrorist attacks. Such attacks may occur during the forced withdrawal phase of peacekeeping operations, when the state of alertness is sometimes lowered. The threat of terrorist attack arises as the crisis situation develops, and in such crisis

situations sabotage and espionage acts are also likely to take place. The attacks conducted by terrorists or other groups or individual persons against naval bases, harbours, and other infrastructure can be accomplished, among other means, in the following manner [12]:

- surface attacks with manned and unmanned vessels used to carry explosives or as weapons platforms;
- underwater attacks using divers, mini subs (manned or remote-controlled), and explosives or sea mines.

These activities are accomplished through the use of a variety of means of transportation, which include cigarette boats and power boats, rigid hull inflatable boats (RHIBs), sailing/leisure boats, midget boats, swimmers/divers (with open/closed breathing systems), and swimmer delivery vehicles (SDVs).

Requirements such as flexibility, rapid reaction, resilience, high-level automation, and modularity have a key role in modern surveillance systems.

This paper proposes a system developed for critical infrastructure protection in accordance with the previous requirements.

## THE CONCEPT OF A MARITIME INFRASTRUCTURE SECURITY SYSTEM

There are many types of commercially available surveillance systems for the protection of large-area objects such as harbours, wind farms, and other offshore critical infrastructure [1, 4, 5, 11, 13]. However, some observations can be made regarding basic concepts of such systems, because there is a general tendency to include such components as:

- radar-visual observation systems with automatic target detection and tracking by a radar, followed by cueing of cameras for visual recognition;
- CCTV paired with thermal cameras for day and night observation capability;
- fusion of daylight and thermal camera images to obtain easy-to-comprehend output for a system operator;
- merging the radar and image data and visualization of the target trajectory on a digital map.

The above systems, primarily developed for land surveillance, are adapted to sea surface monitoring tasks. This sometimes creates problems because radar-visual observation systems can produce significant noise in cases of windy weather and rippled sea. As a result, noise filtration algorithms have to be implemented, both in radar and camera systems [2, 3].

Underwater and surface zones should be also monitored; this monitoring is provided by passive and active systems. Such solutions (sonars and magnetic barriers) are used in restricted harbour areas highly sensitive to unauthorized access (e.g., entrances to gas and oil terminals, pipelines, and ships anchored at terminals) [8, 9]. A system with integrated passive and active sensors, signal processing, and fusion units should be able to detect and identify surface and underwater targets, including divers [6, 7].

Both systems – radar camera for sea surface monitoring and hydroacoustic system for underwater sea area monitoring – are autonomous and can be deployed independently in the protected area. By connecting them via a network, a complex perimeter protection system can be obtained. Such a solution is then suggested by the authors as a coherent system for the protection of sea areas, managed by a single command and control centre, and connected by a cable or radio Ethernet network.

What is more, the proposed observation system is a mobile system, which can easily be transported to a selected point and transferred to another location, depending on needs.

The system consists of two main observation points: a mobile platform that is the main element of underwater and surface observations, and a long-range thermal imaging and long-range camera set on land as a basic element of observation in an air environment. The system integrates different types of sensors (e.g., radar, thermovision, and optical cameras or underwater acoustic and magnetic sensors) which cooperate in a multi-environmental scenario, above water and under water and sea surfaces.

The proposed concept of a protection system assumes the use and arrangement of its individual elements (sensors, system components, tool and software interfaces, and the operator

console) in agreed places, allowing effective protection of a given object or area. The concept assumes the integration, processing, and depiction of situations coming from all sensors of the security system at the command centre, which will be located on land. This information will also be transferred to the patrol boat to allow immediate response in the event of an emergency (Fig. 1).

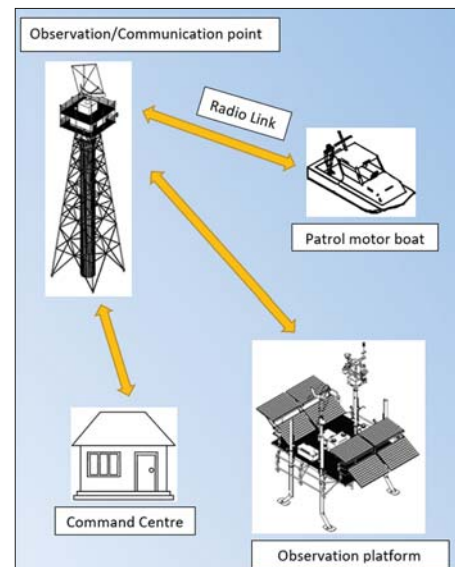


Fig. 1. Elements of the maritime infrastructure security system

## MULTI-SENSOR OBSERVATION PLATFORM

The sensor carrier for detecting objects moving both on and under the water surface is a multi-sensor measuring platform. The concept of the platform is shown in Fig 2. It consists of two main parts:

- an underwater part situated on the sea bottom of a protected water area, consisting of sensors and systems for recording and analysing signals;
- a surface part to which the underwater part is connected. Elements placed on the surface part ensure autonomous work of sensors in terms of energy (i.e., a set of batteries, photovoltaic panels, a wind turbine).

In addition, part of the surface observation sensors and a radio module for sending data to the communication point will be placed on the platform.

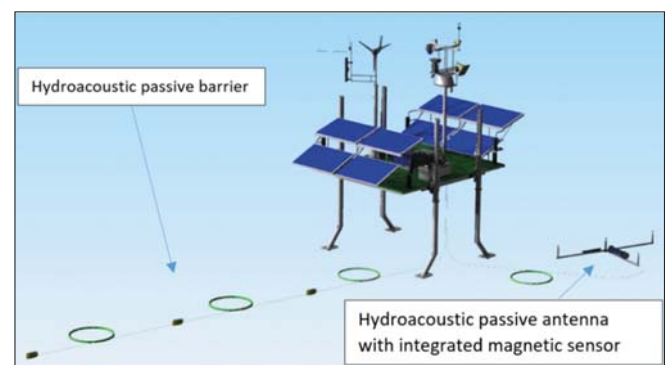


Fig. 2. The concept of a multi-sensor platform

On the platform, surface and underwater sensors are integrated. The measurement data, in full form or in the form of alarms about events, are sent by radio via the communication point to the command centre located on land. These data are also transferred to the patrol boat. The platform is generally designed as a stationary object that can be moved to any point using a specially designed carrier in the form of a catamaran equipped with a motor (Fig. 3). In this sense, the platform is an autonomous floating object.



Fig. 3. Observation platform with a transport catamaran

In addition, the platform is fully autonomous in the energy sense, i.e., powering and measuring devices and data transmission. It is equipped with large capacity batteries and natural, solar and wind energy sources. The platform is energy balance prepared, taking into account the demands of all measuring sensors tied to the platform; this allows us to conclude that given the atmospheric conditions typical of the Polish coast, the platform can operate without service during the spring–summer period for about 6 months. In the event of a lowering of the supply voltage below the permitted value, an alarm is sent to the command centre, from which it is possible to turn off or limit the power supply of selected sensors. The possibility of quick service intervention in such a situation is provided – the platform is equipped with a power generator that allows the batteries to be recharged.

### SURFACE PROTECTION VIA SENSORS INSTALLED ON THE PLATFORM MAST

The measuring platform has been equipped with a group of independent sensors, providing the operator with information about the situation prevailing in the upper hemisphere; these devices include a thermal imaging camera, a visible light camera, and a continuous wave radar. In addition, there are devices on the platform which support the platform's own protection: a searchlight with a remotely controlled head, a fisheye camera, a megaphone for generating messages, and devices necessary for the platform's operation in marine conditions, i.e., top lamp and weather station (Fig. 4).

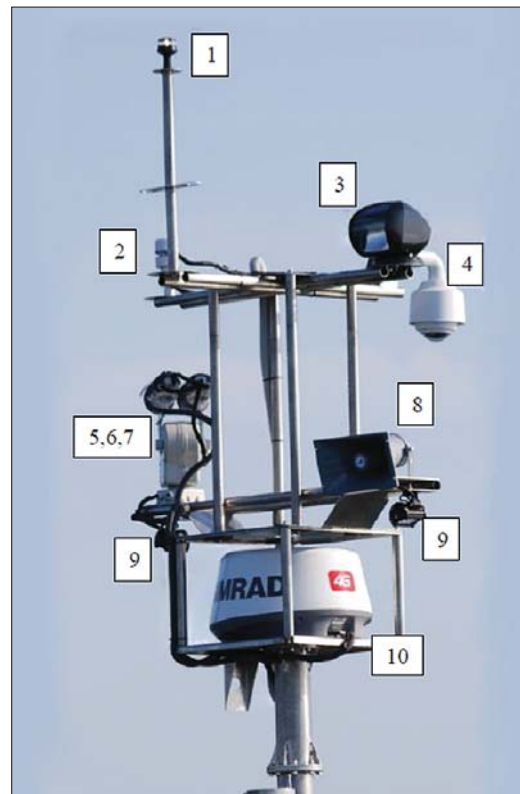


Fig. 4. Devices on the platform mast: 1) top lamp, 2) weather station, 3) searchlight – controlled head, 4) fisheye camera – platform supervision, 5) thermal imaging camera, 6) camera of visible light, 7) positioning system of thermal imaging camera and visible light, 8) megaphone for generating messages, 9) work lighting – LED, 10) radar

The main task of the surface observation subsystem on the platform is to protect the area that is difficult to access for observation from the camera located on the observation tower. This system consists of combined thermal imaging cameras and visible light, as well as a continuous wave radar.

Camera range studies were carried out for various scenarios in order to check the algorithms for detecting and tracking objects, and the quality of the obtained results. On the map (Fig. 5), two zones are marked off from the cameras: Zone I by 400 m–550 m and Zone II by 700 m–950 m. The object used for research – in this case, a pontoon with a length of 3.3 m and a width of 1.3 m driven by a 5 HP engine – moved along the indicated trajectories to obtain images in the following scenarios:

1. Initially, the object is outside the observation zone. Then, it appears on the left side and flows through the entire observation zone (trajectory 2 and trajectory 3).
2. The object has moved away from the camera to the maximum designated distance (trajectory 1).
3. The object approaches the camera from the set maximum distance (trajectory 1).
4. The object moves during the measurements: slowly at the speed of 2 knots, quickly at 10 knots (trajectory 2 and trajectory 3).
5. The object flows next to another object on the water (trajectory 1).

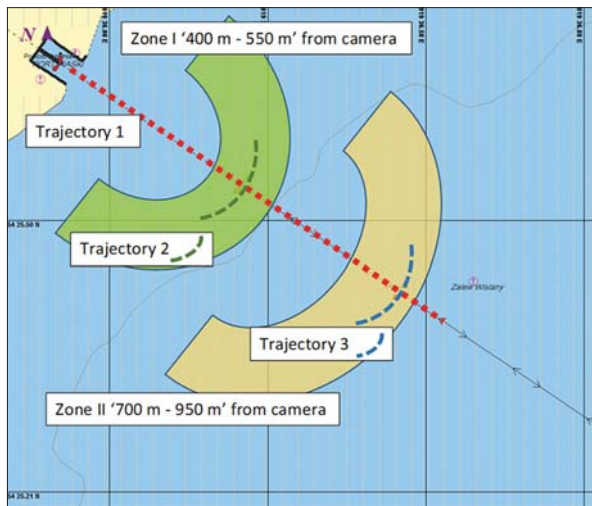


Fig. 5. Scenarios for the coverage of cameras

The object observed during the tests did not have any elements enhancing its image for both the thermal imaging cameras and radar imaging (no electromagnetic wave reflecting system used on ships). Below are two presentations of a pontoon from a thermal imaging camera at a distance of 500 m and 900 m (Figure 6).

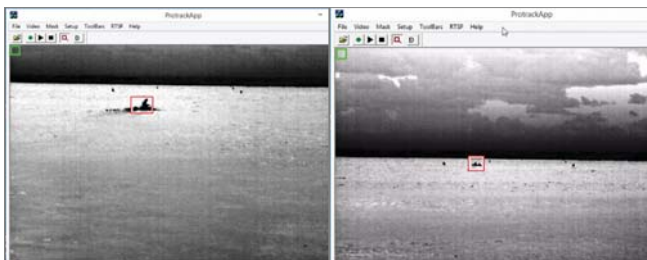


Fig. 6. Image from a thermal imaging camera at a distance of 500 m (left) and 900 m (right). The rectangle means the object 'tracked' using the ProTrack software

In addition, for comparison, the depiction of a visible light camera (Fig. 7) cooperating with a given thermal imaging camera is shown. The image allows full identification of the object and the crew that is on it. Imaging from the infrared camera when the pontoon is away from the sensor at a distance of 900 m enables detection and recognition of the floating object on the surface of the water.

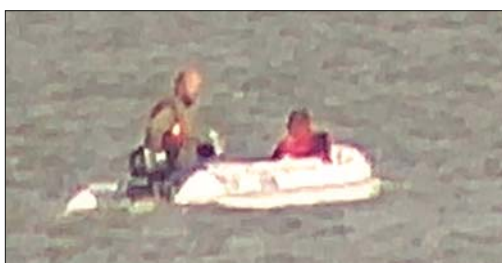


Fig. 7. An image from a video camera at a distance of 500 m

During the tests, the effectiveness of the algorithm for detecting objects moving on the water surface was tested; the ProTrack program was implemented in the software version, integrating the complete system. The detection algorithms

correctly followed a 3.3 m long pontoon at a distance of up to 590 m; most of the tests were carried out in this vessel. To sum up, the optical sensors installed on the mast of the platform enable full supervision of the water reservoir to a distance of about 1 km.

## UNDERWATER SUBSYSTEM INTEGRATED WITH THE PLATFORM

The sensors used for underwater observation were configured in the form of two systems:

- a hydroacoustic antenna integrated with a magnetic sensor;
- multi-sensor hydroacoustic barrier.

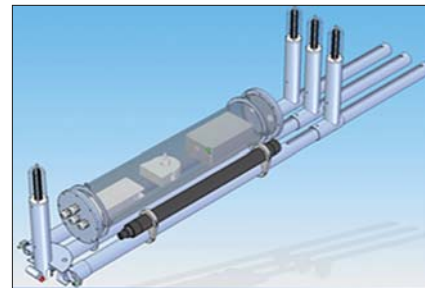


Fig. 8. Hydroacoustic antenna with magnetic sensor

A hydroacoustic antenna consisting of four measuring hydrophones enables the detection of an underwater signal and determination of the parameters of the detected object. By investigating the time of delay of signals arriving to individual hydrophones, we can determine the following parameters: bearing of the object, distance from the sound source, speed of movement of the underwater object, and geographical coordinates of the object.

The magnetic field from objects such as boats made of plastic is at a very low level; that is why the range of the magnetic sensor is a few metres.

A multi-sensor antenna consisting of digital hydroacoustic sensors connected by a cable makes it possible to create an acoustic barrier, for example, between the platform and the land (Fig. 9). Data transmission takes place via an Ethernet connection.

The hydroacoustic antenna and underwater barrier sensors connected to it are powered by a cable connecting the central antenna module with the surface part of this subsystem placed on the platform.

Due to the high mobility of the system, individual elements of the acoustic barrier module are connected in series, which makes it possible to minimize its weight, and also facilitates inserting and taking over the module in a given water reservoir.

The modularity of the system allows adding additional hydrophones, magnetometers, and entire blocks forming a hydroacoustic antenna. As a result, it is possible to easily expand and shape the configuration of the subsystem for detection of events in the lower half-sphere in a way that allows protection of any area of the basin.

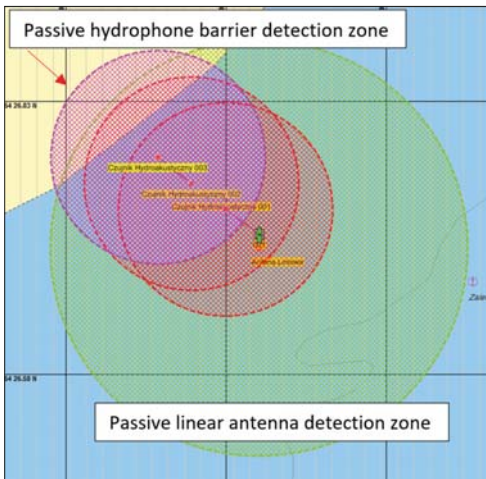


Fig. 9. Boundaries of protected areas by a hydroacoustic antenna (green area) and individual hydrophones included in the acoustic barrier (red circles)

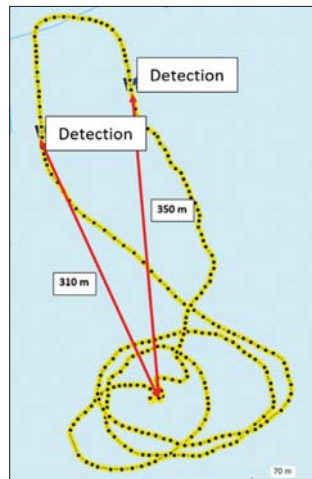


Fig. 10. The movement path of the floating object

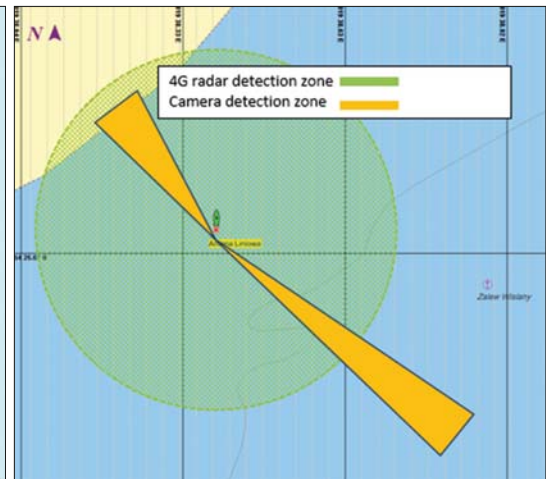


Fig. 11. Limits of the area protected by a hydroacoustic antenna (green area) and the radar alarm zone

## INTEROPERABILITY OF THE RADAR AND UNDERWATER OBSERVATION SYSTEM

Surface and underwater observation subsystems, for which the platform is a base, cooperate in detecting objects at a small distance from the observation point, which is especially important due to the purpose of the system. Observation areas of the underwater subsystem and radar subsystem coincide.

During measurement in natural conditions, tests were carried out in accordance with the following scenario:

A pontoon with a GPS receiver placed on it moves along the water in an irregular way. The observation is carried out simultaneously using:

- radar;
- hydroacoustic sensor barriers;
- a hydroacoustic antenna, which simultaneously sets the bearing on the object;
- and a differential magnetometer.

The movement path of the floating object is shown in Figure 10. The object was noticed and registered by all subsystems. Obtaining an alarm signal from the magnetometer required special procedures; i.e., it had to float in the area where the antenna was placed. There is no possibility of detection of the object from a greater distance, although the gradiometer used is a high quality device.

Underwater noise was received by all hydrophones – individual and included in the antenna – and the trace of the object was visible on the radar screen. In addition, up to the distance of about 350 m, it was possible to set the bearing.

The radar used in the system makes it possible to declare guarded zones (Fig. 11). The radar alarm occurred each time the object appeared in the guarded area.

## LONG-RANGE CAMERA TESTS

Long-range camera coverage tests were performed both during the day and at night. The following two images

(Fig. 12) present the possibilities of transmitting the image by means of a visible light camera and a thermal imaging camera placed on an observation tower on land. The distance from the camera transducers to the observed platform is 733 m; the distance was measured using a laser rangefinder integrated with the camera.



Fig. 12. Image from long-range cameras during the day: visible light camera (left), thermal imaging camera (right)

One of the main advantages of the long-range thermal imaging camera used in the maritime infrastructure support system is the focal variable. It enables observation of distant images by more than 14 km in the absence of visible light.

## INTEROPERABILITY OF A LONG-RANGE CAMERA WITH AN UNDERWATER OBSERVATION SYSTEM

Due to the integration of the system – thanks to which signals received from all observation subsystems as well as control signals of these systems are available in the command centre – it is possible to complement each part with various observation subsystems. The cooperation of the underwater observation system and the long-range thermal imaging camera is particularly important in night conditions when there is no lighting. The occurrence of an alarm from hydroacoustic sensors causes the camera to rotate in the direction of their arrangement, as shown in Fig. 13.

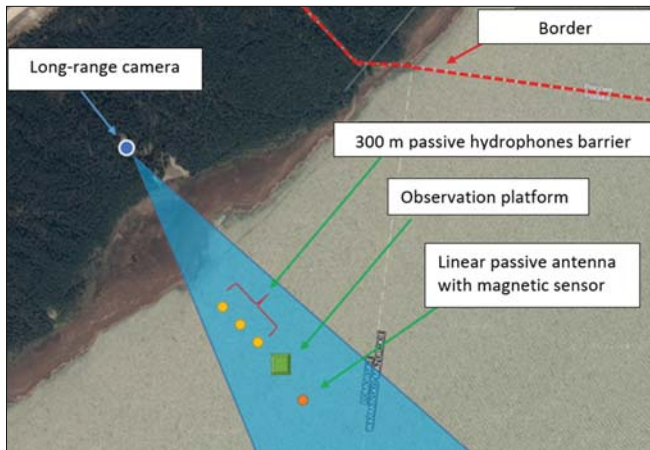


Fig. 13. Rotation of a long-range camera in response to a signal from the subsystem of underwater observation

Broadband observation of the protected zone enables detecting and identifying objects and unwanted people, regardless of the time of day. The system has the ability to visually track an object (human, vessel) that violates the protected zone.

## INTEGRATION OF SUBSYSTEMS: THE COMMAND CENTRE

The designed and implemented support system for maritime infrastructure protection using modern methods of event detection consists of several observation subsystems, from which data are transferred in real time to the command centre.

The command centre actually consists of two parts: the main part is located on land and an auxiliary is located on a patrol boat. In principle, the overriding authority to manage the border protection subsystems has a land station, but in a justified situation these can be programmatically transferred by the system administrator to the station on the patrol boat.

All observation subsystems are integrated in both places. All alarms and auxiliary information from observation subsystems reach both of these positions. Also, from both locations it is possible to manage subsystems in real time, such as changing sensor settings, turning them on or off, viewing camera images, listening to acoustic signals, switching on lights and alarms protecting the subsystems themselves, checking proper functioning of sensors, powering them, switching on emergency power, and broadcasting messages through megaphones, etc.

Our research into the maritime infrastructure protection system, carried

out in natural conditions, enabled us to check the functioning of all subsystems and the ability to transfer data between particular observation and surveillance points, as well as the quality of these signals. On this occasion, information necessary to prepare the visualization of events at the command centre was gathered. On account of limited space, the visualization of events system on the patrol boat console cannot be as extensive as in the case of the command centre on land.

The collected information on the functioning of all subsystems and all sensors in the natural environment was used to develop an interface that was implemented using a multi-layered geoinformatic system. The interface combines the following functions:

- visualization of data on a map covering the protected land and water areas;
- presentation of alarms generated in individual subsystems with the accuracy of individual sensors;
- control of sensor settings (detection thresholds, band filters);
- power system control;
- and control of the data transmission system.

A detailed functional outline of the interface was developed, which is presented in Fig. 14. The diagram depicts a set of sensors from which information should be adopted and presented in the interface.

Visualization of events and system operation takes place on two screens:

- main screen
- secondary screen

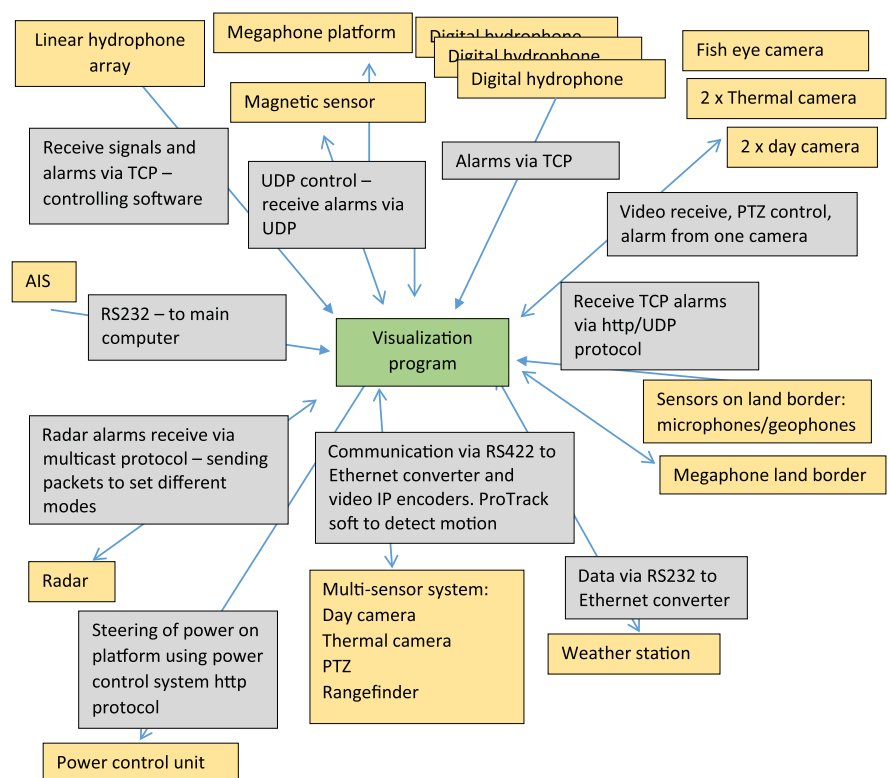


Fig. 14. Functional diagram of the user interface in the Command Centre

On the main screen there is a window with a map of the area under surveillance with the icons marked with points where the sensors are located (Fig. 15) and two windows for reading images from cameras.

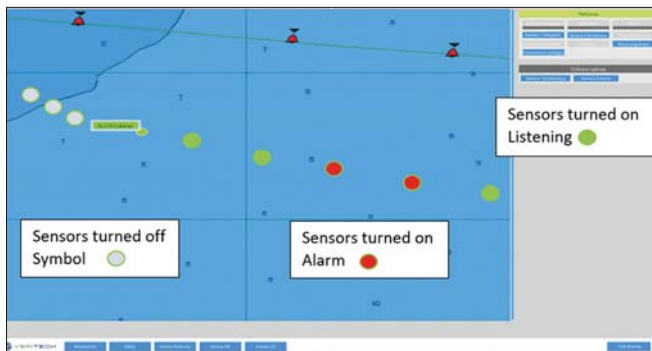


Fig. 15. Map with marked sensors

On the secondary screen there is a window for reading the image from any chosen camera or other sensors and a summary of information on the operating status of the devices in the form of a table (Fig. 16). At this point, the user can also turn on or off the power of individual subsystems or individual sensors.

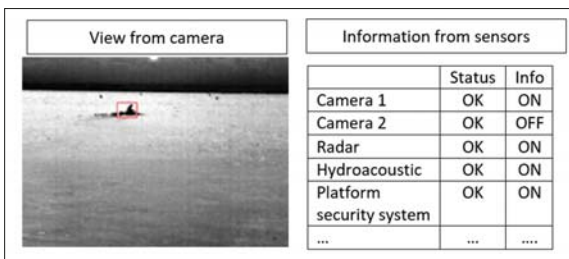


Fig. 16. Auxiliary screen – information on the state of the sensors

In addition, the settings of all devices and sensors operating in the system can be changed on the auxiliary screen (Fig. 17).

## SUMMARY

The presented system for monitoring the areas, both in the air and under water, uses modern methods of observation. Simultaneous operation of several systems allows for a relatively accurate observation of the chosen area. This applies to the area on the water itself as well as the underwater area. Its major advantage is that the independent components of the system can be applied in areas where a global system has areas of shadow. The advantage is also the mobility and energy independence of the observation platform.

The system uses the latest measurement, IT, and telecommunication technologies in image and signal processing from all sensors used for environmental observation and event detection. All software components have been integrated into one common platform. This means, among other benefits, there is access for all modules to shared resources and a possibility of cooperation of various elements in the unified user interface. The created software has interfaces that enable cooperation with other systems and provides full situational information to the command centre. The system has been developed in a way which enables the extension of cooperation with new sensors and devices, as well as systems that may be created in the future, without access restriction or limited implementation possibilities; this ensures the interoperability of the created system.

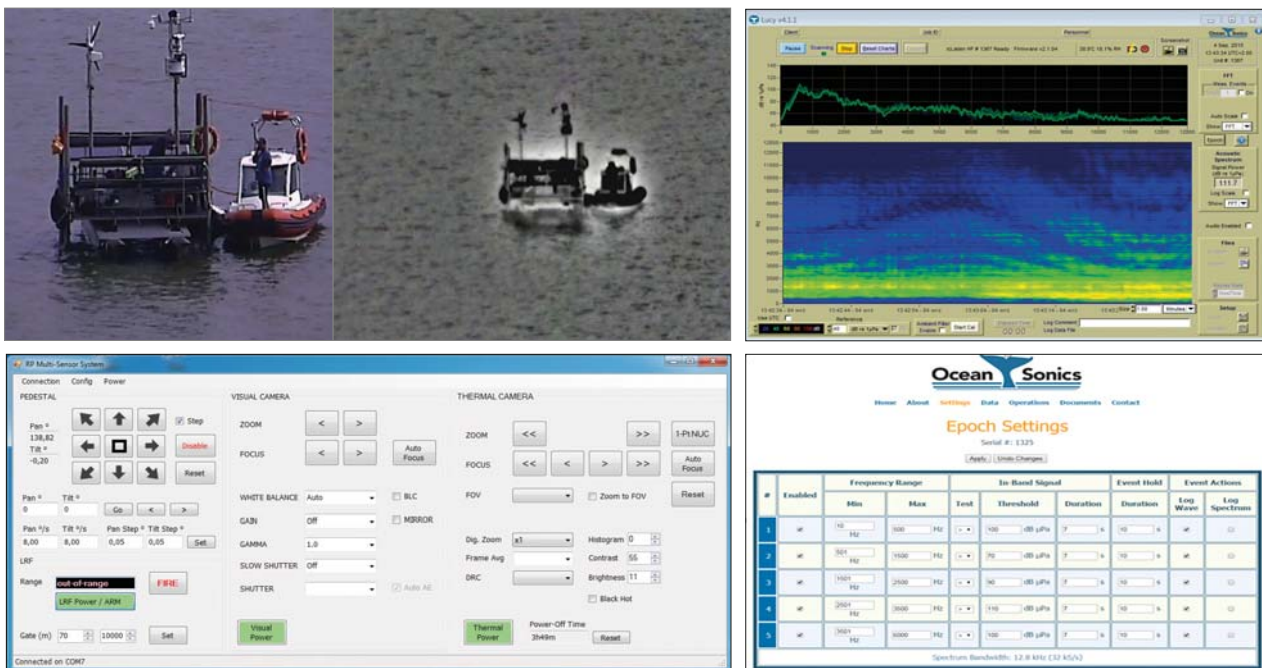


Fig. 17. Auxiliary screen – adjustment of long distance camera settings (left) and one of the hydrophones (right)

## ACKNOWLEDGMENTS

The investigation was supported by the National Centre for Research and Development, Grant No. DOBR/0020/R/ID3/2013/03.

## REFERENCES

1. Caiti A., Munafo A., Vettori G. (2009): System performance trade-off in underwater harbour protection, in *Proceedings of Int. Conf. Underwater Acoustic Measurements 09*.
2. Dobrucki A. B., et al. (2016): System for detection of the border violation on the Vistula Spit (in Polish), in *VII International Tech-Science Conference NATCON 'Naval Technologies for Defence and Security'*, K. Andziulewicz, H. Jando, T. Szubrycht (editors). Gdynia, Maritime Technology Centre, pp. 1–19.
3. Fasano G., et al. (2009): *Flight Test Results for a Multi Sensor Obstacle Detection and Tracking System for Sense and Avoid Applications*, AIAA Infotech and Aerospace.
4. Grelowska G., Kozaczka E., Szymczak W. (2017): *Acoustic Imaging Of Selected Areas Of Gdansk Bay With The Aid Of Parametric Echosounder And Side-Scan Sonar*, Polish Maritime Research, 24(4), 35–41.
5. Kastek, M., et al. (2012): Multisensor system for the protection of critical infrastructure of a seaport: unattended ground, sea, and air sensor technologies and applications XIV, in *Proceedings of SPIE – The International Society for Optical Engineering*.
6. Kozaczka E., Grelowska G. (2018): *Propagation of Ship-Generated Noise in Shallow Sea*, Polish Maritime Research, 25(2), 37–46.
7. Kozaczka E., Grelowska G., Kozaczka S., Szymczak W. (2013): *Diver Observations By Means Of Acoustic Methods*, Acta Physica Polonica A, 123(6), 1098–1100.
8. Luo J., et al. (2013): Denoising and tracking of sonar video imagery for underwater security monitoring systems, in *Proceeding of the IEEE International Conference on Robotics and Biomimetics (ROBIO)*, Shenzhen, China.
9. Piva S. et al. (2009): Heterogeneous sensors data fusion issues for harbour security, in *NATO Security through Science, Series C: Environmental Security*.
10. Rhodes B. J., et al. (2005): Maritime situation monitoring and awareness using learning mechanisms, in *Proceedings of IEEE MILCOM 2005 Military Communications Conference*, Atlantic City, NJ, USA.
11. Seibert M., et al., (2006): SeeCoast port surveillance, in *Proceedings of SPIE 6204*, 62040B.
12. Suchman D. (2005): Basic do's and don'ts of designing, installing and operating a harbor protection system, *Proceedings of TICA'05*.
13. Yan G., et al. (2011): General active position detectors protect VANET security, in *Proceedings of 2011 International Conference on Broadband and Wireless Computing Communication and Applications*, 6103009, 11–17.

## CONTACT WITH THE AUTHORS

**Eugeniusz Kozaczka**

*e-mail: kozaczka@pg.edu.pl*

Gdańsk University of Technology  
Narutowicza 11/12, 80-233 Gdańsk  
**POLAND**

**Grażyna Grelowska**

*e-mail: gragrelo@pg.edu.pl*

Gdańsk University of Technology  
Narutowicza 11/12, 80-233 Gdańsk  
**POLAND**

# STABILITY ANALYSIS OF THE FLOATING OFFSHORE WIND TURBINE SUPPORT STRUCTURE OF CELL SPAR TYPE DURING ITS INSTALLATION

Paweł Dymarski

Czesław Dymarski

Ewelina Ciba

Gdańsk University of Technology, Poland

## ABSTRACT

*The article presents the results of selected works related to the wider subject of the research conducted at the Faculty of Ocean Engineering and Ship Technology of the Gdansk University of Technology, which concerns design and technology of construction, towing, and settlement on the seabed, or anchoring, of supporting structures for offshore wind farms. As a result of this research, several designs of this type of objects were developed, including two stationary types: gravitational and Jack-up, which are placed on the seabed, and two floating types: TLP and SPAR, anchored with tendons and anchors in the form of nailed or suction piles. Below presented is the stability analysis of the new floating CELL SPAR type support structure for offshore wind turbines during its installation in waters with a depth of over 65 m.*

**Keywords:** towing and installation of SPAR platforms, anchoring of SPAR type platforms, calculation of dynamic loads in anchor ropes

## INTRODUCTION

As early as in ancient times, wind energy was used for moving various types of watering devices and mills with the aid of wind turbines, and for driving sailing boats. After inventing electric current generators, in 1888 James Blyth [1] applied a wind turbine with horizontal axis for moving a generator used for home lighting. With time, the designs of wind turbines were improved and their power increased, but until 1973, they were used merely locally to supply individual objects or small groups of them. And only in recent years, rapid grow in wind energy utilisation has been observed, and a large number of wind farms with turbines of several MW capacity, supplying national energy networks, have been built. Due to the limited area of available lands with favourable wind conditions for operation of these farms and the resistance from local communities, mainly caused by the noise emitted by wind turbines, a decision was made by coastal states to build offshore wind farms. Many research centres, including the Gdansk University of Technology,

started design and research projects on this subject. Among other issues, a number of reports and articles were published which presented new designs of turbine tower support structures for different water depths [2], [3], [4], [5], along with methods for their settlement on the seabed [6], or, in the case of floating structures, analyses of their stability and behaviour during towing, installation, and anchoring [7], [8], [9] and [10] and [11]. The first stationary offshore wind farm, with total power of 11x450 kW, was built on the coast of Denmark in 1991, at water depth of 2-4 m [12], while the first floating wind farm, Hywind Scotland, with total power of 5x6 MW and SPAR type foundations, started operation in autumn 2017. [13]. This article presents the structure and stability analysis of a floating platform of CELL SPAR type intended for use with 6 MW wind turbines at water depths of over 66 m.

## PLATFORM STRUCTURE AND EQUIPMENT

In the Polish Exclusive Economic Zone, plots of land for wind farms were firstly allocated in waters with a depth of up to 50 m, as shown in Fig. 1. It is expected that after utilising these areas, more wind power farms will be built in deeper waters, where the use of floating support structures, of TLP or SPAR type for instance, is fully justified.

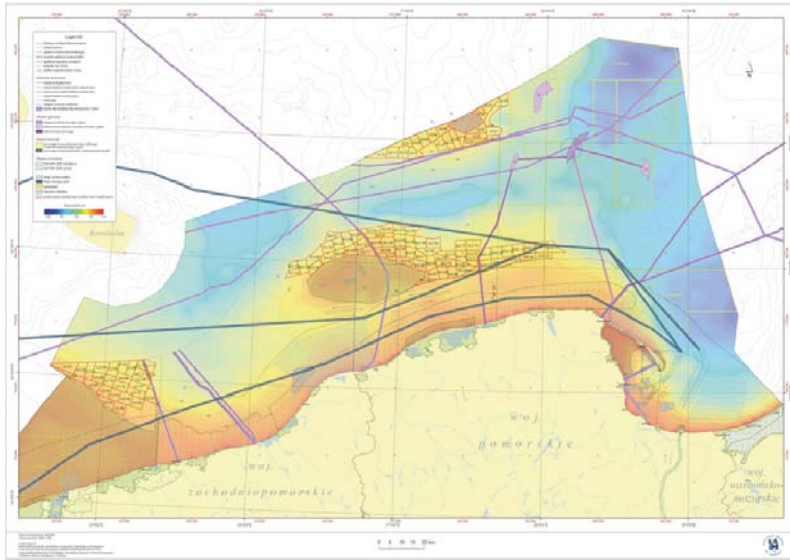


Fig. 1. Planned site of foundation on Baltic area in the Polish Exclusive Economic Zone, north of the town of Leba

When starting the design of a SPAR platform for wind power station with 6 MW turbine, intended to be installed in waters with a depth of over 65 m, the authors had no information about possible installation of the Hywind Scotland wind farm. The main criteria taken into consideration in this design concerned the potential of Polish shipyards to build SPAR platforms and their costs. Therefore, it was considered reasonable for the platform to consist of a set of identical or very similar elements with relatively small overall dimensions, which can be used as air or ballast tanks and, simultaneously, are relatively easy to build. Another requirement taken into consideration was that the platform structure should enable its safe towing and installation.

Fig. 2 shows a simplified view of the platform in four orthogonal projections and axonometric projection, with marked all tanks and chambers.

The designed platform is equipped with a basic ballasting system adapted for cooperation with an external pump unit. It was assumed that during moving the platform from horizontal to vertical position, it is ballasted with seawater and only after its anchoring, the ballast in lower tanks is replaced by pulp, being a mixture of gravel and sand collected from the seabed with seawater. At height of 10 m, the interiors of three columns 8 are separated by horizontal partitions.

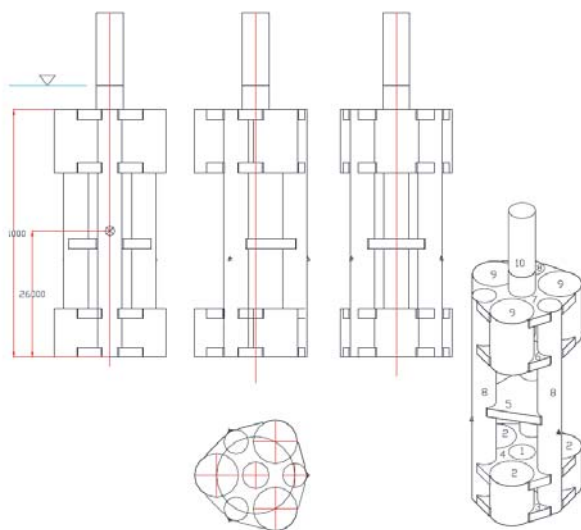


Fig. 2. Simplified view of the platform, with marked tanks and their parameters

1. Lower central tank - 1 -  $D=5,5m, H= 10 m V = 237,6 m^3$ ; 2. Lower tanks - 2 -  $D = 9 m, H = 10 m, 3 \text{ pieces}, V= 1908,5 m^3$ ; 3. Lower chambers - 3 and 4 - 2 pieces,  $V = 2 \times 200 = 400 m^3$ ; 4. Support columns - 8 -  $D = 5 m, H = 51 m, 3 \text{ pieces}, V = 3 \times 1000,1 = 3000,4 m^3$ ; 5. Central column - 10 -  $D = 5,5 m, H = 33 m, V = 784 m^3$ ; 6. Upper chambers - 6 and 7 - 2 pieces,  $V = 2 \times 200 = 400 m^3$ ; 7. Middle chamber - 5 -  $V = 274 m^3$

Other parameters: 1. Platform volume and mass of steel structure -  $V_c = 950,5 m^3, M = 2746 t$ ; 2. Height of centre of gravity of the platform from its bottom,  $X_c = 26 m$ ; 3. Submersion depth of empty platform in horizontal position,  $h_c = 6,5 m$ , and its displacement: 2732 t.

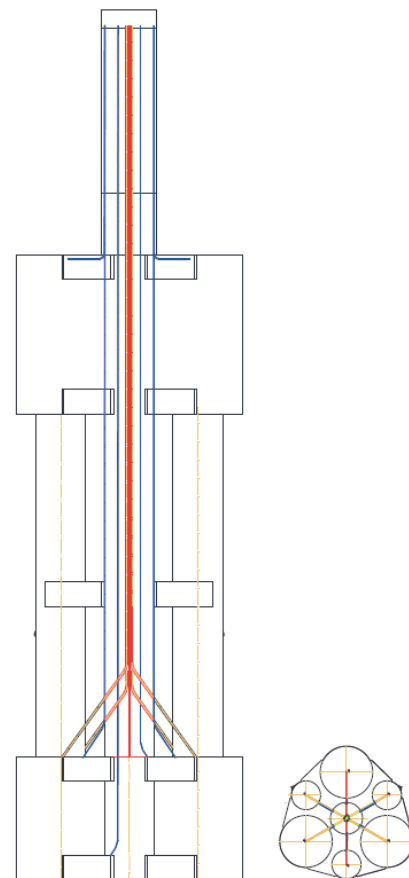


Fig. 3. Distribution of ballast pipelines (orange) and air pipelines (blue) composing the ballasting system.

Upper tanks of these columns can be ballasted with a certain amount of water to provide opportunity for controlling platform submersion, which is indispensable during anchoring, for instance. Two variants of the ballasting system have been developed. In both systems, all valves delivering the ballast water and all air valves are situated on the deck in the upper part of the central column, about 1,5 m below its flange. One of these variants, schematically shown in Fig. 2, assumes that all lower tanks and upper column tanks are connected, via ballast pipelines of larger diameter and air pipelines of smaller diameter, to valves on the central column deck. The ballast valves are situated in the central part of the deck, on the extension of a bundle of vertical pipes symmetrically distributed around the platform axis. The air valves are also distributed symmetrically, but close to the column wall. The unfavourable feature of this system is large number of pipelines, and the resulting problems with uniform distribution of water-gravel pulp to tanks and, in particular, to non-cylindrical chambers. On the other hand, its main advantage is better possibility to control the ballasting process when moving the platform from horizontal to vertical position.

### PLATFORM TOWING

Before starting the towing operation, six polyester anchoring ropes of 240 mm in diameter and approximately 60 m in length, with a loop at each rope end, will be attached to anchoring holders situated on platform's support columns (Item 8 in Fig. 2). These ropes will be tied around the platform circumference and secured against accidental unrolling during platform towing. Small floats will be attached to end loops of the ropes to ensure their floating on water during platform installation. The central column 10 will be covered with a tarpaulin or sufficiently thick foil fixed to the column

flange by screws and, if necessary, metal ring segments. The towing rope holder will be fixed with a number of screws to the lower part of the flange of column 10 (for horizontal position of the platform), or welded to its outer surface close to the flange.

The platform will be towed without ballast in horizontal position and with the column facing forward, as shown in Fig. 3.

### SEABED PREPARATION BEFORE PLATFORM ANCHORING

Preparing the seabed before anchoring the SPAR platform requires a number of identification and research studies concerning: possible ranges of extreme sea conditions (wind, wave, sea currents, temperature changes) [14], structure and strength of the seabed, and the effect of anchoring on natural environment, as well as economic and technical conditions. The present analysis refers to technical and, to some extent, economic aspects, and aims at selecting the best possible devices and technologies.

It was assumed that platform anchoring will be executed using six pre-tensioned ropes, symmetrically distributed in the way shown in Fig. 11. The initial, preliminary assumption was that anchor chains will be used as anchoring tendons. However, numerical analyses of the behaviour of such a chain system in rough sea conditions have revealed very unfavourable dynamic loads of these relatively rigid tendons in the entire range of their possible length changes [15]. That is why a decision was made to replace chains with polyester ropes having the following properties [16]

- material – Polyester
- diameter – 240 mm
- specific weight in air – 43,9 kg/m
- specific weight in water – 11,13 kg/m

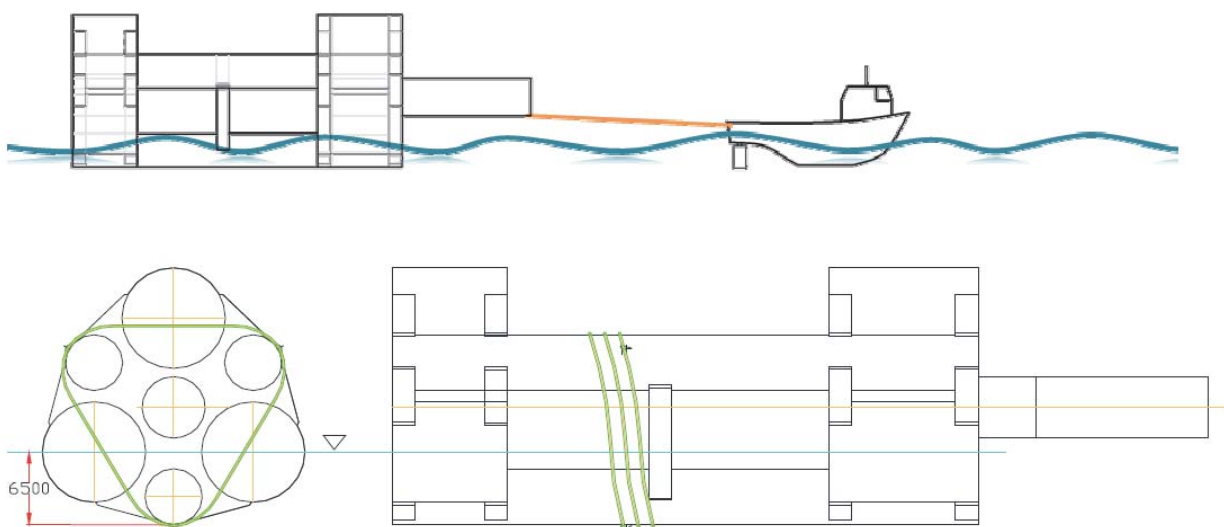


Fig. 4. Simplified drawing of platform during towing, with marked anchor rope attachment. Selected parameters of the towed platform:

- mass of empty platform –  $M_p = 2746$  t,
- height of centre of gravity –  $Z_o = 10,5$  m,
- volume of submerged part –  $V = 2726$  m<sup>3</sup>,
- height of centre of buoyancy –  $Z_v = 3,79$  m,
- moment of inertia of waterplane –  $I_x = 22882$  m<sup>4</sup>,  $I_y = 180036$  m<sup>4</sup>,
- small metacentric radius –  $r_o = 8,39$  m,
- initial metacentric height –  $h_o = 1,68$  m.

- minimal rope breaking force – 10,268 MN
- maximum elongation at 100% load - 22,5 % for new rope
- maximum elongation at 100% load - 16,5 % for rope in service

These ropes are used for anchoring floating objects. They have significant elasticity, at the same time preserving good mechanical strength, which is of high importance in the analysed case. For the anchoring system with geometric parameters shown in Fig. 11, the maximum forces in ropes were calculated, along with loads applied at rope attachment points to piles or other anchoring elements fixed to the ground in least favourable sea conditions. The calculated loads are the following:

- $F_{\max} = 7,418$  MN – maximum force in rope,
- $F_{p\max} = 10,854$  MN – maximum resultant load of a pile or another anchoring element, generated by two loading ropes,
- $F_{\max} = 8,49$  MN – maximum horizontal component of pile load,
- $F_{\max} = 6,76$  MN – maximum vertical component of pile load.

To provide firm and stable anchoring points for the platform, the anchors will have the form of piles driven into seabed, or suction piles. Based on the preliminary analysis, it was recognised that a more favourable solution is to use suction piles fixed to the seabed symmetrically at intervals of  $120^\circ$  about the axis of final platform position, at an approximate radius of  $R_p = \sim 61$  m, as shown in Fig. 11.

## PLATFORM INSTALLATION

### MOVING PLATFORM TO VERTICAL POSITION

The platform installation operation will be performed using a specialistic ship equipped with a deck crane and suspended platform for people, and with other specialised devices, including pumps and air compressors needed for efficient platform ballasting.

After towing it to the installation place, the platform will be kept in position by tugs. During this time, the column cover will be firstly dismantled. Then, temporary elements which immobilised the end loops of the anchoring ropes during towing will be removed and some floats (buoys) will be attached to them to facilitate rope lifting from water during the platform anchoring operation. Next, the platform service crew with necessary equipment and tools will be transported from the specialistic ship to the open column deck above the water surface, where all ballast and air valves for platform tanks are situated. The distribution of these valves is schematically shown in Figs. 3, 4, and 5. The ballast valves are situated centrally, close to the column symmetry axis, while the air valves are close to the cylindrical wall of the column. Next, an elastic pipe will be passed from the ship to the column. After connecting it repeatedly to successive valves, this pipe will be used for transporting pulp (water with sand) or water for platform ballasting. It is noteworthy that ballasting the platform tanks to move the platform from horizontal to vertical position is the most difficult and most challenging operation, during which large structure accelerations can be generated. Taking this into consideration, the authors performed the stability analysis of platform motion when ballasting successive ballast tanks in the sequence given in



Fig. 6. Changes of platform waterplane during ballasting

Fig. 5. For better clarity, the tanks ballasted in different steps are marked with different colours in the figure.

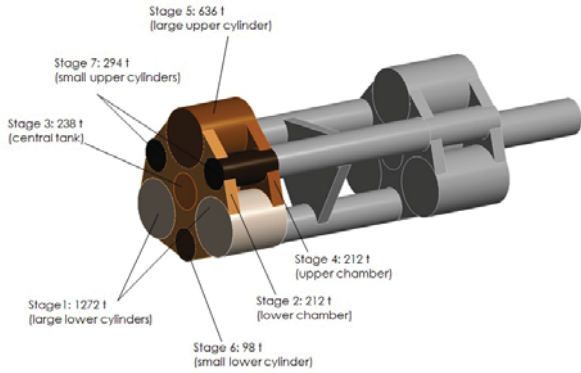


Fig. 5. 3D drawing of the platform in position before ballasting. Different ballast tanks are marked with different colours.

Fig. 6 shows platform waterplane changes during ballasting, starting from the horizontal platform position characteristic for towing, through successive steps of ballasting, up to final vertical position.

The diagram of changes of the platform inclination angle during filling of successive ballast tanks is shown in Fig. 7.

It can be observed that small changes of platform inclination angle, which are characteristic for initial ballasting stages, increase rapidly during the final stage, just before the platform reaches the vertical position.

The ballast introduced to the tanks changes the position of the platform's centre of gravity, which simultaneously results in the change of its centre of buoyancy. The trajectories of these two points during ballasting are shown in Fig. 8.

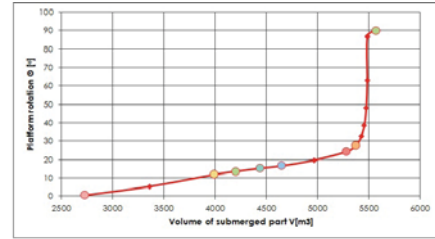


Fig. 7. Changes of platform inclination angle during successive stages of ballast tank filling.

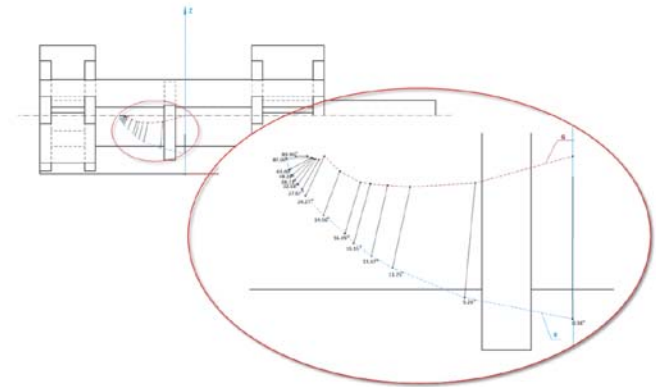


Fig. 8. Position changes of platform's centre of gravity and centre of buoyancy during successive ballasting steps.

The presented data was used for calculating changes of longitudinal and transverse metacentric heights as functions of platform trim. The trajectory of the longitudinal metacentric height of the platform is shown in Fig. 9.

The diagram on the left presents the entire trajectory,

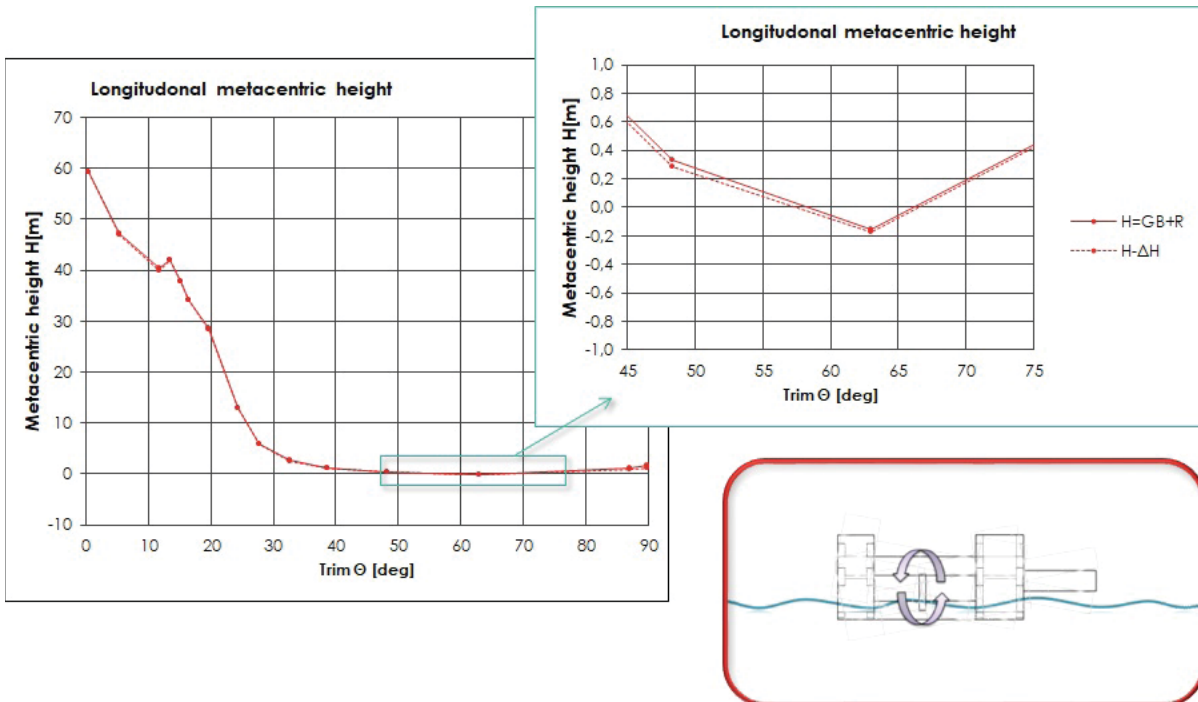


Fig. 9. Changes of platform's longitudinal metacentric height during successive ballasting steps.

while that on the right shows only its magnified fragment, marked as a blue rectangle in the former diagram. The magnified part refers to trim angles at which the metacentric height takes negative values, which may mean loss of platform's stability in the water displacement range of 5480-5550 m<sup>3</sup>. This stability loss may be a source of dynamic behaviour of the platform for angles ranging between 57-67 degrees.

Since for angles between 50-70 degrees, the metacentric height is very close to zero (with the accuracy of up to 0.3%  $GM_L$  determined for  $\theta=0$ ), it is difficult to predict accurately the platform behaviour based on classical methods. A reliable prediction of platform behaviour in this case can only be obtained using CFD methods taking into account the ballast water free surface, or model tests.

The trajectory of the transverse metacentric height of the platform is shown in Fig. 9. This quantity is always positive, which testifies to its stability in the entire range of platform trim angle changes.

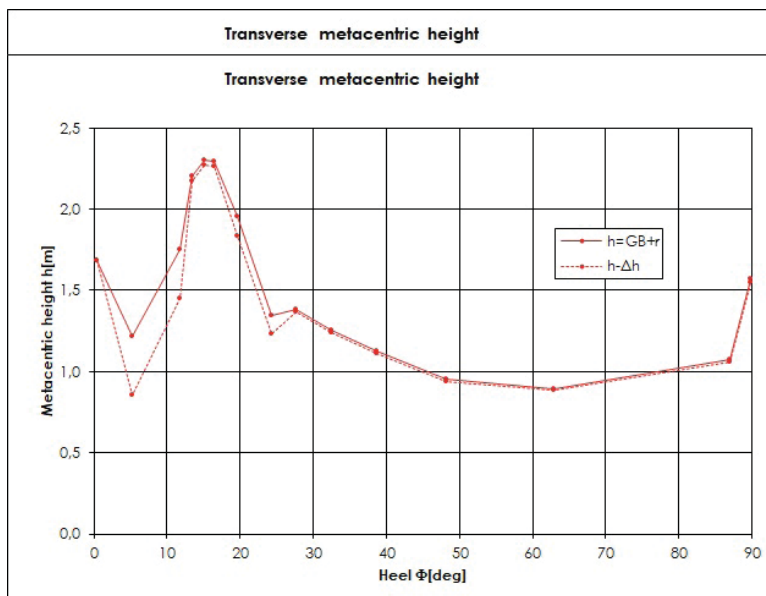
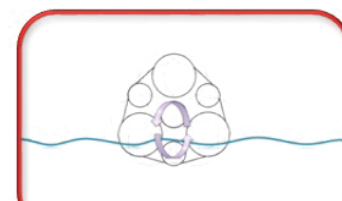


Fig. 10.

of platform's transverse metacentric height during successive ballasting steps



Changes

## PLATFORM ANCHORING

It was initially assumed that the platform anchoring system will be based on suction piles and slightly pre-tensioned polyester ropes. The geometric arrangement and parameters of this system in calm sea conditions are shown in Fig. 11.

Due to the lack of detailed information on the soil structure and characteristics of the seabed on which the platforms will be anchored, a preliminary assessment was made that the calculated loads of anchoring ropes can be carried by suction piles of 5 m in diameter, driven to the seabed soil to the depth of over 20 m. On the cover of each pile, an anchoring bitt will be mounted, which will be inclined in the vertical platform/pile symmetry plane by the angle of ~60 degrees to the horizontal plane, in the opposite direction

to the platform. This bitt will be used for holding loops of two anchoring ropes. The loops on other rope ends will be fastened to the bitts mounted on the platform, at the height of 20 m from its bottom.

Before starting the platform anchoring operation, the crew of the specialistic ship will increase slightly the platform ballast and the resulting draught, for the distance between the pair of bitts on the pile and platform to be slightly smaller than the length of the anchoring rope between the loops. Then the crew will lift floats with the attached anchoring ropes from the sea and move the ship close to the piles driven in the seabed. After that, one rope, with loops already free of floats, will be attached to a specially shaped sling on the crane's lifting cable and dropped on the bitt of the anchoring pile. The same operation will be repeated with the remaining ropes. After checking that all anchoring ropes are properly seated on the bitts, the crew will start partial de-ballasting of the platform, for its draught to reach 20 m at which the

anchoring ropes get a slight tension.

## SUMMARY AND CONCLUSIONS

The presented structural concept of a floating CELL SPAR platform intended for use as a support for a 6 MW wind turbine, along with the method of its towing and installation in water areas with a depth of over 65 m, is a real and relatively cheap technical solution to the problem of installation of offshore wind farms in the Polish Exclusive Economic Zone, at depths of over 65 m.

The proposed platform design takes into consideration the existing infrastructure and potential of Polish shipyards to build platforms of this type. The design underwent

preliminary technological evaluation in the NAUTA Repair Shipyard in Gdynia.

The numerical stability analysis of the platform moved to vertical position via proper ballasting of tanks has revealed that for angles ranging from 50 to 70 degrees (where 90 degrees means that the platform is in the vertical position), the longitudinal metacentric height is close to zero, and in the range of 57-67 degrees takes small negative values, which means the possibility of its dynamic transition to another point of equilibrium.

Determining the platform behaviour during the ballasting operation requires an additional CFD analysis and/or model tests to verify the possibility of appearance of dynamic phenomena and assess their effect on the safety of the platform installation process.

It can be concluded that the presented structural design of the platform and technology of its towing, settlement, and anchoring represent a real solution to the problem of installation of offshore wind farms on the Baltic sea, in the Polish Exclusive Economic Zone.

However, the authors stress that in the case of execution of the presented concept in a given real water area, the real strength and geometric parameters, in particular those referring to the anchoring system, may differ slightly from

the values presented in this article, as they depend on water depth and properties of the seabed soil.

## ACKNOWLEDGEMENT

This research was supported by The Polish National Centre for Research and Development (NCBR) under the project "WIND-TU-PLA" ERA-NET MARTEC II (Agreement No. MARTECII/1/2014)

## BIBLIOGRAPHY

1. Shahan Z. (2014). History of Wind Turbines. Renewable Energy World
2. Tony Burton T., Sharpe D., Jenkins N., Bossanyi E. (2001). Wind Energy Handbook. John Wiley & Sons, LTD, 2001
3. Peyrard Ch. (2015). Offshore Wind Turbine Foundations, EDF R&D – LNHE, Laboratoire d'Hydraulique St Venant. 2015
4. Dymarski P., Dymarski C., Żywicki J. (2015). Design and Strength Calculations of the Tripod Support Structure for Offshore Power Plant. Polish Maritime Research No 1(85) 2015 Vol. 22; pp. 36-46
5. Dymarski P. (2019). Design of jack-up platform for 6 MW wind turbine: Parametric analysis based dimensioning of platform legs. Polish Maritime Research No 2(102) 2019 Vol. 26; pp. 183-197. <https://doi.org/10.2478/pomr-2019-0038>
6. Moo-Hyun Kim et al (2012). Spar platforms. Technology and Analysis Methods. American Society of Civil Engineers
7. Bachynski E.E., Moan T. (2012). Design considerations for tension leg platform wind turbines. Marine Structures 29 (2012) 89-114
8. Żywicki J., Dymarski P., Ciba E., Dymarski C. (2012). Design of structure of Tension Leg Platform for 6 MW offshore wind turbine based on FEM analysis. Polish Maritime Research No S1(93) 2017 Vol. 24; pp. 230-241
9. Dymarski C., Dymarski P., Żywicki J. (2017). Technology concept of TLP platform towing and installation in waters with depth of 60 m. Polish Maritime Research No S1(93) 2017 Vol. 24; pp. 59-68
10. Karimirad M., Moan T. (2017). A simplified method for coupled analysis of floating offshore wind turbines. Marine Structures 27 (2012) 45-63
11. Karimirad M. (2013). Modeling aspects of a floating wind turbine for coupled wave-wind-induced dynamic

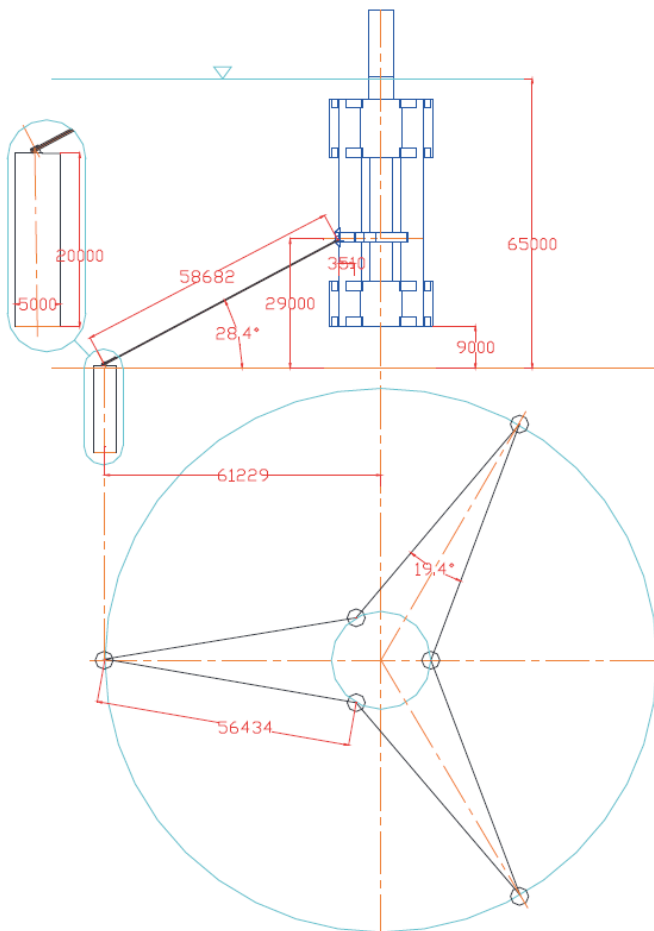


Fig. 11. Scheme of platform anchoring system in calm sea conditions. Suction piles, anchoring ropes, and points of rope attachment to the platform marked black.

analyses. *Renewable Energy* 53 (2013) 299-305

12. Environmental and Energy Study Institute (October 2010). "Offshore Wind Energy"
13. <http://www.4coffshore.com/windfarms/hywind-scotland-pilot-park-united-kingdom-uk76.html>
14. Dymarski P., Ciba E., Marcinkowski T. (2016). Effective method for determining environmental loads on supporting structures for offshore wind turbines. *Polish Maritime Research* No 1(89) 2016 Vol. 23; pp. 52-60
15. Dymarski P. Ciba E. (2017). Design of a cell-spar platform for a 6 MW wind turbine. Parametric analysis of the mooring system. Twenty First International Conference on Hydrodynamics in Ship Design and Operation - HYDRONAV, Gdansk, 28-29 June 2017
16. BRIDON. Fibre Rope Catalogue

## CONTACT WITH THE AUTHORS

**Paweł Dymarski**

*e-mail: pawdymar@pg.edu.pl*

Gdańsk University of Technology  
Narutowicza 11/12, 80-233 Gdańsk

**POLAND**

## IMPROVEMENTS TO A FIRE SAFETY MANAGEMENT SYSTEM

Wojciech Zeńczak

Agata Krystosik-Gromadzińska

West Pomeranian University of Technology Szczecin, Poland

### ABSTRACT

*The statistics invariably show that most onboard fires originate in the engine room. In hazardous conditions, fires can spread to other rooms of the ship and cause the loss of human life, and can cause the ship to be out of service or lost completely. To prevent these serious consequences, the engine room crew should be aware of hazards and ways to prevent them. It is also advisable to support their routine activities and actions in critical situations with an appropriate management system.*

*For this reason, a survey was conducted at the beginning of 2019 of engine room crew members employed by a European shipowner, as a contribution to an analysis of fire safety management. Based on the results of the survey, some of the elements of the fire safety management system of the ship engine room are described. A properly constructed system that is understandable and accepted by the crew is one of the most important factors in increasing fire safety on a ship. Familiarisation with adequate procedures can significantly contribute to the successful prevention of accidents. This paper also proposes a checklist based on suggestions by the crew, which may be helpful in onboard fire prevention.*

**Keywords:** fire safety; management system; engine room; ship accidents

### ABBREVIATIONS

AE	– auxiliary engine
FO	– fuel oil
HFO	– heavy fuel oil
IMO	– International Maritime Organisation
LNG	– liquid natural gas
LO	– lubricating oil
MCC	– motor control center
MDO	– marine diesel oil
ME	– main engine
MES	– maritime evacuation system
EMSA	– European Maritime Safety Agency
ER	– engine room
SOLAS	– Safety of Life at Sea

### INTRODUCTION

Fires onboard ships differ from land-based ones, and are much more dangerous to crew and passengers. Not only is the chance of finding an evacuation route much lower, but escape via a life raft, lifeboat or maritime evacuation system is also much more difficult than escape in land-based situations. Abandonment of the ship is also no guarantee of safety, since the chances of surviving outside of the ship are determined by many unpredictable factors such as weather and the risk of hypothermia.

The Annual Overview of Marine Casualties and Incidents 2018, prepared by the European Maritime Safety Agency (EMSA) [7], gives information on the distribution of casualty events for each type of cargo ship (see Fig. 1). Container ships, general cargoes and bulk carriers are the categories of ships in which most fires originate.

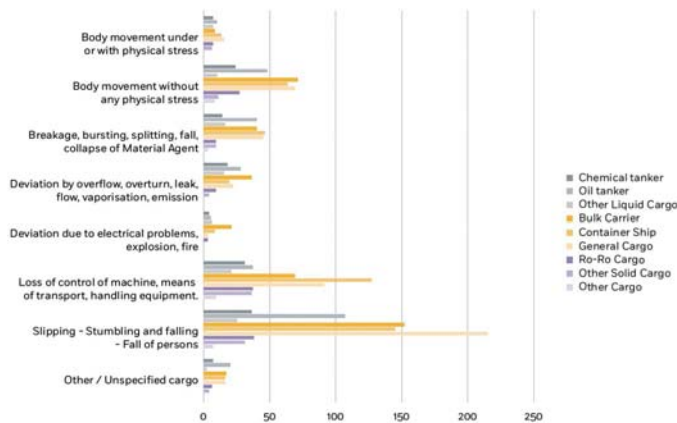


Fig. 1. Distribution of casualty events per cargo ship type for 2011-2017 [7]

Navigation events (loss of control, grounding/stranding, collision, contact) have been most frequent in recent years (Fig. 1), followed by fires and explosions, which have been assessed by EMSA as being in the top five causes of accidents [7, 25].

Most onboard fires originate in the engine room (ER). In hazardous conditions, these can spread to other parts of the ship and cause loss of human life, and may mean that the ship becomes out of service or is lost. The ER is a place where risk factors such as numerous sources of fire and flammable materials are located together within a small, cramped, hot space. The dangers of fire and explosion are determined by the type of fuel, and are different for merchant ships and warships. ER fires are associated with the risk of explosion in ships powered by dual fuel engines (MDO/LNG) due to the potential for a gas leak. In the case of fire and explosion, heavy damage and loss to the surroundings (including the environment), personnel and equipment are to be expected.

Approximately 60–70% of fires in ERs share a common scenario, based on the outflow of combustible liquid and contact with a hot surface. ER fires develop rapidly, and reach temperatures of 700–1000°C [12].

To prevent fires in the ER, the management of fire safety in the ER should form part of all stages of its existence, starting with the design process, continuing in everyday operation, and finally in the inspections conducted by competent and properly qualified agencies and societies. Risk-based assessments of safety in a wider sense, including fire safety, and analysis should also be included [11].

The most important element of this process is the daily routine activities conducted by the ship's ER crew. Controls, overhauls, inspections, repairs, measurements, and keeping spaces tidy and in order may be tedious tasks, but when performed using due and proper procedures supported by experience and care may greatly help in successfully maintaining an acceptable fire safety level in the machinery space.

There is strong evidence that the human element is the main reason for many major accidents, including fires. Erroneous actions by humans are the reason for most accidents during shore management and shipboard operations (57.8% of 1,654

analysed accidents) [7]. Erroneous human actions during shipboard operations are responsible for 70.1% of the total number of fires, and 76.4% of those on cargo ships [7].

## LITERATURE REVIEW

A study conducted in [1] of the factors related to human error in marine engineering identified the following factors: inadequate training (physical limitations, inadequate communication, bad judgement, fatigue, boredom), carelessness (wishful thinking, ignorance, negligence, folly, panic) and ego (laziness, greed, alcohol, mischief, violations). Further analysis identified poor planning/training, poor communication, a low-quality culture, cost-profit incentives, time pressure, the rejection information, ineffective monitoring and low morale of workers. Hence, in safety management, human factors should be analysed in detail.

A literature review on the topic of accidents in shipping, the influence of human errors and interventions to make shipping safer was carried out in [16]. A monograph to be used by chief engineers and others to assess the likelihood of human error in maritime operations was presented in [19], and the authors proposed an assessment tool for the likelihood of human error. The importance of proper communication in English to improve safety in shipping was highlighted [20].

The issue of safety management has been considered [14, 27], and the human factors in water transport have also been studied [2, 9, 15, 17]. Problems with the work culture onboard have been studied for different kinds of ships [6], offshore units, and in the context of crew errors [27], on Greek coastal vessels [10] and for Filipino shipmates [22].

The results of extensive studies concerning safety culture in the Finnish maritime sector have also been presented [26]. The basis for this study was a set of questionnaires and interviews with many representatives of Finnish maritime organisations. It was recommended that a maritime regulatory regime should be developed and a "learning the incident" approach should be well understood by the crew, becoming an element of onboard safety culture [23]. The role of a leader in the safety building process has been described [3, 4, 24], and safety management as an element of safety culture was addressed in [14, 21, 28]. The authors have discussed the human factor in relation to accidents in the maritime industry, and have identified the need for changes in management systems and work cultures to safety-oriented ones.

## REGULATIONS AND RECOMMENDATIONS FOR FIRE SAFETY IN THE ENGINE ROOM

It is generally accepted that rules are the best approach to fire prevention. In Ch.II-2 of the Safety of Life at Sea (SOLAS) Convention [18], the International Maritime Organisation (IMO) provides the key regulatory framework for fire safety on board ships. The objectives of fire safety are to prevent the occurrence of fire and explosions; to reduce the risk to life

caused by fire; to reduce the risk of damage caused by fire to the ship, its cargo and the environment; to contain, control and suppress fires and explosions within the compartment of origin; and to provide adequate and readily accessible means of escape for passengers and crew. In order to achieve these fire safety objectives, the following functional requirements are presented by the IMO: division of the ship into main vertical and horizontal zones by thermal and structural boundaries; separation of accommodation spaces from the remainder of the ship by thermal and structural boundaries; restricted use of combustible materials; detection of any fire in the zone of its origin; containment and extinction of any fire in the space of origin; protection of means of escape and access for fire-fighting; ready availability of fire-extinguishing appliances; and minimisation of the possibility of ignition of flammable cargo vapour. These principles underpin the philosophy of fire safety on board vessels [18].

The ER is a region of the ship where the prevention of ignition of combustible materials, and especially flammable liquids or gases, should be the most important aim, and functional requirements for this are mentioned in SOLAS. In addition to the regulations set out in the convention, an analysis of fire safety should cover the relationships between the people on board.

## FIRE SAFETY MANAGEMENT SYSTEM: A SIMPLIFIED ANALYSIS

A fire safety management system for a ship's ER may be defined as a series of regulations, procedures and actions performed at various stages in the existence of the object by the personnel, directly and indirectly, operating the machinery, equipment and installations and the personnel directly responsible for its safety. The engine room is the place where most marine casualties and accidents occur (Fig. 2), accounting for 1,810 out of 8,040 over the years 2011–2016.

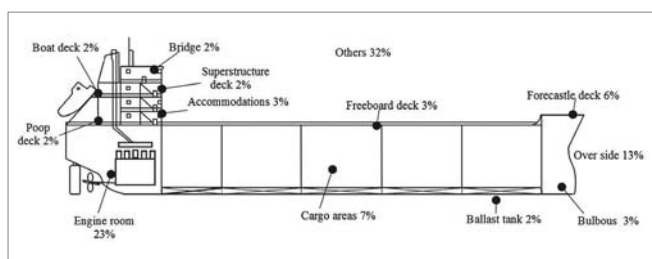


Fig. 2. Distribution of marine casualties and accidents, based on [1]

The personnel involved in the ship's ER fire safety management are the ship's crew, the owner, the classification society, inspectors, designers and shipbuilders.

Fire safety depends to a large extent on the design of the ER, and in particular the proper mutual arrangement of risk objects (potential ignition sources and flammable materials), provision of machinery space with effective structural protection elements and correctly selected and designed fire extinguishers installed in suitable places as well as portable fire extinguishing equipment.

In order to improve the fire safety level in the design phase, a correct plan for the arrangement of machinery should be made, chiefly in respect of the distances between potentially flammable materials and sources of leakage. It is also very important to design adequate routes for piping, and any flexible joints used should not be excessively bent. Easy access to potential risk objects and proper illumination should be provided for inspection.

ER fire safety is also dependent on the owner's actions. These include the provision of correct consumables (types and amounts), the planning of repairs and inspections, and the selection of effective machinery crew who are adequately trained and experienced, and are provided with safe working conditions and the possibility of resting properly. This also includes the planning of test alarms for various hazard scenarios, and compliance with requirements regarding training courses in land-based centres.

Classifiers and other inspectors are responsible for control of the condition of the ship's ER and for the crew meeting all formal requirements.

The last and most important link in the chain of safety management are the crew members, who have a direct influence on the maintenance of an acceptable level of safety. Performing or failing to perform specific activities, or acts of negligence or omission, are likely to be translated into effects on the level of safety. The most significant activities in terms of ER fire safety performed by the crew involve the control of fuel and oil installations with respect to tightness, leakage disclosure, splashes and sprays, control of insulation of hot surfaces, control of equipment and installations on the basis of the accepted regulations and procedural requirements.

Det Norske Veritas–Germanischer Lloyd recommends that areas such as potentially hot surfaces are examined. These include the engine bedplate and cylinder box, indicator valves, cylinder hoods, the exhaust pipe from each cylinder, the tie-in to the exhaust manifold, the exhaust manifold, and in particular overlaps between steel sheets and lagging, foundation and lifting lugs on exhaust ducts, turbochargers (especially flanges), and cut-outs for pressure/temperature sensors, etc. [5].

The potential sources of fuel leakage that should be checked include flexible hoses, couplings, clogged filters and fractured pipes. Attention should be paid to the installation, location and condition of all of these components. It is recommended that fuel oil and lubricating oil systems within the ER on ships in operation are periodically inspected by the shipowner in addition to class inspections [5].

DNV has been conducting temperature analyses of so-called trouble areas in the engine room. The most dangerous trouble areas are generally the exhaust duct insulation (260°C), the indicator valve (260°C), cut-outs for sensors (230°C), flanges between the exhaust manifold and exhaust duct (no insulation; 230°C) and the steel plate covering the exhaust manifold (gaps in insulation with no overlap between; 320°C) [5].

The locations of possible leakages and sources that could cause their ignition are shown in Fig. 3. These should be placed under special supervision.

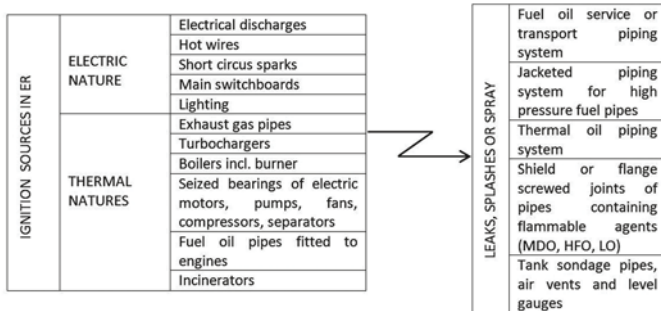


Fig. 3. Identification of ignition sources and leaks

## SURVEY ON FIRE SAFETY IN THE ENGINE ROOM

In order to confirm the factors that have been identified as affecting fire safety in a ship's ER, a list of control questions was formulated in the form of a survey with both closed and open questions, and this was presented at the beginning of 2019 to the ER crew employed by a European shipowner. There were three types of questions: questions with only one possible answer, questions with more than one answer to choose from, and open questions with space for the respondent to write their own answers.

The number of responses in each case was related to the total number of surveys and was presented as a percentage. In the case of questions where it was possible to select several responses, the sum of the responses could exceed 100%. Some of the questions were omitted by the respondents, and in this case, the sum of the responses was less than 100%. Only questions for which only one answer was possible and where all the respondents answered gave a total of 100%.

In total, 154 completed surveys were received. Due to the use of satellite internet connections, feedback from the crew was very fast. This demonstrates that the subject of fire safety is an important issue, and that the crews of ERs understand the need to take action to increase the level of safety and actively engage in this.

The aim of the survey was to ask the crew to identify the fire risk facilities in the ER, to assess the impact of a number of factors on the safety and comfort of both work and leisure, and to obtaining the crews' opinions on formal tools for increasing safety.

Among the factors causing a psychophysical load on the various workplaces in the ship's engine room, translating into the level of fire safety, a majority of respondents highlighted high temperatures (81.8%), noise (70.1%), an insufficient number of crew members (85.7%) and the multinationality of the crew (58.3%). Crew members also pointed to the problem of high levels of stress associated with their work (65%).

Fig. 4 shows the places identified by the crew members as requiring special supervision in the ER as a percentage of the responses to the survey. It can be seen that the respondents identified the separators and auxiliary rooms as requiring the greatest supervision, and the electrical motors as requiring the

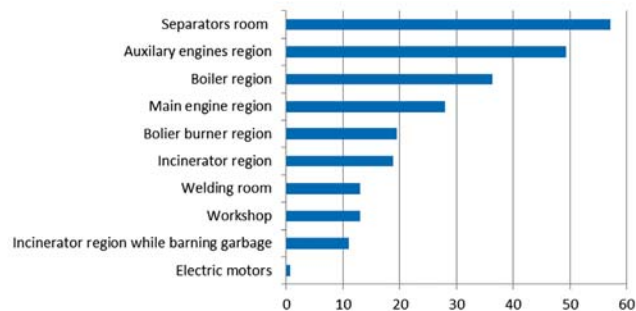


Fig. 4. Places requiring special supervision in the engine room as a percentage of respondents

least. An equally dangerous place, according to the survey, is the region of the auxiliary engine.

To control the risk of fire in the ER and to keep it to an acceptable level, the actions referred to above should be carried out regularly. The crew should also take proper care to ensure order and tidiness in the ER, as this can help in promptly noticing even the smallest leakages which may become a cause of fire.

The crew must be trained in procedures for different scenarios, in accordance with international legislation and safety management processes. This training must be carried out accurately and with the full involvement of the crew, and should be repeated if necessary.

With regard to the development of the fire safety management system, the opinions of the machinery crew based on their practical experience are also extremely important. The respondents were therefore asked about actions that could contribute to increasing the level of fire safety in the ER.

Fig. 5 shows the results of the investigation, with the value for each measure expressed as a percentage of respondents.

Respondents mainly highlighted the good education of the crew, including thinking about and maintaining cleanliness and order. In second place, they mentioned additional courses and training alarms. Only 0.65% of respondents believed that additional instructions or procedures were needed. These attitudes by the crew indicate that the management system should be relatively simple, without excessive formalism.

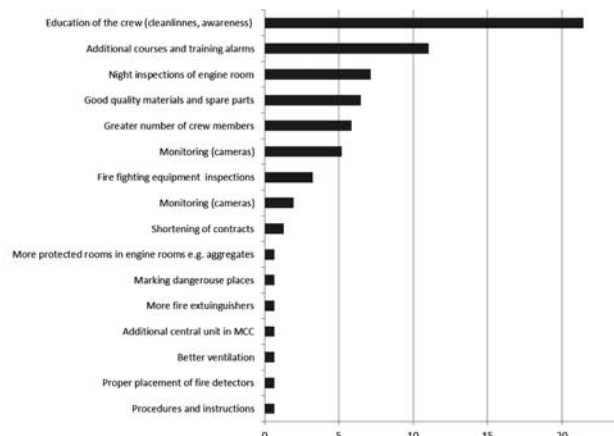


Fig. 5. Actions that can contribute to an increase in the fire safety level in the ER, expressed as a percentage of respondents

Each new fire safety management system, or changes in the existing one, should take into account its current state. Therefore, the crew members were also asked about training, knowledge of rules and conducting post-accident analyses. The results are shown in Fig. 6.

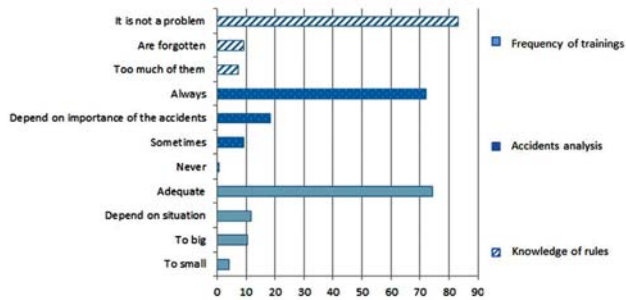


Fig. 6. Training, knowledge of rules and accident analyses, as percentages of respondents

It can be seen that the knowledge of fire safety rules was very good (83.1%). The answers to the questionnaire also indicated that the causes of fire in the ER were always analysed by the crew, and 74% of respondents believed that the frequency of training was adequate.

### ELEMENTS OF ENGINE ROOM FIRE SAFETY MANAGEMENT: PROPOSAL FOR IMPROVEMENT

It must be remembered that fire safety in the ER is an outcome of the combined efforts of the crew, servicemen, owner, authorities and classification societies. Of course, good design, appropriate materials and technology of production, and active and passive means of fire protection are important, but the real level of fire safety is connected with everyday conditions and crew maintenance. This is also reflected in the answers to the survey of crew members (Fig. 5).

For good operation and proper usage of the safety management system, it needs to be accepted by the crew and user friendly. The crew members were therefore asked about formal tools used to increase safety, such as checklists and procedures. The crew were also asked which types of forms, such as traditional paper-based ones or smartphone applications, were the most appropriate. The results are shown in Fig. 7.

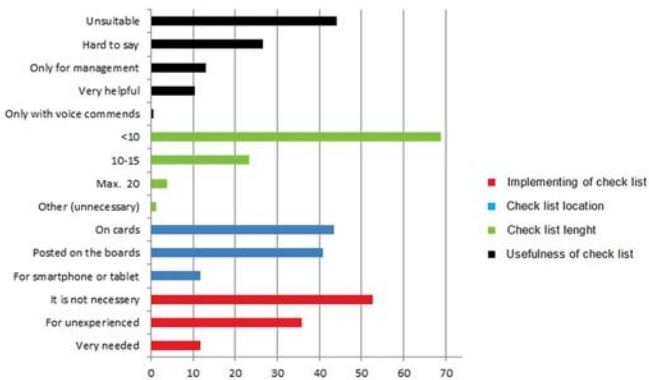


Fig. 7. Implementing of the checklist, its usefulness, length and location as the percentage of respondents

When analysing the results presented in Fig. 7, it can be seen that there are high levels of confidence in their own knowledge and self-confidence among the crew members. Most respondents did not see the need to use checklists, or thought that they could be useful only for less experienced crew members. Their usefulness is very limited under conditions of firefighting due to the need for rapid action, but they can be useful in everyday control and preventive activities. According to the respondents, the checklist should be as short as possible; 69% thought that it should not have more than 10 points. The most useful form of presentation was considered to be printed cards (43.5%), followed by display on boards (40.9%) and only 11.7% thought that displaying checklists on smartphones or tablets would be most effective.

Based on the results of the survey and the recommendations of classification societies, a solution for the fire safety management system in the ship's engine room can be proposed.

Fig. 8 characterises the main components of a fire safety system for an ER, partly based on [8]. Most of these are related to the knowledge and experience of the crew, and maintenance operations.

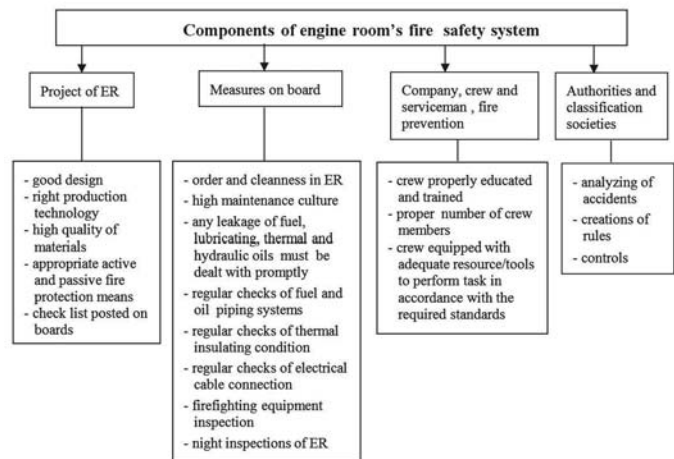


Fig. 8. Components of the fire safety system of an engine room

One of the most important components of the fire safety system of an ER is a checklist for everyday use, which we propose as one of the additional elements of the safety management system. In order to better prevent fires, the person on watch should use a printed copy in a survey of the ER and check the most important fire risk objects to decide if they are safe or unsafe by ticking "v" or "x" as appropriate. An example checklist (Table 1) is presented below. As suggested by responders, this is a user-friendly list that is ready to print for daily inspections, and contains only nine points. It can be easily modified to fit different types of ERs and different arrangements. Due to its simplicity, it can be easily transformed for smartphone applications, or even as a part of an e-management system dedicated to fire safety of the ER. For the inspection of surface temperatures, it is recommended to use devices that can take remote temperature measurements, such as pyrometers and infrared thermometers.

Tab. 1. Example checklist for fire safety inspection of an engine room

No	Inspection Items	Check					
		Cleanliness & orderliness	Oil or fuel spill	Leakages	Isolation	Machines working correctly	Surface temperature
1	Separator	<input type="checkbox"/>	<input type="checkbox"/>	<input type="checkbox"/>	<input type="checkbox"/>	<input type="checkbox"/>	<input type="checkbox"/>
2	AE	<input type="checkbox"/>	<input type="checkbox"/>	<input type="checkbox"/>	<input type="checkbox"/>	<input type="checkbox"/>	<input type="checkbox"/>
3	ME	<input type="checkbox"/>	<input type="checkbox"/>	<input type="checkbox"/>	<input type="checkbox"/>	<input type="checkbox"/>	<input type="checkbox"/>
4	Boiler & burner	<input type="checkbox"/>	<input type="checkbox"/>	<input type="checkbox"/>	<input type="checkbox"/>	<input type="checkbox"/>	<input type="checkbox"/>
5	Incinerator	<input type="checkbox"/>	<input type="checkbox"/>	<input type="checkbox"/>	<input type="checkbox"/>	<input type="checkbox"/>	<input type="checkbox"/>
6	FO piping system	<input type="checkbox"/>	<input type="checkbox"/>	<input type="checkbox"/>	<input type="checkbox"/>	<input type="checkbox"/>	<input type="checkbox"/>
7	LO piping system	<input type="checkbox"/>	<input type="checkbox"/>	<input type="checkbox"/>	<input type="checkbox"/>	<input type="checkbox"/>	<input type="checkbox"/>
8	E-motors	<input type="checkbox"/>	<input type="checkbox"/>	<input type="checkbox"/>	<input type="checkbox"/>	<input type="checkbox"/>	<input type="checkbox"/>
9	Workshop	<input type="checkbox"/>	<input type="checkbox"/>	<input type="checkbox"/>	<input type="checkbox"/>	<input type="checkbox"/>	<input type="checkbox"/>
Comments:							

## CONCLUSION

Onboard engine room fires may spread in and beyond machinery spaces, thus causing the loss of the entire vessel. They constitute a danger to the health and life of both the crew and passengers. Their most frequent cause is leakage from a fuel installation onto a hot surface.

Fire safety crew management is an important factor in preventing fires more efficiently. The results of a survey were presented in which crew members employed by a European ship owner were asked about the risk factors of fires and methods to prevent them. Their answers were used to improve a crew fire management system, and in drawing up a checklist.

The respondents identified that the separators and auxiliary rooms were the riskiest objects in the engine room, and highlighted good crew education, thinking, maintaining cleanliness, order, additional courses and training alarms as the most effective ways to improve fire safety. In the opinions of the respondents, additional tools to improve fire safety management were not necessary; if introduced, these should be short, such as checklists to be used as printed cards. In accordance with the crew's recommendations, an example checklist for everyday inspections of the ER was presented.

## REFERENCES

1. Bea R.G. (1994). *Report SSC-378. The Role of Human Error in Design, Construction, and Reliability of Marine Structures*. Ship Structure Committee. Retrieved from <https://apps.dtic.mil/dtic/tr/fulltext/u2/a288588.pdf>.
2. Berg H.P. (2013). *Human Factors and Safety Culture in Maritime Safety*. International Journal on Marine Navigation and Safety of Sea Transportation, 7(3), 343–352.

3. Bielic T., Predovan D., Culin, J. (2017). *The Role of the Master in Improving Safety Culture Onboard Ships*. Transnav – International Journal on Marine Navigation and Safety of Sea Transportation, 11(1), 121–124.
4. Borgersen H., C., Hystad S.W., Larsson G. et al. (2014). *Authentic Leadership and Safety Climate Among Seafarers*. Journal of Leadership & Organizational Studies, 21(4), 394–402.
5. DNV-GL. (2017). *Hot Surfaces in Engine Room*. Technical Paper, Paper Series 2000-P025. Retrieved from <https://exchange.dnv.com/Documentation/Maritime/FireSafety/Hot%20Surfaces%20Paper.qxd.pdf>.
6. Ek A., Runefors M. and Borell J. (2014). *Relationship Between Safety Culture Aspects – A Work Process to Enable Interpretation*. Marine Policy, 44, 179–186.
7. EMSA. (2018). *Annual Overview of Marine Casualties and Incidents 2018*. Lisboa. Retrieved from <http://www.emsa.europa.eu/emsa-documents/latest/item/3406-annual-overview-of-marine-casualties-and-incident-2018.html>
8. GARD. (2013). *Fire Safety In The Engine Room*. Retrieved from <http://www.gard.no/web/updates/content/53332/fire-safety-in-the-engine-room>.
9. Gausdal A.H., Makarova J. (2017). *Trust and Safety Onboard*. WMU Journal of Maritime Affairs, 16(2), 197-217.
10. I Gemelos I.C., Ventikos, N.P. (2008). *Safety in Greek Coastal Shipping: The Role and Risk of Human Factor Revisited*. WMU Journal of Maritime Affairs, 7(1), 31–49.
11. Gerigk M. (2007). *A Model of Performance-Oriented Risk-Based Assessment of Safety of Container Ships*. Polish Maritime Research, Special issue 2007/S1.
12. Getka R. (2011). *Evacuation Routes From Machinery Spaces – Quantity, Construction and Layout*. Scientific Journals Maritime University of Szczecin, 28(100), 19–26.
13. Hanchrow G.A. (2017). *International Safety Management – Safety Management Systems and the Challenges of Changing a Culture*. Transnav – International Journal on Marine Navigation and Safety of Sea Transportation, 11(1), 125–131.
14. Havold J.I., Nettet E. (2009). *From Safety Culture to Safety Orientation: Validation And Simplification of a Safety Orientation Scale Using a Sample of Seafarers Working for Norwegian Ship Owners*. Safety Science, 47(3), 305–326.
15. Havold, J.I. (2007). *National Cultures and Safety Orientation: A Study of Seafarers Working for Norwegian Shipping Companies*. Work and Stress, 21(2), 173–195.

16. Hetherington C., Flin R., Mearns K. (2006). *Safety in Shipping: The Human Element*. Journal of Safety Research, 37(4), 401–411.
17. Hystad S.W., Nielsen M.B., Eid, J. (2017). *The Impact of Sleep Quality, Fatigue and Safety Climate on the Perceptions of Accident Risk Among Seafarers*. European Review of Applied Psychology – Revue Européenne de Psychologie Appliquée, 67(5), 259–267.
18. IMO (2015): International Convention for the Safety of Life at Sea.
19. Islam R., Yu H., Abbassi R., Garaniya V., Khan, F. (2017). *Development of a Monograph for Human Error Likelihood Assessment in Marine Operations*. Safety Science, 91, 33–39.
20. James A.J. (2018). *Improving Maritime English Competence as the Cornerstone of Safety at Sea: A Focus on Teaching Practices to Improve Maritime Communication*. WMU Journal of Maritime Affairs, 77(2), 293–310.
21. Kongsvik T.O., Storkersen K.V., Antonsen, S. (2014). *The Relationship Between Regulation, Safety Management Systems and Safety Culture in the Maritime Industry*. In: 22nd Annual Conference on European Safety and Reliability (ESREL), Amsterdam, Netherlands, 1013, 467–473.
22. McVeigh J., MacLachlan M. (2019). *A Silver Wave? Filipino Shipmates' Experience of Merchant Seafaring*. Marine Policy, 99, 283–297.
23. Pomeroy R.V., Earthy J.V. (2017). *Merchant Shipping's Reliance on Learning from Incidents – A Habit That Needs to Change for a Challenging Future*. Safety Science, 99, 45–57.
24. Rumawas V., Asbjornslett B.E. (2016). *Human Factors on Offshore Supply Vessels in the Norwegian Sea. An Explanatory Survey*. International Journal of Maritime Engineering, 158(A1), A1-A14.
25. Salem A. (2019). *Vehicle-Deck Fires Aboard Ropax Ships: A Comparison Between Numerical Modelling and Experimental Results*. Polish Maritime Research, 2(102), 26, 155–162.
26. Teperi A.M., Lappalainen J., Puro V., Perttula P. (2018). *Assessing Artefacts of Maritime Safety Culture – Current State and Prerequisites for Improvement*. WMU Journal of Marine Affairs.
27. Veiga J. L. (2002). *Safety Culture in Shipping*. WMU Journal of Maritime Affairs, 1, 17–31.
28. Wang J. (2002). *A Brief Review of Marine and Offshore Safety Assessment*. Marine Technology and SNAME News, 39(2), 77–85.

## CONTACT WITH THE AUTHORS

**Wojciech Zeńczak**

*e-mail: Wojciech.Zenczak@zut.edu.pl*

West Pomeranian University of Technology Szczecin  
Piastów AV. 41, 71-065 Szczecin

**POLAND**

**Agata Krystosik-Gromadzińska**

*e-mail: agata.krystosik@zut.edu.pl*

West Pomeranian University of Technology Szczecin  
Piastów AV. 41, 71-065 Szczecin

**POLAND**

## ANALYSIS OF THE PROJECT OF INNOVATIVE FLOATING TURBINE

Andrzej Tomporowski<sup>1</sup>

Ali Al-Zubiedy<sup>2</sup>

Józef Flizikowski<sup>1</sup>

Weronika Kruszelnicka<sup>1</sup>

Patrycja Bałdowska-Witos<sup>1</sup>

Jacek Rudnicki<sup>3</sup>

<sup>1</sup> UTP University of Science and Technology, Bydgoszcz, Poland

<sup>2</sup> University of Babylon, Faculty of Materials Engineering, Babylon Hilla, Iraq

<sup>3</sup> Gdańsk University of Technology, Poland

### ABSTRACT

*The design of a floating, innovative device for river water aeration and conversion of mechanical energy to electrical energy required the analysis of a number of geometrical and dynamic features. Such an analysis may be carried out on the basis of existing methods of numerical fluid mechanics. Models of pressures, forces and torques characteristic for the conversion of watercourse energy were developed for two basic concepts of innovation. These pressures, forces and torques were calculated, designed, and experimentally determined for the variable geometric form and dimensions of the designed working elements of the innovative roller-blade turbine rotor.*

**Keywords:** design, innovative aeration unit, water roller drive

### INTRODUCTION

For the need of energy and water aeration on the rivers Tigris (length of 1900 km) and Euphrates (length of 2,700 km) (Turkey, Syria, Iraq), an innovative floating turbine has been designed. 98% of Iraqi water comes from rivers Tigris and Euphrates. The design of the floating device used in the process of river water aeration and conversion of mechanical energy to electricity required the analysis of a number of design features. This analysis may be carried out on the basis of the existing methods of numerical fluid mechanics [1–3].

Despite a relatively simple geometry of the system, the flow in the water wheel area is characterized by considerable complexity. The analysed physical phenomenon is the unsteady two-phase flow [4].

Modelling of flows in rotor machines, with the interaction between rotating and stationary elements, is a known issue [5–9], and a number of models were developed to analyse it. However, the analysis of the water flow in the wheel area

requires not only taking into account the movement of the blades, but also their work in different media: water and air, which makes it necessary to apply methods of modelling the interface separation [10, 11].

The complexity of such a model requires time-consuming calculations, including the motion of blades in both media [12–15]. In the light of the identified issues, the specific objectives of the reported research-design work were as follows:

- Developing the model of pressures, forces and torques characteristic for the conversion of watercourse energy, as well as developing the concept of geometric features and parameters of the main working elements of a roll turbine aerator to be used in construction design, manufacturing, and implementation in working components of the innovative power-process unit.
- Experimental recording of pressures, forces and torques in a geometric form having the dimensions of the main working elements of the innovative power-process unit roll turbine aerator.

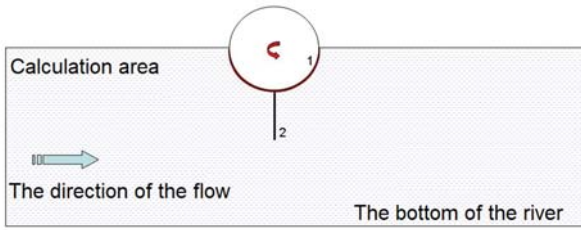


Fig. 1. Calculation area – concept 1A

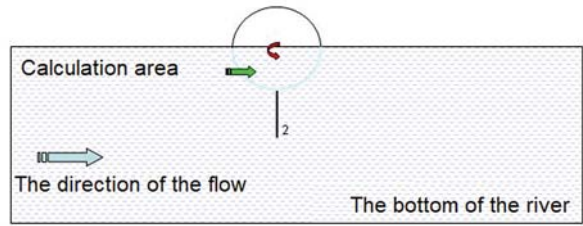


Fig. 2. Calculation area – concept 1B

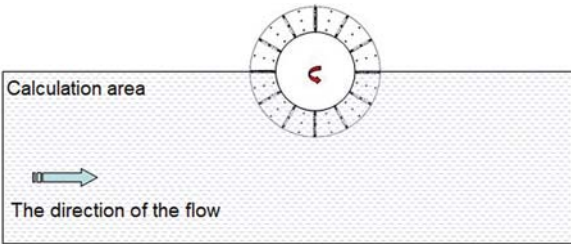


Fig. 3. Calculation area – concept 2A

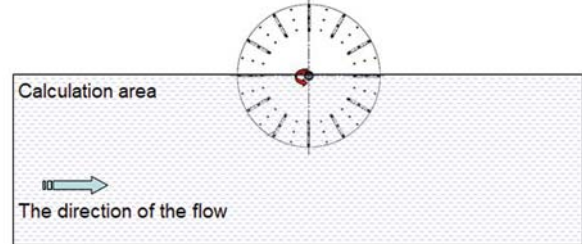


Fig. 4. Calculation area – concept 2B

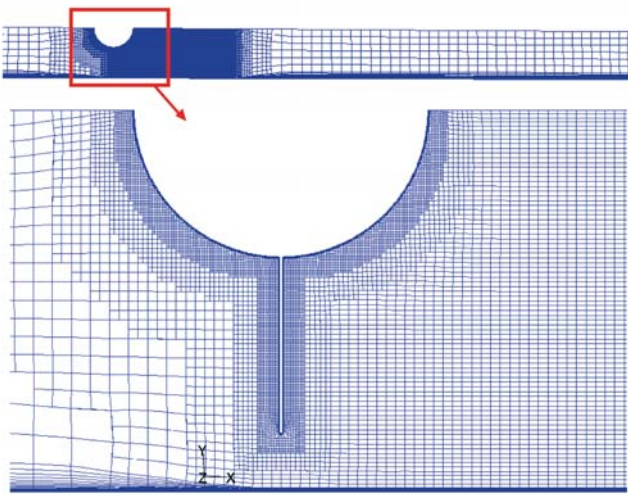


Fig. 5. Calculation grid – variant 1A

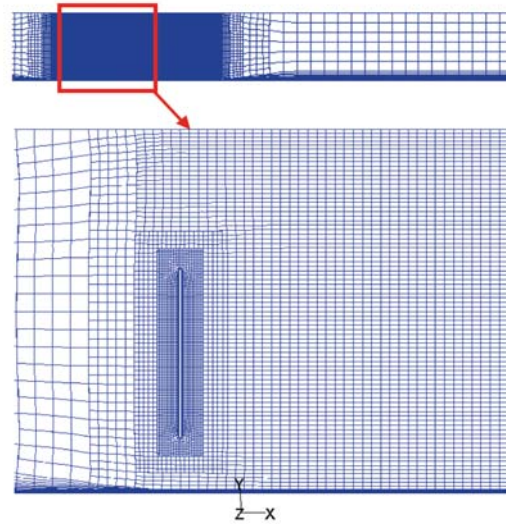


Fig. 6. Calculation grid – variant 1B

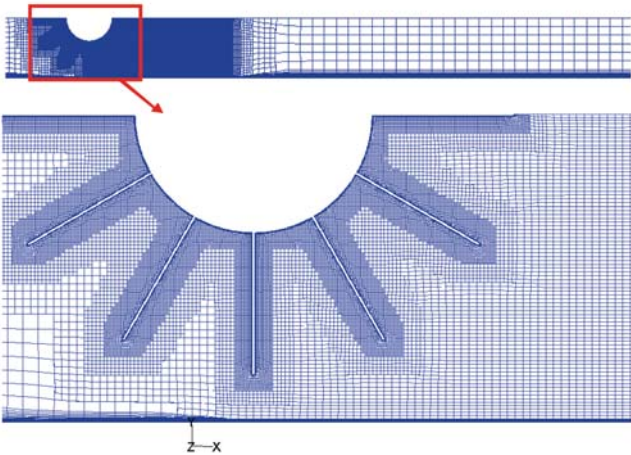


Fig. 7. Calculation grid – variant 2A

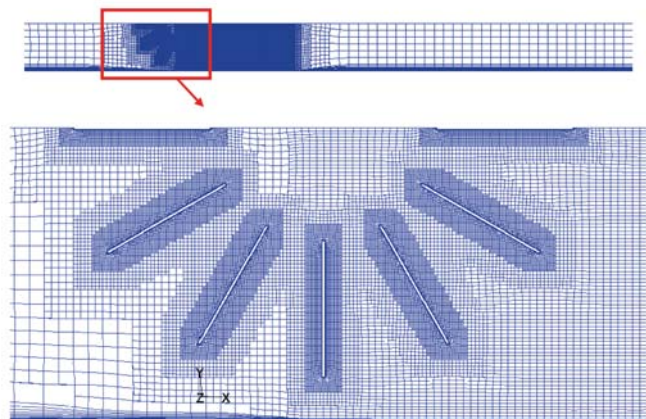


Fig. 8. Calculation grid – variant 2B

## CHARACTERISTICS OF THE CALCULATION MODEL

### GEOMETRIC FEATURES OF THE SOLUTION CONCEPTS

The calculations were made for 4 selected concepts of the innovative solution, the configuration of which is shown in Fig. 1 – Fig. 4 [16]. Each figure shows the calculation area with the fragment of the paddle-wheel. Fig. 1 and Fig. 2 show variants 1A and 1B, in which a single blade is mounted in the paddle-wheel. In variant 1A, the blade (2) is seated in the roller (1) being a closed surface, while in variant 1B, the wheel has an openwork structure to allow the medium to flow through it. The geometry shown in variants 2A and 2B (Figures 3 and 4) makes it possible to analyse half of the wheel with all blades installed. Like in variants 1A and 1B, the wheel geometry has the structure with closed surface in variant 2A, and openwork structure in variant 2B. Comparing the calculation results for the above variants enables the evaluation of the performance of a single paddle blade located in the lower position and the effect of its interaction with the neighbouring blades, in terms of forces and moments.

The calculations were performed for the diameter of wheel (1) equal to 1 m and the length of blade (2) equal to 0.6 m. It was assumed that the wheel is half submerged in water. Moreover, 12 blades evenly distributed on the wheel perimeter were assumed in variants 2A and 2B. The calculation grids were made for the two-dimensional flow model. Examples of calculation grids for each variant are presented in Fig. 5 – Fig. 8. In different configurations, a different number of grid elements was generated as a result of the necessity of its sufficient grid thickening in certain perimeter areas. Variants 2A and 2B are characterized by larger number of grid elements than variants 1A and 1B due to the presence of a larger number of blades.

### CALCULATION OF FLOW PARAMETERS

The equations used to calculate the flow parameters are the mass conservation equation, Eq. (1), and the momentum conservation equation, Eq. (2) (Table 1). After applying the Newton's hypothesis to the stress tensor, Eq. (3), the momentum conservation equation can be rewritten to the form of Eq. (4). The equations Eq. (1) and Eq. (4) constitute a closed system of 4 scalar equations with 4 unknowns:  $u_x, u_y, u_z, p$ , assuming constant density and viscosity of the medium. This equation system allows to obtain a solution taking into account all spatial and temporal scales in the turbulent flow. However, it appears that the minimum number of N grid nodes required to include the vortices at the level of the Kolmogorov scale is proportional to the Reynolds number, Eq. (5), and the number of iterations needed to simulate the flow in a machines rotor ( $Re \approx 10^5$ ) is beyond the capabilities of modern supercomputers.

The analysis of turbulent flows is most often based on the Reynolds hypothesis, according to which the fluid motion is treated as the superposition of the stationary, averaged motion and the unsteady, fluctuating motion.

According to this principle, the value of an arbitrary physical quantity characterising the flow can be presented in the form of Eq. (7). After decomposing the velocity vector  $u$  and pressure  $p$  into stationary and unsteady parts, and then substituting them to Eq. (7), the Reynolds equation, Eq. (8), is obtained. The Reynolds equation including the mass conservation equation (for incompressible fluid), Eq. (9), is a system of 4 equations with unknowns  $\bar{u}_x, \bar{u}_y, \bar{u}_z, \bar{p}$ , and the turbulent stress tensor (Reynolds tensor),  $\rho R$ . This system, Eq. (10), is not closed. Closing the Reynolds equation system requires additional equations determining the components of the turbulence tensor, which is subject to turbulent flow modelling. The method of turbulent flow modelling for which the starting point is the Reynolds equation system belongs to class of RANS (Reynolds Averaged Navier-Stokes) equations, most frequently used in flow analyses. Depending on the formula for the adopted turbulent stress tensor, the following turbulence models can be named [17–20]:

*Tab. 1. Calculation of design parameters of flow aerator in turbine*

Design characteristics	Model equation	No.
Equation of mass conservation	$\frac{\partial \rho}{\partial t} + \text{div}(\rho \vec{u}) = 0$	(1)
Equation of momentum conservation	$\rho \frac{d\vec{u}}{dt} = \rho \vec{f} + \text{div}P$	(2)
Newton's hypothesis for stress tensor	$P = -(p + \frac{2}{3} \mu \text{div}\vec{u})E + 2\mu D$	(3)
Equation of momentum conservation	$\rho \frac{d\vec{u}}{dt} = \rho \vec{f} - \text{grad}p + \mu \Delta \vec{u} + \frac{1}{3} \mu \text{grad}(\text{div}\vec{u})$	(4)
Minimum number N of calculation grid nodes required to account for vortices at the Kolmogorov scale level – proportional to Reynolds number	$N \sim Re^{9/4}$	(5)
Decomposition of arbitrary physical quantity characterizing the flow	$u = \bar{u} + u'$	(6)

Design characteristics	Model equation	No.
Equation of momentum conservation (Navier-Stokes) for incompressible fluid	$\rho \frac{d\vec{u}}{dt} = \rho \vec{f} - \text{grad}p + \mu \Delta \vec{u}$	(7)
Reynolds equation after decomposition of velocity vector $u$ and pressure $p$ , and substituting them into Eq. (7)	$\rho \frac{d\vec{u}}{dt} = \rho \vec{f} - \text{grad}\bar{p} + \mu \Delta \vec{u} - p \text{div}R$	(8)
Mass conservation equation for Reynolds equation (incompressible fluid)	$\text{div}\vec{u} = 0$	(9)
System of 4 equations with unknown $\bar{u}_x, \bar{u}_y, \bar{u}_z, \bar{p}$ and turbulent stress tensor (Reynolds tensor) $\rho R$ – not closed	$\rho R = \rho \overline{u' u'} = \begin{bmatrix} \overline{\rho(u'_x)^2} & \overline{\rho u'_x u'_y} & \overline{\rho u'_x u'_z} \\ \overline{\rho u'_y u'_x} & \overline{\rho(u'_y)^2} & \overline{\rho u'_y u'_z} \\ \overline{\rho u'_z u'_x} & \overline{\rho u'_z u'_y} & \overline{\rho(u'_z)^2} \end{bmatrix}$	(10)
Boussinesq hypothesis based on linear dependence between velocity gradients and Reynolds stress tensor elements	$R_{ij} = -\frac{2}{3} k E_{ij} + \nu_t \left( \frac{\partial \bar{u}_i}{\partial x_j} + \frac{\partial \bar{u}_j}{\partial x_i} \right)$	(11)
Transport equation scalar $\phi$ within single model and two-valued form	$\frac{\partial \phi}{\partial t} + \bar{u}_i \frac{\partial \phi}{\partial x_i} = \frac{\partial}{\partial x_i} D \frac{\partial \phi}{\partial x_i} + \bar{Z}^+(\phi) + \bar{Z}^-(\phi)$	(12)
Transport equations of new variables derived from Navier-Stokes equation	$\frac{\partial \overline{u'_i u'_j}}{\partial t} + \bar{u}_k \frac{\partial \overline{u'_i u'_j}}{\partial x_k} = P_{ij} + d_{ij} + \Phi_{ij} + \epsilon_{ij}$	(13)
Kinetic energy of turbulence and specific rate of its dissipation into internal thermal energy	$\frac{\partial}{\partial t} (\rho k) + \frac{\partial}{\partial x_i} (\rho k u_i) = \frac{\partial}{\partial x_j} \left( \Gamma_k \frac{\partial k}{\partial x_j} \right) + G_k - Y_k$	(14)
	$\frac{\partial}{\partial t} (\rho \omega) + \frac{\partial}{\partial x_i} (\rho \omega u_i) = \frac{\partial}{\partial x_j} \left( \Gamma_\omega \frac{\partial \omega}{\partial x_j} \right) + G_\omega - Y_\omega + D_\omega$	(15)

1. Models using the concept of turbulent viscosity characterizing the relationship between the turbulence stress tensor and the tensor of medium deformation rate. An example maybe the Boussinesq hypothesis based on linear dependence between the variables, Eq. (11).

Further modelling consists in determining the dependence for turbulent viscosity  $\nu_t$ . For this purpose, additional quantities are introduced to the system of equations, followed by additional equations which allow to determine viscosity and turbulent stresses

The scalar transport equation  $\phi$  within one- and two-equation models takes the form of Eq. (12). On the left-hand side of Eq. (12), there is the evolved substantial derivative, on the right – terms that determine the diffusion coefficient  $D$  and positive and negative sources of the given scalar. The equations contain a number of constants, experimentally determined and optimized for several typical flow classes. The turbulence models which are most commonly used now include one-equation models [21] and two-equation models:  $k$ - $\epsilon$  [22, 23], RNG  $k$ - $\epsilon$  [24],  $k$ - $\omega$  [25],  $k$ - $\tau$  [24],  $k$ - $\omega$  SST [26].

2. Models introducing an additional equation for the Reynolds stress tensor of each component:

- 2.1. Algebraic Reynolds stress models (ASM-Algebraic Stress Models), in which the Reynolds stress tensor

components are described by algebraic equations, supplemented with the scalar transport equations, e.g.  $k$  and  $\epsilon$  [27].

- 2.1. Models of stress transport (RSM – Reynolds Stress Models), which introduce  $R_{ij}$  as new variables, with the equations of their transport derived in the form of Eq. (13) from Navier-Stokes equations.

In these models, individual terms on the right-hand side describe successively production, diffusion, and pressure-velocity correlation of deformation and dissipation. These models require an additional transport equation for  $\epsilon$  in order to close the system. Therefore, in the case of three-dimensional flow, additional 7 partial differential equations are added to the system of Reynolds equations [28].

This project uses the two-equation SST  $k$ - $\omega$  turbulence model. In this model, the kinetic energy of turbulence and the rate of its dissipation are calculated according to Eq. (14) and Eq. (15), where  $G_k$  – generation of turbulence kinetic energy;  $G_\omega$  – characteristics of the intensity of rotary motion;  $\Gamma_k$  – diffusion coefficient of turbulence kinetic energy  $k$ ;  $\Gamma_\omega$  – diffusion coefficient of  $\omega$ ;  $Y_k$  – dissipation of  $k$ ;  $Y_\omega$  – dissipation of  $\omega$ ;  $D_\omega$  – term characterizing cross-diffusion.

The system of differential equations describing the fluid motion can be converted to algebraic equations using different

methods [5, 29, 30]. The computational model used in the project is based on the finite volume method. This method uses a form of integral equations of conservation, which is its main characteristic.

The first step of the method is to divide the computational area into sub-areas (control volumes). The calculation points at which the values are unknown functions are placed at the centre of gravity of the control volume. The next step is discretization of partial differential equations, that is, converting them into algebraic equations by integrating after each control volume. The obtained nonlinear algebraic equations are linearized, i.e., nonlinear elements are treated explicitly or implicitly [31–33]. The final stage is interpolation of convective elements and diffusion and source units in the differential schemes. It consists in expressing the average values on the surface of the control volume through the values of the unknown function at the calculated points.

## MODEL PARAMETERS AND BOUNDARY CONDITIONS

The calculations were made using the code Ansys/Fluent 12 and a two-dimensional flow model, assuming its stationarity. The Fluent algorithm is based on the finite volume method, in which transport equations are written in the integral form. The “pressure-based” type solver was used. The convective terms in transport equations were approximated by the 3-rd order MUSCL scheme. The flowing medium was water with constant viscosity of 0.001 kg/m·s, whereas the SST  $k-\omega$  model was used to describe the turbulent motion.

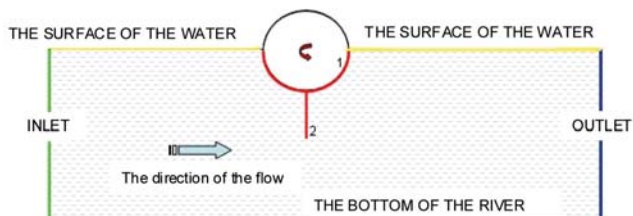


Fig. 9. Scheme of computational area and boundary conditions

The assumed boundary conditions are shown in Fig. 9. At the inlet to the computational area, the “Velocity Inlet” condition was assumed, with the flow velocity value corresponding to the midstream velocity. Additional parameters concerning the turbulence model were the turbulence intensity of 1% and the turbulent-to-laminar viscosity ratio equal to 10. At outlet, the “outflow” condition was assumed. The lower boundary, representing the bottom of the river, was described by the boundary condition “Wall”. In contrast, on the free surface, the symmetry condition was assumed, which means that the medium is not transported through this surface, but only slips along it.

Such a set of boundary conditions is a strong simplification of the real situation, especially near the water wheel. However, such an assumption is considered acceptable taking into account the purpose of the analysis, which is to determine forces and moments acting on the blade.

## DISCUSSION OF RESULTS

The above presented calculation model was used to determine flow characteristics and forces acting on the blade in the examined variants. Below are given selected results for variants 1A and 2A (full wheel), obtained assuming the flow velocity of 0.1 m·s<sup>-1</sup> and the depth of 2 m. The latter parameter is the distance of the blade tip from the bottom of the river. Fig. 10 and Fig. 11 show, respectively, pressure and flow velocity distributions, with alluvial power lines for geometry 1A, whereas Fig. 12 – Fig. 14 show the same distributions for geometry 2A. The pressure values are shown as relative values, where the reference pressure is the ambient pressure. The images of flow velocity and power lines indicate high differentiation of the flow structure and velocity values obtained using different calculation models for a single blade and the complete system of blades.

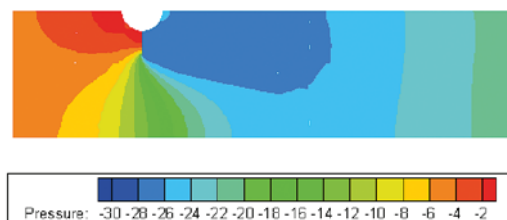


Fig. 10. Static pressure – variant 1A

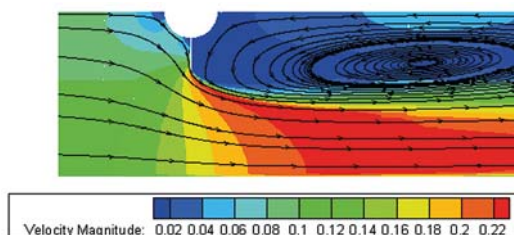


Fig. 11. Velocity and power lines – variant 1A

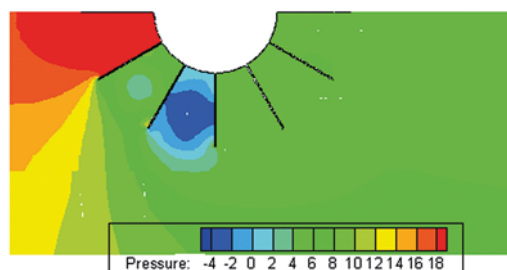


Fig. 12. Static pressure – variant 2A

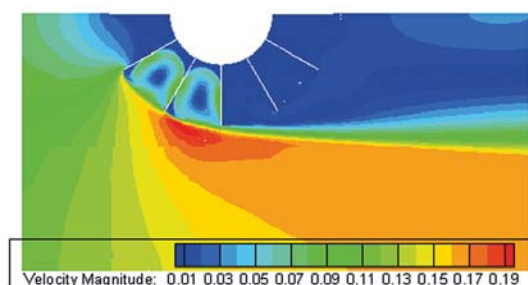


Fig. 13. Velocity – variant 2A

In each variant, the calculations were performed for 3 flow velocity values: 0.1 m·s<sup>-1</sup>, 2.7 m·s<sup>-1</sup> and 5.5 m·s<sup>-1</sup>. Moreover, for each case the rotational velocity of the roller blade unit (Fig. 15) was chosen to meet the following condition:

$$u_{lop} / u = 1 \quad (16)$$

where:

$u$  – flow velocity,

$u_{lop}$  – linear velocity of a blade at 2/3 of its length.

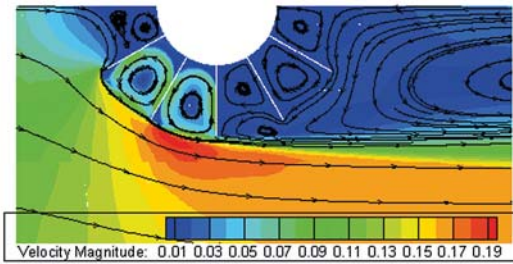


Fig. 14. Velocity and power lines – variant 2A

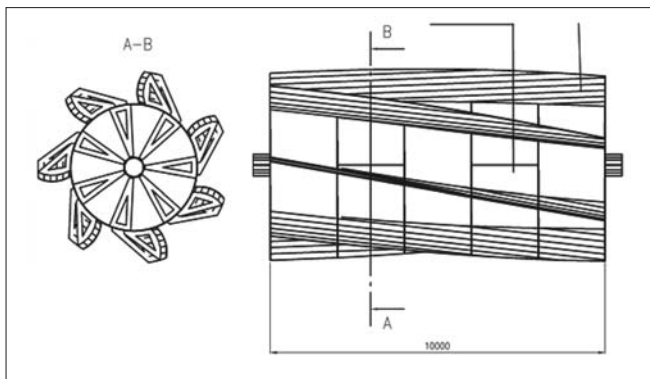


Fig. 15. Turbine roller: constructional form of the cylinder with seven blades ( $L = 10000$  mm)

The resulting rotational speeds of the cylindrical turbine-roller models which met condition (16) for the assumed flow velocities were: 1.06 rpm, 28.6 rpm, and 58.4 rpm. The performed flow calculations allowed to determine the values of moments and forces acting on a single blade or the complete blade system.

In variants 1A and 2A, determining the moment of force is relatively easy and can be obtained from pressure integration over blade surface. These variants are characterized by the existence of a stable solution and stabilized force values in successive steps of the iterative process. Selected time-history of fluctuations of the moment of force recorded during the calculations for variant 1A is shown in Fig. 16. However, determining forces in the presence of unsteady flow in variants 1B and 2B (openwork structure) is more difficult, as it requires unsteady calculations, with further pressure integration not only in space, but also in time. Figs. 17–19 present the time-histories of fluctuations of the moment of force acting on one blade during the calculation process for variant 1B at two different water flow velocities and two water depths. In the case of low flow velocity, the amplitude of fluctuations is

relatively small and decreases with increasing depth. On the other hand, when the flow velocity is higher, of 5.5 m·s<sup>-1</sup>, this amplitude reaches as much as 50% of the average value, which means very large blade load changes and the need to take into account changes in time.

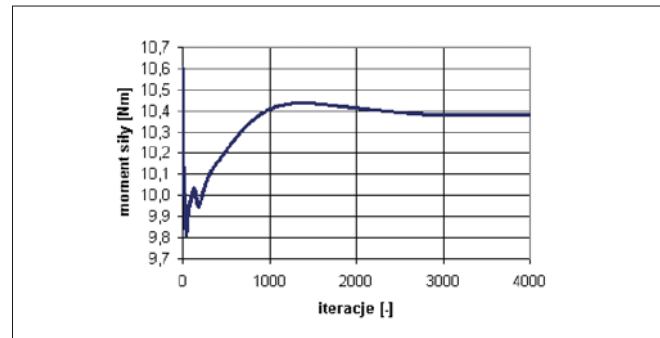


Fig. 16. Moment of force acting on the blade: variant 1A, depth 2 m, water flow speed 0.1 m·s<sup>-1</sup>

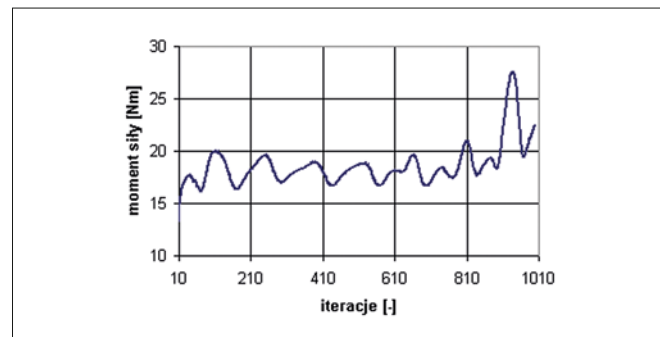


Fig. 17. Moment of force acting on the blade: variant 1B, depth 0.2 m, water flow speed 0.1 m·s<sup>-1</sup>

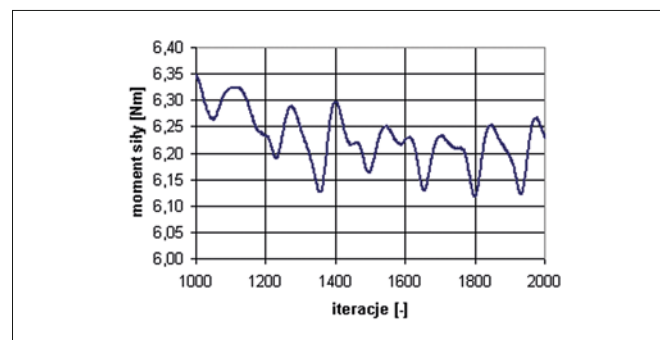


Fig. 18. Moment of force acting on the blade: variant 1B, depth 2 m, water flow speed 0.1 m·s<sup>-1</sup>

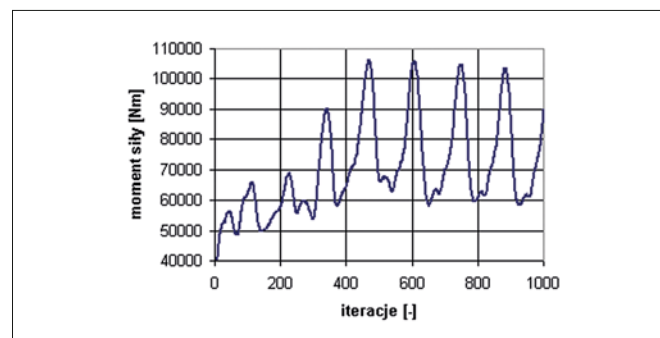


Fig. 19. Moment of force acting on the blade: variant 1B, depth 0.2 m, water flow speed 5.5 m·s<sup>-1</sup>

Tab. 2. Moments of force (Nm)

Flow velocity		0.1 m·s <sup>-1</sup>		2.7 m·s <sup>-1</sup>		5.5 m·s <sup>-1</sup>	
Rotational speed		1.06 rpm		28.6 rpm		58.4 rpm	
Depth		0.2 m	2 m	0.2 m	2 m	0.2 m	2 m
Variant	1A	252	10	183738	7543	763403	31253
	1B	22.5	6.2	16176	4490	89761	24160
	2A	1.55 95 (1 blade)	0.2 -2.3 (1 blade)	2132 69636 (1 blade)	147 -1704 (1blade)	7416 278940(1 blade)	707 -7227 (1 blade)
	2B	9.5 9 (1 blade)	4.2 -0.6 (1 blade)	10468 6500 (1 blade)	2800 -2000(1 blade)	41000 25000 (1 blade)	3400 -2300 (1 blade)

The exact values of moments of forces recorded for particular variants are collated in Table 2. Each time, the moment of force was determined for the unit width of the blade equal to 1 m. The values marked green in variants 1B and 2B were determined as averages of the calculation process. It should be emphasized again that obtaining accurate values required performing unsteady flow calculations.

A significant difference can be observed between the values of the moment of force acting on the isolated blade and when it is part of the blade system. In variants 2A and 2B, for larger depth G, a negative value of the moment acting on the lower blade was obtained (with a positive torque value for the entire system), which is the effect of the earlier presented pressure distribution.

Larger moment fluctuations are caused by the effect of depth (distance of the blade from the bottom). For a smaller depth, the values are significantly overestimated due to the boundary condition of the non-deformable free surface.

For comparison purposes, Table 3 collates the calculated values of the resistance force and moment acting on a plate having the dimensions of the analysed blade and oriented perpendicular to the flow direction. The force was determined from Eq. (17), where the resistance coefficient  $c_d$  was assumed equal to 2 (as appropriate for Reynolds numbers  $Re > 10^5$ ):

$$F_d = c_d 0.5 \rho u^2 A \quad (17)$$

The moment of force was determined from Eq. (18), assuming that the centre of thrust in this case coincides with the centre of the plate. This configuration is most similar to variant 1B, except the effect of the distance to the bottom and top surfaces of the tank:

$$M_d = F_d (0.5L + R) \quad (18)$$

Tab. 3. Resistance force and moment acting on flat plate

Flow velocity, m·s <sup>-1</sup>	0.1	2.7	5.5
Resistance force, N	6	4374	18150
Moment of force, N·m	4.8	3500	14520

There are many solutions, known in the world as small water turbines, which have the form of reaction and reaction turbines, or wastewater, backloading, and backhoe water wheels. The analysed construction of a floating power plant with water turbine consists of a self-supporting, floating roller filled with air. A shaft is placed at the centre of rotation, while coils forming the blades are placed on the circumference of the roller, along the helix. The whole construction is enclosed by a perforated body. The diffuser intensifies taking over the energy from the watercourse. Only some known solutions of the conversion of watercourse energy into the energy of rotational motion were carried out in accordance with the idea of displacement, i.e. the ability to float on the surface or at some favourable depth of the watercourse during energy conversion. In all known solutions, there is a problem with low efficiency [34, 35]. The system collecting the torque from the watercourse is built in such a way that the rotary motion of the positive displacement cylinder is transmitted through the shaft and the mechanical gear to the working unit of the electric power generator. The entire functional system is longitudinally and transversely trapped on the watercourse by blocking it on both sides with anchored ropes. The direction of rotation of the displacement roller with blades results directly from the winding direction of the rotor blades mounted on it. The electric energy generated in the generator is discharged to the users by an electric wire. The water turbine with energy conversion devices, developed according to the presented concept, is characterized by simple and compact structure, which is its unquestionable advantage compared to conventional solutions described, among others, in [36, 37]. The presented structure allowed to eliminate load-bearing units, e.g. as it was used in the solutions presented in [36–38]. The use of a roller with helical blades protects against the destruction of living organisms, including fish, fry, and other aquatic animals. It also generates high torque, according to the Stokes equation, and multiple helices with high coil angle cause low resistance according to Reynolds' dependence, which is an advantage over both the known multi-blade solutions with straight blades, and standard rotors with two and three helical blades [39]. The geometric shape of the working surfaces of the rotor screw coils causes additionally the Magnus effect, which results in the efficiency increase compared to the known solutions of turbines with helical blades [40]. The presented solution may be applied in watercourses as an unconventional

source of renewable energy, especially in places of scarcity and lack of access to the power grid. This device can be used to drive machines and devices without the use of other energy sources, e.g. pumps, and, as a water vehicle propulsion unit, also for educational purposes and popularizing water energy converters.

## SUMMARY

For the selected calculation models of the innovative blade-roller unit, models of pressures, forces and torques were developed to model the conversion of watercourse energy in two basic geometrical design concepts and determine new operational parameters of the main elements of the roll turbine aerator. This is important for the needs of detailed pre-implementation design, construction and manufacturing of working elements of the innovative roller-blade unit. The pressures have been determined experimentally, making the basis for calculating forces and torques for a variable geometrical form and dimensions of the projected working elements of the rotor of an innovative roller-blade turbine assembly (for example Fig. 15). In the design concept 1A (Fig. 1), a single blade (2) was mounted on a roller (1) being a closed surface, while in variant 2A (Fig. 3), the wheel had an openwork structure to allow the medium to flow through it. Determining the moment of force was relatively easy for these two cases and was obtained from pressure integration over blade surfaces. These variants are characterized by the existence of a stable solution and stabilized force values in successive steps of the iterative process. For the selected design concepts, forces and moments were determined for individual configurations in assumed flow conditions, which was the preparation stage for implementation of the roller-blade assembly in the conditions of the Tigris and Euphrates rivers. The obtained results of calculations will enable determination of the flow through the structure and the assessment of its effect on the system of forces in the roller blade. These results were used for initial assessment of basic construction parameters, being the starting point to further more advanced calculations using complex physical models. The calculations were made for the concept of a full roll (roll surface) and open-work structure (without a roll). In both cases the analysis was carried out for a single blade and the complete blade system, assuming two channel depths and 3 watercourse speeds. The results of the calculations lead to the following specific conclusions:

1. The calculation model of two-dimensional, stationary and single-phase flow with the assumption of a non-deformable free surface well reflects the reality only in variants 1A and 2A, provided that the channel has a sufficiently large depth, i.e. the distance of the lower blade tip from the bottom.
2. In variants 1B and 2B, the flow past blades from the side of the lower and top channels causes the formation of the flow structure which requires the use of a non-stationary flow model.

3. The determined forces and moments indicate the significant effect of the depth of the channel on the obtained results. The moment of force increases with decreasing depth.
4. The structure of the flow indicates the need to analyse the entire blade system to determine forces acting on it. The analysis of a single blade can be useful in the design and evaluation of its float. But the difference in the structure of flow and the recorded force values between the simplified configuration and the full blade system will grow with the increase of blade length and the decrease of channel depth. These values can differ by one or, for small depths, two orders of magnitude, which makes the single-blade calculation results useless for design purposes.
5. The analysis of the designed flows, leading to a quantitative assessment of the effect of construction parameters of the floating power roll and aeration, requires time-consuming calculations with the unsteady two-phase model taking into account the motion of roll elements.
6. In variants 1A and 2A, the use of an innovative hydroelectric turbine with the aeration option refers to watercourse conditions with a sufficiently large channel depth, i.e. the distance of the lower blade tip from the bottom. The determined forces and moments indicate a clear influence of channel depth on the obtained values. The torque increases with decreasing depth.
7. The flow structure indicates the need for extending the calculation and for devising drum solutions with a single, preferably oblique, canopy forming the roll/drum.

## REFERENCES

1. Basumatary, M., Biswas, A., Misra, R.D.: *CFD analysis of an innovative combined lift and drag (CLD) based modified Savonius water turbine*. Energy Convers. Manag. 174, 72–87 (2018). <https://doi.org/10.1016/j.enconman.2018.08.025>.
2. Sritram, P., Suntivarakorn, R.: *Comparative Study of Small Hydropower Turbine Efficiency at Low Head Water*. Energy Procedia. 138, 646–650 (2017). <https://doi.org/10.1016/j.egypro.2017.10.181>.
3. Jiyun, D., Hongxing, Y., Zhicheng, S., Xiaodong, G.: *Development of an inline vertical cross-flow turbine for hydropower harvesting in urban water supply pipes*. Renew. Energy. 127, 386–397 (2018). <https://doi.org/10.1016/j.renene.2018.04.070>.
4. Viollet, P.-L.: *From the water wheel to turbines and hydroelectricity. Technological evolution and revolutions*. Comptes Rendus Mécanique. 345, 570–580 (2017). <https://doi.org/10.1016/j.crme.2017.05.016>.
5. Ferziger, J.H., Perić, M.: *Computational methods for fluid dynamics*. Springer, Berlin; New York (2002).

6. Flizikowski, J., Topoliński, T., Opielak, M., Tomporowski, A., Mroziński, A.: *Research and analysis of operating characteristics of energetic biomass mikronizer*. Eksploat. Niezawodn. 17, 19–26 (2015).
7. Tomporowski, A., Flizikowski, J.: *Motion characteristics of a multi-disc grinder of biomass grain*. Przem. Chem. 92, 498–503 (2013).
8. Flizikowski, J.B., Kruszelnicka, W., Tomporowski, A., Mroziński, A.: *A study of operating parameters of a roller mill with a new design*. AIP Conf. Proc. 2077, 020018 (2019). <https://doi.org/10.1063/1.5091879>.
9. Tomporowski, A., Flizikowski, J., Kruszelnicka, W.: *A new concept of roller-plate mills*. Przem. Chem. 96, 1750–1755 (2017). <https://doi.org/10.15199/62.2017.8.29>.
10. Du, J., Shen, Z., Yang, H.: *Effects of different block designs on the performance of inline cross-flow turbines in urban water mains*. Appl. Energy. 228, 97–107 (2018). <https://doi.org/10.1016/j.apenergy.2018.06.079>.
11. Jiyun, D., Zhicheng, S., Hongxing, Y.: *Performance enhancement of an inline cross-flow hydro turbine for power supply to water leakage monitoring system*. Energy Procedia. 145, 363–367 (2018). <https://doi.org/10.1016/j.egypro.2018.04.065>.
12. Kruszelnicka, W., Flizikowski, J., Tomporowski, A.: *Auto-monitoring system of grainy biomass comminution technology*. IOP Conf. Ser. Mater. Sci. Eng. 393, 012076 (2018). <https://doi.org/10.1088/1757-899X/393/1/012076>.
13. Tongphong, W., Saimek, S.: *The Design and Development of an Oscillating Water Turbine*. Energy Procedia. 52, 552–558 (2014). <https://doi.org/10.1016/j.egypro.2014.07.109>.
14. Wang, J., Piechna, J., Müller, N.: *A novel design of composite water turbine using CFD*. J. Hydrodyn. Ser B. 24, 11–16 (2012). [https://doi.org/10.1016/S1001-6058\(11\)60213-8](https://doi.org/10.1016/S1001-6058(11)60213-8).
15. Tomporowski, A., Flizikowski, J., Kasner, R., Kruszelnicka, W.: *Environmental Control of Wind Power Technology*. Rocz. Ochr. Śr. 19, 694–714 (2017).
16. Flaszynski, P.: *Wyniki obliczeń przepływowych w następstwie obliczenia sił i momentów obrotowych uzyskiwanych dla założonych parametrów konstrukcyjnych projektowanej turbiny*, (2011).
17. Boxma, O., Zwart, B.: *Fluid flow models in performance analysis*. Comput. Commun. 131, 22–25 (2018). <https://doi.org/10.1016/j.comcom.2018.07.009>.
18. Tang, M., Yuan, L., He, S., Fu, T.: *Simplified modeling of YPL fluid flow through a concentric elliptical annular pipe*. J. Pet. Sci. Eng. 162, 225–232 (2018). <https://doi.org/10.1016/j.petrol.2017.12.030>.
19. Sondermann, C.N., Baptista, R.M., Bastos de Freitas Rachid, F., Bodstein, G.C.R.: *Numerical simulation of non-isothermal two-phase flow in pipelines using a two-fluid model*. J. Pet. Sci. Eng. 173, 298–314 (2019). <https://doi.org/10.1016/j.petrol.2018.10.018>.
20. Rasti, E., Talebi, F., Mazaheri, K.: *A turbulent duct flow investigation of drag-reducing viscoelastic FENE-P fluids based on different low-Reynolds-number models*. Phys. Stat. Mech. Its Appl. (2019). <https://doi.org/10.1016/j.physa.2019.03.083>.
21. Spalart, P., Allmaras, S.: *A one-equation turbulence model for aerodynamic flows*. In: 30th Aerospace Sciences Meeting and Exhibit. American Institute of Aeronautics and Astronautics (1992). <https://doi.org/10.2514/6.1992-439>.
22. Launder, B., Spalding, D.B.: *Mathematical Models of Turbulence*. Academic Press, London (1972).
23. Launder, B.E., Sharma, B.I.: *Application of the energy-dissipation model of turbulence to the calculation of flow near a spinning disc*. Lett. Heat Mass Transf. 1, 131–137 (1974).
24. Yakhot, V., Orszag, S.A., Thangam, S., Gatski, T.B., Speziale, C.G.: *Development of turbulence models for shear flows by a double expansion technique*. Phys. Fluids Fluid Dyn. 4, 1510–1520 (1992). <https://doi.org/10.1063/1.858424>.
25. Wilcox, D.C.: *Turbulence Modeling for CFD*. DC W Industries, La Cândia, Calif (2006).
26. Menter, F.R.: *Two-equation eddy-viscosity turbulence models for engineering applications*. AIAA J. 32, 1598–1605 (1994). <https://doi.org/10.2514/3.12149>.
27. Launder, B.E., Reece, G.J., Rodi, W.: *Progress in the development of a Reynolds-stress turbulence closure*. J. Fluid Mech. 68, 537–566 (1975). <https://doi.org/10.1017/S0022112075001814>.
28. Gavrillov, A.A., Rudyak, V.Y.: *Reynolds-averaged modeling of turbulent flows of power-law fluids*. J. Non-Newton. Fluid Mech. 227, 45–55 (2016). <https://doi.org/10.1016/j.jnnfm.2015.11.006>.
29. Fletcher, C.A.J.: *Computational Techniques for Fluid Dynamics*, Vol. 1: Fundamental and General Techniques. Springer-Verlag, NY (1991).
30. Hirsch, C.: *Numerical Computation of Internal and External Flows: The Fundamentals of Computational Fluid Dynamics – 2nd Edition*. Elsevier (2007).
31. Tomporowski, A., Flizikowski, J., Wełnowski, J., Najzarek, Z., Topoliński, T., Kruszelnicka, W., Piasecka, I., Śmigiel, S.: *Regeneration of rubber waste using an intelligent grinding system*. Przem. Chem. 97, 1659–1665 (2018). <https://doi.org/10.15199/62.2018.10.6>.

32. Rudnicki, J., Zadrag, R.: *Technical State Assessment of Charge Exchange System of Self-Ignition Engine, Based on the Exhaust Gas Composition Testing*. Pol. Marit. Res. 24, 203–212 (2017). <https://doi.org/10.1515/pomr-2017-0040>.
33. Korczewski, Z., Rudnicki, J.: *An Energy Approach to the Fatigue Life of Ship Propulsion Systems Marine 2015*. In: Salvatore, F., Broglia, R., and Muscari, R. (eds.) VI International Conference on Computational Methods in Marine Engineering – The Conference Proceedings. pp. 490–501. Int Center Numerical Methods Engineering, 08034 Barcelona (2015).
34. Flizikowski, J.: *Apparatus for aerating water courses and disintegrating solid impurities contained in their water*, <http://regserv.uprp.pl/register/application?number=P.308679>, (1999).
35. Green Tech Avenue: *Micro Hydro Power Technology – 5kW WATER TURBINE*, [https://translate.google.com/translate?hl=pl&sl=en&u=http://www.greentechavenue.com/wp-content/uploads/2011/Greentechavenue\\_micro\\_hydro\\_power\\_solution.pdf&prev=search](https://translate.google.com/translate?hl=pl&sl=en&u=http://www.greentechavenue.com/wp-content/uploads/2011/Greentechavenue_micro_hydro_power_solution.pdf&prev=search).
36. Matulewicz, W.: *Floating water – power plant*. Przegląd Elektrotechniczny. 1, 279–283 (2015). <https://doi.org/10.15199/48.2015.09.68>.
37. Dąbała, K., Krzemień, Z., Olszewski, A.: *Micro hydropower station with a spiral turbine*. Zesz. Probl. – Masz. Elektr. 129–133 (2009).
38. Rangan, P.R., Karnyoto, A.S., Ambabunga, Y.A.M., Rambulangi, A.C.: *Design of River Flow Floating Portable Micro-Hydro*. Int. J. Eng. Tech. 4, 593–597 (2018).
39. Nguyen, M.H., Jeong, H., Yang, C.: *A study on flow fields and performance of water wheel turbine using experimental and numerical analyses*. Sci. China Technol. Sci. 61, 464–474 (2018). <https://doi.org/10.1007/s11431-017-9146-9>.
40. Akimoto, H., Tanaka, K., Uzawa, K.: *A conceptual study of floating axis water current turbine for low-cost energy capturing from river, tide and ocean currents*. Renew. Energy. 57, 283–288 (2013). <https://doi.org/10.1016/j.renene.2013.02.002>.

## CONTACT WITH THE AUTHORS

**Andrzej Tomporowski**

*e-mail: a.tomporowski1@wp.pl*

UTP University of Science and Technology  
Al. S. Kaliskiego 7, 85-796 Bydgoszcz

**POLAND**

**Ali Al-Zubiedy**

*e-mail: mat.ali.alzubiedy@oubabylon.edu.iq*

University of Babylon, Faculty of Materials Engineering,  
Najaf Road, 14km from the center of Hilla,

P.O. Box 4 Babylon Hilla

**IRAQ**

**Józef Flizikowski**

*e-mail: fliz@utp.edu.pl*

UTP University of Science and Technology  
Al. S. Kaliskiego 7, 85-796 Bydgoszcz

**POLAND**

**Weronika Kruszelnicka**

*e-mail: weronika.kruszelnicka@utp.edu.pl*

UTP University of Science and Technology  
Al. S. Kaliskiego 7, 85-796 Bydgoszcz

**POLAND**

**Patrycja Bałdowska-Witos**

*e-mail: patrycja.baldowska-witos@utp.edu.pl*

UTP University of Science and Technology  
Al. S. Kaliskiego 7, 85-796 Bydgoszcz

**POLAND**

**Jacek Rudnicki**

*e-mail: jacekrud@pg.edu.pl*

Gdańsk University of Technology  
Narutowicza 11/12, 80-233 Gdańsk

**POLAND**

## BLADE SECTION PROFILE ARRAY LIFTING SURFACE DESIGN METHOD FOR MARINE SCREW PROPELLER BLADE

Przemysław Król

Ship Design and Research Centre, Gdańsk, Poland  
Gdańsk University of Technology, Poland

### ABSTRACT

*The lifting surface model is widely used in screw propeller design and analysis applications. It serves as a reliable tool for determination of the propeller blade mean line and pitch distribution. The main idea of this application was to determine the blade shape that would satisfy the kinematic boundary condition on its surface with the prescribed bound circulation distribution over it. In this paper a simplified lifting surface method is presented – in which the 3D task for the entire blade is replaced by a set of 2D tasks for subsequent blade section profiles.*

**Keywords:** marine propeller, lifting surface, blade section profile, design

### INTRODUCTION

A very common basis for designing a marine propeller blade is the lifting line model, replacing the propeller blade with a concentrated radial bound vortex having variable circulation and adequate vortex wake. In most cases, a real marine propeller blade sharply deviates from such simplification due to the finite chord length, possibly non-symmetrical outline etc. Because of that, a decision on the pitch and camber distribution that satisfies the dynamic requirements for the propeller cannot be done within the frame of the lifting line model alone. This was the reason for the elaboration of numerous lifting surface approaches. The first attempts were quite simple and rather rudimentary – mainly due to the limitations of available computational resources [5]. Moreover, these were applied mainly in the form of pre-calculated correction factors, interpolated in dependency on the main parameters of the designed propellers. One widely known model of this kind was elaborated by Ludweig and Ginzler. Formally, it was limited to three-bladed propellers with a symmetrical outline and elliptical loading distribution. Despite substantial simplifications, their model was widely used in the 1950s and early 1960s – however, recent analysis has revealed that in many cases the designed propellers were hydrodynamically overloaded.

A much more developed model was utilised by Morgan, Silovic and Denny [14] and was widely used for a long time. Even nowadays, “orthodox” propeller designs may be successfully obtained using it.

However, from a theoretical point of view, the best approach is to determine the pitch and camber distribution individually for each particular case. A solution for such task was given by Greeley and Kerwin [4]. They used a simplified vortex wake treatment and algorithm of blade shape determination involving vector operations on the local velocity field, but certain stability problems occurred. However, the model allowed them to elaborate successful designs of propeller blades and stimulated other researchers to pursue better propeller designs through the use of vortex models [3, 10]. Preparing a correct propeller design is especially important nowadays in the present era of increased awareness of the ecological problems connected with greenhouse gas emissions [19].

Although current vortex methods are being displaced by modern RANSE-based codes [15, 16], these still prove to be of interest to researchers [1, 3, 12]. Even for complicated system geometry, they are capable of solving practical technical problems [8, 13].

In the paper, the author’s approach for utilising the lifting surface model in propeller design is presented. The main

idea is to replace the three-dimensional design problem for marine propeller blades with an array of two-dimensional problems solved for blade section profiles.

## DESIGN ALGORITHM

### BLADE SECTION PROFILE DESIGN

The basis for further work presented in this paper is the design algorithm, dedicated to two-dimensional blade section profiles. The main idea is to determine the mean line shape and angle of attack that would satisfy the kinematic boundary condition for the prescribed circulation distribution over the camber surface, representing the profile. The input data that has to be specified is the set of lift force coefficients corresponding to the required lift generated by the particular profile at design conditions. The loading distribution over the profile chord is also freely decided by the designer, as long as zero loading is preserved at the trailing edge. The most basic and well recognised ones are “roof-top” NACA  $a = 0.8$  and elliptical distributions, but the possible applications are obviously not limited to these two. It is, however, to be underlined that convergent geometry could be obtained for NACA  $a = 1.0$ , which has a constant loading distribution from the leading to the trailing edge, but this would not meet its assumed parameters in real fluid, due to ignoring the Kutta condition.

The designer has to specify the thickness of the profile. Limitations arise from the source-sink representation of thickness effects, which makes it necessary to apply a zero thickness value at the trailing edge, to preserve the mass-conservation in the flow.

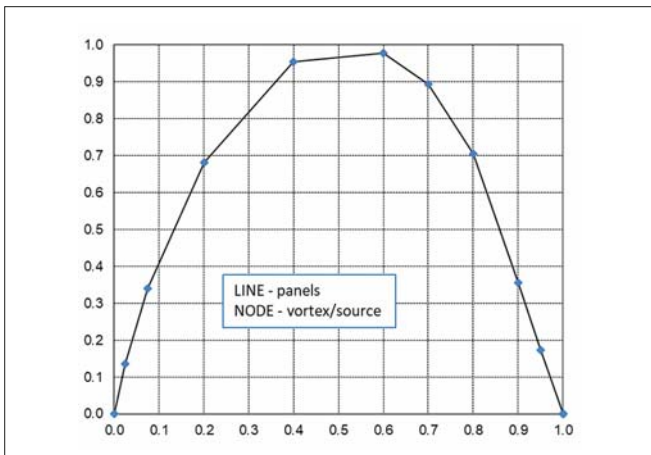


Fig. 1. Discrete lifting surface grid for profile design (different scales on  $x$  and  $y$  axis)

With a simple rearrangement of the well-known Zhoukovsky equation, the relation between the total bound circulation of the profile and the required lift force coefficient may be found:

$$\Gamma = \frac{1}{2} c U_0 C_L \quad (1)$$

where  $c$  is the profile chord length and  $U_0$  is the external flow speed in which the profile operates. The bound circulation  $\Gamma$  is distributed along the profile continuously, generating local circulation density  $\gamma$ :

$$\gamma = \frac{\partial \Gamma}{\partial c} \quad (2)$$

The function describing the chordwise distribution of circulation density  $\gamma$  depends on the selected loading distribution. In the numerical application, discrete vortices are used instead of a continuous circulation distribution. If the blade section is described with a grid consisting of  $N$  straight line segments (these are spaced over the mean line), then the circulation of the particular discrete vortex is given as:

$$\Gamma_i = c \int_{x_i}^{x_{i+1}} \gamma dx_c \quad (3)$$

where  $i$  is the index referring to the subsequent discrete element of the vortex grid and  $x_c$  is a dimensionless chord fraction. At the same points as the vortices, the sources are placed also, to represent thickness effects. Their intensity is given as:

$$Q_i = U_0 (t_{i+1} - t_i) \quad (4)$$

where  $t_i$  is the profile thickness at the corresponding  $x_{c,i}$  chordwise position. When both the vortices circulations and the sources intensities are known, induced velocities may be easily found at each point over the profile. Summing them with the external velocity gives the total velocity field, which is used for determination of the blade section shape:

$$\gamma = c \int_{LE}^{TE} \frac{U_y}{U_x} dx_c \quad (5)$$

where  $U_x$  and  $U_y$  are the total velocities in the  $x$  and  $y$  directions respectively, at the considered point.

As all the calculations are conducted for dimensionless parameters, the external velocity has a prescribed value equal to  $V = 1$  m/s in the  $x$  direction. After determination of the blade section coordinates, the calculations may be repeated – as the singularities positions will update respectively. This leads to an updated velocity field, of course, which will result in a slightly different profile form. This loop converges quite swiftly, under approx. 10 times for moderately loaded profiles. When the geometry solution has converged, the angle of attack value is calculated as the one between the external velocity (practically: the  $x$  axis) and a straight line connecting the first and last singularity over the mean line. Accordingly, mean line offsets are determined as the distance between the abovementioned straight line and the respective point on the mean line.

The algorithm described above was applied to a design blade section with a lift force coefficient equal to  $C_L = 0.20$  with NACA  $a = 0.8$  loading distribution. Fig. 2 gives the comparison between the designed mean line and tabular one [5]:

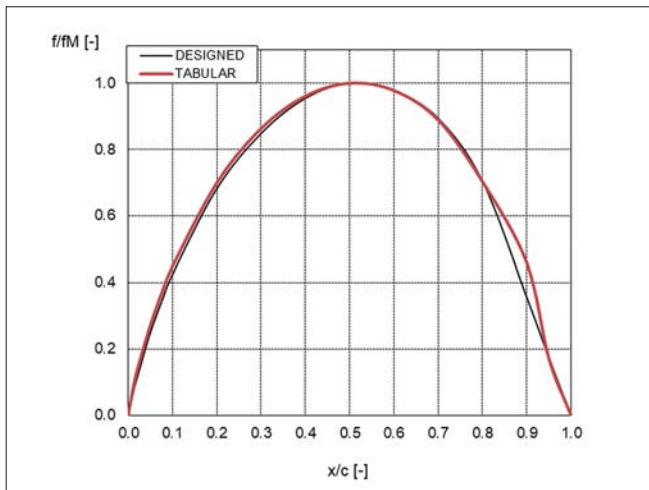


Fig. 2. Mean line designed for NACA  $a = 0.8$  loading distribution and tabular mean line NACA  $a = 0.8$  (different scales on  $x$  and  $y$  axis)

## PROPELLER BLADE DESIGN

In the previous paragraph a blade section placed in two-dimensional flow was considered. The flow conditions over the marine screw propeller are substantially different from that, and three-dimensionality has to be included in the analysis. It was, however, possible to successfully replace the three-dimensional design task for a screw propeller blade with an array of sub-tasks of designing two-dimensional blade section profiles.

The initial part of the propeller blade design is to determine the radial bound circulation distribution that would satisfy the delivered thrust / consumed power requirements for the propeller, to decide the blade outline etc. This can be done with any of the well-known algorithms [5, 6], so it is not a subject of consideration here. The part of the design algorithm which is focused on starts from the determination of the pitch and camber distributions. Consequently, it has been assumed that all the necessary data, especially the radial bound circulation distribution and local values of induced advance angles, are known. What the designer has to decide are – similarly to the case of blade section profile design – the chordwise loading and thickness distributions.

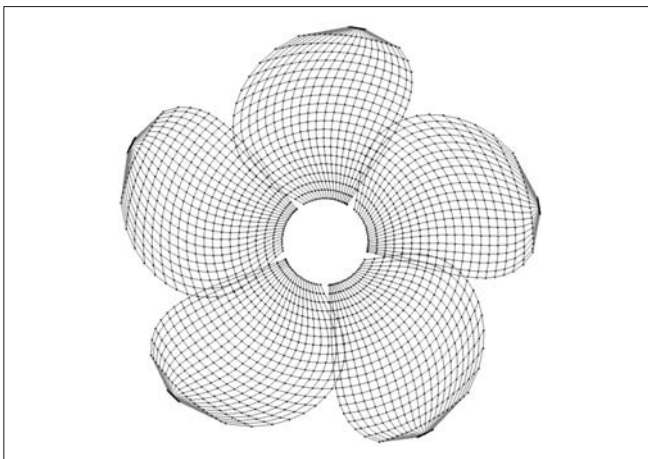


Fig. 3. Discrete lifting surface grid for propeller design

In the first step, the induced velocities at each panel middle-point are calculated to obtain the total velocity at each of these. Subsequently, it is summed with the external velocity – consisting of the axial speed in non-uniform inflow and the tangential one resulting from propeller rotation:

$$U_{\text{total}} = V(1 - w_r) + \omega \times r + u_{\text{ind}} \quad (6)$$

where  $w_r$  is the average wake fraction coefficient at the respective radius, and  $u_{\text{ind}}$  is the local induced velocity vector. The induced velocity vector is the sum of the vortex and source line elements. Vortex-induced velocities are obtained by means of the Biot–Savart law. Source line elements are replaced with point sources in such number that the distance between each source element is at least 5 times smaller than the distance between the point source and a calculation point [18].

After calculating the total velocity vector for each point, it is divided into axial and tangential components. In further calculations, these are treated as components of the two-dimensional velocity field, which allows the blade section profile algorithm to be applied directly. The radial component of velocity is neglected; however, this simplification turned out to be justified by the agreement obtained between the design input values and corresponding ones determined during towing tank tests with the designed propeller. This will be considered in a further part of the text.

Similarly to the case of a two-dimensional blade section, obtaining the blade geometry is an iterative process. In the case adopted for practical application, 6 iterations were enough to receive a convergent solution. The applied vortex grid was a uniform one, with 20 x 20 radial x chordwise vortex segments. The first attempt was to use non-uniform mesh, which was denser towards the blade tip. As a result, it turned out to generate a blade with a very small pitch ratio (around 0.25 of mean value) and very high camber in the tip region.

The outer radii pitch angles may be smaller than the induced advance angles calculated with the lifting line method at respective positions, specifically for the lifting surface method. This effect is known in the literature and increases with the increasing propeller expanded area ratio and blades skew. The effect is weaker for warped propellers compared with non-balanced skew-induced rake propellers [2].

## INFLUENCE OF VORTEX WAKE

The possibility of including the influence of the vortex wake directly instead of using a simplified lifting line is the significant advantage of the lifting surface algorithm. First of all, using a discrete representation of the vortex wake allows an iterative relaxation algorithm to be applied, like the one described in [9] or [11] to determine its geometry adequate to the particular case. Also, experimental data on wake geometry as described in [17] may then be utilised even at this stage of blade design.

The initial guess for the vortex wake shape is a variable pitch helical surface, where the pitch angle at each radius is taken as equal to the induced advance angle coming from preceding lifting line calculations. In this “zero-iteration” propeller, slipstream contraction is neglected. Fig. 4 presents two blade pitch distributions – one determined at the vortex wake left as in the initial guess, and the second determined for iteratively relaxed wake. It has to be underlined that, as the induced velocities depend not only on the singularities strength but also on their position, the wake relaxation has to be repeated after each iterative update of the blade geometry.

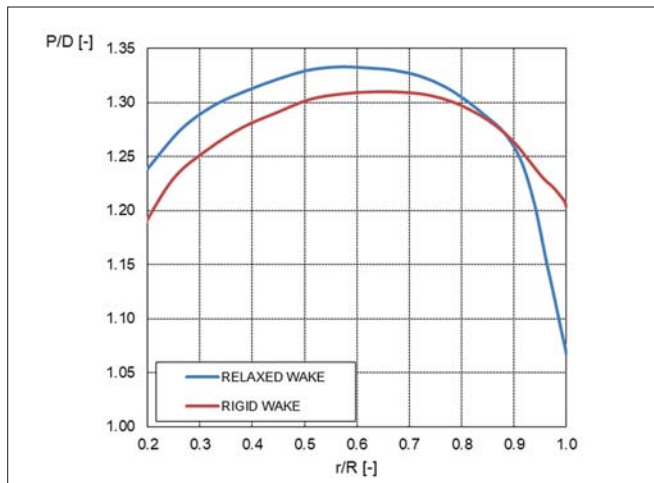


Fig. 4. Influence of vortex wake on blade's pitch

It can be easily seen that applying relaxed wake resulted in significant tip unloading with respect to the rigid wake calculations with a parallel increase in loading over the remaining part of the blade.

## EXPERIMENTAL VALIDATION

Using the method described above, two propellers were designed for the Kreso Container Ship (KCS). Their models were manufactured and tested in the Ship Hydromechanics Division of CTO. The numbers of these propeller models are P759 and P766. The first one was designed with a half-mature version of the design software, implementing the methods described above. Moreover, it was not designed as a wake-adapted propeller but for an entirely averaged velocity field, so it is effectively designed as an open-water propeller. Accordingly, propeller P766 was designed with a complete version of the software as a wake-adapted one.

The design assumptions for these propellers were taken as follows: diameter  $D = 7900$  mm, number of blades  $Z = 5$ , ship speed  $V_s = 24.0$  knots, rate of revolution  $n = 80.00$  rpm. For propeller P759 the required thrust force was taken as  $T = 2121$  kN. After conducting a self-propulsion test with this propeller, a new value of the thrust deduction factor  $t$  was available and hence a required thrust of  $T = 2134$  kN was adopted for the design of P766. The propellers differ in the frame of the expanded area ratio, which was  $EAR = 0.896$  for P759 and  $EAR = 1.029$  for P766. The differences result from a cavitation analysis that showed that a notably higher  $EAR$  value was required to limit the cavitation phenomena on the final propeller. This was not considered in detail in the case of P759 as it is in fact designed as an open-water propeller and hence, by definition, was not expected to operate free of cavitation. The pitch ratio at dimensionless radius  $r/R = 0.7$  is equal to  $P_{0.7}/D = 1.320$  in the case of propeller P759 and  $P_{0.7}/D = 1.327$  for propeller P766. Fig. 6 presents the pitch and camber distributions of both propellers.

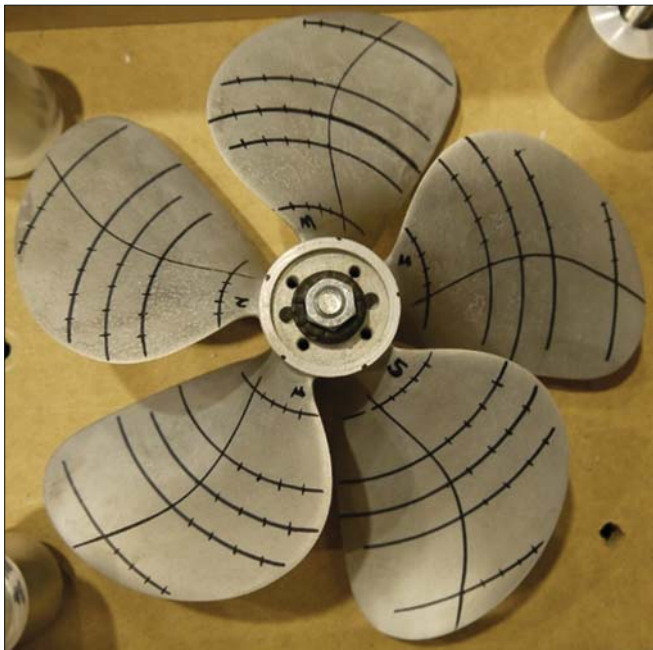


Fig. 5. Propeller model P759, suction side (left) and propeller model P766, pressure side (right)

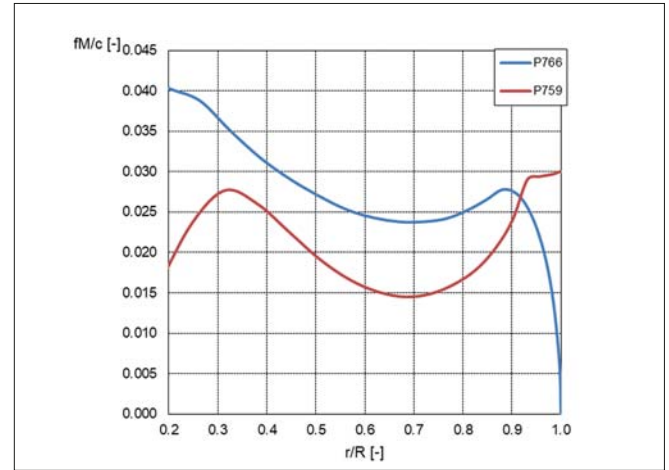
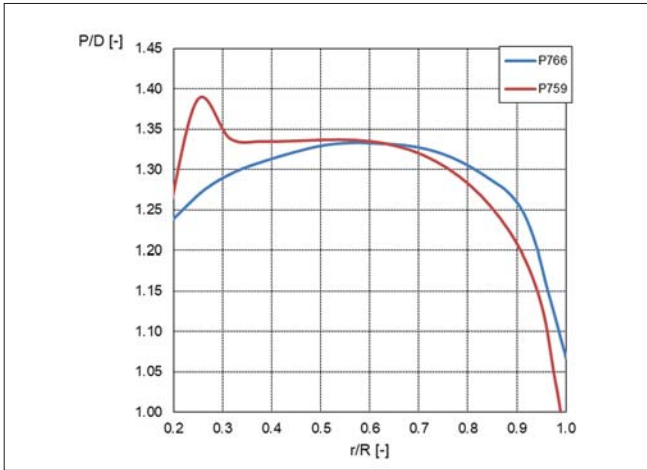


Fig. 6. Designed propellers pitch (left) and camber (right) distributions

In the case of both propellers, the camber ratio for radii above 0.90 was reduced to below the theoretical values for technological reasons. The reduction was much more robust in the case of the P759 propeller, which resulted in a discontinuous camber distribution above radius 0.90 for it. A purely theoretical camber

distribution would notably increase in the tip region, which would lead to an unnatural spoon-like shape of the tip. Analytical calculations conducted with the lifting surface model confirmed that reducing the tip camber did not influence the propellers' hydrodynamic properties significantly.

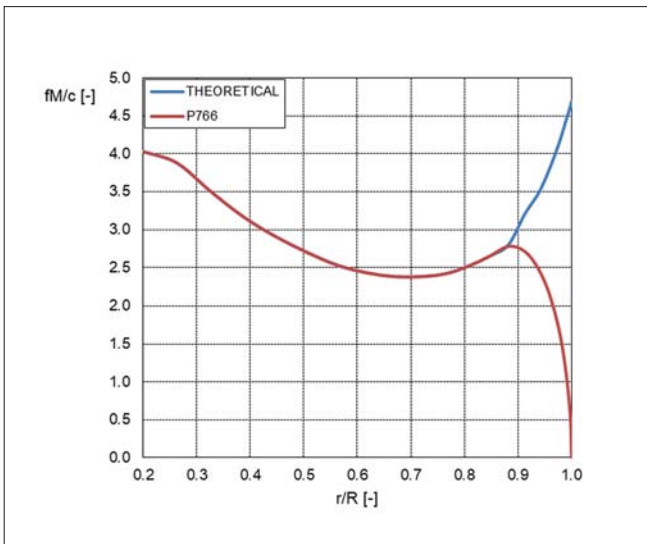


Fig. 7 gives the comparison between the theoretical camber distribution and the one adopted for propeller P766 design:

Fig. 8 gives the dimensional mean line ordinates vs. the non-dimensional chord fractions of selected profiles – after the first iteration and after the final iteration adopted for the propeller P766 design respectively. The presented mean lines are given after tip camber reduction. The initial guess for the mean line is a non-cambered flat profile so it is not presented here.

The main differences between the shapes of the mean lines are concentrated in the vicinity of the trailing edge. At the beginning of the iteration process, this region reveals a discontinuity of the mean line shape, but this disappears swiftly. It can be seen also that the maximum camber is slightly lower for the outer radii in the case of the final geometry.

The radial distributions of the design operation parameters for both propellers are given in Figs. 9–12.

Fig. 7. Theoretical and applied camber, propeller P766

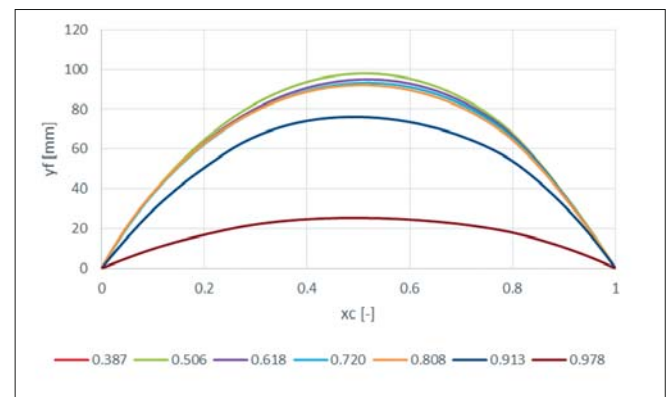
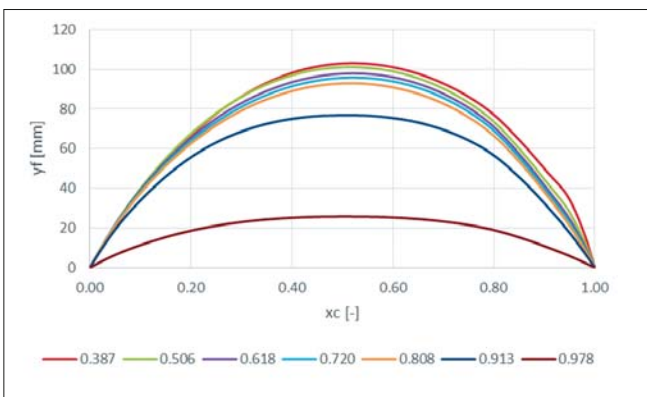


Fig. 8. Wake-adapted propeller P766 mean lines for selected radii, after first iteration (left) and final iteration (right)

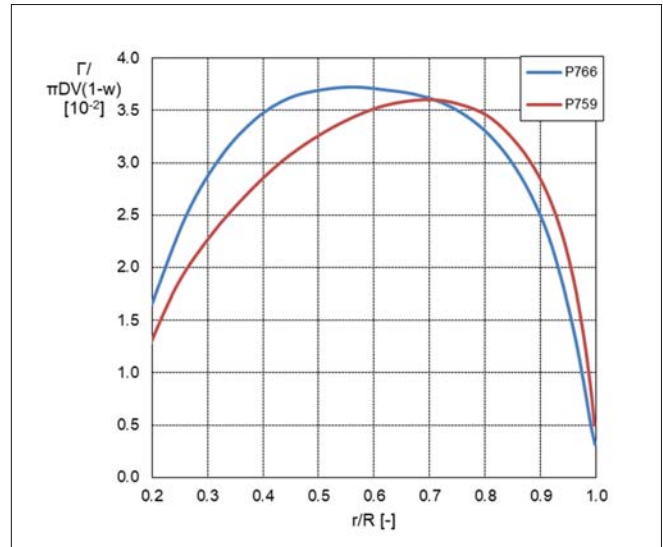
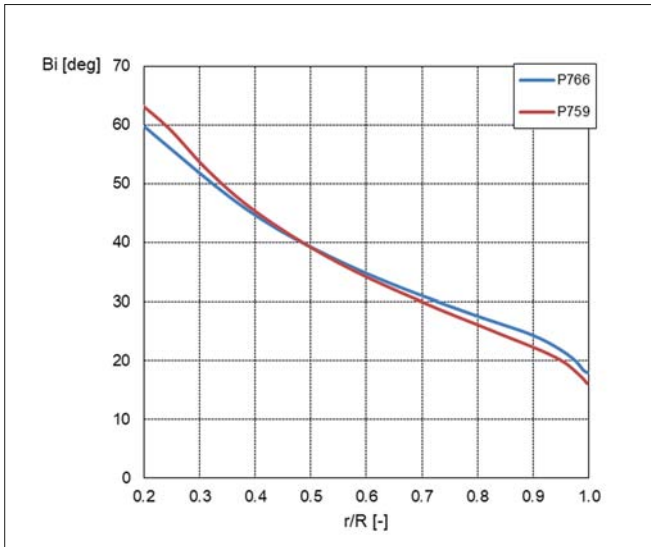


Fig. 9. Induced advance angle (left) and non-dimensional bound circulation (right) distributions

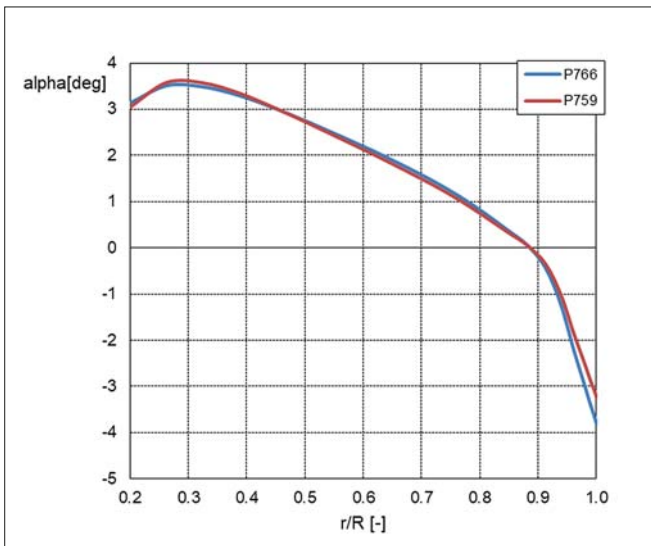


Fig. 10. Angle of attack distributions

Both propellers were subject to open water and self-propulsion tests. All tests were conducted in the CTO Ship Hydromechanics Division at a scale ratio of  $\lambda = 30.4502$ . Lifting surface calculations were conducted to evaluate the propellers' hydrodynamic properties at their design points. In the case of propeller P759, the comparison of numerical and experimental results is as follows:

Tab. 1. P759 – numerical and experimental results

Case	$J$	$K_T$	$K_Q$
Calculations	0.8839	0.2793	0.0579
Experiment		0.2829	0.0601

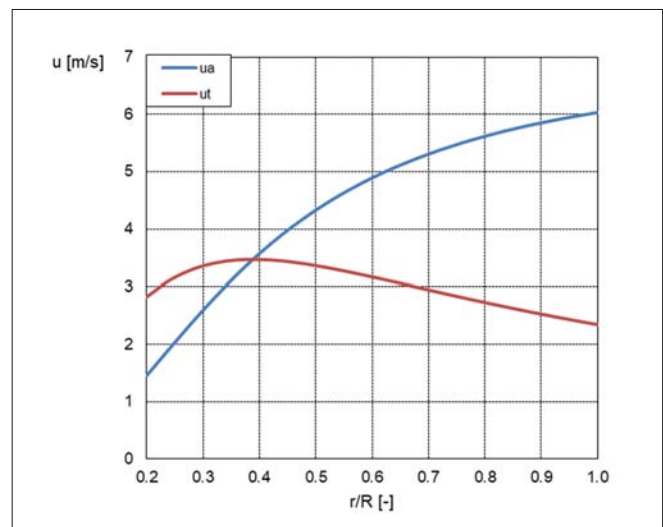
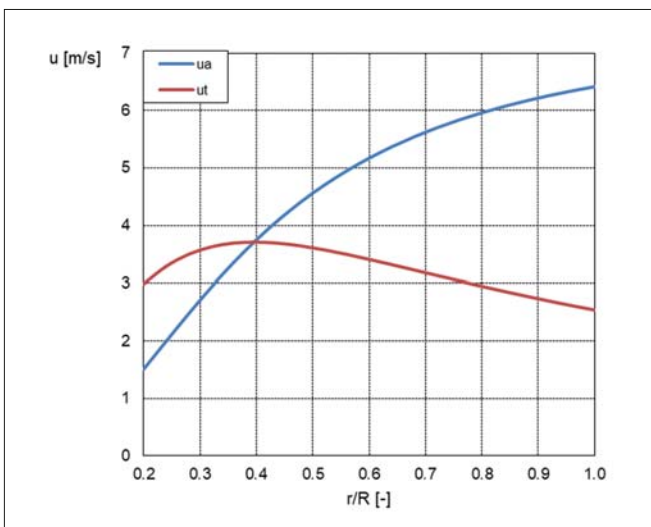


Fig. 11. Induced velocity distributions, P759 (left) and P766 (right)

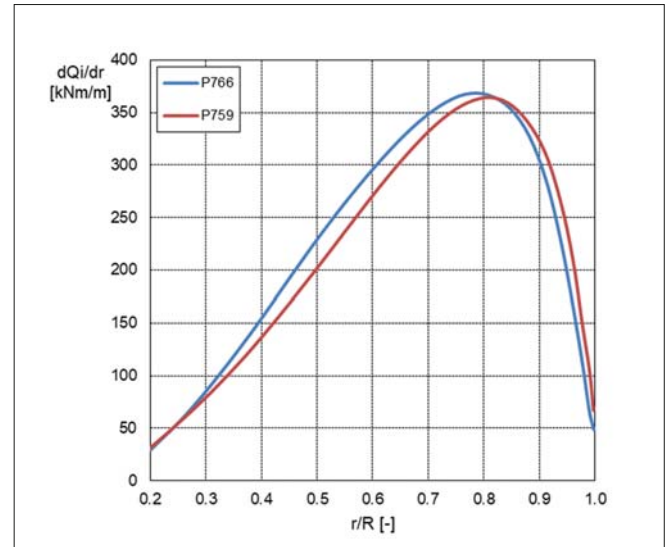
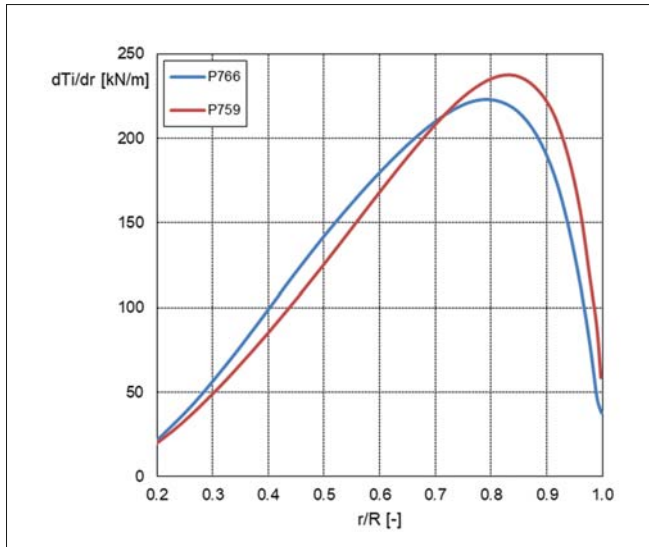


Fig. 12. Inviscid thrust (left) and torque (right) distributions

As the propeller P759 was chronologically the first one, the relation between its numerical and empirical characteristics was utilised to correct the results of the numerical calculations for propeller P766, by altering the calculated  $K_T$  and  $K_Q$  values times correction factor  $\alpha$ , which is defined as:

$$\alpha = \frac{K_{T/Q\_exp}}{K_{T/Q\_num}} \quad (7)$$

The following results were produced for P766:

Tab. 2. P766 – numerical and experimental results

Case	$J$	$K_T$	$K_Q$
Calculations	0.8979	0.2965	0.0639
Calculations corrected		0.3004	0.0664
Experiment		0.2979	0.0666

The basic measure of blade design correctness is agreement between the assumed rate of revolution at the design point and the obtained value. In this frame, it can be stated that propeller P766 was designed with full success.

Tab. 3. Results of self-propulsion test, rate of revolution

Case	Assumed	P759	P766
$n$ [rpm]	80.0	81.6	79.7

## CONCLUSIONS

The lifting surface model forms a reliable basis for designing blade section profiles and screw propeller blades.

The approach described in this paper may be utilised also for axial turbines, after slight modifications, and other rotating machinery consisting of lifting blades.

The incorporation of vortex wake deformation allows the propeller pitch distribution to be obtained and adjusted to local inflow conditions.

The simplification applied in the presented design approach, to neglect the radial component of induced velocity, results in a relatively simple and stable algorithm that is nevertheless still capable of providing reliable results.

Further work should reveal the possibility of applying the lifting surface model for designing more complex propulsor systems like a propeller with a guide vane or tandem propellers.

## ACKNOWLEDGEMENT

The paper has been elaborated within the frames of the Ship Design and Research Centre's own research program in 2018.

## REFERENCES

1. Bugalski T., Streckwall H., Szantyr J. A. (2013): *Critical review of propeller performance scaling methods, based on model experiments and numerical calculations*. Polish Maritime Research, 4(80), Vol. 20, 71–80.
2. Brockett T. (1981): *Lifting-Surface Hydrodynamics for Design of Rotating Blades*, Propellers '81 Symposium.
3. Gaggero S., Gonzalez-Adalid J., Perez Sobrino M. (2016): *Design of contracted and tip loaded propellers by using boundary element methods and optimization algorithms*. Applied Ocean Research, Vol. 55, 102–129.

4. Greeley D. S., Kerwin J. E. (1982): *Numerical methods for propeller design and analysis in steady flow*. SNAME Transactions, Vol. 90, 415–453.
5. Jarzyna H., Koronowicz T., Szantyr J. A. (1996): *Design of marine propellers, Selected problems*. Ossolineum, Wrocław.
6. Kobyliński L. (1955): *Śruby okrętowe (in Polish)*. Wydawnictwo Komunikacyjne, Warszawa.
7. Koyama K. (1993): *Comparative calculations of propellers by surface panel method, Workshop organized by 20th ITTC Propulsor Committee*. Papers of Ship Research Institute.
8. Król P., Bugalski T. (2018): *Application of vortex flow model in propeller – stator system design and analysis*. Polish Maritime Research, 1(97), Vol. 25, 35–44.
9. Król P., Tesch K. (2018): *Experimental and numerical validation of the improved vortex method applied to CP745 marine propeller model*. Polish Maritime Research, 2(98), Vol. 25, 57–66.
10. Lee K. J., Hoshino T., Lee J. H. (2014): *A lifting surface optimization method for the design of marine propeller blades*. Ocean Engineering, Vol. 88, 472–470.
11. Lee T., Park S. O. (2009): *Improved iteration algorithm for nonlinear vortex lattice method*. Journal of Aircraft, Vol. 46, No. 6.
12. Luca G., Roberto M., Claudio T. (2014): *Marine propellers performance and flow-field prediction by a free-wake panel method*. Journal of Hydrodynamics, Vol. 26 (5), 780–795.
13. Miclea-Bleiziffer M., Untaroiu A., Delgado A. (2014): *Development of a novel design method for marine propellers by computing the exact lift of arbitrary hydrofoils in cascade*. Ocean Engineering, Vol. 83, 87–98.
14. Morgan B., Silovic V., Denny S. B. (1968): *Propeller Lifting-Surface Corrections*. SNAME Transactions, Vol. 76, 309–347.
15. Muscari R., Mascio A., Verzicco R. (2013): *Modeling of vortex dynamics in the wake of a marine propeller*. Computers & Fluids, Vol. 73, 65–79.
16. Noosomton J., Gunnuang W. (2017): *Case study on CFD simulation and experiment of new developed propeller for training Thai boat*. Fifth International Symposium on Marine Propulsors – SMP'17, Espoo.
17. Suchecki W. (2018): *Studies on velocity fields around the cavitation vortices generated by the model of a rotating blade*. Polish Maritime Research, 2(98), Vol. 25, 66–70.
18. Szantyr J. (1984): *Deformable lifting surface method for determination of unsteady cavitation on screw propeller blade and its hydrodynamic results (in Polish)*. IMP PAN Gdańsk.
19. Zeraatgar H., Hossein Ghaemi M. (2019): *The analysis of overall ship fuel consumption in acceleration manoeuvre using hull-propeller-engine interaction principles and governor features*. Polish Maritime Research, 1(101), Vol. 26, 162–173.

## CONTACT WITH THE AUTHORS

**Przemysław Król**

*e-mail: krolprz30@gmail.com*

Ship Design and Research Centre  
Szczecińska 65, 80-392 Gdańsk

Gdańsk University of Technology  
Gabriela Narutowicza, 80-233 Gdańsk,  
**POLAND**

# COMPARATIVE STUDIES OF THE SEATINGS OF PROPULSION PLANTS AND AUXILIARY MACHINERY ON CHOCKS MADE OF METAL AND CAST OF RESIN PART I. MOUNTING ON STEEL CHOCKS

Paweł Grudziński  
Konrad Konowski

Zachodniopomorski Uniwersytet Technologiczny w Szczecinie, Poland

## ABSTRACT

*This paper presents a description and the results of experimental studies of the deformation, friction and structural damping occurring in foundation bolted joints of propulsion plant components and auxiliary machinery that is rigidly mounted on sea-going ships. The rigid mounting of these devices to the ships' structural foundations can be implemented in a traditional way, i.e. on chocks made of metal (usually of steel), or in a modern way, i.e. on chocks cast of resin, specially designed for this purpose. The main goal of this study is to perform a comparative analysis of these two solutions and to give a scientific explanation for why chocks cast of resin perform better in machinery seatings than the steel chocks traditionally used for this purpose. The paper consists of two parts. Part I presents the details of the rigid mountings of machinery to the foundations, and contains the results of experimental studies performed on a model of a foundation bolted joint with a traditional steel chock. Part II contains the results of similar studies carried out for a model of a bolted joint with a modern chock cast of resin. Next, a comparative analysis and evaluation of the results obtained for both investigated bolted joints was carried out, and conclusions were formulated to highlight important aspects of the problem from the point of view of science and engineering practice.*

**Keywords:** sea-going ships, propulsion plants, auxiliary machinery, seating, bolted joints, chocks

## INTRODUCTION

The intensity of vibration, quality of operation, reliability and durability of propulsion plants and auxiliary machinery installed on sea-going ships depend not only on their design and workmanship quality; to a large extent, they also depend on the type and quality of their seatings onto the structural foundation. In the modern approach to this problem, the plant components, their foundations and fastening systems should form an integrated mechanical (dynamic) system, with a stable structure and stable parameters.

This problem will be discussed here using the example of the seating of a main propulsion engine on a sea-going ship's structural foundation, due to the special role of these objects and the particularly high requirements which these engines must meet. The issues discussed here are, to

a greater or lesser extent, also relevant in relation to the seatings of other propulsion plant components and other types of auxiliary machinery installed on sea-going ships, and in particular those that generate large dynamic forces and vibrations.

The mounting of a large propulsion engine onto a ship's structural foundation must be done in accordance with the installation instructions of the manufacturer and the regulations set by the classification society supervising the construction of the ship. According to instructions set out by the engine manufacturer Wärtsilä [9] and the regulations of Germanischer Lloyd (GL) [2], there are generally two methods of mounting machinery to a ship's structural foundations: rigid mounting and resilient mounting.

The term 'rigid mounting' is used when a component of a propulsion plant or another item of equipment is attached

directly to the ship's structural foundation, or if rigid chocks are properly fitted between the foundation and the machine base. A resilient mounting is a connection between the plant components to the structural foundation of the ship, using resilient mounting components such as rubber pads or special vibrato-isolators.

The study presented in this paper considers only the rigid mountings of the plant components to the foundations (understood in the manner specified in the regulations [2, 9]). They involve the majority of the main propulsion engines and gearboxes, as well as most auxiliary equipment installed under and on the deck of sea-going ships. An example of a rigid mounting of a propulsion engine to a ship's structural foundation is shown in Fig. 1 [3].

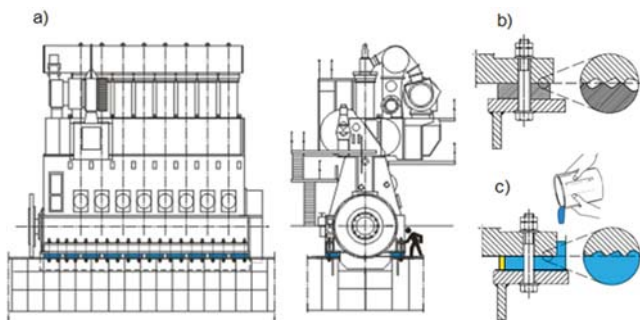


Fig. 1. (a) Schematic diagram of a rigid mounting of a propulsion engine to a ship's structural foundation using (b) chocks made of steel and (c) cast from resin

The use of chocks in the mounting of heavy machinery to the foundations arises from the difficulty of properly fitting the large bearing surfaces of the machine base and the foundation top plate with each other, and also from the necessity of properly setting and aligning the associated plant components, for example the main engine with the gearbox and the drive shaft of a ship.

According to the existing regulations [2, 9], the chocks used in this kind of rigid machinery mounting can be made of metal (steel or possibly iron) or cast in a resin compound specially developed for this purpose. The use of conventional steel chocks (Fig. 1b) has a long tradition. It also has many significant disadvantages, particularly in regard to the mounting of large propulsion engines on sea-going ships. This kind of mounting is characterised by high complexity, difficult and time-consuming installation, low technical quality and significant unreliability in operation [1, 3, 8]. Fastening systems of this type require continuous monitoring and frequent maintenance.

Various methods have been developed to improve the situation, for example using reusable adjustable metal chocks [4]. Although these are generally acceptable [9], they have not been widely used in the ship building industry. Significant progress was made in this area only after developing and applying special pourable resin compounds. Making chocks of these materials by pouring in place (Fig. 1c) greatly simplified the technology of machinery seating, shortened the time required and reduced the cost of implementation. As an unexpected result, this also significantly improved the technical quality of the seatings in comparison to that of conventional steel chocks.

In view of this, an important question arises as to why chocks cast in resin perform better in this kind of rigid mounting, i.e. guarantee better operation and higher stability, reliability and durability of the seated devices than conventional chocks made of steel, despite the fact that resin has much lower strength and stiffness than steel.

The answer to this question is not a simple or an easy one. Adequate knowledge is needed of the physical phenomena occurring in the real foundation bolted joints, in terms of their installation and operation. In order to obtain this knowledge, several experimental investigations were carried out. These investigations were performed on models of the foundation bolted joints with a traditionally made steel chock and with a modern chock cast in a resin compound designed for this purpose. A comparative analysis of their behaviour under similar loading conditions was then carried out.

The dynamic load acting on the foundation bolted joints of machines during their operation may be normal and tangential to the supporting surface. Taking these possibilities into account, separate studies were conducted using suitable models of foundation bolted joints under both normal and tangential loads. In earlier work [5, 6], a description and test results for models of foundation bolted joints subjected to normal loads were presented. The current paper presents a description and the results of experimental studies carried out on models of foundation bolted joints with a steel chock and a chock cast of resin, subjected to a constant normal load and time-varying tangential loads. The results obtained from these studies are presented in two parts, constituting two separate publications. This article forms Part I of this research.

## THEORETICAL FUNDAMENTALS

The starting point for these investigations was the idea that the general division of structural connections into rigid and resilient joints, which is adopted widely in engineering theory and practice, makes sense only in a certain specific context. In fact, there are no perfectly rigid structural connections. The modelling of the foundation bolted joints of propulsion plants and auxiliary machinery mounted to the structural foundations of ships as a group of rigid connections (as in [2, 9]), is a considerable simplification. This suggests that their deformations are small and irrelevant, and that their description and analysis can be omitted, distorting our picture of the phenomena occurring within them and hindering a proper understanding of the role they play in seated objects.

The results of many studies and practical experience show [6] that fastening systems of many machines and devices that are made in the traditional manner using steel chocks are often the weakest links in the entire mechanical systems in which they are used, and do not ensure adequate integration; they therefore cause many problems to the users of these different machines and equipment.

It is worth noting that the number of chocks in the seatings of large machines and devices on foundations is usually much larger than three, and is often a dozen or even several dozen.

An example of a main propulsion engine of a sea-going ship is shown in Fig. 1a. In such cases, the fastening systems form multifold, statically indeterminate mechanical systems, which are not only very difficult to model and calculate but are also difficult to implement. This particularly applies to the appropriate individual fitting of each foundation chock; even a very small mismatch in their heights can cause large unpredictable mounting stresses and deformations in the whole mechanical system in which they are used.

Due to shape errors, i.e. the waviness and roughness of the mounting surfaces, a perfect fit between metal chocks over their entire nominal bearing surfaces and the foundation top plate and machine base is practically impossible. True contacts between two such surfaces develop only between the uneven tops of each surface (Fig. 1b). The true contacts are separate micro-areas where the uneven tops from one surface are squeezed against the uneven tops of the other surface. Depending on the conditions, the asperities may deform elastically or elastic-plastically.

The real area of contact in such chocks is only a very small fraction of their nominal contact area. This has very serious practical consequences, particularly under dynamic loads. However, an exact fit between contact surfaces is possible and easily achievable when using resin chocks that are poured in place (Fig. 1c).

As noted above, the foundation bolted joints of machines (with both steel and cast resin chocks) should not be regarded as rigid connections. In real foundation bolted joints, complex deformations and closely related physical phenomena (vibration, friction, structural damping, wear) occur during operation. These have a major impact not only on the behaviour of these joints, but very often also on the entire mechanical system of which they constitute a part. A thorough understanding of these phenomena is therefore necessary in order to evaluate the quality of these joints and to achieve a proper understanding of the role they play in machines and devices seated on foundations. In particular, it is required for a proper understanding and explanation of why chocks cast in resin in the seatings of machines perform better than the steel chocks traditionally used for this purpose.

## TEST METHOD

Experimental studies were performed on specially designed and constructed bolted joints, as shown in Fig. 2. These were models of the foundation bolted joints of machines, and consisted of two interconnected steel members, a spacer member (quadratic, with a side of 80 mm and a thickness of 20 mm, with a hole of 24 mm in the centre) located between them and a fixing bolt M20x1.25 with a nut. The connected steel members represented some clippings of the structural foundation top plate and the base of the machine, respectively, and the spacer member between them, which was made of steel or cast of resin, represented the chock of the seated machine (Fig. 1). The bolt with glued strain gauges was properly calibrated and served as a dynamometer to achieve a proper mounting clamp for the connected elements and

control during the tests. A special spring washer and an axial ball bearing with a spherical washer (NSK Bearings 52204U) were placed under the nut in order to increase the elastic flexibility of the tensioning system and the uniformity of the pressure acting on the chock.

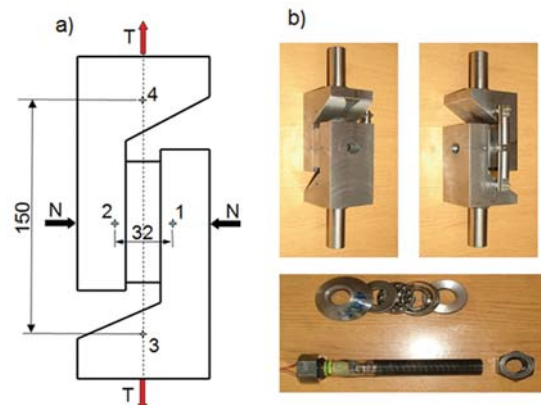


Fig. 2. Bolted joint used in a study of the characteristics of tangential displacements, friction and structural damping: (a) schematic with points marked for measurement of the relative displacements; (b) view of the joined elements and the bolt with glued strain gauges to measure the clamping force  $N$

The joints were designed for a study of the characteristics of tangential displacements, frictional forces and structural damping, at a constant clamping force and with time-varying tangential loads. The tests were performed on a modern servo-hydraulic testing machine (INSTRON 8850). The heads of the machine were equipped with hydraulic clamp jaws (Fig. 3a). This enabled dynamic loading of the tested joint by applying tensile and compressive forces, with a continuous and smooth transition through zero.

Instron extensometers (Fig. 3) were applied to measure the relative displacements of the joined elements. The displacements were measured on the side surfaces at two locations, between points 1 and 2, and between 3 and 4, as shown in Fig. 2. Extensometer 1 (Fig. 3) measured the relative tangential displacements of the combined elements at points 1 and 2 (Fig. 2), while extensometer 2 measured the mutual change in the distance between points 3 and 4, which were at a considerable distance from each other ( $l = 150$  mm), along the line of operation of the loading force  $T$  (Fig. 2a).

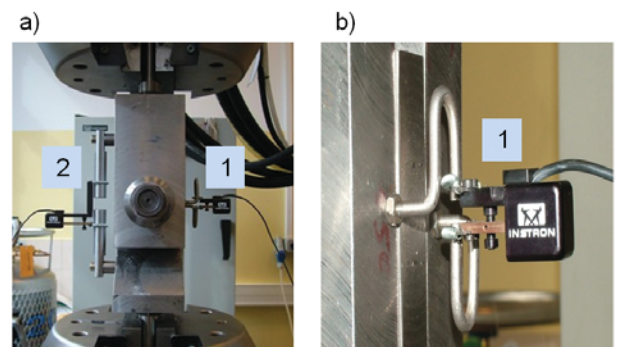


Fig. 3. Testing of a bolted joint with extensometers to measure the relative displacements of the connected elements: (a) general view; (b) fragment

We used Instron's Wave Matrix (v. 1.5.318), an intelligent software package designed for the dynamic testing of materials and components. It formed the basis for creating special programs for the dynamic loads or displacements to be applied to the system and for the computer-control of their implementation, with a very high accuracy and repeatability. Dynamic tests are generally characterised by the fact that all input and output quantities are treated as functions of time.

The studies were first performed for the bolted joint with a chock made of steel, as traditionally used for this purpose, and then (in Part II) with a chock cast in resin.

## IMPLEMENTATION AND RESULTS OF THE STUDIES

The contact surfaces of the two joined elements were milled, and the measured roughness parameters of these surfaces had values  $R_a = 2.47\text{--}2.51\ \mu\text{m}$ ,  $R_z = 13.40\text{--}13.50\ \mu\text{m}$ . The contact surfaces of the steel chock (thickness 20 mm), were turned and had roughness parameters  $R_a = 2.29\text{--}3.60\ \mu\text{m}$ ,  $R_z = 11.69\text{--}17.25\ \mu\text{m}$ . The preloading force in the bolt was  $N = 51700 \pm 200\ \text{N}$ . This induced a bolt tensile stress of  $\sigma = 199.7\ \text{MPa}$  and an average surface pressure on the chock of  $p = 8.69\ \text{MPa}$ . When determining the bolt mounting tension, the requirements of the classification societies in the maritime industry were taken into account. For the main engines and gears, the average allowable surface pressure for the material used was  $5\ \text{N/mm}^2$  (PRS, GL, LRS, RMRS, BV, DNV),  $15\ \text{N/mm}^2$  (ABS),  $15\ \text{N/mm}^2$  (PRS) for mechanisms for which coaxiality is not required,  $30\ \text{N/mm}^2$  (PRS) for anchor and mooring winches, and  $< 60\ \text{N/mm}^2$  (PRS) for temporary loads.

The tests carried out using the testing machine are shown in Fig. 3a. Several experiments were carried out on the tested joints by applying various computer-controlled programs for loads or displacements at the input. Detailed descriptions and results of these experiments are contained in an earlier report [7]. Some of the results of these experiments are presented below.

### EXPERIMENT 1

This experiment studied the relative tangential displacements of the connected elements, as measured at points 1 and 2. The system was loaded with an increasing force  $T$ , with some interruptions, and with several unloading (to zero) and re-loading cycles. The results of this experiment are shown in Fig. 4. The last unloading curve on the graph did not stop at zero, but passed the zero line in a continuous and smooth way, meaning that the load acting on the tested system changed from tension to compression. The compressive load was continued until the initial state of the tested system was reached, i.e. a zero value of the force  $T$  (shear stress  $\tau$ ) and tangential displacement  $\delta_t$  (Fig. 4).

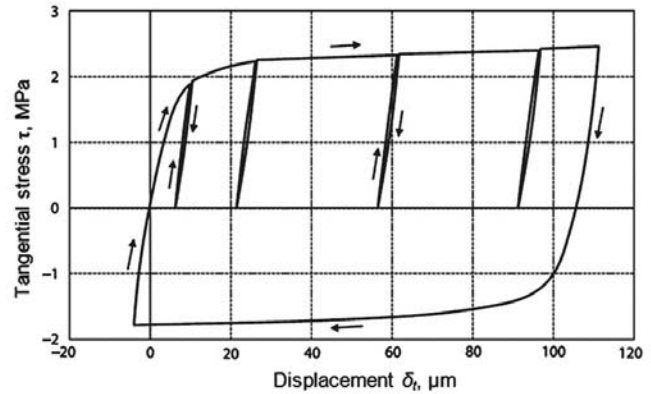


Fig. 4. Relationship between tangential stress  $\tau$  (force  $T$ ) and relative displacement  $\delta_t$  of the connected elements for the bolted joint with the steel chock

During unloading and re-loading, the system behaves elastically until the re-loading force reaches the point on the graph at which the unloading process begins. After reaching this point, and with continued loading, further micro-slips occurred with a very low increase in the loading force. During unloading and re-loading, some slight elastic hysteresis loops were clearly visible, as shown in Fig. 4.

The mechanism of the relative tangential displacements  $\delta_t$  at points 1 and 2, caused by the force  $T$  acting tangentially to the contact surface, is illustrated in Fig. 5. In this case, the measured relative displacements  $\delta_t$  are the result of the elastic shearing strains  $\gamma$  of the material of the joined elements ( $\delta_t' = \gamma h$ ), the elastic tangential contact deformations of the surface asperities and micro-slips occurring at the interfaces of the interacting surfaces.

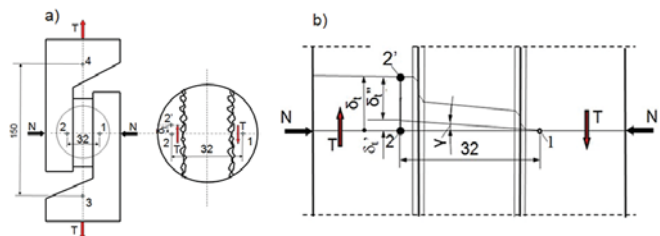


Fig. 5. Schematic diagrams of (a) loading and (b) deformation for the tested joint with the steel chock

The graph in Fig. 4 also shows the variation in the frictional force, which balances the given external load  $T$ . From these results, it follows that the development of the frictional force is associated with the tangential displacement  $dt$  of the connected elements, which only have an elastic nature to a small extent. The micro-slips play the dominant role here, and can achieve significant values before the contact is broken and macro-slipping occurs. The values of the elastic tangential contact deformations (the tangential contact flexibility) can easily be determined at any point by unloading and re-loading the joint (Fig. 4).

Note: In the above experiment, the tested joint was not loaded to the point of breaking of the contact and the occurrence macro-slipping, due to the possible damage to the costly extensometers.

## EXPERIMENT 2

The purpose of this experiment was to investigate the behaviour of the system for a given program of forced oscillation of the relative displacements of the connected elements. A schematic of the test joint and the program of assumed relative displacements (sinusoidal oscillations), measured at points 1 and 2 are shown in Fig. 6.

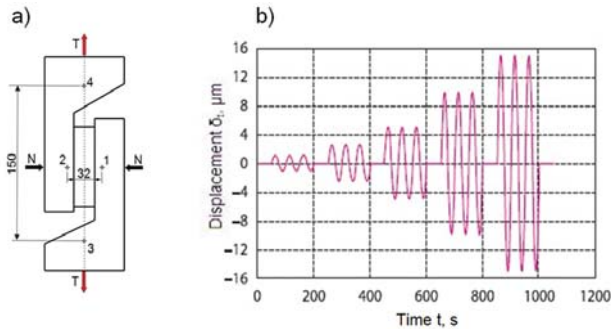


Fig. 6. (a) Schematic of the test joint and (b) the assumed program of sinusoidal oscillations; the amplitudes of these oscillations had values of  $\delta_a = 1, 2.5, 5, 10$  and  $15 \mu\text{m}$

The task of the testing machine equipped with the program for dynamic research was to provide an adequate time period for loading, which would ensure the implementation of the assumed oscillations shown in Fig. 6b. Figure 7 shows the results of this experiment.

These graphs show (a) the time evolution of the oscillations (the relative displacements  $\delta_i(t)$  of the connected elements measured at points 1 and 2) performed by the testing machine; (b) the time evolution of the force  $T(t)$  used to realise the assumed displacements; (c) the time evolution of the average shear stresses  $\tau(t)$  acting on the chock; and (d) the relationships between the stresses  $\tau$  and displacements  $\delta_i$  and the hysteresis loops for the selected oscillation amplitudes shown in Fig. 7a. The high accuracy of the sinusoidal displacements (oscillations), with very small amplitudes (from 1 to  $15 \mu\text{m}$ ), and the irregular complex time evolution of the force needed for their implementation should be noted. The hysteresis loops (Fig. 7d) show that the system behaves quasi-linearly only at sufficiently small displacement amplitudes (max.  $5 \mu\text{m}$ ). At higher oscillation amplitudes in the tangential direction, substantial micro-slips and large hysteresis loops are clearly visible. This shows the loss of the elastic integrity of the tested joint and the dissipation of a large amount of vibration energy.

A positive effect of this phenomenon is good vibration damping, and a negative result is the intensive wear of the interacting surfaces, which leads to rapid destruction of the joint. In well-designed bolted joints, significant micro-slipping should not take place. One important issue is to establish a reasonable limit for micro-displacements at a contact that allows for safe long-term operation of the bolted joints loaded by variable tangential forces.

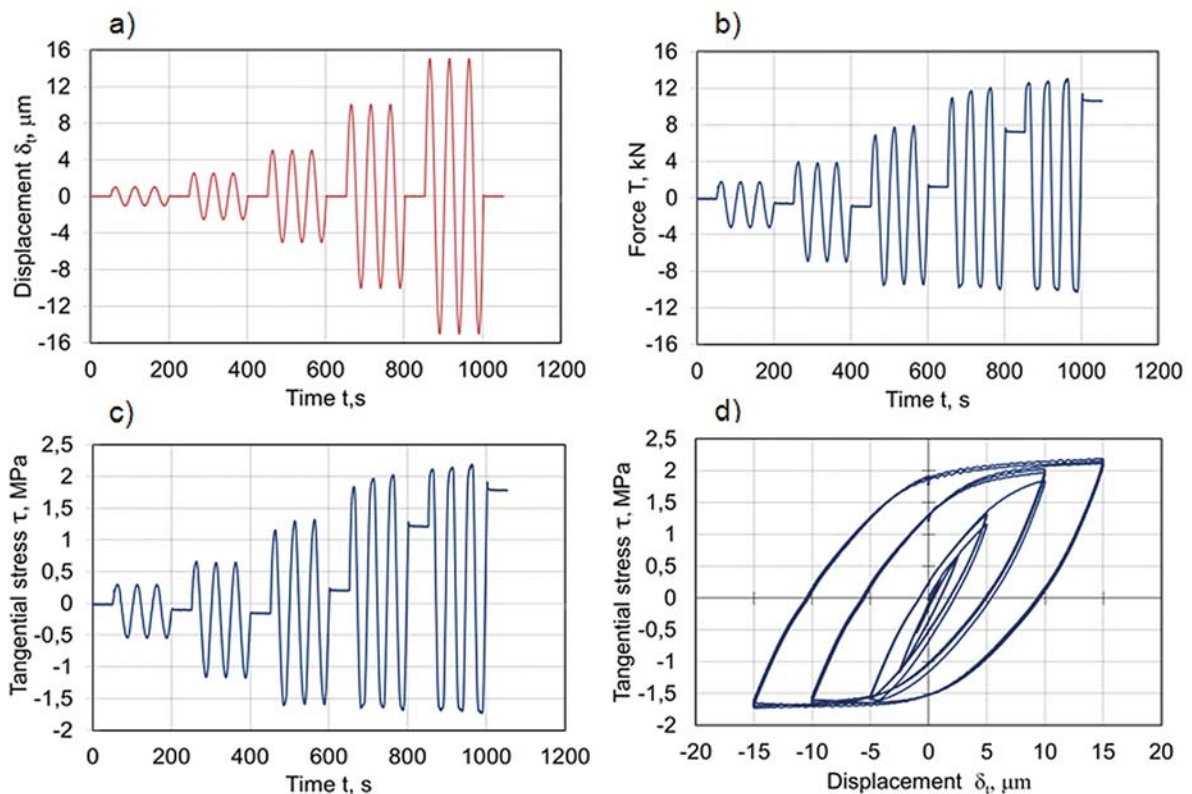


Fig. 7. Results of experiment 2: (a) time evolution of the implemented relative displacements of the connected elements using the testing machine; (b) time evolution of the force  $T$  used to realise the displacements; (c) time evolution of the average shear stresses acting on the chock; and (d) relationships between the stresses  $\tau$  and displacements  $\delta_i$

### EXPERIMENT 3

In experiment 3, the tested joint was loaded cyclically, with controlled displacements  $s(t)$  of the head of the testing machine. The results of this experiment are shown in Fig. 8.

Figure 8a shows the given displacement program  $s(t)$  (sinusoidal vibrations with amplitudes of 25, 50, 75, 100 and 125  $\mu\text{m}$ ) performed by the head of the testing machine. Figure 8b shows the time evolution of the relative displacements  $\delta_t(t)$  of the connected elements (measured at points 1 and 2), and Fig. 8c shows the time evolution of the average shear stresses acting on the chock for the given kinematic excitations (shown in Fig. 8a). Figure 8d shows the relationships between the stresses  $\tau$  and displacements  $\delta_t$  and the hysteresis loops for the oscillation amplitudes shown in Fig. 8a.

The measurement results show (Fig. 8) that the tested system behaves in a linear elastic manner only at very small amplitudes of vibrations excited kinematically by the head of the machine (up to 0.05 mm). The system behaves nonlinearly at higher amplitudes of vibration. In such cases, complicated nonlinear relationships arise between the given harmonic excitation  $s(t)$  and the response of the system. Significant micro-slipping occurs at the contact between the mating surfaces, which in conjunction with the friction forces form large hysteresis loops. Tangential forces carry out much of the work, and this in turn can cause high wearing of the interacting surfaces, and the quick loosening and destruction of this type of bolted joint.

### CONCLUSIONS

This study has shown that foundation bolted joints with steel chocks, classified in the literature and in engineering practice as a group of rigid connections, are not perfectly rigid. During operation, in addition to small elastic deformations in the tangential direction, there can be significant micro-slips (plastic displacements) of the elements connected with each other. These cause abrasion of the asperity tops of the interacting surfaces, the occurrence of fretting corrosion, loosening of the foundation bolted joints and an increase in the intensity of vibrations. The result is not only rapid destruction of the mounting system, but often also intensive wear of many parts of the seated device and various failures. These phenomena and problems are well known in the engineering practice, as well as in shipbuilding. For comparison purposes, similar studies were performed for a bolted joint with a chock cast of resin. A description and the results of these studies and the conclusions that can be drawn are presented in Part II.

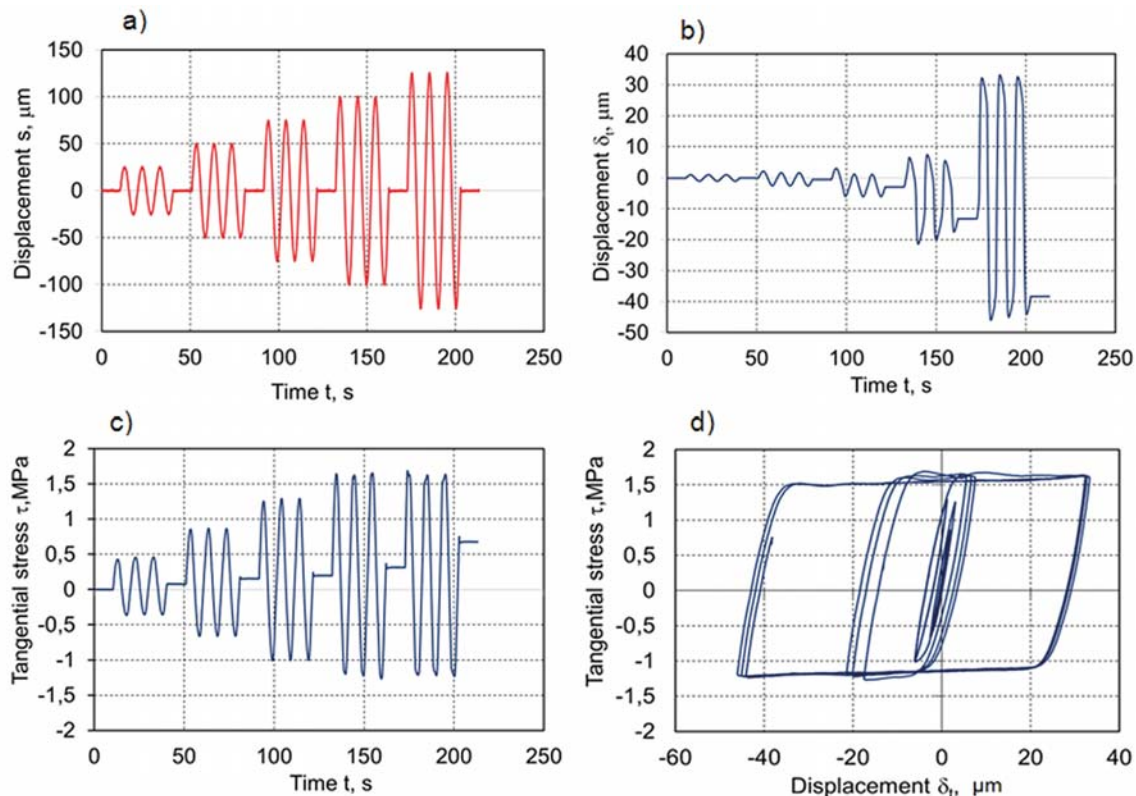


Fig. 8. Results of Experiment 3: a) time evolution of the assumed displacements  $s(t)$  performed by the head of the testing machine; b) time evolution of the relative displacements  $\delta_t(t)$  of the connected elements; c) time evolution of the average shear stresses acting on the chock; and d) relationships between the stresses  $\tau$  and displacements  $\delta_t$ .

## REFERENCES

1. Cherry E., Church J.E. (2014): *Shipboard Maintenance of Machinery. Engine Foundations. ITW Chockfast Marine – Industrial Grouts, Adhesives, Repair Products and Coatings*. Retrieved from: <http://www.chockfast.com/reference.html>.
2. Germanischer Lloyd (2010): *Guidelines for the Seating of Propulsion Plants and Auxiliary Machinery*. Rules for Classification and Construction, VI, Part 4, Chapter 3.
3. Grudziński K., Jaroszewicz W. (2002): *Seating of Machines and Devices on Foundation Chocks Cast of EPY Resin Compound*. ZAPOL, Dmochowski & Sobczyk Registered Partnership, Szczecin, 2002 (in Polish), 2004 (in English), 2005 (in Russian).
4. Grudziński P., Konowalski K. (2012): *Studies of Flexibility of Steel Adjustable Foundation Chock*. *Advances in Manufacturing Science and Technology*, 36(2), 79–90.
5. Grudziński P., Konowalski K. (2014): *Experimental Investigations of Normal Deformations of Foundation Chocks Used in the Seating of Heavy Machines and Devices*. *Advances in Manufacturing Science and Technology Part I: Theoretical fundamentals and investigations of a steel chock*, 38(1), 63–76; Part II. *Experimental investigations of a chock cast of EPY resin*, 38(2), 51–61.
6. Grudziński K. (2008): *Comparative Analysis of the Seatings of Reciprocating Compressors on the Foundations of Concrete and Steel Structures* (in Polish). Report No. 1/08, Politechnika Szczecińska, Katedra Mechaniki i Podstaw Konstrukcji Maszyn, Szczecin (unpublished).
7. Grudziński P. (2013): *Research into the Vibration Isolating Properties of EPY Resin and the Possibility of Its Use to Reduce the Vibrations and Insulation of Structure-Borne Sound* (in Polish). Sprawozdanie merytoryczne z wykonania projektu badawczego nr N N502 194938, Zachodniopomorski Uniwersytet Technologiczny w Szczecinie, Katedra Mechaniki i Podstaw Konstrukcji Maszyn, Szczecin 2013 (unpublished).
8. Piaseczny L. (2002): *Designing of Power Plant Rechocking Using a Pourable Polymer on Example of Ship's Power Plant*. *Eksploatacja i Niezawodność* Nr 2, 26–38, 2002.
9. Wärtsilä (2014): *Product Guide W32-1/2014, 15. Foundation*, Wärtsilä, Ship Power Technology, Vaasa.

## CONTACT WITH THE AUTHORS

**Paweł Grudziński**

*e-mail: pawel.grudzinski@zut.edu.pl*

Zachodniopomorski Uniwersytet Technologiczny  
w Szczecinie, al. Piastów 19  
70-310 Szczecin  
**POLAND**

**Konrad Konowalski**

*e-mail: konrad.konowalski@zut.edu.pl*

Zachodniopomorski Uniwersytet Technologiczny  
w Szczecinie, al. Piastów 19  
70-310 Szczecin  
**POLAND**

# INVESTIGATION OF THE COMBUSTION PROCESSES IN THE GAS TURBINE MODULE OF AN FPSO OPERATING ON ASSOCIATED GAS CONVERSION PRODUCTS

Oleksandr Cherednichenko

Admiral Makarov National University of Shipbuilding, Ukraine

Serhiy Serbin

Admiral Makarov National University of Shipbuilding, Ukraine

Marek Dzida

Gdańsk University of Technology, Poland

## ABSTRACT

*In this paper, we consider the issue of thermo-chemical heat recovery of waste heat from gas turbine engines for the steam conversion of associated gas for offshore vessels. Current trends in the development of offshore infrastructure are identified, and the composition of power plants for mobile offshore drilling units and FPSO vessels is analyzed. We present the results of a comparison of power-to-volume ratio, power-to-weight ratio and efficiency for diesel and gas turbine power modules of various capacities. Mathematical modeling methods are used to analyze the parameters of an alternative gas turbine unit based on steam conversion of the associated gas, and the estimated efficiency of the energy module is shown to be 50%. In the modeling of the burning processes, the UGT 25000 serial low emission combustor is considered, and a detailed analysis of the processes in the combustor is presented, based on the application of a 35-reaction chemical mechanism. We confirm the possibility of efficient combustion of associated gas steam conversion products with different compositions, and establish that stable operation of the gas turbine combustor is possible when using fuels with low calorific values in the range 7–8 MJ/kg. It is found that the emissions of NO<sub>x</sub> and CO during operation of a gas turbine engine on the associated gas conversion products are within acceptable limits.*

**Keywords:** thermo-chemical heat recovery, gas turbine engine, associated gas, combustor

## INTRODUCTION

Oil and gas production on the sea and ocean shelf is currently one of the main sources of global energy resources, and has a significant impact on the economies of both individual countries and entire regions. Shallow-water production has been exploited for a long time, and now accounts for over 30% of global oil production and 25% of gas production. There are significant oil and gas deposits in the deep-sea areas of the world's oceans, but their development requires large financial investments and the introduction of new technologies.

A large and diverse fleet of offshore vessels [1] has been created to support work on offshore fields (Fig. 1).

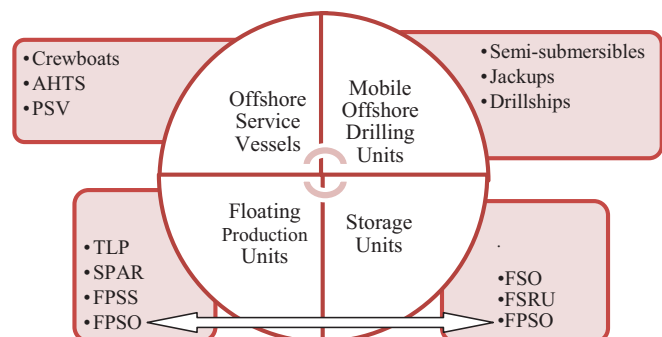


Fig. 1. Offshore vessels and floating units.

Abbreviations: AHTS – Anchor Handling Tug Supply Vessel; PSV – Platform Supply Vessel; TLP – Tension-Leg Platform; SPAR – Spar Platform; FPSS – Semisubmersible Floating Production System; FPSO – Floating Production Storage And Offloading System; FSO – Floating Storage Offloading Unit; FSRU – Floating Storage And Regasification Unit

Floating offshore infrastructure includes major ship groups and floating units such as offshore service vessels (OSVs), mobile offshore drilling units (MODUs), floating production units and storage units.

## IDENTIFICATION OF THE INVESTIGATION OBJECT

One of the main factors ensuring the efficient operation of the first link in the supply chain (i.e. production, transportation and supply) of offshore oil and gas is related to the energy efficiency indicators of offshore vessels and floating units. MODU and floating production storage and offloading (FPSO) installations are of primary interest in energy efficiency research. The production systems on such vessels determine the stability and efficiency of production processes, and those of FPSOs determine the processing and shipping efficiency. These processes involve significant energy consumption. The composition and characteristics of the installations of the offshore infrastructure object vary widely, but the main drive engines are typically gas turbine engines (GTEs) and medium speed four-stroke diesel engines (4SDEs).

Deep-water platforms and drilling vessels can operate at depths of over 3.5 km. Extraction at great depths is expensive: the cost of newly built drilling vessels can reach 900 million USD, and for semi-submersible platforms, this may be 600 million USD. All semi-submersible platforms and drillships incur additional energy costs, since they are equipped with powerful dynamic positioning systems, and fuel costs can reach 100,000 USD per day [2]. For drilling ships and platforms, 4SDEs are preferred. For example, the installation on the drilling ship Stena Drill MAX consists of six main engines to drive the vessel's main generators, and each Wärtsilä 16V32 engine has an output of 7.3 MW [3]. The Stena Don semi-submersible floating drill platform consists of nine Wartsila 16V25 main generators (3.5 MW each) [4]. The Aker H-6e semi-submersible floating drill platform consists of eight main Rolls Royce diesel engines (5.3 MW each) [5].

It should be noted that despite the high capital (CAPEX) and operating (OPEX) expenses, the share of deep-sea production is increasing, and has a significant impact on the global economy. This is evidenced by the fact that analytical reviews and forecasts of regional hydrocarbon energy markets are based on an assessment of the key factors of onshore and offshore oil and gas production, taking into account an analysis of the situation with respect to shallow and deepwater production [1].

The increase in production in deep-sea regions and areas remote from ground infrastructure has also led to an increase in the number of FPSO vessels. At the end of 2018, 183 FPSO vessels were operating in the offshore fleet, and according to forecasts, another 55 such vessels will be built by 2022 [6, 7]. FPSO power plants are characterized by the presence of gas turbine and combined type installations. Thus, on the FPSO vessel Global Producer III, the power plant consists of two 16 MW Alstom GT 35 gas turbines and waste heat recovery

units that provide all of the heat for the oil separation process [8]. The general power plant of the Armada Olombendo FPSO consists of three 21 MW dual fuel turbines [9]. This FPSO's Dhirubhai-1 power plant contains of three 4 MW gas turbine generators and two main boilers, giving a total capacity of 88 t/h for three 5 MW and two 1 MW steam turbine generators [10]. The FPSO's Pioneiro de Libra installation provides three 27.5 MW gas turbine generators, which operate at 50% load, and four diesel generators [11]. The FPSO's Cidade de Itajaí installation consists of four gas turbine generators with 36 MW of power, and two 2 MW diesel generators [12]. Power generation on the FPSO TRITON is provided by two LM6000 gas turbines (42 MW ISO rating) [13].

Leading manufacturers of power equipment have developed power modules for MODUs and FPSOs with diesel generators (DGs) and gas turbine generators (GTGs) [1416].

The following indicators can be used as criteria for comparing the characteristics of energy modules:

$\dot{V} = P_e/V_m$ , power-to-volume ratio, where  $P_e$  is the power generated by the module (kW) and  $V_m$  the module volume ( $m^3$ ).

$\dot{M} = P_e/M_m$ , power-to-mass ratio, where  $M_m$  is the module weight (tons).

$\eta = P_e/(m_f \cdot LCV)$ , module efficiency, where  $m_f$  is the fuel mass flux (kg/s) and LCV the low calorific value of the fuel (kJ/kg).

Figure 2 presents the results of a comparison of power-to-volume ratio, power-to-weight ratio and efficiency for diesel and gas turbine power modules of various capacities.

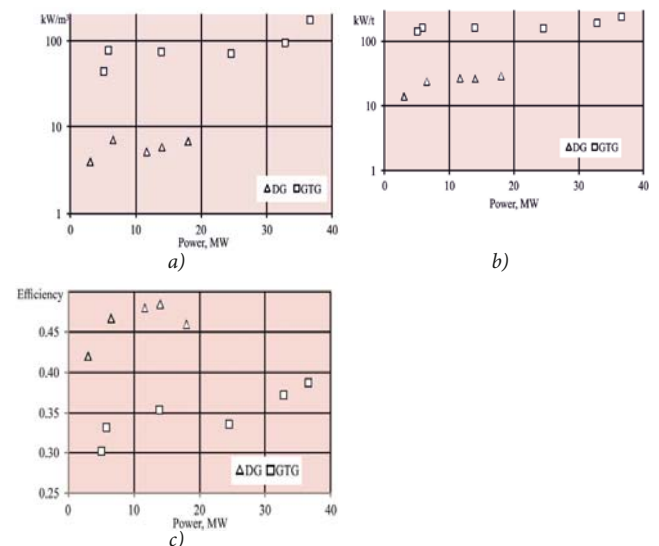


Fig. 2 Comparison of energy module characteristics for offshore vessels: (a) power-to-volume ratio; (b) power-to-mass ratio; (c) efficiency.

Abbreviations: DG - 18V51/60DF (18 MW), 16CM46DF (14 MW), 12CM43C (11.6 MW), 12CM32C (6.5 MW), 6CM34DF (3 MW); GTG - SGT A35 (36.6 MW), SGT 700 (32.8 MW), SGT 600 (24.5 MW), SGT 400 (13.9 MW), SGT A05 (5.8 MW), SGT 100 (5 MW)

Energy modules based on gas turbine technologies have a significant advantage in terms of their mass and size characteristics, but are inferior to diesel options in terms of fuel efficiency. A number of publications have been devoted to improving the efficiency of marine power modules using

advanced and combined cycle plants [17, 18]. However, experience with offshore drilling platforms in Norway has shown that their large dimensions make combined cycle installations impractical for offshore vessels [19].

For FPSOs and MODUs, which operate in deep-sea and remote areas of production, the requirements for the mass and size of the equipment are the most stringent, as these are related to ensuring dependability. As shown in [20, 21], one effective means of ensuring the reliability of a ship's power plant is redundancy. Ship power plants, including offshore vessels, are characterized by the use of structural redundancy, which provides the ability to connect reserve power in case of failure of the main equipment. This practice is widespread in the offshore fleet; the use of a single unit to ensure basic production needs is considered undesirable, and in practice this does not apply. In [22], aspects of the running of 192 gas turbines operating in offshore infrastructure were considered, and based on the analysis presented in this study, it follows that the average load of gas turbine engines during operation is about 50%. A total of 97% of gas turbine engines operate as part of an energy module with more than one unit and with load sharing.

To reduce  $\text{NO}_x$  and CO emissions from offshore vessels, gas turbine engines with modified combustion systems known as dry low emissions (DLE) are used. Although in some cases the operation of gas turbine engines with DLE in partial load modes may increase the  $\text{NO}_x$  and CO emissions, and the fuel gas composition significantly affects performance [22], the use of such technology is promising. This article discusses the possibility of its applicability to an FPSO vessel equipped with a gas turbine module.

Thermo-chemical technologies are a promising direction for increasing the efficiency of heat engines, and can allow for the conversion of base fuel using the thermal energy of the exhaust gases. When such technologies are applied on offshore vessels, natural gas, associated petroleum gas of various compositions or gaseous fuel based on heavy hydrocarbons (ethane, propane, butane and others) can be used as the main fuel. Earlier studies [23,26] have considered the use of thermo-chemical heat recovery from GTE exhaust gases for the steam conversion of LNG, methanol and associated gases of different compositions. Further analysis of the appropriateness and applicability of thermo-chemical technologies in the energy complexes of offshore vessels and floating drilling platforms requires investigation of the working processes in a gas turbine combustor operating on associated gas conversion products.

## CHARACTERISTICS OF THE PROCESSES IN A GAS TURBINE COMBUSTOR OPERATING ON ASSOCIATED GAS CONVERSION PRODUCTS

Investigations carried out earlier by the current authors have made it possible to identify the main parameters that influence the process of associated gas conversion [26]. It

was found that an increase in the process pressure leads to an increase in the temperature, which is necessary for effective conversion. In addition, a rise in pressure leads to an increase in the proportion of the steam that must be fed into the reactor. It is not possible to avoid conversion at a pressure of below 2–2.5 MPa, since the effective organization of the working processes in the gas turbine combustor requires that the fuel supply pressure exceed the air pressure behind the compressor.

Mathematical modeling methods [27] were used to analyze the parameters of an alternative gas turbine installation with steam conversion of associated gas (Fig. 3).

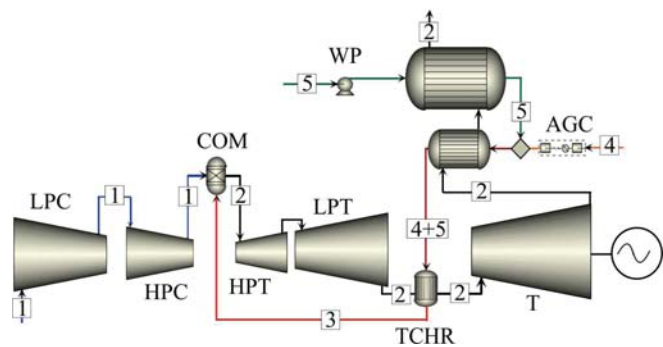


Fig. 3 Simplified calculation scheme for a power plant: 1 – air; 2 – gas; 3 – syngas; 4 – associated gas; 5 – water (steam); LPC – LP compressor; HPC – HP compressor; CAG – associated gas compressor; COM – combustor; SG – steam generator; LPT – LP turbine; HPT – HP turbine; T – power turbine; TCHR – thermo-chemical reactor; WP – water pump

The basic parameters of the UGT 25000 gas turbine simple cycle installation are adopted. This dual-rotor turbine engine with a free power turbine is designed for electric power generation, natural gas transportation and marine propulsion.

The investigations conducted here allowed us to determine the following:

- for a dual-rotor gas turbine engine, it is advisable to install a thermo-chemical reactor behind a low-pressure turbine;
- a significant increase in the volume of working fluid supplied to the reactor (and then to the combustor and the turbine flow section) requires the operation of serial gas turbine engines in partial mode when using the products of steam conversion of associated gas as the main fuel.

The following limitations of the turbocompressor unit were modeled:

- operation of the GTE at partial load mode;
- a fixed turbine inlet temperature;
- environmental parameters taken from ISO 19859: 2016.

Associated gas was adopted as the initial fuel, with the following composition (vol.): methane ( $\text{CH}_4$ ) 62.8–73.7%; ethane ( $\text{C}_2\text{H}_6$ ) 6.7–17.7%; propane ( $\text{C}_3\text{H}_8$ ) 6.1–9.0%; butane ( $\text{C}_4\text{H}_{10}$ ) 2.4–5.0%; pentane and heavier ( $\text{C}_5+$ ) 1.0–3.7%; carbon dioxide ( $\text{CO}_2$ ) 0.6–9.2%; nitrogen ( $\text{N}_2$ ) 0.0–4.4%; hydrogen sulfide ( $\text{H}_2\text{S}$ ) 0.0–2.8 [26,28]. Since the gas temperature behind the steam generator was above the dew point temperature, the maximum allowable steam/gas mass ratio was 6–7, depending on the composition of the associated gas. The use

of thermo-chemical regeneration can increase the efficiency of the FPSO's gas turbine energy module by up to 50%.

By modeling the processes in the thermo-chemical heat recovery circuit, we established that the content of the initial associated gas slightly affects the composition of the synthesis gas. The main components of the synthesis gas obtained by thermo-chemical regeneration are hydrogen and steam. In this case, the low calorific values of the synthesis gas lie in the range 7–8 MJ/kg.

The UGT 25000 serial low emission combustor was used to model the burning processes. The combustor of a 25 MW power gas turbine engine has a cannular design (Fig. 4) in which dry combustion of a lean partially premixed mixture is carried out [29, 30]. The main element of this chamber is a burner consisting of two radial swirlers, one for each of the two channels, behind which the annular mixing chambers are located. The air flow distribution between the first and second swirlers as a percentage of total air flow through the flame tube is about 12–61 %. Gaseous fuel is supplied through a set of holes in the vanes of the radial swirlers in both channels.

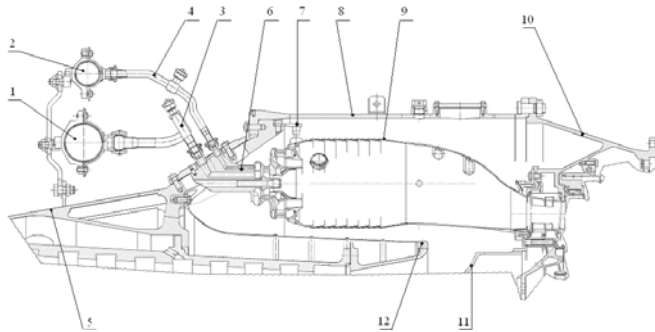


Fig. 4 Low-emission combustor of a GTE with power 25 MW: 1, 2 – collectors of the first and second channels; 3, 4 – delivery pipes of the first and second channels; 5 – compressor body; 6 – burner; 7 – holder; 8 – combustor casing; 9 – flame tube; 10 – load-carrying body; 11 – diffuser; 12 – inner casing

The modeling of physical and chemical processes in a gas turbine combustor is based on solutions to the differential equations of mass, impulse and energy conservation for the multi-component, turbulent, chemically reacting system [3135]. The equations for the conservation of mass can be written as follows:

$$\frac{\partial \rho}{\partial t} + \nabla \cdot (\rho \vec{v}) = S_m \quad (1)$$

where  $\rho$  is the fluid density,  $\vec{v}$  is the velocity vector, and  $S_m$  is the mass added to the continuous phase from the dispersed second phase. The equation for conservation of momentum is:

$$\frac{\partial}{\partial t} (\rho \vec{v}) + \nabla \cdot (\rho \vec{v} \vec{v}) = -\nabla p + \nabla \cdot (\tau_{eff}) + \rho \vec{g} + \vec{F} \quad (2)$$

where  $p$  is the static pressure,  $\tau_{eff}$  is the stress tensor, and  $\rho \vec{g}$  and  $\vec{F}$  are the gravitational and external body forces, respectively. The energy equation is:

$$\frac{\partial}{\partial t} (\rho E) + \nabla \cdot (\vec{v} (\rho E + p)) = \nabla \cdot (k_{eff} \nabla T - \sum_j \vec{J}_j + (\vec{\tau}_{eff} \cdot \vec{v})) + S_h \quad (3)$$

where  $k_{eff}$  is the effective conductivity, and  $\vec{J}_j$  is the diffusion flux of species  $j$ .  $S_h$  includes the heat of chemical reaction and any other volumetric heat sources. To determine this term, we use the relation:

$$S_h = -\sum_j \frac{h_j^0}{M_j} R_j \quad (4)$$

where  $h_j^0$  is the enthalpy of formation of species  $j$ ,  $R_j$  is the volumetric rate of creation of species  $j$ , and  $M_j$  is the molar mass of species  $j$ .

If it is necessary to consider the equations for the chemical components, we can obtain the concentration of each component  $Y_j$  by solving the equation for its convection-diffusion transfer. In general, this equation has the following form:

$$\frac{\partial}{\partial t} (\rho Y_j) + \nabla (\rho \vec{v} Y_j) = -\nabla \cdot \vec{J}_j + R_j + S_j \quad (5)$$

where  $S_j$  is the level of additional formation of the  $j$ -th component from a dispersed phase or other source.

The RNG-based  $k$ - $\epsilon$  turbulence model was used for aerodynamic prediction [32]. The **transport equations** have similar form to that of a standard  $k$ - $\epsilon$  model:

$$\frac{\partial}{\partial t} (\rho k) + \frac{\partial}{\partial x_i} (\rho k u_i) = \frac{\partial}{\partial x_j} \left[ (\alpha_k \mu_{eff}) \frac{\partial k}{\partial x_j} \right] + G_k + G_b - \rho \epsilon - Y_M, \quad (6)$$

$$\begin{aligned} \frac{\partial}{\partial t} (\rho \epsilon) + \frac{\partial}{\partial x_i} (\rho \epsilon u_i) = \\ = \frac{\partial}{\partial x_j} \left[ (\alpha_\epsilon \mu_{eff}) \frac{\partial \epsilon}{\partial x_j} \right] + C_{1\epsilon} \frac{\epsilon}{k} (G_k + C_{3\epsilon} G_b) - C_{2\epsilon} \rho \frac{\epsilon^2}{k} - R_\epsilon \end{aligned} \quad (7)$$

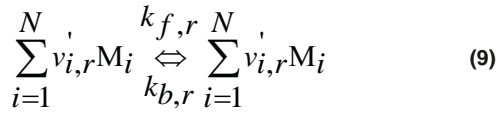
In these equations,  $G_k$  represents the generation of turbulence kinetic energy due to the mean velocity gradients,  $G_b$  is the generation of turbulence kinetic energy due to buoyancy, and  $Y_M$  represents the contribution of the fluctuating dilatation in compressible turbulence to the overall dissipation rate. The quantities  $\alpha_k$  and  $\alpha_\epsilon$  are the inverse effective Prandtl numbers for  $k$  and  $\epsilon$ , respectively.

The main difference between the RNG and standard  $k$ - $\epsilon$  models lies in the additional term in the  $\epsilon$  equation, which is given by

$$R_\epsilon = \frac{C_\mu \rho \eta^3 (1 - \eta / \eta_0) \epsilon^2}{1 + \beta \eta^3} \frac{1}{k} \quad (8)$$

where  $C_\mu$ ,  $\eta_0$ ,  $\beta$  are the empirical constants.

Let us consider the chemical reactions  $r$ , formed as follows:



where  $N_r$  is the number of chemical components in the system;  $\nu_{i,r}$  is the stoichiometric coefficient for the  $i$ -th reagent in the reaction  $r$ ;  $\nu_{i,r}$  is the stoichiometric coefficient for the  $i$ -th product of the reaction  $r$ ;  $M_i$  is the symbol for the  $i$ -th chemical component;  $k_{f,r}$  is the direct velocity constant for the reaction  $r$ ; and  $k_{b,r}$  is the reverse velocity constant for the reaction  $r$ . The net source of the  $i$ -th chemical component obtained via the reaction  $R_i$  is calculated as the sum of sources  $N_R$  of the Arrhenius reactions in which the components take part:

$$R_i = M_{\omega,i} \sum_{r=1}^{N_R} R_{i,r} \quad (10)$$

where  $M_{\omega,i}$  is the molar mass of the  $i$ -th component, and  $R_{i,r}$  is the Arrhenius velocity of formation/decomposition of the  $i$ -th component in the reaction  $r$ .

The velocity constant for the direct reaction  $r$  is calculated using the Arrhenius expression:

$$k_{f,r} = A_r T^{\beta_r} e^{-E_r/RT} \quad (11)$$

where  $A_r$  is a pre-exponential factor;  $\beta_r$  is the temperature exponent;  $E_r$  is the activation energy for the reaction; and  $R$  is the universal gas constant.

If the reaction is reversible, the reverse velocity constant is defined as follows:

$$k_{b,r} = \frac{k_{f,r}}{K_r} \quad (12)$$

where  $K_r$  is the balance constant for the reaction  $r$ .

The Eddy dissipation concept (EDC) model (based on detailed Arrhenius chemical kinetics incorporated in flames with turbulent fluctuations) has been used for calculation of a gas turbine combustor [30]. The EDC model assumes that the reaction occurs in small turbulent structures called fine scales. Species react in these fine structures over a given timescale governed by Arrhenius rates, and the reactions are integrated numerically using the ISAT algorithm. Thus, to calculate the net source of species  $i$  via chemical reaction, it is necessary to find the fine scale and time scale. The length fraction and time scales are:

$$\xi^* = \tilde{N}_\xi \left( \frac{v\varepsilon}{k} \right)^{3/4}, \quad \tilde{N}_\xi = 2.377 \quad (13)$$

$$\tau^* = \tilde{N}_\tau \left( \frac{v}{\varepsilon} \right)^{1/2}, \quad \tilde{N}_\tau = 0.4082 \quad (14)$$

The detailed expanded chemical mechanisms that describe the combustion of hydrocarbon fuel are developed for the combustion of CO/H<sub>2</sub> mixtures. There are also additional simplified or so-called global mechanisms for CFD modeling, which are mainly used for calculations of the oxidation of hydrocarbon fuels and synthesis gases.

In the present work, we use an approved early [36, 37] simplified 35-reaction reducing mechanism (Table 1) to carry out a detailed analysis of the combustion operating processes.

Tab. 1. Reactions in the reducing mechanism

H+O <sub>2</sub> → OH+O	OH+O → H+O <sub>2</sub>	O+H <sub>2</sub> → OH+H
OH+H → O+H <sub>2</sub>	OH+H <sub>2</sub> → H <sub>2</sub> O+H	H <sub>2</sub> O+H → OH+H <sub>2</sub>
OH+OH → H <sub>2</sub> O+O	H <sub>2</sub> O+O → OH+OH	H+O <sub>2</sub> +M → HO <sub>2</sub> +M
HO <sub>2</sub> +H → OH+OH	HO <sub>2</sub> +H → H <sub>2</sub> +O <sub>2</sub>	HO <sub>2</sub> +OH → H <sub>2</sub> O+O <sub>2</sub>
CO+OH → CO <sub>2</sub> +H	CO <sub>2</sub> +H → CO+OH	CH <sub>4</sub> (+M) → CH <sub>3</sub> +H(+M)
CH <sub>3</sub> +H(+M) → CH <sub>4</sub> (+M)	CH <sub>4</sub> +H → CH <sub>3</sub> +H <sub>2</sub>	CH <sub>3</sub> +H <sub>2</sub> → CH <sub>4</sub> +H
CH <sub>4</sub> +OH → CH <sub>3</sub> +H <sub>2</sub> O	CH <sub>3</sub> +H <sub>2</sub> O → CH <sub>4</sub> +OH	CH <sub>3</sub> +O → CH <sub>2</sub> O+H
CH <sub>2</sub> O+H → HCO+H <sub>2</sub>	CH <sub>2</sub> O+OH → HCO+H <sub>2</sub> O	HCO+H → CO+H <sub>2</sub>
HCO+M → CO+H+M	CH <sub>3</sub> +O <sub>2</sub> → CH <sub>3</sub> O+O	CH <sub>3</sub> O+H → CH <sub>2</sub> O+H <sub>2</sub>
CH <sub>3</sub> O+M → CH <sub>2</sub> O+H+M	HO <sub>2</sub> +HO <sub>2</sub> → H <sub>2</sub> O <sub>2</sub> +O <sub>2</sub>	H <sub>2</sub> O <sub>2</sub> +M → OH+OH+M
OH+OH+M → H <sub>2</sub> O <sub>2</sub> +M	H <sub>2</sub> O <sub>2</sub> +OH → H <sub>2</sub> O+HO <sub>2</sub>	H <sub>2</sub> O+HO <sub>2</sub> → H <sub>2</sub> O <sub>2</sub> +OH
H+OH+M → H <sub>2</sub> O+M		H+H+M → H <sub>2</sub> +M

The validity of using this simplified mechanism in three-dimensional investigations of synthesis gas combustion was demonstrated in [38]. To analyze the possibility of using a low-emission gas turbine combustor (Fig. 4) for low-calorie synthesis gas burning, the corresponding three-dimensional calculations were performed. The synthesis gas supplied to the combustor has the following composition (vol.): water vapor (H<sub>2</sub>O) 53.4%; hydrogen (H<sub>2</sub>) 34.9%; carbon monoxide (CO) 4.3%; carbon dioxide (CO<sub>2</sub>) 6.6%; methane (CH<sub>4</sub>) 0.7%; nitrogen (N<sub>2</sub>) 1.0%.

Figure 5 shows the aerodynamic structure of the working fluid flow inside the combustor. After the high-pressure compressor, the air entering the chamber diffuser undergoes a complex motion, reversing direction twice. As it moves within the space of the annular combustor, it enters the flame tube through the secondary air and film cooling holes, and then twists, passing through the two radial swirlers of the

first and second channels and the annular mixing chambers in the front burner unit.

The airflow passing through the radial swirlers of the first and second channels deviates from the original direction, and spreads out in the form of circular swirling jets along the lateral surface of the annular mixing chambers in the area of the frontal device. The rotational movement of the air leads to the appearance of centrifugal forces, causing increased pressure at the periphery of the stream (near the walls) and reduced pressure in its axial part. Thus, a circulating backflow occurs in the central part of the frontal device.

This recirculation zone is a powerful combustion stabilizer. Hot combustion products circulate in it and ignite fresh portions of the air-fuel mixture, ensuring low-calorific, stable combustion of the synthesis gas. The contours of the gas temperature inside the combustor are shown in Fig. 6.

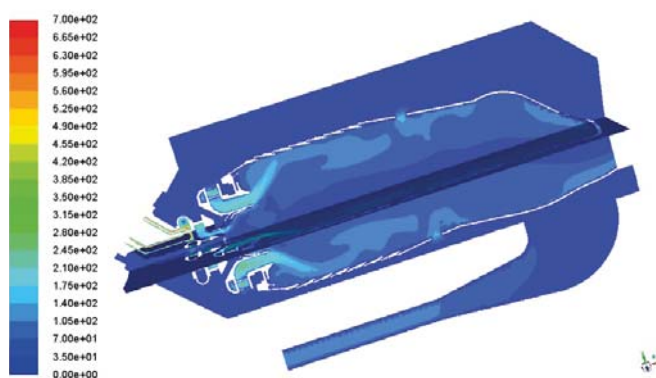


Fig. 5 Distribution of the magnitude of the velocity (m/s) inside the combustor

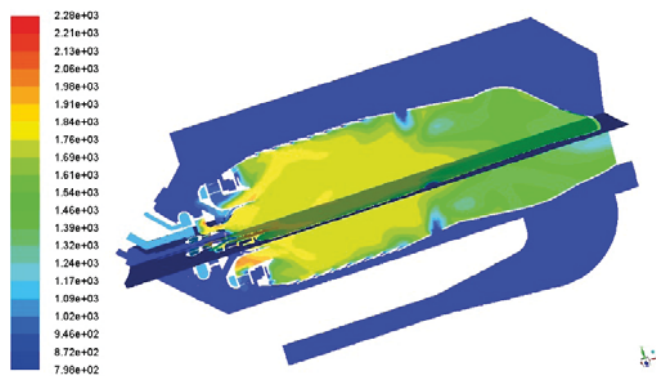


Fig. 6 Contours of the temperature (K) inside the combustor

The maximum temperature zone begins in the central prechamber sections, where despite the significant content of water vapor, the combustion of the synthesis gas is stabilized by the recirculation zone. Note that in some cases, in order to improve the flame stabilization conditions, a method of plasma-chemical combustion intensification [33, 39] may be applied.

The contours of the NO, CO, H<sub>2</sub> and CO<sub>2</sub> mass fractions are shown in Fig. 7. During burning of the synthesis gas at a low average flame temperature, the formation of thermal nitrogen

oxides in the combustor volume is significantly suppressed due to the large amounts of steam, and the calculated content of nitrogen oxides in the exit section of the combustor does not exceed 10 ppm. This complies with modern European standards for the emission of toxic components by gas turbine engines.

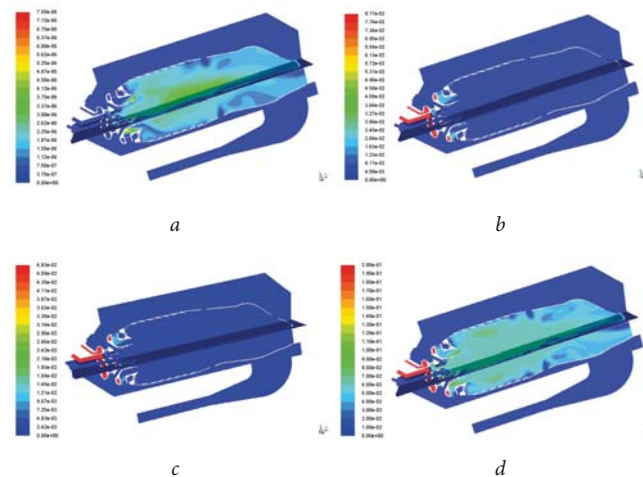


Fig. 7 Contours of the mass fraction of (a) NO; (b) CO; (c) H<sub>2</sub>; and (d) CO<sub>2</sub> inside the combustor

Due to the presence of steam, the reactions of complete carbon monoxide CO oxidation are delayed, and the calculated emission of CO at the exit of the combustor is equal to 85 ppm, which also does not exceed the emission standards even for gas turbines that operate on natural gas. The volumetric concentration of CO<sub>2</sub> at the combustor exit is 2.37%, which is lower than the emission of this greenhouse gas by gas turbine engines working on natural gas.

Along with the identified advantages (its high stability of operation on fuels with a high steam content, and low emission of toxic components), the serial combustor considered here needs some structural improvements when operating on synthesis gas, for example: (a) prevention of the possibility of flashback in the region of radial swirlers due to the high temperature of the synthesis gas; (b) changes to the size of the gas supply pipelines due to an increase in the flow rate of synthesis gas compared to natural gas; and (c) development of a more effective means of cooling the flame tube walls, especially in the frontal device area. These will be the subject of further investigation.

## CONCLUSION

The use of thermo-chemical heat recovery from the gas turbine energy module of a FPSO makes it possible to obtain synthesis gas with a fairly stable composition, regardless of the methane content of the associated gas used as fuel.

At the maximum permissible mass ratio of steam/gas, i.e. in the range 6–7, the efficiency of the gas turbine energy module of an offshore vessel is about 50%. Three-dimensional calculations of the low-emission gas turbine combustor

demonstrated the possibility of efficient use of associated gas conversion products as the main fuel, and the stability of the burning process. The estimated emissions of the main toxic components (NO<sub>x</sub> and CO) are in line with current European emission standards for gas turbine engines.

## REFERENCES

- Organization for Economic Co-operation and Development (2014): *Offshore Vessel, Mobile Offshore Drilling Unit & Floating Production Unit Market Review*. Retrieved from [http://www.oecd.org/officialdocuments/publicdisplaydocumentpdf/?cote=c/wp6\(2014\)13/final&doclanguage=en](http://www.oecd.org/officialdocuments/publicdisplaydocumentpdf/?cote=c/wp6(2014)13/final&doclanguage=en).
- Visiongain (2012): *The Mobile Offshore Drilling Units (MODU) Market 2012–2022*. Retrieved from <https://www.marketresearch.com/product/sample-6889468.pdf>.
- Stena Drilling (2018): *Stena Drill MAX*. Retrieved from [http://stenadrillingmediabank.s3-eu-west-1.amazonaws.com/stena/wp-content/uploads/2018/04/11110204/Stena-DrillMAX\\_Technical-Specification\\_APR2018.pdf](http://stenadrillingmediabank.s3-eu-west-1.amazonaws.com/stena/wp-content/uploads/2018/04/11110204/Stena-DrillMAX_Technical-Specification_APR2018.pdf).
- Stena Drilling (2018): *Stena Don*. Retrieved from [https://www.stena-drilling.com/stena/wp-content/uploads/2017/08/80845\\_Stena\\_DON\\_Brochure\\_A4\\_FINAL\\_LO.pdf](https://www.stena-drilling.com/stena/wp-content/uploads/2017/08/80845_Stena_DON_Brochure_A4_FINAL_LO.pdf).
- OCYAN (2017): *FPSO Pioneiro de Libra*. Retrieved from <http://www.ocyansa.com/en/fleet/fpso-pioneiro-de-libra>.
- Offshore Magazine (2018): *OTC 2018: FPSO Market Recovery Under Way, Says EMA Report*. Retrieved from <https://www.offshore-mag.com/production/article/16804111/otc-2018-fpso-market-recovery-under-way-says-ema-report>.
- Offshore Technology (2018): *Report: 55 FPSOs to Start Operations by 2022*. Retrieved from <https://www.offshore-technology.com/news/report-55-fpsos-start-operations-2022/>.
- Offshore Magazine (2002): *Leadon FPSO Delivered on Time, Complete, Within Budget*. Retrieved from <https://www.offshore-mag.com/production/article/16759844/leadon-fpso-delivered-on-time-complete-within-budget>.
- ENI (2016): *Block 15-06 East Hub Development Project*. Retrieved from [https://www.eni.com/docs/en\\_IT/enicom/publications-archive/publications/brochures-booklets/countries/brochure\\_eni\\_angola\\_ese\\_web.pdf](https://www.eni.com/docs/en_IT/enicom/publications-archive/publications/brochures-booklets/countries/brochure_eni_angola_ese_web.pdf).
- Aker Floating Production (2009): *FPSO Dhirubhai-1*. Retrieved from <http://www.akerfloatingproduction.com/s.cfm/3-12/FPSO-Dhirubhai-1-Operation>.
- OCYAN (2017): *FPSO Pioneiro de Libra*. Retrieved from <http://www.ocyansa.com/en/fleet/fpso-pioneiro-de-libra>.
- OCYAN (2017): *FPSO Cidade de Itajaí*. Retrieved from [https://api.ocyansa.com/sites/default/files/2018-09/cidade\\_do\\_itajai\\_0.pdf](https://api.ocyansa.com/sites/default/files/2018-09/cidade_do_itajai_0.pdf).
- Offshore Technology (2018): *Triton Oil Field, North Sea Central*. Retrieved from <https://www.offshore-technology.com/projects/triton/>.
- MAN Diesel & Turbo (2013): *Offshore Power Module*. Retrieved from [https://marine.man-es.com/docs/default-source/shopwaredocumentsarchive/offshore-power-module.pdf?sfvrsn=c2dd9a8\\_4](https://marine.man-es.com/docs/default-source/shopwaredocumentsarchive/offshore-power-module.pdf?sfvrsn=c2dd9a8_4).
- Caterpillar Global Petroleum (2013): *Offshore Power Generation Module*. Retrieved from <https://s7d2.scene7.com/is/content/Caterpillar/C10340375>.
- Siemens (2019): *We Power the World with Innovative Gas Turbines: Siemens Gas Turbine Portfolio*. Retrieved from <https://new.siemens.com/global/en/products/energy/power-generation/gas-turbines.html>.
- Olszewski W., Dzida M. (2018): *Selected Combined Power Systems Consisted of Self-Ignition Engine and Steam Turbine*. Polish Maritime Research, No.1, Vol. 25, 198–203.
- Domachowski Z., Dzida M. (2019): *Applicability of Inlet Air Fogging to Marine Gas Turbine*. Polish Maritime Research, Vol. 26, No.1, 15–19.
- Mazzetti M.J., Nekså P., Walnum H.T., Hemmingsen A.K. (2014): *Energy-Efficient Technologies for Reduction of Offshore CO<sub>2</sub> Emissions*. Oil and Gas Facilities, Vol. 3, No. 1, 8996.
- Tarelko W. (2018): *Application of Redundancy in Ship Power Plants of Offshore Vessels*. New Trends in Production Engineering, Vol. 1, No. 1, 443–452.
- Tarelko W. (2018): *Redundancy as a Way Increasing Reliability of Ship Power Plants*. New Trends in Production Engineering. Vol. 1, No. 1, 515–522.
- The UK Oil and Gas Industry Association Ltd. (2015): *Offshore Gas Turbines and Dry Low NO<sub>x</sub> Burners. An Analysis of the Performance Improvement*. Retrieved from <https://oilandgasuk.co.uk/wp-content/uploads/2015/05/produccys-cayrgory.pdf>.
- Cherednichenko O., Serbin S. (2018): *Analysis of Efficiency of the Ship Propulsion System with Thermochemical Recuperation of Waste Heat*. Journal of Marine Science and Application, Vol. 17, No.1, 122–130.

24. Cherednichenko O. (2015): *Analysis of Efficiency of Diesel-Gas Turbine Power Plant with Thermo-Chemical Heat Recovery*. MOTROL: Commission of Motorization and Energetics in Agriculture. Vol.17, No. 2, 25-28.
25. Cherednichenko O. (2019): *Efficiency Analysis of Methanol Usage for Marine Turbine Power Plant Operation Based on Waste Heat Chemical Regeneration*. Problemele Energeticii Regionale, No.1, 102-111.
26. Cherednichenko O., Serbin S., Dzida M. (2019): *Application of Thermo-Chemical Technologies for Conversion of Associated Gas in Diesel-Gas Turbine Installations for Oil and Gas Floating Units*. Polish Maritime Research, 3(103), Vol. 26, 181187.
27. Dzida M., Girtler J. (2016). *Operation Evaluation Method for Marine Turbine Combustion Engines in Terms of Energetics*. Polish Maritime Research, 4(92), Vol. 23, 6772.
28. Farry M. (1998): *Ethane from Associated Gas Still the Most Economical*. Retrieved from <https://www.ogj.com/articles/print/volume-96/issue-23/in-this-issue/gas-processing/ethane-from-associated-gas-still-the-most-economical.html>.
29. Budanova N.A., Vantsovskiy V.G., Korotich E.V. (2004): *Development of the Low-Emission Combustion Chambers for the Gas Turbine Engines DN70, DN80, DB90*. Marine and Energetic Gas Turbine Building, Vol. 1, GTR&PC "Zorya-Mashproekt", Nikolaev, 31-35.
30. Serbin S. I., Matveev I. B., Mostipanenکو G. B. (2011): *Investigations of the Working Process in a "Lean-Burn" Gas Turbine Combustor With Plasma Assistance*. IEEE Transactions on Plasma Science, Vol. 39, No. 12, 3331-3335.
31. Launder B.E., Spalding D.B. (1972): *Lectures in Mathematical Models of Turbulence*. Academic Press, London.
32. Choudhury D. (1993): *Introduction to the Renormalization Group Method and Turbulence Modeling*. Fluent Inc. Technical Memorandum TM-107, 1993.
33. Serbin S.I. (1998): *Modeling and Experimental Study of Operation Process in a Gas Turbine Combustor with a Plasma-Chemical Element*. Combustion Science and Technology, Vol. 139, 137-158.
34. Serbin S.I. (2006): *Features of Liquid-Fuel Plasma-Chemical Gasification for Diesel Engines*. IEEE Transactions on Plasma Science, Vol. 34, No. 6, 2488-2496.
35. Matveev I., Serbin S., Mostipanenکو A. (2007): *Numerical Optimization of the „Tornado” Combustor Aerodynamic Parameters*. Collection of Technical Papers - 45th AIAA Aerospace Sciences Meeting, Reno, Nevada, AIAA 2007-391, Vol. 7, 4744-4755.
36. Serbin S., Goncharova N. (2017): *Investigations of a Gas Turbine Low-Emission Combustor Operating on the Synthesis Gas*. International Journal of Chemical Engineering, Vol. 4, 1-14.
37. Serbin S.I., Matveev I.B., Goncharova N.A. (2014): *Plasma Assisted Reforming of Natural Gas for GTL. Part I*. IEEE Transactions on Plasma Science, Vol. 42, No. 12, 3896-3900.
38. Matveev I.B., Serbin S.I., Vilkul V.V., Goncharova N.A. (2015): *Synthesis Gas Afterburner Based on an Injector Type Plasma-Assisted Combustion System*. IEEE Transactions on Plasma Science, Vol. 43, No. 12, 3974-3978.
39. Gatsenko N.A., Serbin S.I. (1995): *Arc Plasmatrons for Burning Fuel in Industrial Installations*. Glass and Ceramics, Vol. 51(11-12), 383-386.

#### CONTACT WITH THE AUTHORS

##### **Oleksandr Cherednichenko**

*e-mail: cherednichenko.aleksandr65@gmail.com*  
Admiral Makarov National University of Shipbuilding,  
Heroyiv Ukraine av. 9, 54025 Mykolaiv  
**UKRAINE**

##### **Serhiy Serbin**

*e-mail: serbin1958@gmail.com*  
Admiral Makarov National University of Shipbuilding,  
Heroyiv Ukraine av. 9, 54025 Mykolaiv  
**UKRAINE**

##### **Marek Dzida**

*e-mail: dzida@pg.edu.pl*  
Gdańsk University of Technology,  
11/12 Gabriela Narutowicza Street, 80-233 Gdańsk  
**POLAND**

# DESIGN AND OPERATIONAL INNOVATIONS IN ADAPTING THE EXISTING MERCHANT RIVER FLEET TO COST-EFFECTIVE SHIPPING

Teresa Abramowicz-Gerigk  
Zbigniew Burciu  
Gdynia Maritime University, Poland

## ABSTRACT

*Modernisation of the existing river fleet adapted for the local conditions of the Middle and Lower Vistula can be considered as a solution to slow down the progressive decrease of river transport in this area. The implementation of technical improvements, smart technologies and enhancement of transport performance may partially solve the problem of growing demand for multimodal transport of containers and oversized loads in a shorter perspective than the expected period of planned revitalisation of the river. The paper presents investigations on the modernisation of river convoys adapted to the current navigational conditions of the Lower Vistula. The different options have been discussed by the authors with river fleet operators and the best recognised solution was agreed to be the use of river convoys combining modernised motor barges and the pushed barges previously used in this area. Improvement of the transport profitability, reduction of fuel consumption, air pollution and noise can be achieved at minimum costs by modernisation of the main power-propulsion systems of outdated motor barges and the implementation of innovative steering systems on pushed barges. The demand for power-propulsion and manoeuvring performance of modernised convoys is discussed in the paper.*

**Keywords:** river convoy capacity; integrated steering system; smart river unit

## INTRODUCTION

The ten-year perspective of inland waterways modernisation in Poland anticipated in the assumptions made by the Ministry of the Maritime Economy and Inland Navigation [6] is the economic justification for the modernisation of the existing means of transport before the expected navigational requirements are satisfied.

The technological and economical study presented here aimed to determine technical assumptions for inland waterborne transport units intended for navigation on the Lower Vistula, currently used mainly for the individual transport of bulk and oversized loads.

The growing demand for container transport via inland waterways is the reason for the development of technical solutions related to ecological river training, planning river

ports with logistic centres and transport means adapted to the local conditions within the framework of European programmes [3, 10], as well as feasibility studies commissioned by the Polish government. The systemic approach to waterborne inland transport development should include comprehensive logistic planning [7].

The ship-owners currently operating river vessels have recognised the construction of a new river fleet for current river conditions as non-negotiable. However, modernisation of the existing fleet adapted for local conditions should be considered and should slow down the further decrease of river transport. The developments should be based on the types of barges currently being used.

The latest study on the implementation of smart ships in waterborne transportation [21] presents the view that the first fully autonomous ships will be put into service in less than five

years, so new designs and developments of existing waterborne transport units should take into account the rapid introduction of smart technologies in river transport.

The wide implementation of ICT technologies will increase the flexibility and efficiency of operations and enable areas previously not available for manned vessels to be used for safe and efficient transport [21].

## DEVELOPMENT OF SMART RIVER TRANSPORT IN EUROPE

The main tendencies in modern waterborne transport development are the implementation of smart technologies and economies of scale.

### SMART TECHNOLOGY APPLICATIONS

There are six basic levels of ship autonomy [21]: level 0, which means manual operation; level 1 – automatic control over the set route; level 2 on which the calculated route can be updated by an external system; level 3 on which the decisions on navigation and ship operation are calculated by the system and controlled by the operator in case of uncertainty; level 4 on which the decisions worked out by the system should be approved by a human operator; level 5 on which the monitored autonomy needs a human response only in situations that are uncertain for the system; and level 6 – full autonomy based on artificial intelligence.

Remote control of operations requires the automation of all the main systems on board, and their integration into a single communication channel [11, 12]. The transition from level zero to level one of autonomy means, as a first step, the integrated control of steering and propulsion devices.

DNVGL class guidelines regarding autonomous and remotely operated ships, introduced in September 2018, recommend that onboard “systems and components supporting the propulsion function shall be arranged with redundancy and capacity sufficient to ensure that the vessel can maintain a navigable speed in case of potential failures of single systems and components” [9].

The conditions of smart inland waterborne transport development should be included in the design assumptions for both the new builds and modernised units.

### ECONOMY OF SCALE OF RIVER TRANSPORT UNITS

The well-known development of economies of scale with respect to maritime transport cannot be simply transferred to the inland waterborne transport environment. However, in the last ten years the tendency of a growing tonnage of transport units has been observed within the main inland fleets in Western Europe.

Inland waterway transport is energy-efficient, as an inland vessel is able to transport one tonne of cargo almost four times further than a truck using the same consumption of energy

(370 km as against 300 km by rail and 100 km by truck). The transport cost is competitive and the unit cost decreases over long distances.

Transporting goods on inland waterways is advantageous, as convoys of pushed barges can transport more goods per distance unit (tkm) than any other type of land transport and could help to reduce road traffic. In the first quarter of 2018, the transport performance on European inland waterways reached 34.9 billion tkm [5].

The observed tendencies of changes in the size of river units towards greater tonnages since 2005 are presented in Fig. 1 [15].

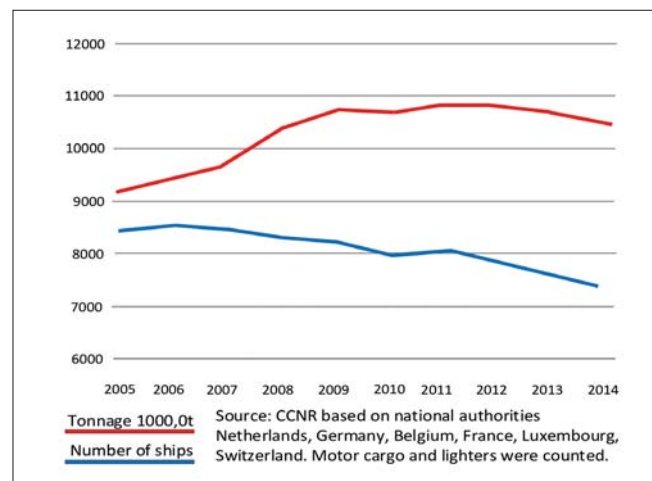


Fig. 1. Growing tendencies in decrease of the number of river units and increase of their tonnage in Western Europe since 2005 [15]

The waterborne inland transport of dry goods in Western Europe is dominated by Dutch vessels. These account for 49% of West European vessels and 56% of their tonnage. There are around 10000 inland vessels operating on the Rhine and more than 3000 vessels operating on the Danube. 75% of the waterborne transport means on the Rhine are dry cargo self-propelled units or dumb barges, while 15% are tanker vessels. Push and tug boats account for 13%. 7% of the total number of inland vessels in the Danube countries are tankers, while push and tug boats account for 18% of the total vessels [5].

The transport performance on European inland waters presented an increase of 4% in the first quarter of 2018 compared to the first quarter of 2017. In the same period, the waterborne inland transport performance in Poland presented a 27% decrease.

Waterborne inland transport in Poland in the period 2000–2017 decreased from 0.8% to 0.3% [8].

### POSSIBILITIES OF COST-EFFECTIVE CARGO TRANSPORT ON LOWER VISTULA

The number of transport units operated by Polish ship-owners has not changed much in recent years. The number of barges BP-500 was 509 and decreased by 7 units. The fleet of pushers and tug boats was 219 units and increased by 5 units in 2017. The total number of barges BM-500 was 89, a decrease of 2 units from 2017 [8].

The main Polish ship-owners: OT Logistics Group [24] including: OT Logistic SA, Deutsche Binnenreederei and Rentrans Cargo, Navigar [23], Żegluga Szczecińska [25] and Fabico [22], operate their fleets in Western Europe, in Poland mainly on the Oder Waterway and the Lower Vistula in small amounts.

## PERSPECTIVES OF DEVELOPMENT OF RIVER NAVIGATION

The Polish Ministry of Maritime Economy and Inland Navigation has carried out several feasibility studies related to the modernisation of Polish rivers. The detailed scope of investment in the short-term perspective includes the following tasks: the building of a new dam below Włocławek, a feasibility study and investment documentation of Lower Vistula cascades [6].

The Kujawsko-Pomorskie Voivodeship together with the City of Bydgoszcz carried out, within the EMMA European Project, a location study for the construction of a multimodal platform: a river port and logistics centre in the area between Bydgoszcz and Solec Kujawski [10].

The inland waterway of the Vistula River, planned within the II priority of Assumptions for the plans of inland waterways development in Poland in 2016/2020, with the perspective to 2030 [6], and the proposed location of a new river port and logistics terminal in Otorowo [10] are presented in Fig. 2.



Fig. 2. Planned inland waterway of Vistula River and proposed location of a river port and logistics terminal in Otorowo [6, 10]

The main navigational limits on the Gdansk–Otorowo section are related to the water depth and air draft. The transit depth is 1.8 m, so the maximum mean draft of vessels is 1.5 m. The maximum lengths and breadths of convoys are limited by the dimensions of the lock at Przegalina: 188.37 m length and 11.91 m breadth.

### Transport units

The river convoys operated on the Middle and Lower Vistula are different combinations of pushing and towing trains [18].

There are BP type barges: pushed barges BP-1000, BP-500, BP-400, self-propelled motor barge BM-500, and Galar-1 and Galar-2 barges adapted to the local conditions.

The main parameters of the barges BP-500 and BM-500 are presented in Table 1.

Tab. 1. Main particulars of the barges BP-500 and BM-500 operated on the Lower Vistula River

Main particulars	BP-500	BM-500
Length [m]	45	56.5
Breadth [m]	9.5	7.5
Draft [m]	1.6	1.7

The fleet characteristics influencing transport costs are the fleet age and operational parameters, including the power-propulsion performance. The development of river navigation on the basis of modernisation of the existing fleet, including self-propelled barges BM-500 and pushed barges BP-500, has been discussed with river fleet operators as a best possible solution in the 10–15 year period of the planned river revitalisation.

The improvement of transport units' profitability can be achieved at minimum costs by modernising the outdated main power-propulsion and steering systems to reduce fuel consumption, air pollution and noise.

The hybrid diesel electric propulsion and integrated steering system, including the bow hydrodynamic rotors and dynamic coupling of barges, have been considered.

The new river pushed train proposed for operation on the Lower Vistula combines modernised barges: barge BM-500 and one or two barges BP-500 will have a greater transportation capacity and efficiency than a pushed train combining a pusher and barges. The available power of the modernised motor barge power-propulsion system should be not less than the power of the pusher [13].

The convoy of a motor barge BM-500 and pushed barges BP-500 with dynamic coupling and a bow steering system on the pushed barge has already been tested with respect to resistance and manoeuvrability using the physical scale model and CFD simulations [1].

## TRANSPORT CAPACITY OF RIVER CONVOYS BASED ON MODERNISED BP-500 AND BM-500 BARGES

The presented analysis of possible transport units and convoys for the Lower Vistula has been carried out on the basis of previous experience of river fleet operators. It has been assumed that the analysed convoys operate during a navigational season of 250 days on not less than II class waterways. The port operations time was assumed to be 24 hours with 12 working hours a day. For the considered Gdansk–Otorowo section of the Lower Vistula, 198 km in

length, the corresponding maximum air draft has been limited to two layers of containers.

### RIVER CONVOYS CONFIGURATIONS

The single BP-500 motor barge and three configurations of river convoys were selected to compare the transport capacity:

- single motor barge BP-500,
- pusher with two pushed barges: pusher Bizon and 2 BP-500 barges,
- motor barge BM-500 pushing one pushed barge BP-500,
- motor barge BM-500 pushing two pushed barges BP-500.

The operational parameters of motor barge BM-500 are presented in Table 2.

Tab. 2. Operational parameters of BM-500 motor barge

Parameter	Voyage up the river	Voyage down the river
Loading capacity (tonnes)	380	380
Loading capacity (TEU)	20	20
Average speed of the loaded barge (km/h)	7.1	12.6
Average time of the voyage (h)	28	16

The main operational parameters of the convoys are presented in Tables 3–5.

Tab. 3. Operational parameters of convoy: pusher and 2 BP-500 barges

Parameter	Voyage up the river	Voyage down the river
Loading capacity (tons)	880	880
Loading capacity (TEU)	48	48
Average speed of the loaded barge (km/h)	4.4	10.4
Average time of the voyage (h)	45	20

The configuration of the convoy of barges BM-500 and BP-500 is presented in Fig. 3.

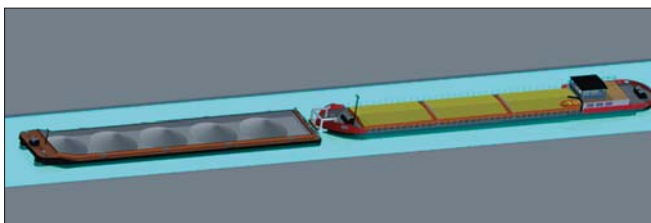


Fig. 3. Convoy of BM-500 and BP-500 barges

The proposed configuration of the convoy of BM-500 and 2 BP-500 barges is presented in Fig. 4.

Tab. 4. Operational parameters of the convoy: BM-500 and BP-500 barges

Parameter	Voyage up the river	Voyage down the river
Loading capacity (tons)	820	820
Loading capacity (TEU)	44	44
Average speed of the loaded barge (km/h)	5.7	10.4
Average time of the voyage (h)	34	20

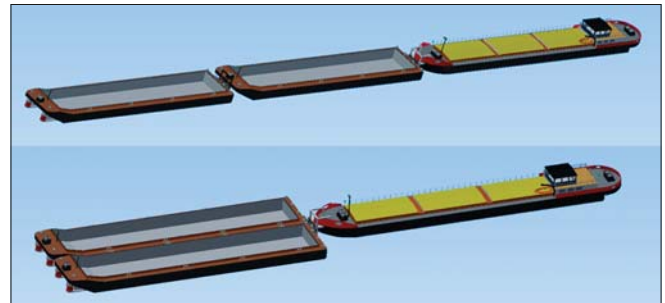


Fig. 4. Convoy of BM-500 and 2 BP-500 barges: up-river configurations (upper drawing) and down-river configurations (bottom drawing)

Tab. 5. Operational parameters of the convoy: BM-500 and 2 BP-500 barges

Parameter	Voyage up the river	Voyage down the river
Loading capacity (tons)	1260	1260
Loading capacity (TEU)	68	68
Average speed of the loaded barge (km/h)	5.7	10.4
Average time of the voyage (h)	34	20

### ECONOMICALLY EFFECTIVE TRANSPORT CAPACITY OF RIVER CONVOYS

Transport capacities in the navigational season in relation to operations between Gdansk and Otorowo estimated for the considered convoys are presented in Table 6. The assumed numbers of round voyages were as follows: 32 for a BM-500 barge, 20 for the pusher with 2 BP-500 barges, 31 for a BM-500 pushing a BP-500 barge, 31 for a BM-500 pushing 2 BP-500 barges.

The unit costs of transport and time of a round voyage without time of port operations and night breaks are presented in Table 7. The costs include fuel costs, personnel costs, depreciation costs, maintenance costs and overheads due to conducting business – assumed as 35%.

The unit cost of transport of the convoy of a modernised BM-500 and two BP-500 barges is estimated to be less than the unit cost for a pusher and two pushed barges. It is about 26 PLN/t for bulk cargo and 490 PLN/TEU for containers. The difference is 10% for bulk cargo and 7% for containers; however, it is dependent on the operational cost of the modernised barges.

Tab. 6. Transport capacities for different configurations of pushed convoys

Convoy configuration	Transport capacity	
	tons	TEU
BM-500	24320	1280
Pusher (Bizon) 2 BP-500	35200	1920
BM-500 BP-500	50840	2728
BM-500 2 BP-500	59520	3200

Tab. 7. Unit transport costs for different configurations of pushed convoys

Convoy configuration	Time of the round voyage days	Transport capacity	
		PLN/t	PLN/TEU
BM-500	1.83	36	700
Pusher (Bizon) 2 BP-500	2.71	29	531
BM-500 BP-500	2.25	31	577

The number of round cruises in the average navigational period of 250 days may be increased due to a decrease of port operations time.

## REQUIREMENTS WITH RESPECT TO MANOEUVRABILITY OF A RIVER CONVOY

The pushed convoy of a BM-500 and BP-500 has worse manoeuvring characteristics than the convoy consisting of a pusher and barge BP-500 [1, 13]. The analysis of new solutions of river convoys based on a motor barge and pushed barges for coal transport on the Oder Waterway was presented in 2012 by Kulczyk [13]. Due to the manoeuvrability required, the authors proposed a Schottel pump jet as a bow rudder. The Schottel pump jet is an azimuth thruster that can be operated in shallow water conditions – with 0.3 m under-keel clearance. The pump jet used as an auxiliary propulsion unit greatly increases the possibility of convoy control, but it is expensive, limits the cargo space in the bow hold and generates thrust streams that influence the river environment [16].

The innovative solution of the bow steering system presented in [1], installed on the bow of the pushed barge, and flexible coupling between the motor barge and pushed barge, can significantly improve the manoeuvrability of the convoy.

With respect to the Polish Register of Shipping rules [17], the push train manoeuvring characteristics should satisfy the criteria for pushed convoys based on trials performed in deep water conditions and shallow water conditions with the water depth to draft ratio in the range of 0.5–1.2 (Table 8).

Tab. 8. Manoeuvrability criteria for river convoys [17]

Obligatory test	Criteria
Minimum speed through the water	Should be not less than 13 km/h
Stopping distance over the ground in shallow water for convoys having length equal to or less than 110 m and beam equal to or less than 11.45 m.	- Shall be no greater than 480 m in flowing water with current velocity of 1.5 m/s in direction of flow, until speed over ground is 0 m/s,  - Shall be no greater than 305 m in standing water.
Evasive action test: zig-zag trials: - 20°/20° - 45°/45° both performed to port and starboard.	Turning speed (Fig. 5) $r_1=r_2$ should be: 20°/min in 20°/20° trial, 40°/min in 45°/45° trial. Time $t_4$ should be: - 150 s for $h/T < 2$ , - 110 s in deep water.
Turning test	Is not considered for convoys longer than 86 m.

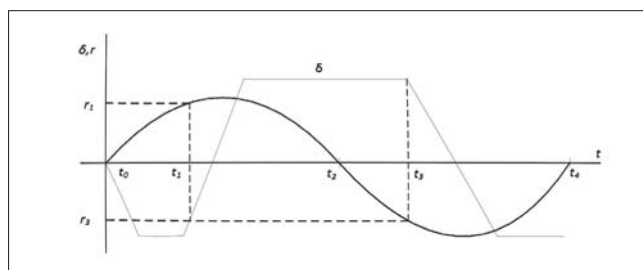


Fig. 5. Diagram of the evasive manoeuvre,  $\sigma$  – rudder angle [°],  $t_i$  – time to reach turning speed  $r_i$  [17]

For practical ship design for operation and for safety, the local environmental conditions should be taken into account – especially the possible widening of the safe manoeuvring area due to strong wind [14]. This is important for convoys with big windage areas carrying oversized goods or containers.

The results of model tests presented in Fig. 6 [1, 2] allowed the estimation of the turning ability of a motor barge and pushed barge convoy of 100 m length equipped with bow rotors and dynamic coupling.

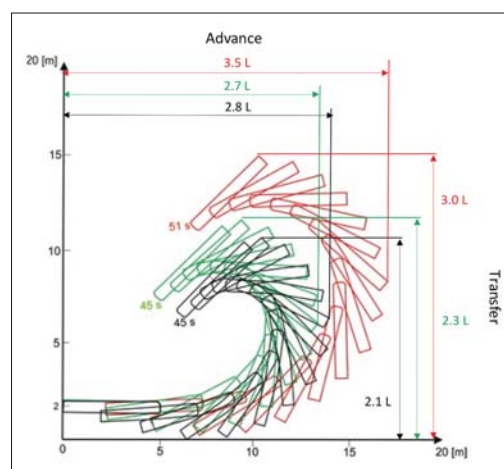


Fig. 6. Turning manoeuvre of the push train using bow rotors (red), stern rudders and bow rotors (green), stern rudders, bow rotors and dynamical coupling system (black)

The parameters of the turning trial performed using different combinations of steering devices are presented in Table 9.

Tab. 9. Parameters of the push barge model turning using different control devices

Parameter	Advance	Transfer
Turning with stern rudders [2]	3.0 L	2.6 L
Turning with bow rudders	3.5 L	3.0 L
Turning with bow and stern rudders	2.7 L	2.3 L
Turning with stern rudders, bow steering system and dynamic coupling	2.8 L	2.1 L

The differences between the performance of the convoy with and without dynamic coupling were 10% in advance and 20% in transfer distances.

The stopping distance over the ground for the push barge should be less than 305 m in standing water. If the turning is used as an anti-collision manoeuvre, the advance for the push barge without bow rotors is equal to 300 m and is only a little less than the stopping distance. The use of bow rotors decreases the advance to 270 m. The difference is equal to one third of the push barge length.

The turning performance of the BM-500 and BP-500 barges convoy is presented in Fig. 7.



Fig. 7. Turning performance of convoy: BM-500 and BP-500, turning control by bow steering system and dynamic coupling

The turning performance of the convoy of a BM-500 and 2 BP-500 barges is presented in Fig. 8. Turning using the bow steering system and dynamic couplings between barges give numerous possibilities of push train handling in winding rivers.

The necessary developments of modernised convoys are hybridisation and electrification of shipboard systems.

The replacement of the conventional drive used on the BM-500 (with main engine power 2 x 88–100 kW) with a hybrid diesel-electric drive with increased power corresponding to the pusher (Bizon: 2 x 118 kW; Koziorozec 2 x 120 kW) should provide the necessary power for the convoy [13].

The power required by the convoy should also take into account changing river depth [19, 20]. It has been confirmed by CFD calculations [1] that the predicted resistance of a 100 m

length convoy at 10 km/h speed in deep water is 25.5 kN; the resistance at 15 km/h in 5 m deep water, which means a 0.6 shallow water Froude number, is 70 kN.

Diesel-electric drive and automatic steering accompanied by the integration of all the main on-board control systems [11] introduces the possibility of applying remote operation via a single communication channel.

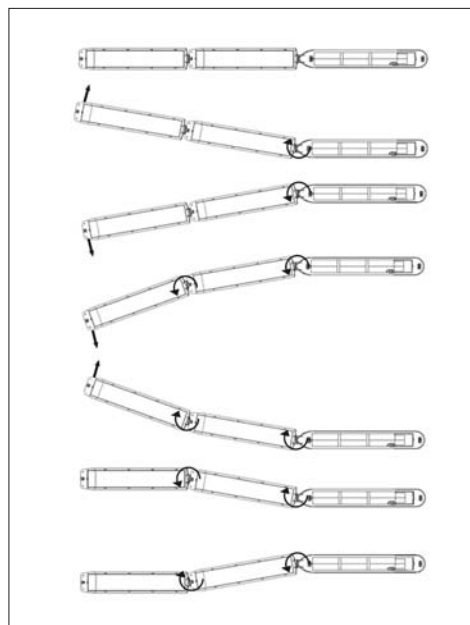


Fig. 8. Turning performance of convoy: BM-500 and 2 BP-500, turning control by bow steering system and dynamic couplings between barges

## CONCLUSIONS

The three configurations of river convoys presented in the paper were compared with respect to their transport capacity over the navigational season. The capacity for the pusher Bizon with two pushed barges was estimated to be 31% less than the capacity of the modernised motor barge BM-500 in convoy with a barge BP-500. The capacity of the motor barge BM-500 pushing two BP-500 barges was estimated to be 15% greater than the capacity of the modernised motor barge BM-500 pushing one BP-500 barge.

The design and operational innovations presented in the paper have been proposed for adapting the existing merchant river fleet of BM-500 and BP-500 barges built in the middle of the last century, and operating on the Lower Vistula River, to cost-effective modern shipping.

Improvement of the manoeuvrability and reduction of the required manoeuvring area for the push train can be obtained by installing new steering devices including a dynamic coupling system and bow rotors on the pushed barge. The model tests confirmed the increase of the turning capacity of a modernised BM-500 barge dynamically coupled with a BP-500 barge and equipped with bow rotors. The transfer during convoy turning for the dynamically coupled barges with rotors is 0.9 L less than for the conventional convoy using stern rudders only.

The system should be flexible to allow for different levels of autonomy, depending on location, congestion or emergencies. The integrated control of onboard systems should be a step forward in the implementation of smart technologies – satisfying the requirement that the navigation system should be able to maintain the ship's route, adapt it to the changing river conditions, avoid collisions and operate the ship efficiently.

## REFERENCES

- Abramowicz-Gerigk T., Burciu Z., Jachowski J. (2017): *An innovative steering system for a river push barge operated in environmentally sensitive areas*. Polish Maritime Research, 4 (96) Vol. 24, 27–34.
- Abramowicz-Gerigk T., Burciu Z. (2018): *Manoeuvring characteristics of the push train with an auxiliary steering device*. Journal of KONES Powertrain and Transport, Vol. 25 (2), 7–14.
- Abramowicz-Gerigk T., Burciu Z., Krata P., Jachowski J. (2017): *Steering system for a waterborne inland unit*. Patent application P. 420664.
- Abramowicz-Gerigk T., Blachuta J., Burciu Z., Granatowicz J., Jacyna M., Kulczyk J., Mazurek M., Nowakowski T., Picinska-Faltynowicz J., Skupien E., Tubis A., Werbinska-Wojciechowska S., Wieckowska M., Winter J. (2014): *INVAPO, European project Upgrading of Inland Waterway and Sea Ports*. Report of WP5 coordinated by Gdynia Maritime University, Gdynia 2014.
- Annual Report Year 2018 (2018): *Freight traffic on inland waterways and in ports*. Retrieved from <http://www.inland-navigation-market.org/en> (accessed 01.03.2019).
- Assumptions for the plans of inland waterways development in Poland in 2016/2020 with the perspective to 2030*. (2016): Ministry of Maritime Economy and Inland Navigation. Document accepted by the Council of Ministers 14 June 2016.
- Bai B., Jawale M., Noche B. (2016): *Evaluative Comparison of Inland Shipping with Multimodal Transports for Seasonal Commodity Supplies through Simulation*. 16th COTA International Conference of Transportation Professionals.
- Bawelska A., Brzezinska J., Radlinska M. (2018): *GUS, Inland waterways transport in Poland in 2014–2017*. Statistics Poland. Statistical Office in Szczecin. Warszawa, Szczecin 2018.
- DNVGL (2018): *Autonomous and remotely operated ships*. CLASS GUIDELINE. Edition DNVGL-CG-0264, September 2018.
- EMMA *Enhancing freight mobility and logistics in the BSR by strengthening inland waterway and river sea transport and promoting new international shipping services* – project funded by Interreg Baltic Sea Region Programme 2014–2020 (2019): retrieved from <http://project-emma.eu> (accessed 12.03.2019).
- Gerigk M. K. (2015): *An Integrated Model of Motion, Steering, Positioning and Stabilization of an Unmanned Autonomous Maritime Vehicle*. TransNav – The International Journal on Marine Navigation and Safety of Sea Transportation, Vol. 9 (4), 591–596.
- King K. K., Yasukawa H., Hirata N., Kose K. (2008): *Manoeuvring simulations of pusher-barge systems*. Journal of Marine Science and Technology, Vol. 13, 117–126.
- Kulczyk J., Lisiewicz T., Nowakowski T. (2012): *New generation of the fleet on Oder Waterway*. Prace Naukowe Politechniki Warszawskiej, 82.
- Liu J., Hekkenberg R., Rotteveel E. A. (2014): *Proposal for Standard Manoeuvres and Parameters for the Evaluation of Inland Ship Manoeuvrability*. European Inland Waterway Navigation Conference 2014, Budapest, Hungary.
- Market Observation Report on Inland Navigation in Europe (2016): *First annual report published by the CCNR in collaboration with the European Commission*. CCNR Press Release Ref: CC/CP (16)05 | 30.
- PIANC (2008): *Considerations to reduce environmental impacts of vessels navigation*. PIANC Report N° 99, 2008. Inland Navigation Commission. [www.pianc.org](http://www.pianc.org).
- PRS Rules (2010): *Navigability and manoeuvrability tests of inland waterway vessels and convoys*. Polish Register of Shipping.
- Rabant H., Habel M., Babinski Z. (2016): *Transport of the oversized goods on the Vistula waterway. The basic waterway parameters and main difficulties*. Works of Commission of Communication Geography PTG 2016, 19(3), 7–17.
- Skupien E., Prokopowicz J. (2014): *Methods of calculating ship resistance on limited waterways*. Polish Maritime Research, 4, Vol. 21, 2–17.
- Tabaczek T., Kulczyk J., Zawislak M. (2007): *Analysis of hull resistance of pushed barges in shallow water*. Polish Maritime Research, 1 (51), Vol. 14, 10-15.
- Van Dijk T., Moonen H., van Doorser H., Negenborn R., van den Berg R. (2018): *Smart ships and the changing maritime ecosystem. How digitalization and advanced automation of barges, service vessels and sea ships create new opportunities and challenges for the maritime industry*. Smart Port 09/2018.

22. [www.fabico.pl](http://www.fabico.pl) (accessed 12.03.2019).
23. [www.navigartrans.pl](http://www.navigartrans.pl) (accessed 12.03.2019).
24. [www.otlogistics.com.pl](http://www.otlogistics.com.pl) (accessed 12.03.2019).
25. [www.zegluga.szn.pl](http://www.zegluga.szn.pl) (accessed 12.03.2019).

#### CONTACT WITH THE AUTHORS

**Teresa Abramowicz-Gerigk**  
*e-mail: [t.gerigk@wn.umg.edu.pl](mailto:t.gerigk@wn.umg.edu.pl)*

Gdynia Maritime University  
Morska 81-87, 81-225 Poland  
**POLAND**

**Zbigniew Burciu**  
*e-mail: [z.burciu@wn.umg.edu.pl](mailto:z.burciu@wn.umg.edu.pl)*

Gdynia Maritime University  
Morska 81-87, 81-225 Poland  
**POLAND**

## EFFECTS OF WATER INTAKE LAYOUT ALONG THE WHARF SHORELINE ON SHIPS

**Xian-wei Kong**

School of Civil Engineering, Tianjin University, China

National Engineering Laboratory for Port Hydraulic Construction Technology, Tianjin Research Institute for Water Transport Engineering, China

**Lei Ding**

College of Marine and Environmental Sciences, Tianjin University of Science & Technology, China

Tianjin Marine Environmental Protection and Restoration Technology Engineering Center, China

**Hai-cheng Liu**

School of Civil Engineering, Tianjin University, China

National Engineering Laboratory for Port Hydraulic Construction Technology, Tianjin Research Institute for Water Transport Engineering, China

**Jing Qu**

National Engineering Laboratory for Port Hydraulic Construction Technology, Tianjin Research Institute for Water Transport Engineering, China

**Xiao-song Li**

National Engineering Laboratory for Port Hydraulic Construction Technology, Tianjin Research Institute for Water Transport Engineering, China

### ABSTRACT

*The construction of a water intake along the wharf shoreline can realise the intensive and comprehensive utilisation of the shoreline. However, since the water intake will increase the lateral flow at the wharf and also the hydrodynamic forces on ships, it will bring risks to ships mooring and leaving. The effects of the water intake on ships are studied using a physical model, numerical model and standard formulas. The results show that it leads to an increase of the hydrodynamic forces acting on the ship when the standard formulas are used to calculate the forces without considering the water level difference between the two sides of the ship. The results of the physical model are closer to the real situation. Measures that can effectively reduce the influence of the water intake on ships are proposed by increasing the distance between the wharf front and the front of the water intake as well as the depth of the water inlet windows.*

**Keywords:** water intake, physical model, numerical model, lateral flow, hydrodynamic force

### INTRODUCTION

A section of coastline is planned for the construction of a large-scale wharf. However, it is also intended to build a water intake in a section of the shoreline area to serve the needs of power plants and desalination projects. This will enable the comprehensive utilisation of the shoreline. The water intake will increase the lateral flow at the wharf and also the hydrodynamic forces on ships. It will have some impact on the security of the mooring and berthing operation of ships.

In previous research, Huang studied the incorporation engineering of the Xiamen Eastern Natural Gas Power Plant water intake and the 1<sup>st</sup> berth in the eastern port [5]. Liu et al.

investigated the interaction between the 50000 ton (t) coal unloading wharf of Suizhong Power Plant and the water intake using a numerical model [6]. A study of the hydraulic structures of the water intake of the second phase of the Dongjiakou Huaneng project in Qingdao Harbour has been carried out by Liu and Qiao [7]. Xie et al. reported the influence of the construction of a water intake on flood defences [10]. Xie and Wu checked the water intake status of Jiaying Power Plant in Zhejiang Province and determined the reasons for a temperature rise [11]. Ge compared three wharf layouts of Anqing Power Plant, and the one which combines the water intake was recommended [2]. The eclipsed form and march-past method of water intake-outlet arrangements in a power



## TWO-DIMENSIONAL NUMERICAL MODEL FOR TIDAL CURRENT

The governing equations consist of the following continuity and momentum equations:

$$\frac{\partial h}{\partial t} + \frac{\partial(hu)}{\partial x} + \frac{\partial(hv)}{\partial y} = 0 \quad (1)$$

$$\frac{\partial hu}{\partial t} + \frac{\partial hu v}{\partial y} + \frac{\partial}{\partial x} (hu^2 + \frac{1}{2} gh^2) = gh(S_{fx} + S_{0x}) + f_c hv + f_w \sqrt{w_x^2 + w_y^2} w_x + S_{vx} \quad (2)$$

$$\frac{\partial hv}{\partial t} + \frac{\partial hu v}{\partial x} + \frac{\partial}{\partial y} (hv^2 + \frac{1}{2} gh^2) = gh(S_{fy} + S_{0y}) - f_c hu + f_w \sqrt{w_x^2 + w_y^2} w_y + S_{vy} \quad (3)$$

where  $u$  and  $v$  are the depth-averaged velocity in the  $x$  and  $y$  direction, respectively;  $g$  is the gravitational acceleration;  $h$  is the water depth;  $S_{fx}$  and  $S_{fy}$  are the bottom friction term in the  $x$  and  $y$  direction, respectively;  $S_{0x}$  and  $S_{0y}$  are the bottom slope term in the  $x$  and  $y$  direction, respectively;  $f_c$  is the Coriolis parameter;  $w_x$  and  $w_y$  are the wind speed in the  $x$  and  $y$  direction, respectively;  $f_w$  is the wind drag coefficient;  $S_{vx}$  and  $S_{vy}$  are the horizontal viscosity term in the  $x$  and  $y$  direction, respectively. The tidal elevation is imposed on the open boundary. The normal velocity is set to zero at the land boundaries. The initial sea level and velocity are set to zero.

## OVERVIEW OF PHYSICAL MODEL TEST EQUIPMENT AND MEASUREMENT SYSTEM

The ship model and the physical model are designed according to the gravitational similarity criterion. The geometric scale of the model is determined to be 80 according to the test site, ship scale and water flow. A pump is used for water supply. The water level is accurately measured by the probe. The flow rate of the water intake is controlled by a weir. The flow velocity is accurately measured by a Vectrino ADV. In the model, the length of the harbour is 25 m and the width is 15 m. There are also 32 water inlet windows for each water intake. There are 28 windows with a hole size of 0.053 m × 0.053 m, and 4 windows with a temporary hole size of 0.046 m × 0.046 m. The elevations of the water inlet windows for the three projects are -0.075 m, -0.1 m and -0.125 m, respectively. The flow rates of both intakes 1<sup>#</sup> and 2<sup>#</sup> are 1.84 L/s and are controlled by weirs and valves. The layout of the physical model can be seen in Fig. 4. The model ship is similar in scale to the prototype vessel and is shown in Fig. 5. The ballasting method is utilised, i.e., the appropriate weight is placed in the right place. This meets the weight and distribution requirements and ensures that the draught and displacement are similar. The measurements and data recording start after the pumping flow rate becomes steady.

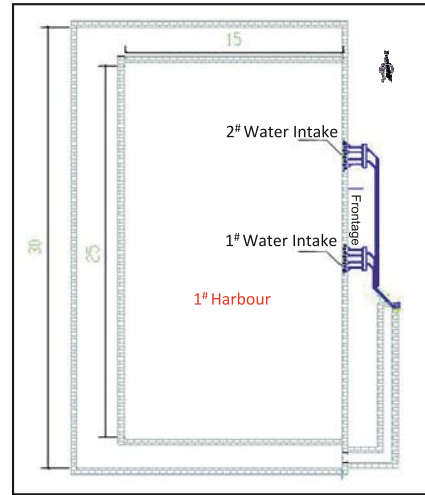


Fig. 4. Layout of the physical model



Fig. 5. Ship model in the test

The impacts of mooring ships on the water intake of a power plant are investigated. The water level in the connecting shaft and the flow rate around the water intake are measured when different types of ships dock at the front of the wharf. The tests include: flow rate measurement and flow regime observation around the water intake in the condition of no ship; flow rate measurement at the water inlet windows in the condition of no ship; water level measurement at the ship side, water intake and in the connecting shaft when different types of ship dock.

The effects of the water intake on the mooring and berthing operation of ships are studied. The hydrodynamic forces on different types of ship are measured in conditions of different elevation schemes for the water inlet windows.

## STANDARD FORMULAS FOR HYDRODYNAMIC FORCE ON SHIP

The hydrodynamic forces on a ship usually include lateral force, longitudinal force and yaw moment. For the bollard pull required, the maximum lateral forces exerted by a crosswise current are important. In order to calculate the lateral force, the standard formula recommended by Tug Use in Port:

A Practical Guide [4] and also Design Code of General Layout for Sea Ports [8] is given:

$$F_{yc} = 0.5C_{yc}\rho V^2 L_{BP}T \quad (4)$$

where  $F_{yc}$  is the lateral force;  $C_{yc}$  is the lateral force coefficient;  $\rho$  is the density of water;  $V$  is the flow velocity;  $L_{BP}$  is the length between perpendiculars;  $T$  is the draft. The  $C_{yc}$  differs according to a ship's underwater shape, draft, trim and angle of attack, and is also affected strongly by the under-keel clearance. Therefore, a simplified formula is applied in this paper:

$$F_{yc} = 150V^2 L_{BP}T \quad (6)$$

This requires that the under-keel clearance is about 20% of the ship's draft. It should be mentioned that the outcome is given in kilograms (kg) instead of Newtons (N).

## RESULTS AND DISCUSSION

### TIDAL CURRENT

The flow fields at maximum flood and ebb tide are shown in Fig. 6 and Fig. 7. It is suggested that the flow in the harbour is restricted by the boundary and the flow direction is almost north–south. It is also weak due to the existence of the breakwater at the entrance. The maximum velocity is less than 0.2 m/s.

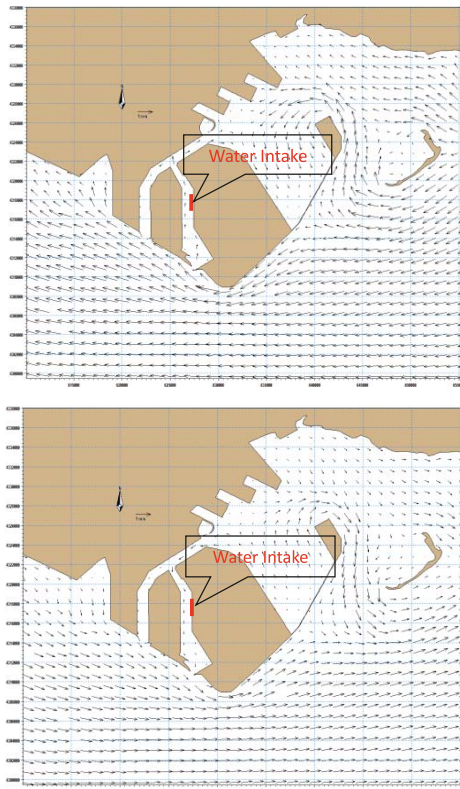


Fig. 6. Flow field at maximum flood tide (Top) and maximum ebb tide (Bottom)

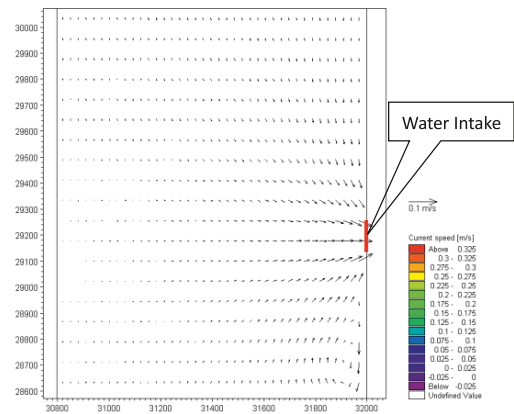


Fig. 7. Flow field near the water intake at maximum flood tide

The model results also show that the water intake has a small effect on the flow. The maximum change of velocity is 0.02~0.03 m/s at 50 m in front of the wharf and the influence range is within 150 m in front of the wharf.

### PHYSICAL MODEL TEST

The flow velocity near the water intake is measured first. Fig. 8 gives the flow field at the maximum flow rate of the water intake. It should be mentioned that the results have been converted into prototype units hereinafter. This indicates that the flow velocity is larger in the middle of the two water intakes and it decreases on the two sides. The maximum velocity at the water inlet windows is about 0.30 m/s and the average velocity is 0.19 m/s. This is less than 0.35 m/s, which is the velocity limit of ship operation. The flow velocity is no more than 0.10 m/s at a distance of 64 m and farther. The velocity distribution in the vertical direction is smaller for the surface layer and the bottom layer. It is also compared with the numerical simulation. It shows that the measured maximum velocity is a little larger than the simulated one in front of the wharf without the ship.

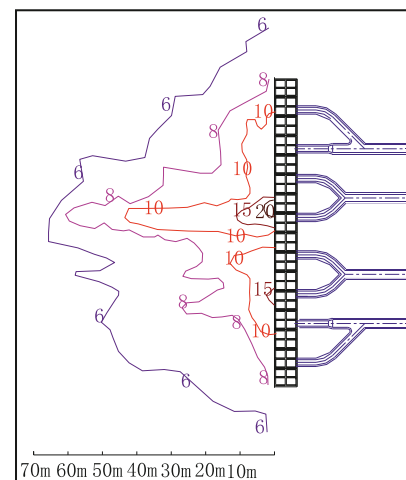


Fig. 8. Flow field near the water intake (0.01m/s)

Then the effect of the positions of different ships on the water level in the connecting shaft is investigated. The position of the vessel relative to the water intake and the position of the probes are shown in Fig. 9. The results of water level measurement without a ship and with different types of ship are given in Table 2. It can be seen that the bigger the berthing ship, the greater the impact on the water level in the connecting shaft. The 150000 DWT container ship and the bulk carrier berthing just in front of the wharf (ignoring the fender effect, i.e., the distance between the ship and wharf front is 0.0) have the largest impact on the water level in the connecting shaft. The water level is reduced by about 0.24 m relative to the non-ship condition for the 150000 DWT container ship and about 0.26 m for the 150000 DWT bulk carrier. For the 20000 DWT general cargo ship, the water level in the connecting shaft is basically the same as that when there is no ship. The maximum difference is no more than 0.02 m. It is also demonstrated that the farther away from the wharf, the smaller the influence on the water level in the connecting shaft. When the distance exceeds 5 m, there is almost no influence.

Tab. 2. Water level measurement with and without ship

Conditions		Probe number		
		1#	2#	3#
Water level (no ship, m)		0.53	0.53	0.53
Ship type	Distance between ship and wharf front (m)	Water level reduction relative to the non-ship condition (m)		
150000 DWT container ship	0.0	0.02	0.02	0.24
	1.0	< 0.01	< 0.01	0.07
	2.0	< 0.01	< 0.01	0.02
	4.0	< 0.01	< 0.01	< 0.01
150000 DWT bulk carrier	0.0	0.02	0.02	0.26
	1.0	< 0.01	< 0.01	0.07
	2.0	< 0.01	< 0.01	0.02
	4.0	< 0.01	< 0.01	< 0.01
20000 DWT general cargo ship	0.0	< 0.01	< 0.01	0.02
	1.0	< 0.01	< 0.01	< 0.01

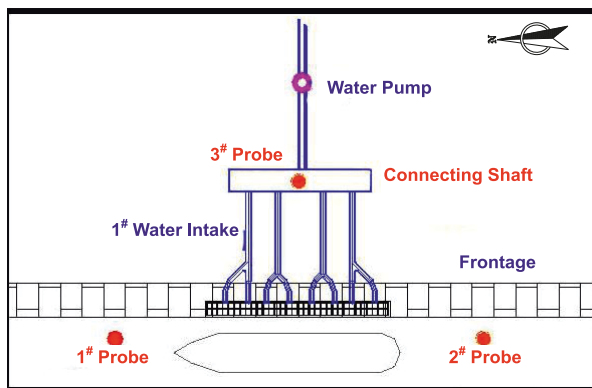


Fig. 9. Water level measurement in the test

The lateral forces on different types of ship in full load condition are measured under different elevation schemes for the water inlet windows. The results are shown in Table 3 and Fig. 10. The unit of the lateral force has been converted from kg to t. It is shown that the larger the distance between the ship and the wharf front is, the smaller the lateral force is. Taking the 150000 DWT container ship in Project 3 as an example, the lateral force on the ship is 129.5 t, 103.9 t and 81.4 t at a distance of 1.0 m, 1.8 m and 2.5 m, respectively. It is also found that the lower the location of the water inlet windows is, the smaller the lateral force is. For example, when the distance from the wharf front is 1.0 m, the lateral force on the 150000 DWT container ship is 198.1 t, 141.8 t and 129.5 t at the elevation of -6 m, -8 m and -10 m, respectively.

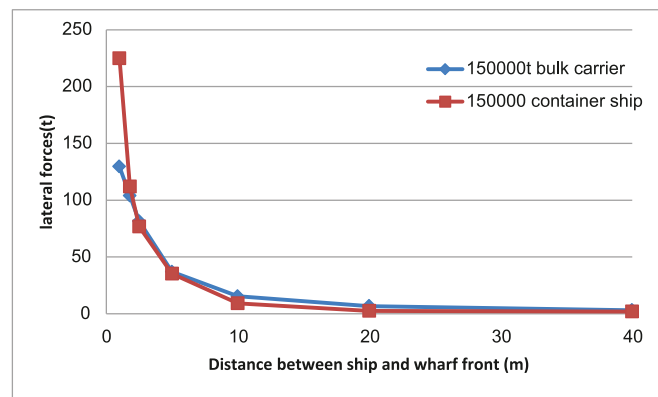


Fig. 10. Measured lateral force in the test (Project 3)

Tab. 3. Measured lateral force in the test

		Ship type	Distance between ship and wharf front (m)	Lateral force (t)
Project 1	150000 DWT container ship		1.0	198.1
			1.8	157.2
			2.5	108.5
			5.0	63.0
			10.0	18.4
			20.0	8.2
			40.0	4.6
	150000 DWT bulk carrier		1.0	224.8
			1.8	112.1
			2.5	76.8
			5.0	35.3
			10.0	9.2
			20.0	2.6
			40.0	2.0

	Ship type	Distance between ship and wharf front (m)	Lateral force (t)
Project 2	150000 DWT container ship	1.0	141.8
		1.8	102.4
		2.5	77.3
		5.0	37.9
		10.0	18.4
		20.0	8.2
		40.0	4.1
	150000 DWT bulk carrier	1.0	160.9
		1.8	73.2
		2.5	55.3
		5.0	21.5
		10.0	9.7
		20.0	2.6
		40.0	1.0
Project 3	150000 DWT container ship	1.0	129.5
		1.8	103.9
		2.5	81.4
		5.0	36.9
		10.0	15.4
		20.0	6.7
		40.0	3.1
	150000 DWT bulk carrier	1.0	136.0
		1.8	83.1
		2.5	57.0
		5.0	22.5
		10.0	9.2
		20.0	1.0
		40.0	0.5

The calculated lateral forces using Eq. are given in Table 4. The flow velocity is set as 0.2 m/s in terms of the numerical model results. It can be seen that the calculated lateral force in the full load condition is quite different from the measured one when the ship is very close to the wharf front. For example, the calculated lateral force is only 31.0 t, while the measured is 224.8 t for the 150000 DWT bulk carrier in Project 1. The latter is about 7.3 times as large as the former. The reason for the gap is that the lateral force calculated by the standard formula does not take into account the difference in the water level on either side of the ship. The flow structure is changed near the wharf front due to the presence of the ship and the force increases. The force induced by the difference of water level on the two sides of the ship cannot be ignored. When the ship is far away from the wharf, the water level difference between the two sides of the ship decreases rapidly. When the distance reaches 5.0 m, it can be seen that the lateral force calculated by the standard formula is equivalent to that measured by the test.

Tab. 4. Calculated lateral force using the standard formula

Ship type	Lateral force (t)
150000 DWT container ship in full load condition	35.2
150000 DWT container ship in ballast condition	24.2
150000 DWT bulk carrier in full load condition	31.0
150000 DWT bulk carrier in ballast condition	14.9

## CONCLUSIONS

The physical model, numerical model and standard formulas are applied to investigate the influence of a water intake along the wharf shoreline on ships. The conclusions and suggestions are as follows. The flow velocity in the harbour is small. The influence range of the water intake on the flow field is only near the water inlet windows. The distance between the ship and wharf front and the location of the water inlet windows have impacts on the hydrodynamic forces acting on ships. The larger the distance and the lower the location is, the smaller the lateral force is. Therefore, the increment of distance between the wharf front and the front of the water intake, as well as the depth of the water inlet windows, are effective measures to reduce the influences of the water intake on ships. It is suggested that the fender size should be adjusted in the wharf design so that the distance between the wharf front and the front of the water intake is at least 5.0 m. Meanwhile, the elevation scheme for the water inlet windows in Project 3 should be utilised. It is also advised that the wharf structure should be adjusted from gravitational caissons to a high-piled wharf in order to reduce the lateral force.

## REFERENCES

- Cheng Y., Ying B. (2007): *Numerical Simulation and Comparison of Water Intake-outlet Methods in Power Plants*. Journal of Hydrodynamics, Ser. B, 5, Vol. 19, 623-629.
- Ge D. J. (2014): *Comparative Analysis of Advantages of Anqing Power Plant's Pier Site Options*. Port & Waterway Engineering, Vol. 10, 76-80.
- Hamrick J. M., Mills W. B. (2000): *Analysis of Water Temperatures in Conowingo Pond as Influenced by the Peach Bottom Atomic Power Plant Thermal Discharge*. Environmental Science & Policy, Vol. 3, Supplement 1, 197-209.
- Hensen C. H. (2003): *Tug Use in Port: A Practical Guide*. The Nautical Institute, London.
- Huang W. L. (2005): *Study on Incorporation Engineering Harmonizing Building of Water-taking Gap of Power Plant in Eastern Xiamen and Berth #1 of Eastern Port Area*. Port & Waterway Engineering, Vol. 8, 30-34.

6. Liu F., He F. B., Liu T. (2015): *Mutual Influence Research on Suizhong Power Plant 50 000 Tons Engineering and Plant Water Intake*. Port Engineering Technology, 7, Vol. 52, 6-9.
7. Liu Q., Qiao W. (2014): *Feature and Innovation of Hydraulic Structure in Huaneng Second Engineering Dongjiakou Qingdao*. China Water Transport, 12, Vol. 14, 275-276.
8. Ministry of Transport of the People's Republic of China (2013): *Design Code of General Layout for Sea Ports*. JTS 165-2013, Beijing.
9. Wang Y. S., Politano M., Ho H. C., Muste M., Michell F., Stallings J. (2014): *Assessment of Ice Plugging of a Cooling Water Intake by a Numerical Model*. Journal of Hydraulic Research, 8, Vol. 52, 81-92.
10. Xie C. S., Yu W. Q., Yu M. H. (2005): *Calculation and Analysis of Influence on Flood Control by Port and Intake Construction*. South-to-North Water Transfers and Water Science & Technology, 4, Vol. 3, 54-58.
11. Xie D. F., Wu X. G. (2013): *Present Situation and Influence Factors of the Drainage and Water Intake in Jiaying Power Plant*. Zhejiang Hydraulics, Vol. 2, 50-52.
12. Zeng P., Chen H., Ao B., Ji P., Wang X., Ou Z. (2002): *Transport of Waste Heat from a Nuclear Power Plant into Coastal Water*. Coastal Engineering, 1, Vol. 44, 301-319.

## CONTACT WITH THE AUTHORS

### Xian-wei Kong

*e-mail: tkykxw@vip.126.com*

School of Civil Engineering, Tianjin University,  
No. 92, Weijin Road, 300072 Tianjin

**CHINA**

National Engineering Laboratory for Port Hydraulic  
Construction Technology, Tianjin Research Institute  
for Water Transport Engineering,  
MOT, 300456 Tianjin

**CHINA**

### Lei Ding

*e-mail: leiding2012@tust.edu.cn*

College of Marine and Environmental Sciences, Tianjin  
University of Science & Technology,  
No. 29, 13th Avenue, TEDA, 300457 Tianjin

**CHINA**

Tianjin Marine Environmental Protection and Restoration  
Technology Engineering Center,  
300457 Tianjin

**CHINA**

### Hai-cheng Liu

*e-mail: 85379533@qq.com*

School of Civil Engineering, Tianjin University,  
No. 92, Weijin Road, 300072 Tianjin

**CHINA**

National Engineering Laboratory for Port Hydraulic  
Construction Technology, Tianjin Research Institute  
for Water Transport Engineering,  
MOT, 300456 Tianjin

**CHINA**

### Jing Qu

*e-mail: 554154837@qq.com*

National Engineering Laboratory for Port Hydraulic  
Construction Technology, Tianjin Research Institute  
for Water Transport Engineering,  
MOT, No. 2618, Xingangerhao Road, 300456 Tianjin

**CHINA**

### Xiao-song Li

*e-mail: 395192415@qq.com*

National Engineering Laboratory for Port Hydraulic  
Construction Technology, Tianjin Research Institute  
for Water Transport Engineering,  
MOT, No. 2618, Xingangerhao Road, 300456 Tianjin

**CHINA**